GL01181

PHOENIX Geophysics Inc.

(303) 425-9353

4891 INDEPENDENCE STREET SUITE 270 WHEAT RIDGE, COLORADO 80033

OIL AND GAS EXPLORATION

USING

SPECTRAL INDUCED POLARIZATION

Phoenix Geophysics has designed a highly efficient and reliable system for conducting Spectral Induced Polarization (SIP) surveys for oil and gas exploration. The application has been developed during an extensive research project in 1981 and 1982. SIP surveys have been conducted over a number of known oil and gas fields in the United States and Canada. Well defined resistivity and IP anomalies have been observed coincident with nearly every field studied. These anomalous features are thought to be due to geochemical alteration of the rocks overlying hydrocarbon accumulations.

The geochemical alteration may include deposition of fine grained pyrite which would explain the observed IP anomalies. The reactions by which pyrite can be deposited are well understood, and are summarized in the accompanying diagram. What is not well understood at the present time is the driving force by which the reductants (H_2S or CH_4) are transported upward from the hydrocarbon reservoir into the overlying rocks. It is probable that a combination of processes are operative, including diffusion, buoyancy, and water flushing. The same phenomena probably are responsible for the low resistivity anomalies which are commonly observed. These resistivity anomalies may be in some way associated with highly conductive oil field brines.

Head Office: 200 Yorkland Blvd., Willowdale, Ontario, Canada M2J 1R6 (416) 493-6350
214-744 West Hastings St., Vancouver, British Columbia, Canada V6C 1A6 (604) 669-1070

Of all the "unconventional" techniques which have been developed for hydrocarbon exploration, SIP may be the most sensitive and the most reliable. The reasons for this are two-fold. SIP surveys could be considered as a geochemical tool which can detect small concentrations of pyrite contained in rocks within several thousand feet of the earth's surface. Because such large volumes of rock are involved, sampling errors and near surface fluctuations can be avoided. The second advantage is that SIP would measure cummulative effects rather than present day flows or concentrations. The volume precent of pyrite deposited would depend on the length of time that the seepage phenomena persisted in addition to its intensity.

The equipment used for SIP surveys was designed and manufactured by Phoenix Geophysics. The receiver, the IPV-3, is the most efficient SIP receiver commercially available. It utilizes six voltage channels for simultaneous measurement on six different dipole separations. It also uses automatic switching between frequencies to further speed the measurements. The transmitter, the IPT-3, is the most powerful transmitter ever built for SIP surveys. The high currents attainable (up to 95 Amperes) over the frequency range d.c. to 128 Hz enable high quality data to be gathered with fewer stacks and in less time than any other system.

Phoenix Geophysics will soon have the capability to transfer data on a daily basis from the field to it's Denver office, using Telenet. This will enable geophysicists in the Denver office to provide over-night direction to field personnel.

The Phoenix SIP system operates over a wide frequency range, typically 1/32Hz to 128Hz. These broadband measurements are required in order to separate the IP response from the electromagnetic or induction effects which are encountered in sedimentary environments. In addition, it appears that the response of well casings and metal pipes can in some cases be separated from the IP response. The accompanying figures show observed spectral data obtained with the following:

1) fine grained pyrite in a hand specimen, measured in the laboratory,

2) fine grained pyrite measured with short dipole length to reduce EM coupling.

3) typical field example from a sedimentary environment displaying an anomalous IP response,

4) typical field example from a sedimentary environment showing background IP response,

5) typical field example from a sedimentary environment showing well casing response.

Fine grained pyrite produces a maximum IP response usually at a frequency of 1Hz or greater. When similar mineralization is encountered in the field, electromagnetic effects are superimposed on the data. The amount of electromagnetic coupling increases as the dipole length increases. Because of the weak IP response often encountered, and because of the strong electromagnetic coupling, data must be gathered over a broad frequency range in order to separate the two effects. Well casings and pipes studied to date have a response different enough from the IP response of fine grained pyrite that their influence can be recognized and sometimes eliminated in the data processing.

The field studies which have been completed to-date are part of a research project sponsored by the following oil companies:

Sohio Petroleum Company
Chevron Resources Company
Phillips Petroleum Company
Marathon Oil Company
Sunmark Exploration Company
Texaco U. S. A.
Amoco Prod. Company
Union Oil Company of California
Superior Oil Company
PanCanadian Petroleum Limited
Aquitaine Company of Canada Limited
Canadian Hunter Exploration Limited
Hudson's Bay Oil and Gas Company Limited
Gulf Research & Development Company

The results obtained from the various sites are confidential. They cannot be released at the present time except to representatives of the above companies. The observed response, however, can be described as follows. Oil fields often show weak to moderate resistivity lows and weak to moderate IP highs. These features are not always directly above the reservoirs, but

are sometimes offset laterally.

The results obtained so far in the research project are encouraging. Spectral Induced Polarization may be a reliable technique for indirect detection of oil and gas deposits. With its six-channel receiver and high power tranmitter, Phoenix Geophysics is able to provide this exploration service in the most cost effective manner currently available to the oil industry.

Explanation of Figures

The five figures showing SIP data are described as follows. Observed amplitude (O) and observed phase angle (+) are plotted versus frequency, with logarithmic scales used for each variable. The broad symmetric phase peaks represent the IP response. The steeper curves with peak at high frequency represent the component due to electromagnetic coupling. The sum of the two individual components is the total observed response. The difference between anomalous and background IP response can be fairly subtle and show up mainly in the phase at low frequency.

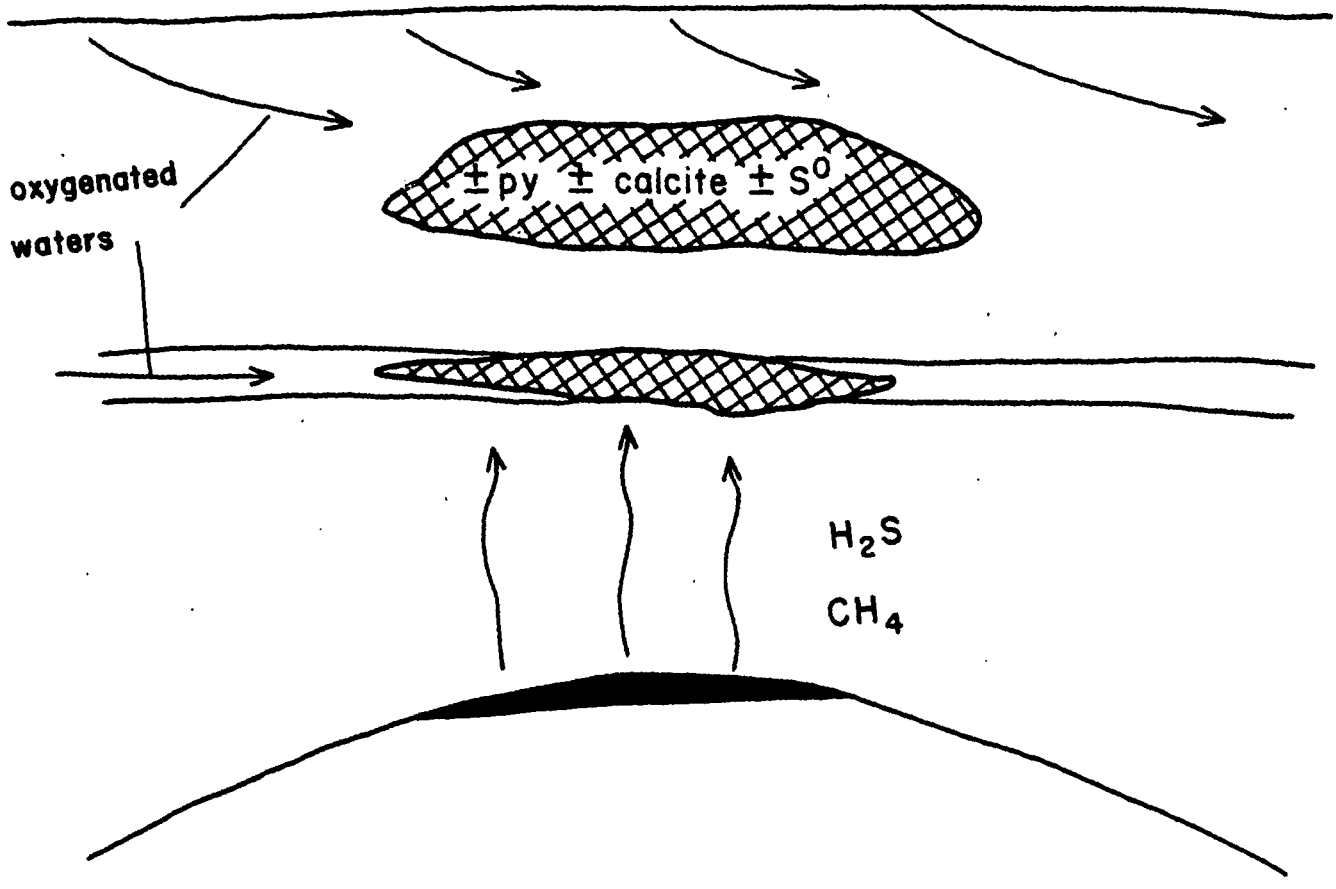

$$CH_4 + \begin{cases} O_2 \rightarrow CO_2 \\ SO_4^{=} \rightarrow CO_2 + H_2S \end{cases} \rightarrow CaCO_3 + \begin{cases} Fe^{2+} \rightarrow FeS_2 \\ O_2 \rightarrow S^0 \end{cases}$$

HAND SPECIMEN WITH FINE GRAINED PYRITE

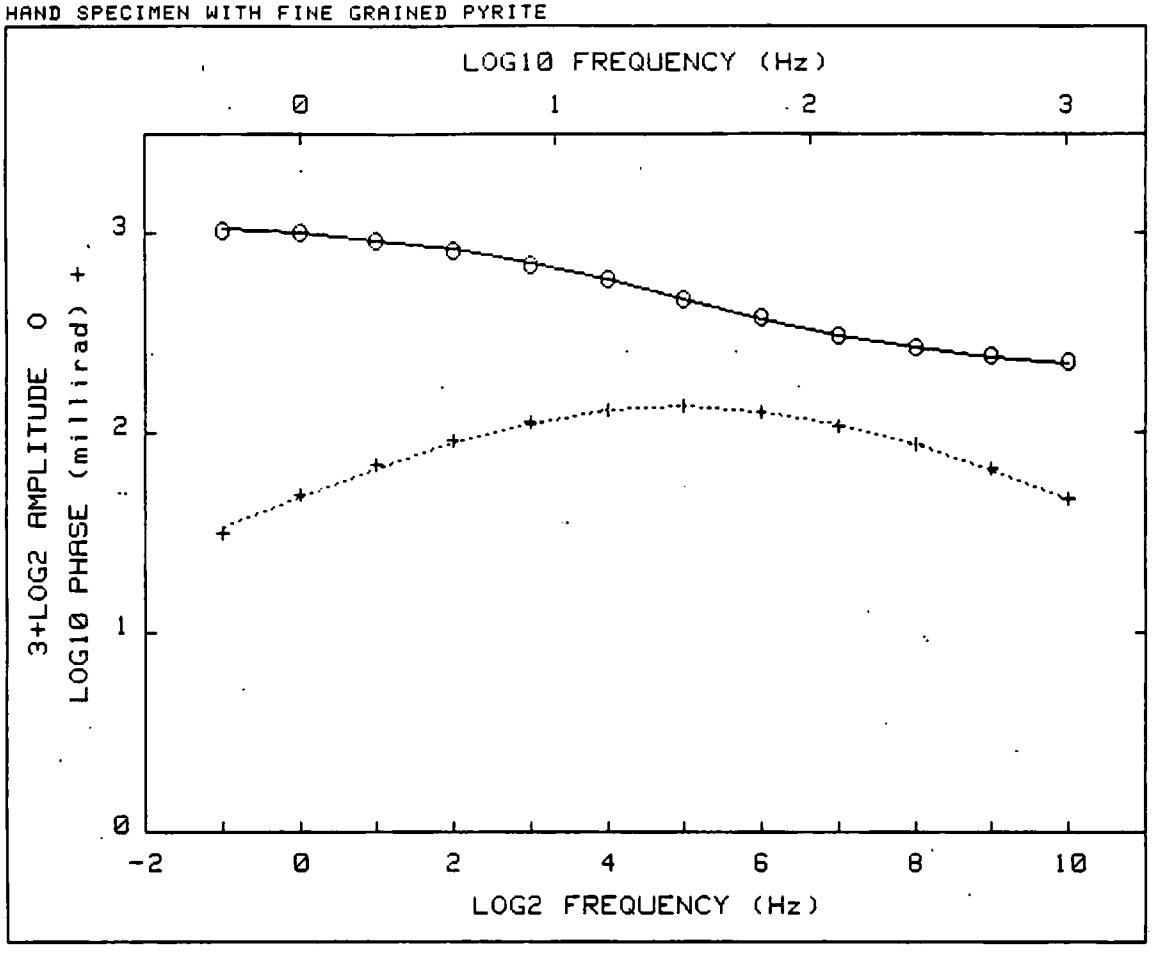

FINE GRAINED PYRITE - SHORT DIPOLE LENGTH

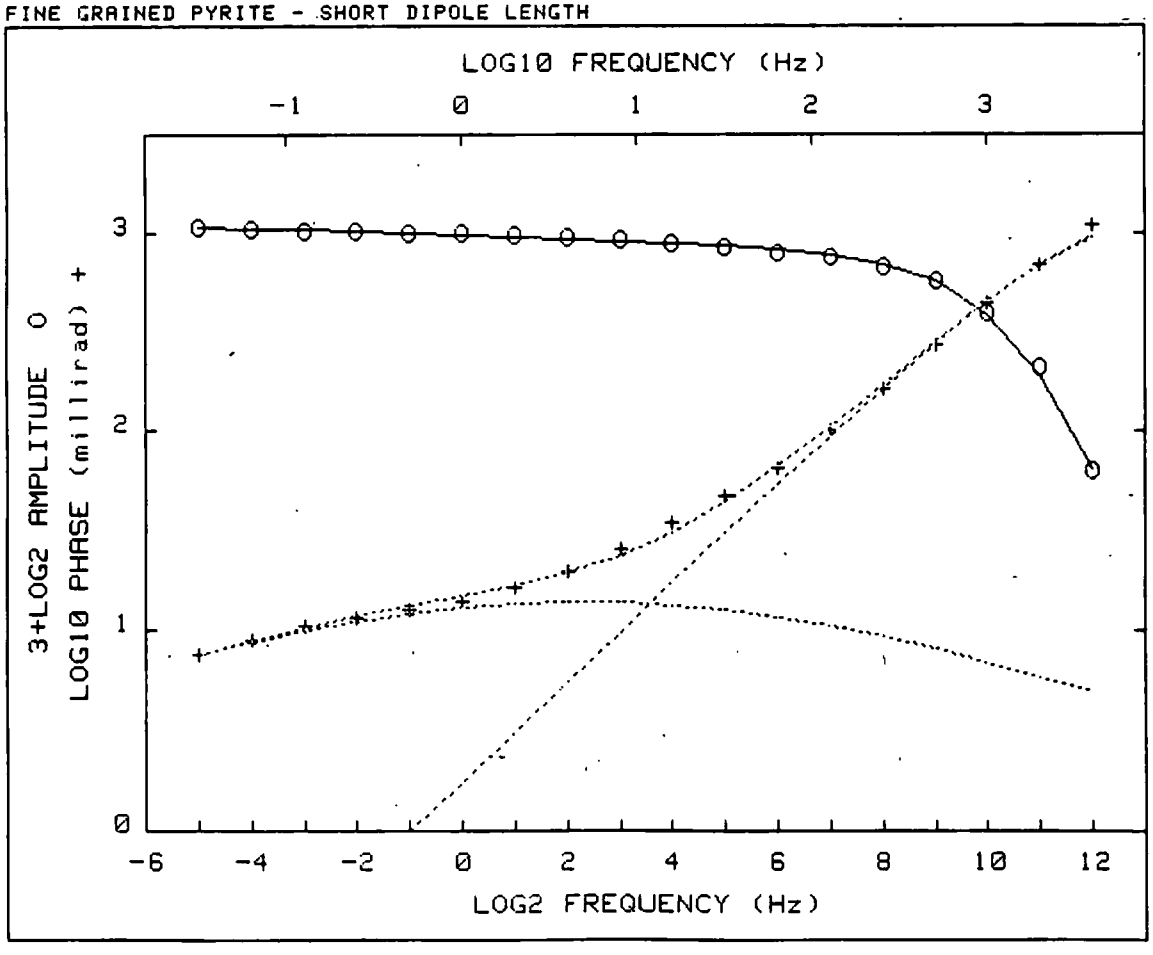

TYPICAL FIELD EXAMPLE WITH BACKGROUND IP RESPONSE

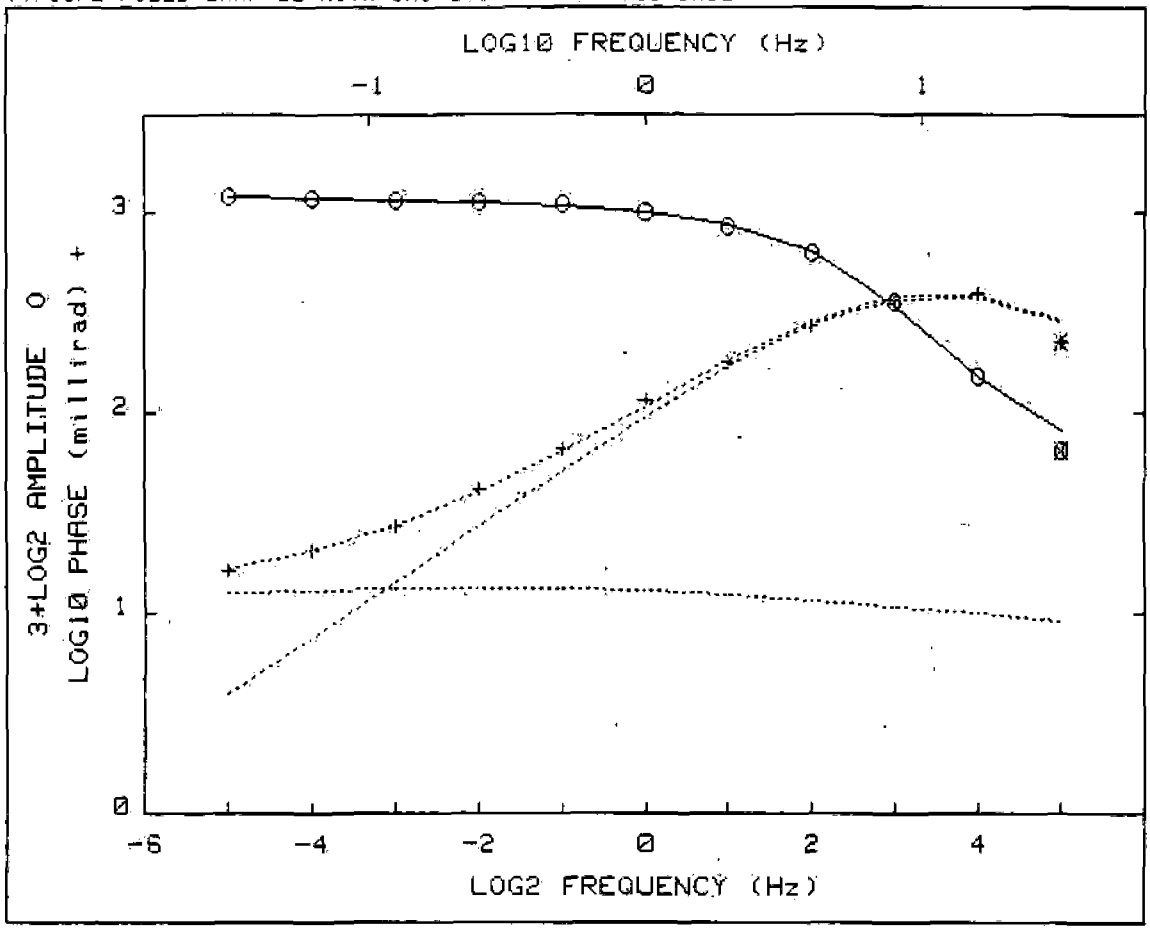

TYPICAL FIELD EXAMPLE WITH ANOMALOUS IP RESPONSE

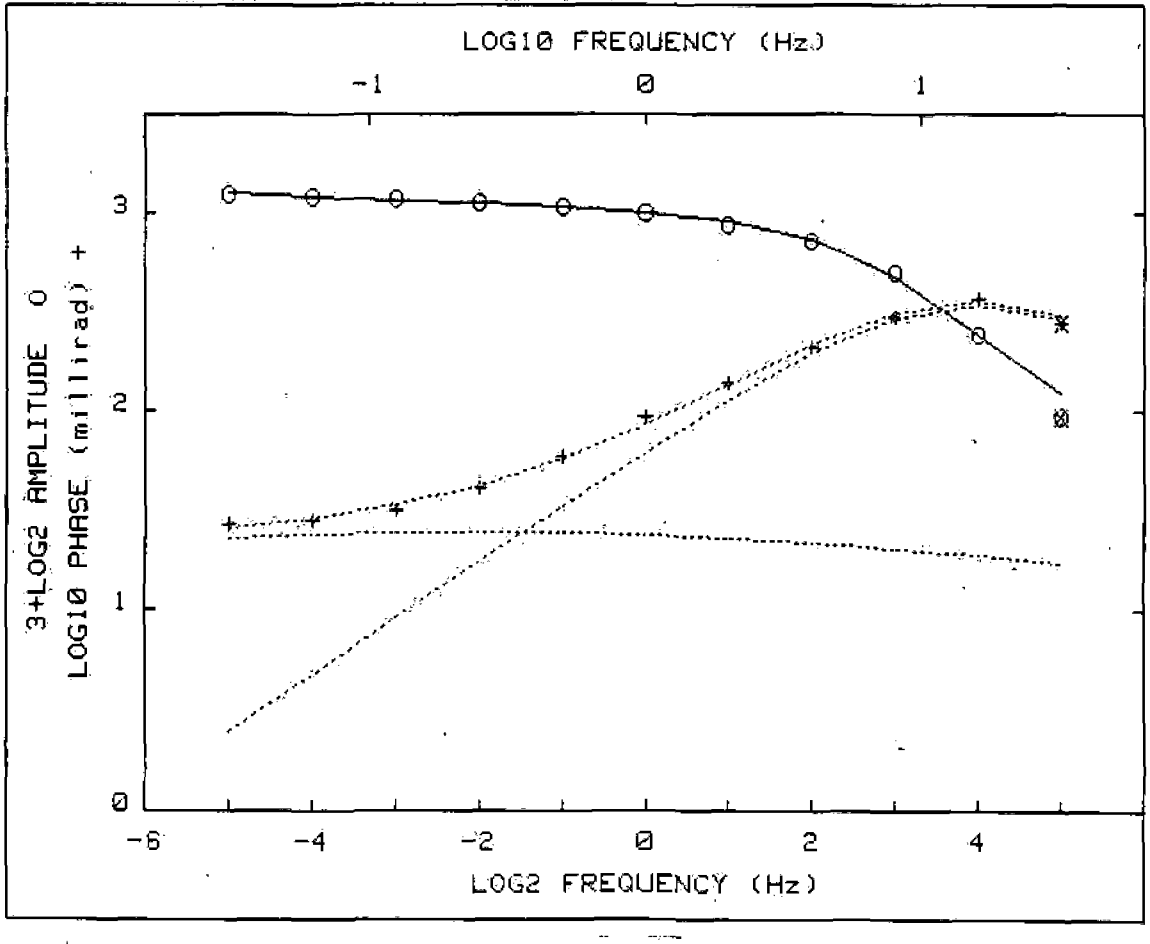

WELL CASING RESPONSE

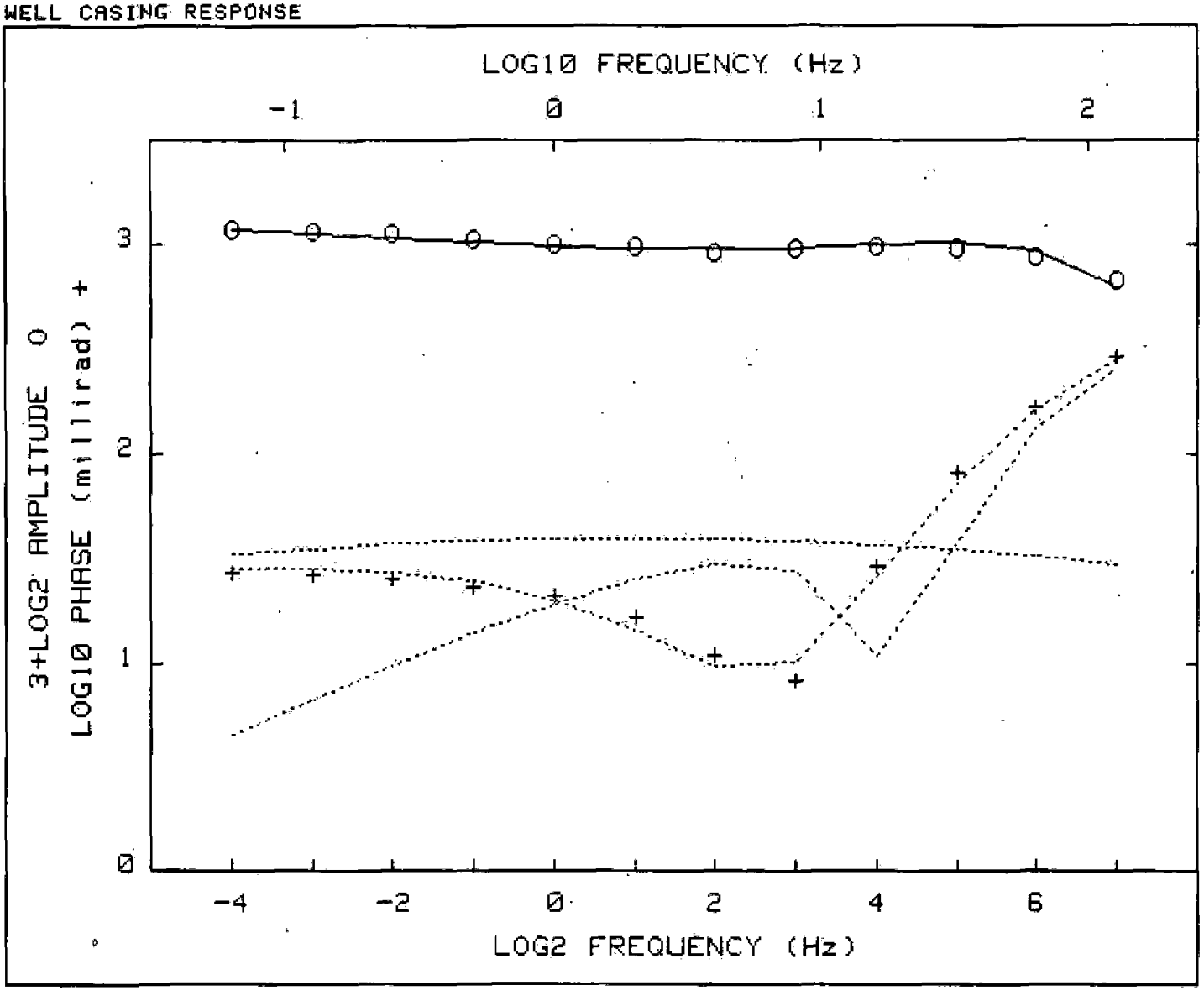

IPT-3 HIGH POWERED HIGH FREQUENCY TRANSMITTER

Specifications

Timing:	Standard IPT-1 waveforms in both time and frequency domain. Variable duty cycle is optional. Frequency range DC to 128Hz.
Power:	Nominal 100kw. 2000v/100A maximum. Can be driven by any 400Hz, three-phase, 208v motor generator from 15kw to 100kw.
Weight:	Approximately 800 lbs. (360 kg.) in two cabinets. Suitable for trailer/van/pickup truck mounting.
Current Regulation:	Approximately 0.1% within voltage/power constraints.
Other Features:	Open circuit to ground during time-domain "OFF" time.

IPV-3

Seven Channel Spectral IP Receiver

- **Simultaneous Measurement of Transmitter Current and Six Receiving Dipoles**
- **Microprocessor-Controlled Real-Time Signal Stacking and Averaging in Time and Frequency Domains**
- **Automatic Deconvolution at each Frequency**
- **Coherent Detection and Automatic Scan 2^{-14} to 2^{16} Hz**
- **Digital Filtering for High Cultural Noise Rejection**
- **Statistical Data Logged on Magnetic Tape and Alphanumeric Printer**

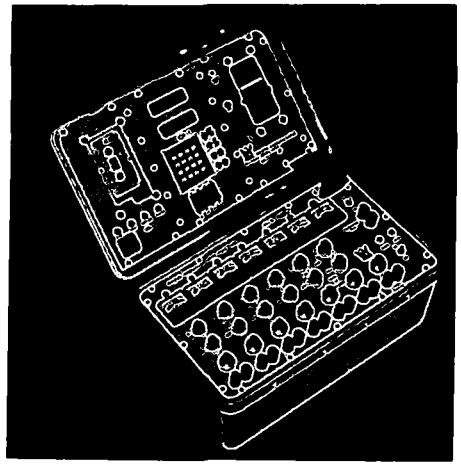

Specifications

INPUT

Channels : Seven input channels allow the current and six dipole voltages to be measured simultaneously.

Impedance : 1000 Megohms.

Protection : The input is protected from excessive voltages by a 10,000 ohm fuse resistor.

Ranges : 3V full scale to 30 microvolt full scale in eleven 10db steps.

SP Cancellation : Cancellation is manual in four ranges of $\pm$200 mV and $\pm$2V.

OPERATION

Frequencies : 2^{-14} Hz to 2^{16} Hz (.000061 Hz to 65536 Hz) in 31 binary steps. An automatic frequency scan is initiated by selecting Fhigh and Flow to be different values. The scan can step by a factor of 4 or by a factor of 2.

Transmitter Drive : The transmitter is slaved to the receiver timing circuitry through an isolated, RF modulated signal passed along a two conductor connecting cable.

Current Monitor : The exact shape of the transmitter waveform is continuously being relayed back to the receiver via a second isolated, RF modulated signal link. This monitoring capability is essential for high precision, broadband IP measurements.

Deconvolution : The physical quantity which we are attempting to determine is the resistivity transfer function. Since it is not possible to control kilowatts of power passing through unstable current electrodes to an accuracy of 1 part in 10000, it is necessary to monitor both current and voltage and then to deconvolve the current from the voltage to obtain the true spectral IP response. This deconvolution is carried out automatically in the IPV-3 at each frequency by dividing the voltage amplitude by the current amplitude and by subtracting the current phase from the voltage phase for all six voltage channels.

Operating Sequence : START sets the receiver and transmitter to 1 Hz and allows the operator to cancel SP and adjust gain for each channel.
ENTER is pressed after each of the operating parameters is input through the keypad.
- A averaging time
- B number of channels
- C current in amperes
- D dipole identification
- E electrode interval in meters
- F frequency range (Fhigh, Flow)

The six parameters are held in memory. Only a few are usually changed from station to station along a line.
PRINT prints out the six operating parameters if it is desired to check their values.
RUN starts the automatic frequency scan. The unit first measures, calculates and prints the resistivity at 1 Hz. It then proceeds to Fhigh, makes the required measurements, displays and prints the results, proceeds to the next frequency and so on, down to Flow.
TAPE is pressed if the scan is satisfactory and it is desired to make a tape copy of the results.

SIGNAL PROCESSING

Filtering : The filtering in the IPV-3 is entirely digital. Both 50 Hz and 60 Hz fall at notches in the digital filters.

Coherent Detection : The signal is stacked and averaged in real time. Signal to noise enhancement is proportional to the square root of the measurement time.

Standard Deviation : Averaging is carried out in the frequency domain as well as in the time domain. This permits accurate calculation of both the mean and standard deviation of the amplitude and phase.

PHOENIX GEOPHYSICS LIMITED

Geophysical Consulting and Contracting, Instrument Manufacture, Sale and Lease.

Head Office: 200 Yorkland Blvd., Willowdale, Ontario, Canada M2J 1R5
Telephone: (416) 493-6350 Telex: 06-986856 Cable: PHEXCO TORONTO

Vancouver Office: 214-744 West Hastings Street, British Columbia V6C 1A6 Tel: (604) 669-1070

Denver Office: 4891 Independence St., Suite 270, Wheatridge, Colorado, 80033, U.S.A. Tel: (303) 425-9393

Specifications

INPUT

Analog Display : A meter for each input channel allows easy adjustment of SP and gain.

Digital Display : Two six digit LCD displays provide continuous readout of the mean and standard deviation of the resistivity, phase or amplitude of any selected channel. Resistivity is calculated at 1 Hz and displayed in ohm-m. Phase is displayed from -PI radians to +PI radians with a resolution of 0.1 milliradian. The amplitude is normalized by its value at 1 Hz and is displayed with five digit resolution. The display is constantly refreshed with the latest stacked and averaged results.

Printer : A 12 character alphanumeric thermal printer records resistivity at 1 Hz and amplitude and phase and their standard deviations for each dipole at each frequency.

Tape Drive : The printed results are also stored on tape cartridge for plotting and further processing.

GENERAL

Temperature : Storage temperature range is -50°C to +70°C. Operating temperature range is -20°C to +50°C.

Humidity : The instrument is moisture proof and may be operated during light showers.

Altitude : -1600 m to 10000 m.

Vibration : Suitable for transport in light aircraft and bush vehicle.

Batteries : Six 9V transistor radio batteries are used for SP cancellation. Twelve 2V Gates 5.0 AH rechargeable X cells (PN 0800-0004) form the main 24V supply. Operating time without recharging is 8 hours at -20°C. Two 12V chargers are used for recharging.

Case : Fiberglass. This provides electrical insulation and freedom from tearing or denting.

Weight : 23 kg.

Dimensions : 25 x 42 x 36 cm.

Features

EXTREMELY BROAD FREQUENCY RANGE

The IPV-3 was designed to cover the entire frequency range of interest for electrical measurements. Its complete frequency range is nine decades.
With a top frequency of 65.5 kHz it can be considered a multifrequency EM unit as well as a spectral IP unit. High frequency measurements may be made very quickly, and provide useful, detailed data about the resistivity section. Pseudosection plots of the high frequency phase angles provide geometric as well as parametric EM information.
The lowest frequency of 1 cycle/4.5 hours is about as low as the most enthusiastic researcher would wish to go in determining, for example, the complete spectral response of graphite. The intermediate frequencies allow very accurate removal of electromagnetic coupling from IP data, and provide information on mineral type, which in certain situations can result in considerably more cost-effective exploration programs.

DESIGNED FOR BOTH RESEARCH AND PRODUCTION

The IPV-3 has been designed to be both an extremely powerful research instrument as well as the fastest production IP unit available. The conversion is accomplished simply by changing the limits of the frequency scan. Reconnaisance work might be carried out at a single frequency, in which case the measurements are extremely fast and accurate. If an anomaly is encountered, the scan may be widened to provide additional data useful for the evaluation and removal of inductive coupling, and useful for purposes of mineral discrimination.

SEVEN CHANNEL CAPABILITY

The multichannel capability of the IPV-3 can decrease measurement time by a factor of six over conventional units.

REAL TIME DECONVOLUTION

Any variations in the transmitter waveform are closely monitored and accurately compensated for. This is equivalent to continuous calibration of the transmitter electrodes. All calculations are made in real time. No measurement time is wasted waiting for the processor, even at 65 kHz.

MEAN AND STANDARD DEVIATION

Both mean and standard deviation are continuously displayed and recorded. Thus a constant record is maintained of the precision of the measurement. If the desired accuracy is achieved early, time can be saved by pressing NEXTF. The processor then prints the results and proceeds with the next frequency.

FLEXIBILITY

Electronic technology is changing at an extremely rapid rate. In order to guard against obsolescence, the IPV-3 was constructed as four modules comprising the input section, processor, printer and tape drive. Any one of these modules as well as cards within the modules may be up-graded in the field.
For truck-mounted operations or laboratory applications, the half of the IPV-3 which contains the input section may be directly connected via a 16 bit parallel interface to any Hewlett Packard 9800 series desktop computer. The other half of the IPV-3 is essentially a dedicated, low power, field portable substitute for a desktop computer.

SYSTEMS APPROACH

The IPV-3 was designed as part of a complete data acquistion, presentation and interpretation system. All data handling is entirely automated. Either an HP 9845 or 85 desktop computer may read the data stored on tape in the IPV-3. Currently two software packages are available:

SW-3: Pseudosection plotting and contouring
SW-4: Inductive coupling removal and Cole-Cole parameter fitting.

Further software for AMT, CSAMT and MT using the IPV-3 are projected for 1981.

Phoenix pioneering

New electrical method in oil hunt studied

By David J. Salter,
Marketing Manager,
Phoenix Geophysics Ltd.

Exploration for hydrocarbons is still based primarily upon the interpretation of seismic data, although in some situations gravity and/or magnetic data can also be of assistance to the geophysicist. Recent advances in digital electronics and the use of information theory have led to considerable improvements in seismic equipment, data gathering procedures and the interpretational techniques used, but with very few exceptions the interpretations are still limited to the delineation of favorable sedimentary structures, based upon the measurements of seismic velocities in the subsurface.

At the same time, there has been only a little progress made in any alternative technique that could be successfully employed to indicate the possible presence of hydrocarbons themselves. However, there have been suggestions that some characteristics of geophysical data, or of the rocks themselves, are possible phenomena which could be diagnostic, for example:

1) Color changes in the rocks above the hydrocarbon accumulation or color variations in the surface foliage due to volatile compounds emanating from the hydrocarbon pool.

2) Slight changes in the porosity of the overlying sediments due to alteration attendant with the passage through the rocks of such volatile compounds. These changes in the porosity might be expected to give rise to slight variations in the seismic velocity and the electrical resistivity of the rock column through which the volatile compounds have passed.

3) Direct detection at the surface of volatile gases (H_2S, SO_2 *etc.*) which may emanate from the hydrocarbon pool and escape to the surface.

4) The use of the electrical insulating properties of oil itself, within the otherwise quite conductive sedimentary section.

5) Formation of the metallic mineral pyrite in the sedimentary section above hydrocarbon accumulations. One mechanism for this would be the reduction of the iron oxide mineral hematite (almost always present in sediments) to the iron sulphide mineral pyrite by the action of H_2S.

Russian claims

This postulated mechanism would place the pyritized zone considerably closer to the surface than the hydrocarbon pool itself, and if this pyritic alteration zone were within the concentration limits and depth range of surface Induced Polarization and resistivity measurements it should be detectable. Indeed, Russian geophysicists claim to have measured increased Induced Polarization effects in the sedimentary column above hydrocarbon accumulations, compared to the effect measured at some distance to the side.

Having over 22 years' experience in the measurement of I.P. and resistivity parameters in the mineral environment, the geophysical and engineering staff of **Phoenix Geophysics** have commenced a thorough study aimed at testing this last hypothesis. With a view to the potential benefit of such a relatively low cost electrical method in hydrocarbon exploration, a number of major oil companies are supporting the project. These participants are providing access to an appropriate selection of survey sites which will yield data from a wide range of structures and environments. Phoenix is uniquely qualified for its role by virtue of the operating experience of its crew and the sophistication of the measurement hardware and interpretational software it has developed for mineral exploration.

The lower resistivity environment of the sedimentary basin has necessitated development of a 100 kw high power transmitter, but otherwise standard equipment and interpretational techniques are being used. The core of the system is the Phoenix IPV-3 Multi-Frequency Spectral I.P. Receiver, which has already proven its value in the mineral field. The large volumes of data acquired are processed initially on site to verify quality and to allow flexibility in the measurement program, but full analysis and interpretation is accomplished using the company's VAX-11/750 computer.

Over 45 sites have been selected throughout Alberta, British Columbia and 12 of the U.S. states, classified as "Mature," "Immature," "Prospect" or "Unknown." They are representative of typical geological structures, e.g. reef, channel sand, bar sand, anticline, fracture zone, which are of interest to the hydrocarbon

While the majority of sites are proprietary to individual participating oil companies, three are somewhat different, due to their association with the joint GEOSAT-NASA/JPL Test Case Program. This program flies potential spaceborne remote sensing systems over known deposits of hydrocarbons, uranium and porphyry copper, and as a supporting member of the GEOSAT Committee Phoenix has undertaken to provide geological ground-truth data for the following sites:

1) Coyanosa Field, Texas
2) Lost River, West Virginia
3) Patrick Draw, Wyoming

A major element of the satellite data for these sites is derived from the Thematic Mapper (T.M.) operating in the 1-3 micron region. By optimizing reflectance wave lengths the T.M. can regionally discriminate sedimentary rocks, alteration zones, metamorphic rocks and soils.

In parallel with the field measurements, a program of geochemical studies and laboratory measurements on chip samples is under way. This work will provide a better understanding of the geochemical environment in which pyrite may form, and enable development of a viable geochemical model which in turn will provide criteria for both future test site selection and data interpretation.

Over-all, this study is probably the most ambitious attempt to date to establish a sound scientific basis for many of the claims made by proponents of electrical methods for oil exploration. Such claims have frequently rested on hypotheses derived from empirical interpretation rather than hard data, but their existence would seem to indicate some record of success using some type of electrical measurement. But clearly, accurate interpretation of field data is not aided by false assumptions regarding the nature of the measurements.

At a time when high energy stakes justify enormous expenditures for "conventional" exploration, the development of a complementary, consistent, low-cost alternative based on data from a different measurement domain, is of extreme importance. Making no claims whatsoever at this point, Phoenix' work will surely be observed with more than casual interest by the oil and gas industry.

Economic Geology
Vol. 74, 1979, pp. 331–338

The Ontario Carbonatite Province and Its Phosphate Potential

GEORGE ERDOSH

Abstract

The only known concentration of carbonatite complexes in North America is in northern Ontario and western Quebec, in a petrographic province here named the Ontario Carbonatite Province. This petrographic province has some 50 known carbonatite complexes over an area of 1.3 million km². Almost all of the carbonatite bodies occur along recognizable major tectonic features, three of which are most probable, and one predicted. According to their ages, the carbonatite bodies belong to four groups; the two younger groups, dated 120 and 570 m.y., are restricted to the Ottawa graben, whereas the two older groups, dated 1,100 and 1,700 m.y., are situated along the Kapuskasing High and the Albany Forks and Carb structures. All four structures are major tectonic features probably related to the Mid-Continent High. No carbonatite complexes have been recognized to date along the Mid-Continent High in Minnesota and Wisconsin, but their existence is predicted.

A number of complexes were examined for their mineral potential. They all contain apatite in the carbonatite phase, in amounts of 5 to 25 percent, and some contain significant enrichments of apatite through leaching out of carbonates.

Such enrichment occurs on the Cargill complex, located on a branch structure off the Kapuskasing High. The complex contains a unique, very high grade residual phosphate deposit associated with a well-developed karst topography now buried under glacial lake clays. During karst development carbonates were dissolved from the carbonatite, and residual minerals, mainly apatite, were concentrated in sink holes and troughs. Sorting and reworking of apatite-rich residuum by surface and subsurface water formed concentrations of nearly pure apatite sand, locally several tens of meters thick. Unusual concentrations of rare earth minerals are present in a discontinuous thin blanket of secondary weathering products on top of the residuum. Widespread occurrences of vermiculite suggest further possible economic potential.

Introduction

THE carbonatite petrographic province[1] in the Precambrian Shield of northern Ontario and adjacent western Quebec is the only such province in North America, with a cluster of some 50 known carbonatite complexes. A few isolated carbonatite bodies also occur elsewhere on the continent in the younger fold belts but these are sporadic occurrences.

Due to their circular shape and distinct magnetic expression, most of these complexes were discovered during regional aeromagnetic surveys in the mid-1960s. Many of the complexes are poorly exposed or unexposed in this glaciated and heavily drift-covered terrane and chances are that some, lacking a strong magnetic signature and a circular shape, have escaped detection to date.

[1] In its strict definition neither the term "petrographic province" nor "tectonic province" should be used for this cluster of carbonatites since they intrude a wide range of rocks in various tectonic settings. Nevertheless the author feels that the term is justified, insofar as these complexes have a strong genetic link in space and time and they overprint the preexisting terrane by a petrographic province of their own.

The Ontario Carbonatite Province

Size and age

Inasmuch as the concentration of carbonatite bodies is mainly in Ontario, the name "Ontario Carbonatite Province" is proposed. The area of this petrographic province, as known to date, is some 1.3 million km². There is regional aeromagnetic coverage of excellent quality and detail throughout this area; thus the eastern, western, and northern limits are reasonably well known. The southern boundary, however, is not yet defined. Carbonatite occurrences stop abruptly at the Ontario-Minnesota border and at the northern shores of Lake Superior and Lake Huron. To the author's knowledge no carbonatite bodies are known in northern Minnesota, Wisconsin, or Upper Michigan, although alkalic rocks and one kimberlite body occur. The only carbonatite body reported, which may have a distant connection with the Ontario Carbonatite Province, is in Nebraska (Brookins et al., 1975). The fact that carbonatite bodies have not been discovered in the adjacent United States to date may be related to absence of good quality magnetic coverage and to the progressive southward deepening of the Paleozoic cover. Chances are thought to be

good for finding carbonatite bodies in this region especially in northeast Minnesota and northwest Wisconsin within the Mid-Continent Gravity High. Due to their relative susceptibility to weathering under the local climatic conditions, these assumed carbonatite bodies are expected to be poorly exposed or unexposed, and only detailed aeromagnetic surveys or drilling are likely to reveal them.

When age dating on 14 carbonatite bodies became available in 1967 (Gittins et al., 1967), it was recognized that the carbonatites fell into four age groups: near 1,700, 1,100, 570, and 120 m.y. Since that time four more carbonatite bodies have been dated (Bell and Watkinson, in prep.; Charbonneau, 1973; Doig and Barton, 1968) and these ages also fall close to the above dates (Table 1). A whole-rock Rb-Sr isochron by Owen and Faure (1977) has confirmed the general accuracy of earlier K-Ar dates on biotites at Lackner Lake.

Distribution

When the Ontario Carbonatite Province is viewed as a whole, several features become apparent. The first is the distribution of carbonatite bodies according to age. Complexes of the two younger age groups occur only in the southeastern part of the carbonatite province along the Ottawa graben described by Kumarapeli and Saull (1966) and Kumarapeli (1976), whereas the remainder of the dated complexes is north and west of this graben (see Fig. 1).

The apparent structural control of most of the carbonatite bodies is another noteworthy feature. Currie (1976) has noted and described such control for the alkalic rocks, including carbonatites, and he has given names to some major structures. However, he used the term "alkaline province" for each of these structures which is not only misleading but an incorrect use of the term. His names, thus, were not adopted in this paper.

TABLE 1. Carbonatite Ages in the Ontario Carbonatite Province

Carbonatite	K-Ar age (m.y.)	Reference
Oka	124	Fairbairn et al. (1963)
St. Honoré (Niobec)	564	Doig and Barton (1968)
Manitou	565	Lumbers (1971)
Mercier	973	Charbonneau (1973)
Big Beaver House	1,005	Gittins et al. (1967)
Clay-Howells	1,010	"
Nemegosenda	1,012	"
Firesand	1,048	"
Portage	1,069	"
Lackner	1,090	Lowdon et al. (1963)
Seabrook	1,103	Gittins et al. (1967)
Prairie	1,112	"
Schryburt	1,145	Bell and Watkinson (in prep.)
Argor	1,655	Gittins et al. (1967)
Goldray	1,695	"
Township 107	1,790	Watkinson and Grimes (1974)
Cargill	1,823	Gittins et al. (1967)
Carb	1,824	Bell and Watkinson (in prep.)

The most pronounced structural controls are the following.

1. The Ottawa graben along which at least nine carbonatite complexes from Oka to Iron Island are aligned and, although the graben was originally not postulated that far, the Township 107 and Seabrook complexes are also on a straight line in the extension of the graben, extending a distance of at least 750 km.

2. The Kapuskasing High, a gravity and magnetic high along a rift zone running southwesterly for at least 400 km from near James Bay to a point where it apparently dies out before reaching the Ottawa graben. Nine complexes from Argor to Seabrook are known along this high whereas two more, the Cargill and Firesand complexes, appear to be on a subsidiary branch subparallel to the Kapuskasing High.

3. A structure, which is here named the Albany Forks structure, is relatively short, perhaps 200 km long, but nine complexes are known along or near it (Poplar to Nagagami), all buried under deep Paleozoic cover.

4. A possible structure, here named the Carb structure; though not as obvious as the previous three, this one is strongly suggested by alignment of several alkalic complexes with Carb at the north end, Big Beaver House and Schryburt in the middle, and Prairie with two alkalic ultramafic intrusives, Killala and Port Coldwell, clustered at the Lake Superior end. Carb, Big Beaver House, and Schryburt are exactly on a straight line and Prairie complex is only a few kilometers from the southeasterly extension of this line, 780 km from the Carb complex. This linearity is thought to be an expression of structural continuity.

Implications

It seems apparent that the principal carbonatite magmatism occurred during two distinct periods in the Superior geologic province, first around 1,700 m.y., then a second period, probably mainly along the same structural zones, at 1,000 to 1,100 m.y. Two younger episodes are suggested along the Ottawa graben at about 570 and 120 m.y. During these younger episodes the remainder of the Superior province did not experience rejuvenation of carbonatite magmatism. This geographical distribution of carbonatite ages strongly suggests an easterly migration of carbonatite magmatism, an idea originally proposed by Gittins et al. (1967), or, conversely, a relative westerly movement of the continent over a deep source of carbonatite magma generation.

Another remarkable, though not unexpected, fact

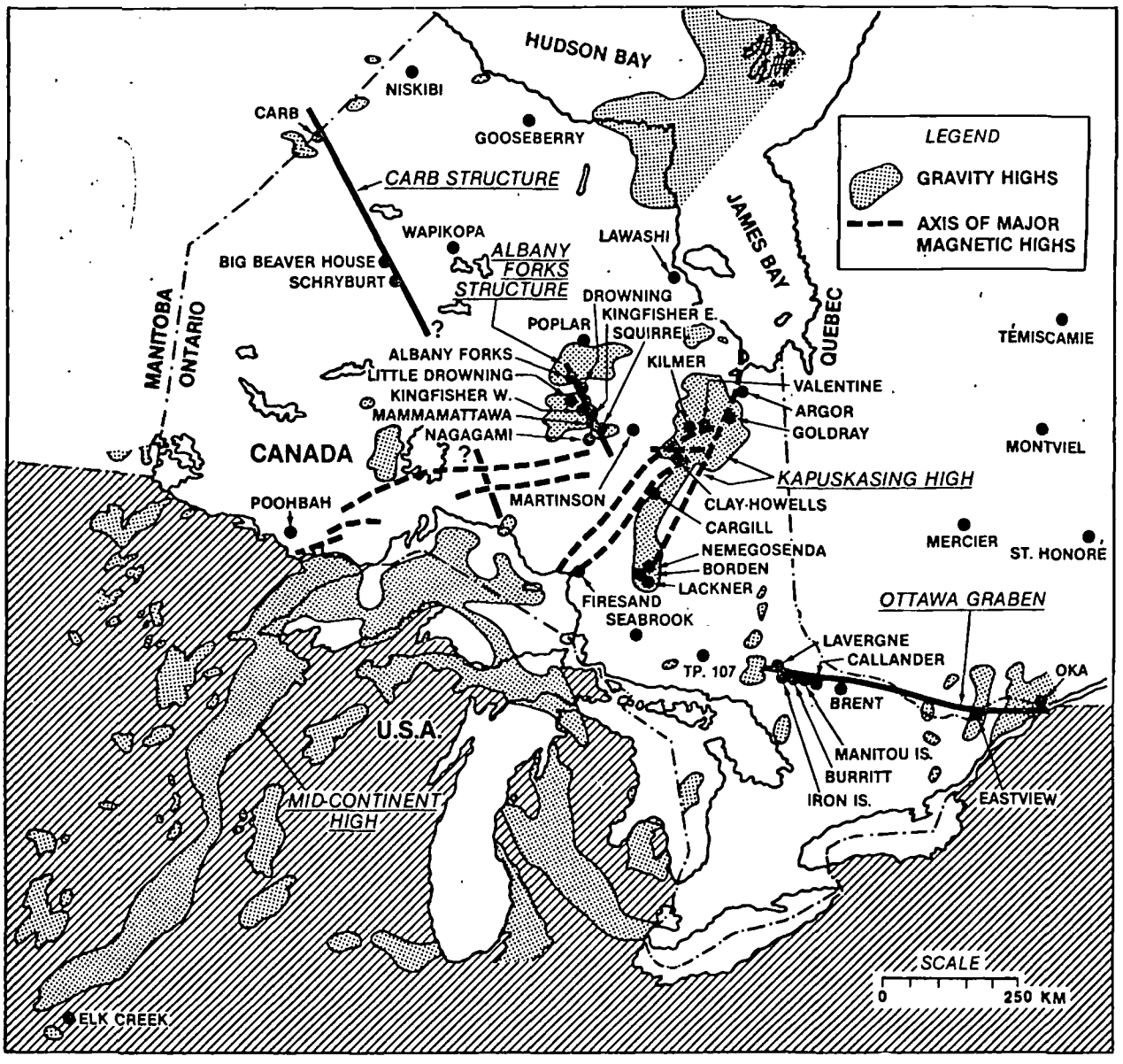

FIG. 1. The Ontario Carbonatite Province showing location of carbonatite complexes, gravity and magnetic highs, and major structures.

becomes apparent when the regional gravity and magnetic highs are superimposed on the location map (Fig. 1). A great majority of carbonatite complexes are found associated with gravity highs as well as with the axes of magnetic highs, thus strengthening the suspicion that most structural controls are major rift zones of continental scale and significance.

Phosphate Potential

In spite of their significant place in continental tectonic history and their unusual petrographic character, carbonatite complexes have only recently become targets for mineral exploration in Canada.

In other carbonatite provinces, such as in South Africa, East Africa, and Brazil, mineral deposits in or related to carbonatite bodies have been mined for some years. Many are in dry, hot climates where the carbonate-rich complexes tend to remain as resistant hills and are well known. In the cool, moist climate of northern Ontario and Quebec, the carbonate-rich rocks weather to topographic lows and are rarely exposed. Since recognition of these carbonatite bodies, a number of exploration programs have tested them by drilling, mainly for columbium, but also for rare earths, copper, vermiculite, magnetite, or titanium. However, only two complexes

have become mines, the Oka and St. Honoré complexes (see Fig. 1), both columbium producers.

Because of limited success, exploration interest in Canadian carbonatite complexes had declined prior to 1974 when International Minerals and Chemical Corporation (IMC) undertook a program to re-examine the carbonatite province for its phosphate potential. After preliminary screening in the field, the Cargill complex, located on a branch structure about 50 km west of the Kapuskasing High (Fig. 1), was selected as the first drilling target. This complex had been explored by other exploration companies three or four times and drilled twice with discouraging results. IMC's program was based on a new geologic concept predicting a topographic depression created by the weathering of carbonates with the resultant concentration of resistant minerals including apatite. Drilling in early 1975 confirmed the postulated model with the intersection of a substantial thickness of high-grade apatite residuum. Further extensive, systematic drilling of the Cargill complex has defined a potentially economic concentration of this material.

TABLE 2. Phosphate Content of Canadian Carbonatites

Complex	Rock type	Approx. range of P_2O_5 (%)
Argor	Biotite-calcite carbonatite	2.7– 4.4
Big Beaver House	Biotite pyroxenite	1.4– 5.3
	Calcite carbonatite	1.7– 2.9
Carb	Calcite carbonatite	2.3– 4.8
Cargill	Calcite carbonatite	2.0–10
	Leached carbonatite	10.0–20
	Residuum	20.0–41
Clay-Howells	Magnetite-calcite carbonatite	1.9– 4.8
Crevier	Carbonatite	~4
Firesand	Calcite carbonatite	0.1– 5.0
	Dolomite carbonatite	0.3– 3.5
	Mafic rocks	2.5– 7.0
Lackner	Apatite-magnetite rock	9.2
Mercier	Calcite carbonatite	1.9– 5.5
Nemegosenda	Calcite carbonatite	1.7– 3.8
	Mafic rock	1.1– 1.5
Oka	Carbonatite	1.8–11.6
Prairie	Calcite carbonatite	1.5– 9.2
	Ijolite	0.9– 8.2
St. Honoré	Carbonatite	0.5– 6.9
St. Véronique	Biotitite	1.2– 3.6
	Pyroxenite	2.9– 3.2
	Shonkinite	3.2– 4.0
Schryburt	Calcite carbonatite	2.5– 8.9
	Mafic calcite carbonatite	5.7–14.8
	Leached carbonatite	18.9–19.6
Seabrook	Calcite carbonatite	1.7– 7.7
	Mafic rocks	0.6– 1.7
Township 107	Biotite-calcite carbonatite	1.0– 4.9

IMC continued the program with detailed study and exploration of several more complexes but failed to find another significant residual concentration. Nevertheless, it was found that all carbonatites contain apatite, some in minor, some in near-economic quantities. Table 2 summarizes the approximate range of phosphate content of each complex. It should be noted that many of the figures are based on too few analyses to be significant statistically, giving a very rough estimate only. Some figures are not the result of IMC's work but taken from published sources.

Residual Phosphate Deposits—Cargill Complex

General geology

The geology of the complex and petrography of rock units were described in detail in two earlier papers (Sandvik and Erdosh, 1977; Erdosh and Sandvik, 1976) which are here briefly summarized.

In its petrographic make-up the Cargill complex is a typical alkalic carbonatite complex with two major groups of rocks: carbonatite and pyroxenite-amphibolite. (In the latter unit both rock types are present and both are believed to be primary; see Allen, 1972.) In its surface magnetic expression, however, the complex is atypical, as it appears to be broken up into three parts of subcomplexes; two large ones, designated as the south and north subcomplexes, and a smaller one, the west subcomplex (Fig. 2). This complexity may be the result of displacement along faults or separate emplacement at the time of intrusion.

The area of the Cargill complex was covered during glacial times by the huge Lake Barlow-Ojibway. This lake left a relatively thin but uniform clay cover throughout the region. As a consequence, very few rock outcrops are present over the complex and, with one exception, all of these expose only the pyroxenite-amphibolite unit. Figures 3 and 4 illustrate the general geologic setting of the south subcomplex, the only one drilled in detail to date.

Fenitization

Fenitization, a typical alkalic metasomatism surrounding most carbonatite bodies and alkalic complexes, has not been recognized in the south subcomplex. In the vicinity of the complex the host quartz diorite gneiss, where intersected in drill holes, is fresh, apparently unchanged by the intrusion. However, since fenite zones are frequently narrow around even large carbonatite bodies (sometimes less than 10 m in width), such a narrow, presumably vertical

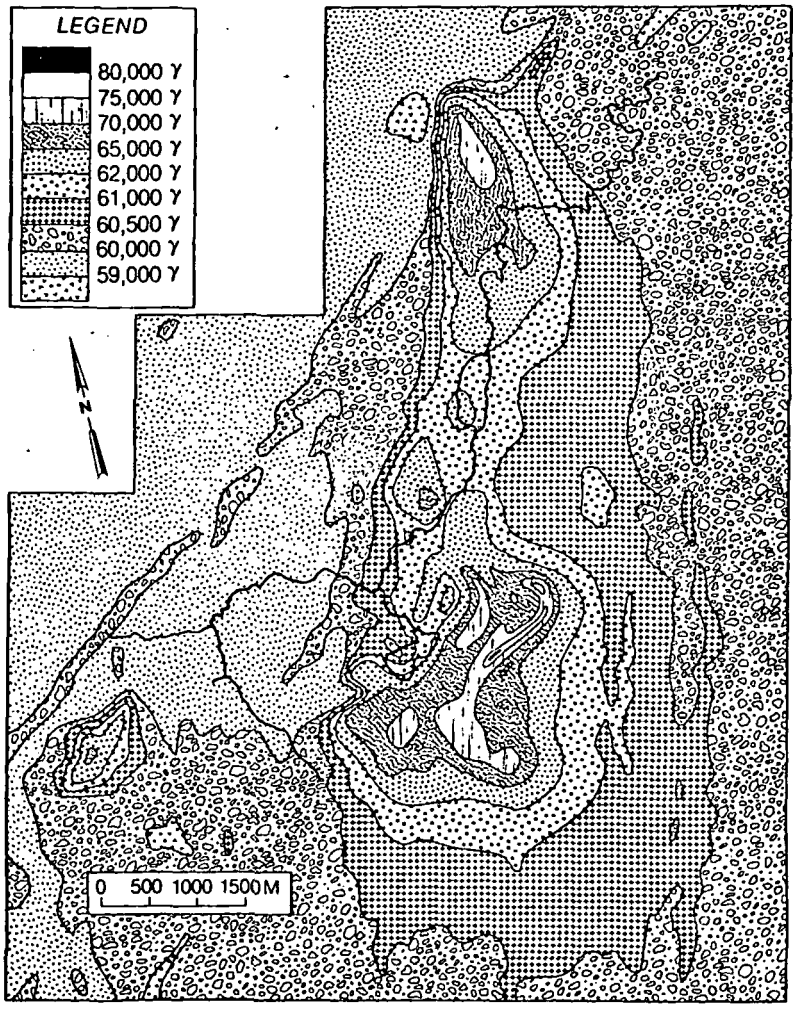

FIG. 2. Aeromagnetic expression of the Cargill alkalic complex.

zone may have easily been missed by the vertical drilling program.

Banded quartz diorite outcrops near the unexposed and yet unexplored, but presumably related, west subcomplex have distinct fenitization around the magnetic anomaly that defines this subcomplex, suggesting that fenitization may eventually be found around the main intrusions as well.

Primary zoning of carbonatite

Primary zoning is expressed by the distribution of carbonate minerals. In the south subcomplex zoning is expressed by calcite to the east which gives way to dolomite westward, with an intermediate zone containing both calcite and dolomite. Near the west side siderite-ankerite dominate, accompanied by their oxidation product, goethite, while calcite and dolomite become minor.

This zoning is poorly understood and could not be studied in any detail for the same reason given in the description of fenitization; the zones are vertical, consequently few contacts were intersected in the similarly oriented vertical drilling program. Nevertheless, field relations tentatively suggest that contacts between calcite and dolomite carbonatites are gradational over a few meters or tens of meters, while the siderite carbonatite has a sharp contact with the dolomite carbonatite.

This sequence from calcium to magnesium to iron carbonate is a classic differentiation sequence, the calcite being the highest temperature (earliest) and siderite the lowest temperature (latest) intrusion phases.

Since calcite and dolomite carbonatite[2] bodies

[2] Carbonatite terminology, such as beforsite or rauhaugite, is deliberately avoided in this paper because it is not only confusing but inconsistently used in the literature. The author believes that simple petrographic terms such as dolomite carbonatite or ankerite carbonatite would be well understood for the expert and novice alike and urges the use of such terminology.

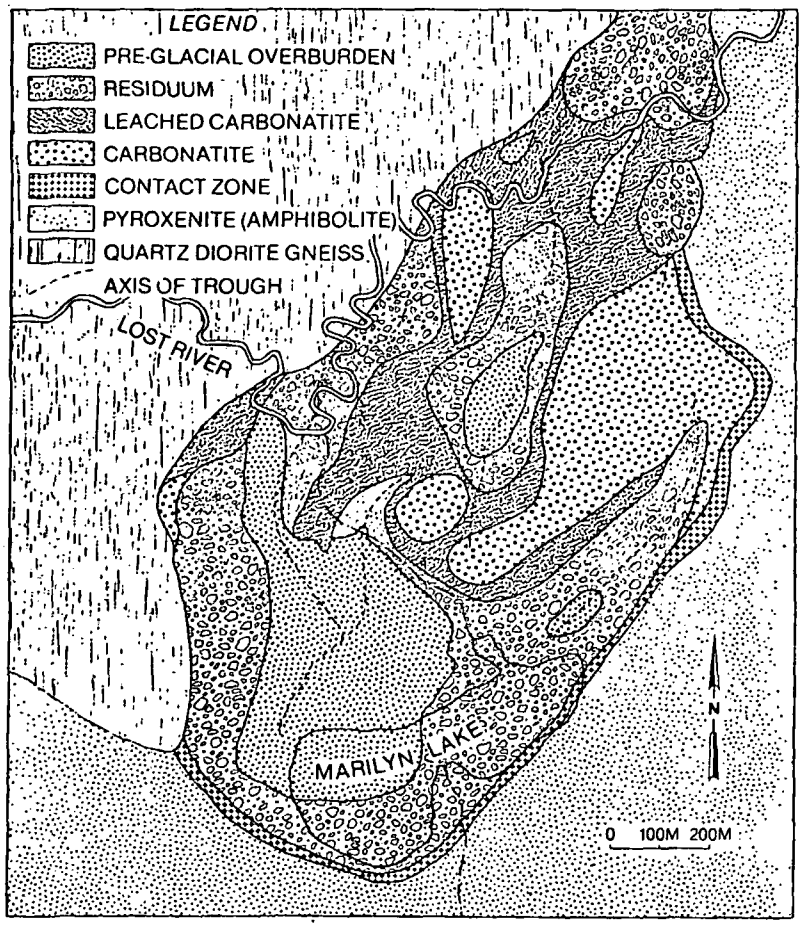

FIG. 3. Geology of the south subcomplex, 50-meter level (measured from the surface).

grade into each other, the intrusion of one may have followed the other closely. Siderite carbonatite, on the other hand, may have been intruded as a distinct, late phase after sufficient cooling of the dolomitic phase to prevent mixing.

In pipelike carbonatite intrusive complexes, the late low-temperature portion of the complex frequently occurs as a central plug surrounded concentrically by the earlier, higher temperature intrusive phases. Following this model, the initial geometry of the Cargill pipe is inferred to have had a similar concentric configuration, with sideritic material in the center, dolomite and calcite progressively further out as ringlike bodies surrounding the core. However, the existing geometry at Cargill departs from the classic model. Siderite carbonatite, the inferred core material, is in direct contact with quartz diorite gneiss along the west side of the complex and part of the inferred dolomitic and calcitic rings are missing. This combination of the disrupted zoning pattern and the northeast extension of the carbonatite, together with the regional and local magnetic patterns, suggest that the north subcomplex represents a fault-displaced segment of the original single intrusive complex.

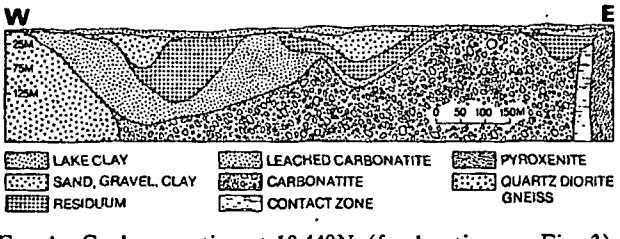

FIG. 4. Geology section at 10,440N (for location see Fig. 3).

Karst subsurface topography and development of the residuum

A well-developed, typical karst topography that developed over the carbonate-rich rocks of the south subcomplex has been described elsewhere (Sandvik and Erdosh, 1977). Figure 4 illustrates a cross section of this karst topography, now buried under a thin blanket of glacial lake clays.

The karst weathering and leaching at Cargill developed possibly during Lower Cretaceous, at the same time when the Mattagami Formation of the large Moose River Basin a hundred miles north was

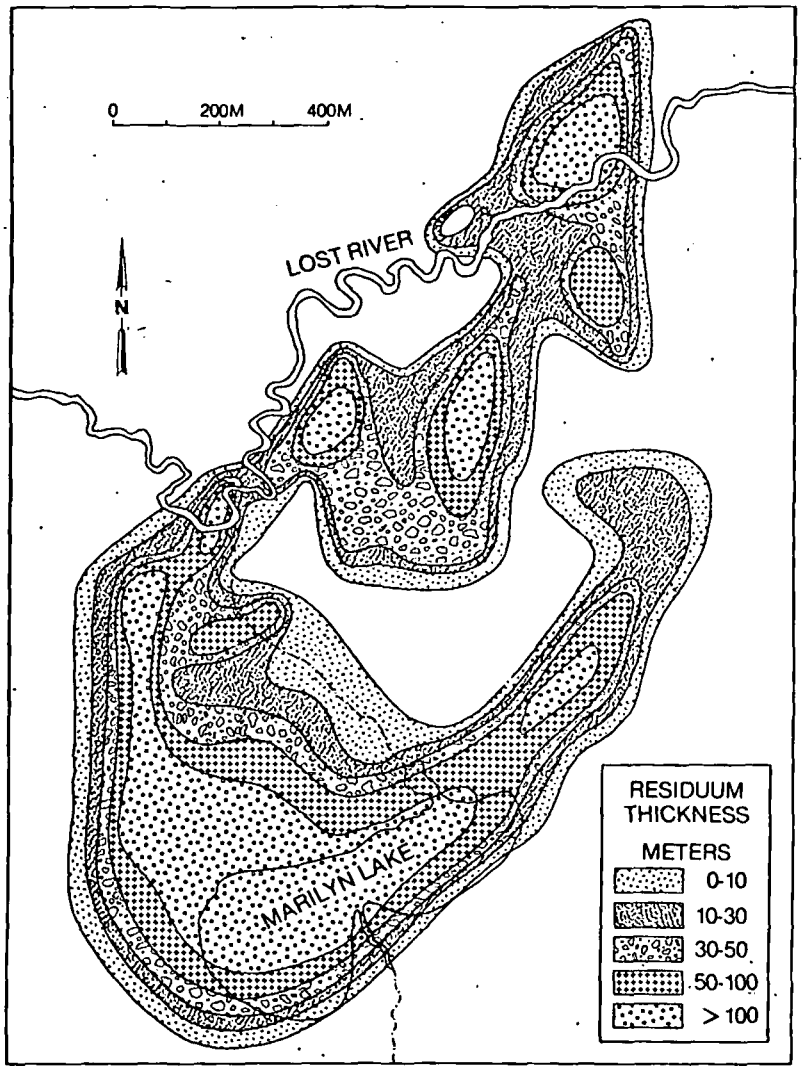

FIG. 5. Isopach map of residuum, south subcomplex.

deposited. This tentative conclusion is based on a pollen analysis from the fossil plant-bearing quartz sand and clay that overlies the karst-scarred complex. Some pollen was identified by J. Norris of the University of Toronto as Upper Cretaceous to Paleocene Maastrichtian (R. P. Sage, pers. commun., 1977).

During karst development the slightly acid rainwater dissolved the carbonate minerals which are readily soluble at cool temperatures. Along joints and/or faults solution proceeded at a more rapid rate and subsurface drainage resulted, carrying carbonate-rich solutions away.

With time the joints and faults enlarged by solution into troughs and at intersection of such structures deep sinkholes were developed (Fig. 5). At the same time at weaker points large underground solution cavities were formed which later collapsed, creating depressions and other sinkholes on the surface.

At the time of the principal development of the karst surface with its overlying blanket of thick residuum, the Cargill carbonatite was a circular depression surrounded by topographically higher quartz diorite gneiss and pyroxenite. Water entered the system, principally from local rainfall. Intermittent lakes occupied the deepest parts of the basin, the largest being a crescent-shaped one in the southwest with smaller circular lakes occupying some of the deeper depressions. During periods of heavy rainfall some of the lakes coalesced, but water continually drained downward through the fractured bed rock, so that the lakes expanded and contracted intermittently.

The minerals of the carbonatite that resisted both chemical and physical weathering, namely apatite, clays, and goethite, remained on the lowering bedrock surface and became thickest in the troughs and sinkholes where they were accompanied by slumping

and some alluvial action. Clean, well-sorted accumulations of nearly pure apatite sand, in places tens of meters in thickness, were formed in underground streams and caverns (Fig. 5).

Weathering products of the surrounding rocks also accumulated by washing and slumping into the lakes and troughs, forming clean, unweathered, well-sorted quartz sand several tens of meters in thickness and interbedded organic clay and tree remains. Occasional thick pure kaolinite layers are also interbedded with the quartz sand.

A thin crandallite-rich blanket, in which high rare earth values occur, is present in some places at the top of the apatite residuum unit. Several rare and unusual minerals are also associated with this blanket but only the rare earths are thought to have economic significance. The crandallite-rich blanket is the result of secondary weathering or leaching processes. Concentration of secondary pyrite has also been noted near the top of the residuum.

Vermiculite is extensive and probably significant in many places, both in unconsolidated and solid rocks, especially near the pyroxenite, but its economic importance has not yet been evaluated.

Only preliminary drilling with 240-meter centers has explored the northern subcomplex which shows that the karst development extends to that area as well. Accumulation of apatite is deeper here but so far the geology and mineral potential of this subcomplex is not well known.

Other known residual apatite deposits

As mentioned earlier, residual deposits of limited extent, including apatite concentrations overlying carbonatite complexes, are not unusual in tropical climates. In the earlier stages of apatite mining at Jacupiranga, Brazil, for instance, residual concentrations containing 22 percent P_2O_5 (Melcher, 1966) were exploited in subsurface karst hollows on the carbonatite.

The development of mature karst topography and concentration of apatite in substantial thickness on the scale observed at the Cargill complex, however, is geologically very unusual and rare. A similar occurrence is reported in Finland in the Sokli carbonatite complex, (Paarma, 1970), and possibly in another complex in the adjacent USSR, and one in southern Siberia (Paarma, pers. commun.).

Acknowledgments

The writer is most grateful to Dr. Donald L. Everhart, Project Manager of National Uranium Resource Evaluation of ERDA, for his helpful criticism, comments, and discussions during exploration of the Cargill alkalic complex and I would also like to thank him, in his previous capacity as Vice President of Geology and Exploration for International Minerals and Chemical Corporation, for permission to publish this paper. Thanks are also due to Ronald P. Sage, Ontario Division of Mines, Toronto, for his review of the manuscript and for useful suggestions.

Geology and Exploration
International Minerals and Chemical Corp.
Libertyville, Illinois 60048
Present Address
Texasgulf Inc.
5934 McIntyre St.
Golden, Colorado 80401
September 29, 1978

REFERENCES

Allen, C. R., 1972, The petrology of the ultramafic suite associated with the Cargill alkaline ultramafic-carbonatite complex, Kapuskasing, Ont.: Master's thesis, Univ. Toronto, 179 p.

Brookins, D. G., Treves, S. B., and Boliva, S. L., 1975, Elk Creek, Nebraska, carbonatite: strontium geochemistry: Earth Planet. Sci. Letters, v. 28, p. 79–82.

Charbonneau, B. W., 1973, A Grenville Front magnetic anomaly in the Megiscane Lake area, Quebec: Canada Geol. Survey Paper 73-29, 20 p.

Currie, K. L., 1976, The alkaline rocks of Canada: Canada Geol. Survey Bull. 239, 228 p.

Doig, R., and Barton, J. M., Jr., 1968, Ages of carbonatites and other alkaline rocks in Quebec: Canadian Jour. Earth Sci., v. 5, p. 1401–1406.

Erdosh, G. and Sandvik, P. O., 1976, The apatite deposit of the Cargill carbonatite complex, Canada [abs.]: Internat. Geol. Cong., 25th, Sydney 1976, v. I, p. 160–161.

Fairbairn, H. W., Faure, G., Pinson, W. H., Hurley, P. M., and Powell, J. L., 1963, Initial ratio of Sr^{87} to Sr^{86}, whole-rock age, and discordant biotite in the Montereğion igneous province, Quebec: Jour. Geophys. Research, v. 68, p. 6515–6522.

Gittins, J., MacIntyre, R. M., and York, D., 1967, The ages of carbonatite complexes in eastern Canada: Canadian Jour. Earth Sci., v. 4, p. 651–655.

Kumarapeli, P. S., 1976, The St. Lawrence rift system, related metallogeny, and plate tectonic models of Appalachian evolution: Geol. Assoc. Canada Spec. Paper 14, p. 301–320.

Kumarapeli, P. S., and Saull, V. A., 1966, The St. Lawrence Valley system: a North American equivalent of the East African rift valley system: Canadian Jour. Earth Sci., v. 3, p. 639–658.

Lowdon, J. A., Stockwell, C. H., Tipper, H. W., and Wanless, R. K., 1963, Age determinations and geological studies: Canada Geol. Survey Paper 62-17, 140 p.

Lumbers, S. B., 1971, Geology of the North Bay area, District of Nipissing and Parry Sound: Ontario Dept. Mines, Geol. Rept. 94, 104 p.

Melcher, G. C., 1966, The carbonatites of Jacupiranga, Sao Paulo, Brazil, *in* Tuttle, O. F., and Gittins, J., eds., Carbonatites: New York, Wiley, p. 169–181.

Ontario Dept. Mines, 1970, Aeromagnetic maps of carbonatite-alkalic complexes in Ontario, Prelim. Map P-452.

Owen, L. B., and Faure, G., 1977, Rb-Sr dating of the Lackner Lake complex, northern Ontario, Canada: Precambrian Research, v. 5, p. 299–303.

Paarma, H., 1970, A new find of carbonatite in northern Finland, the Sokli plug in Savukoski: Lithos, v. 3, p. 129–133.

Sandvik, P. O., and Erdosh, G., 1977, Geology of the Cargill phosphate deposit in northern Ontario: Canadian Inst. Mining Metallurgy Bull., v. 69, p. 90–96.

Watkinson, D. H., and Grimes, J. H., 1974, The Spanish River alkalic rock-carbonatite complex, Township 107 and 108, Ontario [abs.]: 20th Ann. Inst. Lake Superior Geology, Sault Ste. Marie, Ontario, Proc., p. 38.

Oxymin Details Plans for In Situ Leach Project in Arizona

Officials of Occidental Minerals Corp., intent upon developing a copper deposit located beneath the town of Miami, Ariz., presented their plans for extracting the metal to the Miami town council on September 12.

Oxymin signed an option for the Van Dyke copper property in 1968 and conducted an exploration program which extended until 1975. At that time, about 40 holes had been drilled throughout the deposit, delineating approximately 100 million tons of oxidized copper mineralization with an average grade of 0.5%. Unlike most of the other deposits in the Globe-Miami copper district, the Van Dyke deposit does not outcrop. It is completely buried under the Gila Conglomerate and underlies part of the town of Miami. Within the town limits, the deposit lies at a depth of from 335 to 610 m (1100 to 2000 ft) beneath the surface.

Leach Tests Successful

Due to the depth of the deposit, the low grade of the mineralization, and the fact that the major portion of the deposit is under the town, no conventional mining method appears to be feasible. In January 1976, Oxymin decided to start in situ-leach pilot testing through surface drill holes. Two holes were drilled to a depth of slightly more than 305 m (1000 ft), spaced 23 m (75 ft) apart. The specific zone to be leach-tested was then hydrofractured with water and a fluid connection was established between the holes. Further testing with a weak sulfuric acid solution has proven the feasibility of in situ leaching of the deposit; however, company officials noted that further testing remains to complete the design and to prove that the process is economically sound. They stressed that hydrofracturing, as used in the Van Dyke deposit, will extend the hairline fractures in the copper mineralization a maximum of approximately 60 m (200 ft) from the point of fluid injection, and that tests have indicated that blasting will probably not be necessary to increase the permeability of the material.

Commercial Drilling Underground

If further pilot test work proves the economic feasibility of commercial production, Oxymin anticipates in situ leach mining from underground workings. A vertical shaft would be sunk outside the town limits and a gridwork of nearly horizontal drifts will be driven below the town. The solution injection and recovery wells will be drilled and operated from the underground drifts. Copper in the leach solution will be recovered by a conventional solvent extraction and electrowinning plant on the surface. The barren solution from the plant will then be recycled into the leaching circuit.

To monitor the effects of the operation on ground water, Oxymin has sunk two wells in the alluvium of Bloody Tanks Wash northeast of the deposit. The wells are about 30 m (100 ft) deep, and are located 760 m (2500 ft) downstream of the test site. Representative ground water

(Continued on page 16)

INDUSTRY NEWSWATCH

(Continued from page 13)

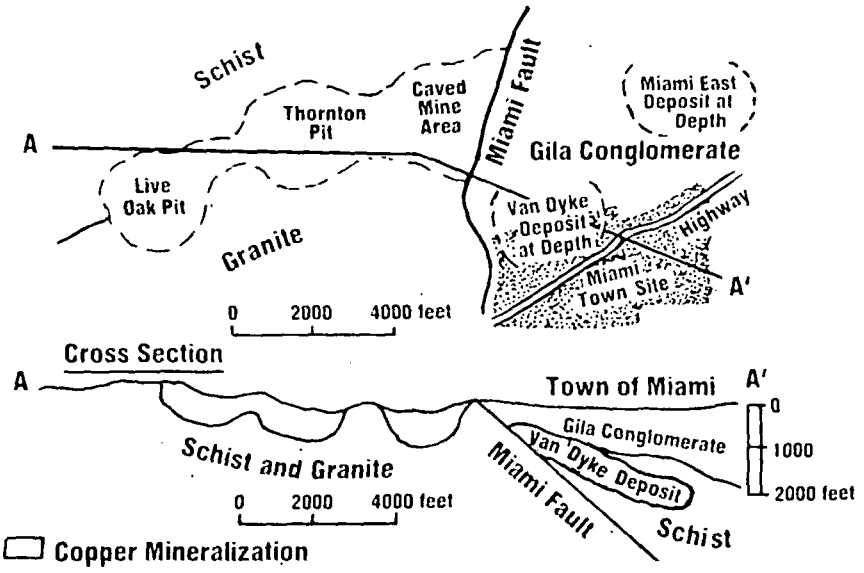

Plan view of the Miami, Ariz., area.

samples are obtained by pumping from the alluvial aquifer in the wash, and factual data are submitted to the Miami Town Council. According to company officials, the data indicate that no significant change in chemical constituents in the ground water has occurred during the pilot test leaching activities.

Ground water from the alluvium in the wash is not used for municipal supply except in extremely dry periods when it is added in fractional amounts to the water taken from the Central Heights area, which is about 4.8 km (3 miles) northeast of the Van Dyke deposit and is the town's main water supply.

The Question of Mineral Rights

Oxymin told the town council the "mineral estate" was severed from the surface rights prior to creation of the "surface estate" and surface owners purchased the surface to a depth of 12 m (40 ft). Standardized deed restrictions, consistent with the grant of the severed mineral estate, were incorporated in the surface deeds at the time the surface parcels were first offered in 1909 for sale to individual purchasers. In the language of the deeds, these restrictions absolve the mineral estate owners from liability to the surface owners in the event of subsidence resulting from mining operations conducted under them. During the development of the town of Miami, the owners of the minerals, Van Dyke Copper Co. and Sho-Me Copper Co., conducted exploration, development, and mining operations in, under and adjacent to the town, beginning in 1916 and continuing to the present.

The present mineral right owners and Oxymin have indicated a willingness to compensate surface property owners for damage that might be caused by mining operations underground. The company stated that compensation for damage would not be based on a predetermined formula, but rather on a case-by-case basis taken from an appraisal made at such time any damage occurs.

The company noted that it plans to employ a work force including as many as 200 Miami residents if further testing proves successful. □

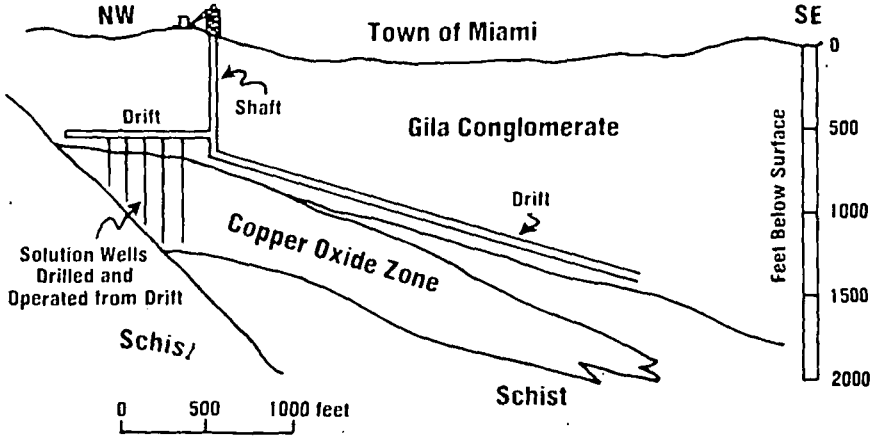

Proposed Oxymin in situ leach plan for the Van Dyke copper deposit. Right-hand drift will contain additional solution wells.

Optimum Depth of Wells in Crystalline Rocks[a]

by S. N. Davis and L. J. Turk[b]
Member NWWA

Abstract

Water-bearing properties of crystalline rocks are dependent on the occurrence of joints and faults and the extent of weathering. Interstitial openings caused by weathering are mostly at depths of less than 100 feet. Joints are less abundant and openings along joint planes are smaller as depth increases. Openings along fault surfaces also tend to close with depth. These geological observations which indicate a decrease in rock permeability with depth are verified by a study of well yields and water-injection tests. Mean yields per foot of well are 0.23 to 0.30 gpm at 100 feet but only 0.013 to 0.04 gpm at 1000 feet. Mean injection rates per foot of drill hole under 100 psi pressure are 0.11 to 0.4 gpm at 100 feet but only 0.014 to 0.038 gpm at 1000 feet. Median values of both well yields and injection rates are from one-half to one-third of the mean values. Geologic structure is more important than rock type in determining yields and injection rates. The decrease in rock permeability with depth indicates an increase in the unit cost of water with depth. The optimum depth of a well is, therefore, determined largely by economic factors. Unless geologic factors are favorable, wells in crystalline rocks should be less than 600 feet deep. In general, domestic wells should be less than 150 to 250 feet deep.

Introduction

The scientific location of water wells in regions of dense crystalline rock is commonly made difficult by the presence of soil, vegetation, and broken rock rubble which cover the structural features of the rock. Geophysical techniques are of some use if large contrasts in rock properties are present, as for example, the contrast between a zone of deep rock weathering and underlying dense unweathered rock. In most situations, however, geophysical methods do not locate narrow openings which yield water in the unweathered rock. General observations of topography and positions of surface streams can also be useful guides for drilling in regions where detailed studies of exposed rock are not possible (LeGrand, 1962). Nevertheless, even under the best conditions, results of drilling are difficult to predict. Under the worst conditions, blind probing must be used and results can be predicted only in a general way through statistical information gathered from drilling in comparable rocks situated in similar topographic positions.

The purpose of this paper is to summarize [illegible] from wells drilled in crystalline rock in order to assess [illegible] in regional planning of water development, to serve [illegible] a guide to the probable success or failure of drilling [illegible] and to help determine the optimum depth of wells. Emphasis in this paper will be on the problem of determining the optimum depth.

Origin and Depth of Permeable Zones

The term, *crystalline rock*, as used in this report refers to igneous and metamorphic rocks such as schist, gneiss, granite, diorite, and gabbro. Carbonate rocks, which commonly develop solution openings, are not considered.

Unweathered and unfractured crystalline rocks generally will have less than one per cent porosity and will have permeabilities so small as to be almost negligible. Weathering will cause differential expansion of various mineral grains due to partial hydration. The expansion and differential movement will produce, in turn, intergranular pore space. Also, circulating water may increase local porosity by the dissolution of unstable minerals. Porosities produced by weathering commonly range from 30 to 50 percent (Figure 1). If the rock is originally coarse-grained

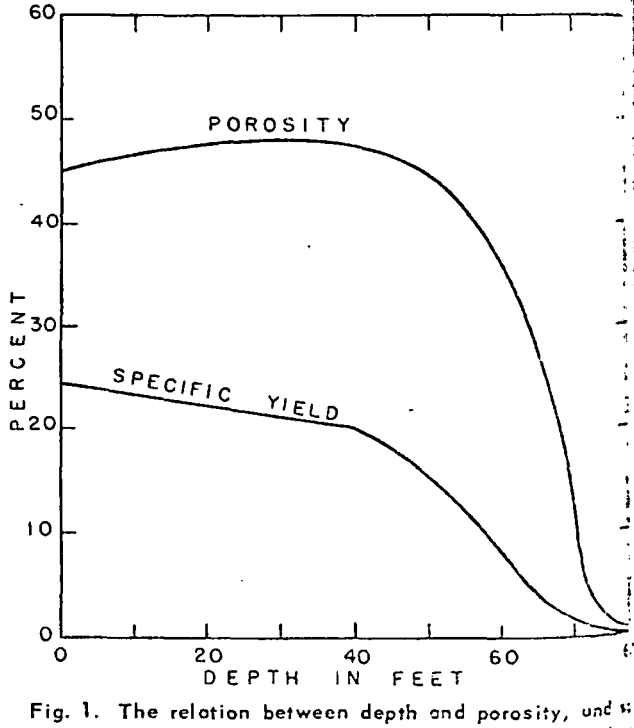

Fig. 1. The relation between depth and porosity, and specific yield in weathered metamorphic rocks north of Atlanta, Georgia. Curves from 0 to 65 feet are from measurements by Stewart (1962); extensions to 80 feet are hypothetical.

[a] Paper presented at National Water Well Exposition, San Francisco, California, September 30, 1963.

[b] Associate Professor, Department of Geology, Stanford University; and Geologist, Socony Mobil Oil Company, Libya, respectively.

Discussion open until June 1, 1964.

with a moderate abundance of stable minerals such as quartz, a relatively high permeability may result from the weathering. Wells producing between 10 and 50 gallons per minute (gpm) from the zone of weathering are common.

The thickness of the zone of weathering depends on the geologic history of an area. In areas of rapid erosion, fresh rock may be at the surface. In contrast, maximum depths of almost 300 feet of weathered rock may be encountered in areas of little natural erosion. Depths between 10 and 100 feet, however, are more typical. The transition from weathered into unweathered rock is moderately abrupt and may take place through a vertical distance of only 10 to 20 feet (Figure 1).

Permeability will be significant in unweathered crystalline rocks only along fractures that have been developed in response to volume changes in the rock or to externally applied forces such as those that produce faulting. Horizontal joint surfaces, which probably form in response to rock expansion associated with erosional unloading, tend to be concentrated near the surface and are spaced much wider apart as depth increases (Jahns, 1943).

Other joints also may tend to decrease in frequency at depth (Crosby, 1881). In addition, there are good theoretical reasons for believing that many joints caused by tension at or near the ground surface will die out rapidly with increasing depth (Lachenbruch, 1961). Surfaces or rupture associated with incipient landslides also will be confined to relatively shallow depths.

Tunneling and mining operations, nevertheless, have demonstrated amply the existence of permeable zones at depths of several thousand feet. Most of this permeability appears to be associated with faulting. Even along vertical fault zones, however, slight amounts of rock creep should tend to close small fractures so that some decrease in permeability should be experienced in deeper zones. Low-angle faults will tend to close at depth due to the load of overlying rocks.

All general lines of reasoning, therefore, indicate a reduction of permeability with depth. The data accumulated for the study substantiate this reasoning, and the analyses give a quantitative idea of the reduction of permeability for crystalline rocks.

Although the matter was not studied, it is likely that similar depth-permeability relations exist in consolidated sedimentary and volcanic rocks, such as some types of arkoses and welded tuffs. The only information on this topic comes from careful pressure tests in jointed quartzite of the Shawangunk Formation in New Jersey which have shown a regular decrease in permeability with depth (Smith, 1962).

Collection and Organization of Data

Water Wells

Records were compiled from published descriptions of 2,336 water wells in granite and schist. All of these wells were in the eastern part of the United States. In addition, information concerning 239 wells in crystalline rocks of the Sierra Nevada was collected (Turk, 1962). Most of these wells are in granodiorite, although a number of metamorphic rocks also are involved. Wells used in the study have records of diameter, total depth, rock type penetrated, and final production. Some of the wells in eastern United States and all of the wells in California have records of static water levels, casing lengths, and perforation intervals. Information on topographic position of wells, although very important, was not available in enough publications to be included in the present study. Yields per foot were calculated by dividing the total yield of the well, as reported by the driller, by the depth of the well below the water table. Where water-table information was lacking, an average value computed from other wells was used.

Water-Pressure Tests

Study of 1,291 water-pressure tests in 340 drill holes at dam sites and tunnel lines provided additional information on depth-permeability relationships (Davis and Turk, 1963). Data were obtained from the United States Corps of Engineers, the United States Bureau of Reclamation, and the California Department of Water Resources. These tests were in various rock types and were performed with varying amounts of pressure.

To standardize data from the several sources, the quantity of water injected, or water take, was corrected to that expected at a pressure of 100 pounds per square inch (psi), assuming that water take varies directly with pressure. Tests of several zones using differing pressures were studied, and the direct ratio between pressure and water take was relatively consistent when pressures were over 50 psi; thus 50 psi was the minimum pressure for tests used in this study. Owing to lack of information concerning static water levels, corrections were not made for varying depths to the water table.

The mean vertical depth for each zone tested was calculated; if a hole was not vertical, its mean depth was found by trigonometry. Holes less than 45 degrees from horizontal were not used. The average water take per foot of hole was calculated by dividing the length of hole tested by the amount of water accepted during the test. Also computed was the percentage of pressure tests in each depth increment which failed to inject water into the rock. These are called "zero water take percentages" in this report.

Three rock types were studied separately in water-pressure tests to determine whether rock type is a major factor in deep circulation of ground water. These types are:

1. Granitic rocks.
2. Amphibolite.
3. Miscellaneous rocks including serpentine,

greenstone, slate, schist, quartzite, phyllite, metarhyolite.

Interpretation of Data

The data were compiled and graphs were plotted illustrating the variation of water take and/or yield with depth. The major relationships among variables of interest are shown in Figures 2, 3, 4, 5, 6, and 7. All curves clearly verify the qualitative conclusion based on general geological evidence that permeability decreases with depth. However, the scatter of the data is large. As might be expected, natural variations of structure and rock type give rise to large differences in the permeability of individual fracture zones as well as the overall abundance of the zones. A good example of this contrast is shown in data from the Roberts Tunnel, Colorado (Wahlstrom and Hornback, 1962). In highly fractured Precambrian gneiss and quartzite associated with thrusting, an average of one

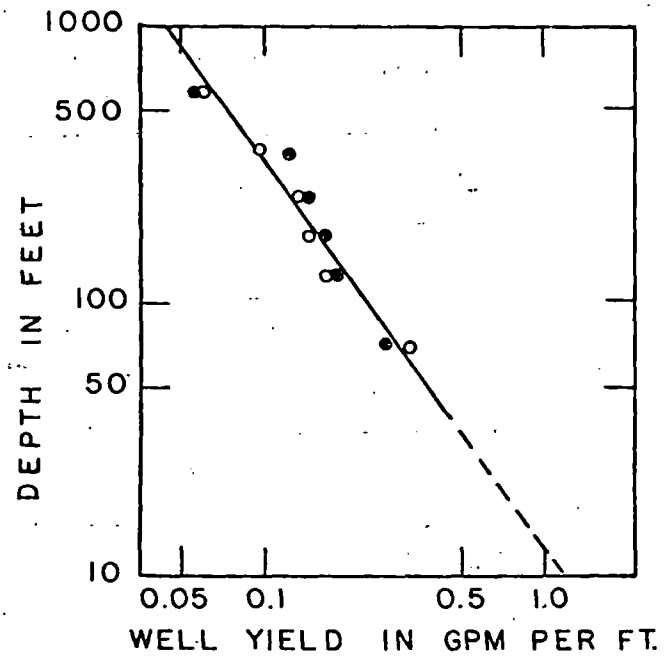

Fig. 2. Yields of wells in crystalline rock of eastern United States. Open circles represent mean yields of granitic rock based on a total record of 814 wells. Black dots represent mean yields of schist based on a total record of 1522 wells (compiled by Turk, 1963).

fault per ten feet of tunnel was encountered. Water seeping into the tunnel through the faults and other fractures averaged slightly more than one gpm for each foot of tunnel. In contrast, a Tertiary quartz monzonite had one fault per 30 feet of tunnel and only 0.05 gpm of water for each foot. The two rock types were tunneled at about the same distance below the ground surface.

Variables other than those of the geologic environment also account for some of the scatter in the data. Diameters of wells and drill holes, testing methods, casing lengths, depths to water, completion methods, and a host of other factors vary from one hole to another. Although methods of pressure testing

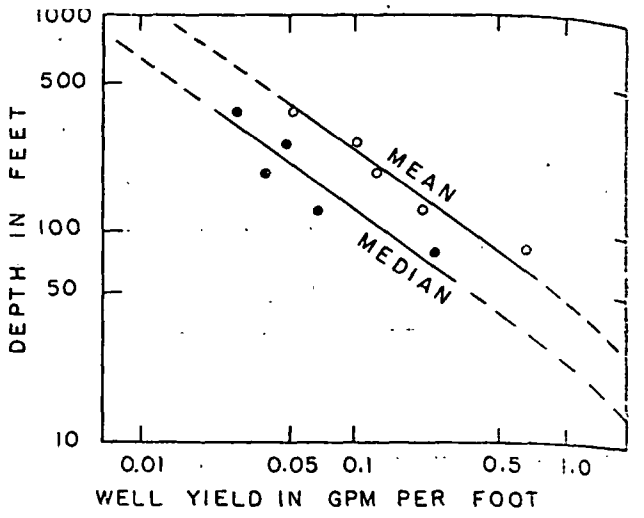

Fig. 3. Depth-yield relations for crystalline rocks of the Sierra Nevada, California, based on data from 239 wells (Turk, 1963). Most wells are in granodiorite or closely related rocks.

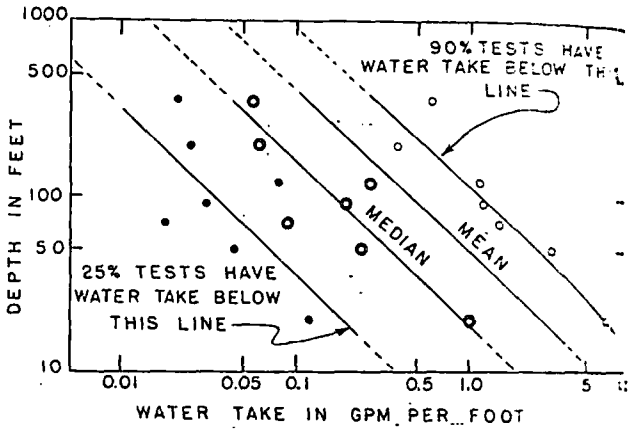

Fig. 4. Water-injection data from Oroville dam site, California. Although mean points for the class intervals are not shown, computed values have about the same scatter in relation to the "mean line" as do the median values to the "median line." Diagram is based on the results of 31 injection tests in amphibolite.

tend to be more uniform than methods in water-well drilling, equipment and techniques are not always the same from one agency to another.

Despite the many factors causing the data to scatter, several clear-cut relationships are evident. These are:

1. Crystalline rocks have roughly the same depth-permeability relationships. The similarity is particularly striking in data from water wells in granite and schist in eastern United States, Figure 2, and from pressure tests in amphibolite and granitic rock in California, Figures 4 and 5. Data from pressure tests in miscellaneous rock types, Figure 6, show departures in the depth-permeability relations. The rocks tested include low-grade metamorphic rocks which are not actually crystalline in the usual meaning of the word. These rocks have low strength and tend to close their fractures rapidly with depth.

2. The percentage of pressure tests having zero water take increases rapidly with depth in the miscel-

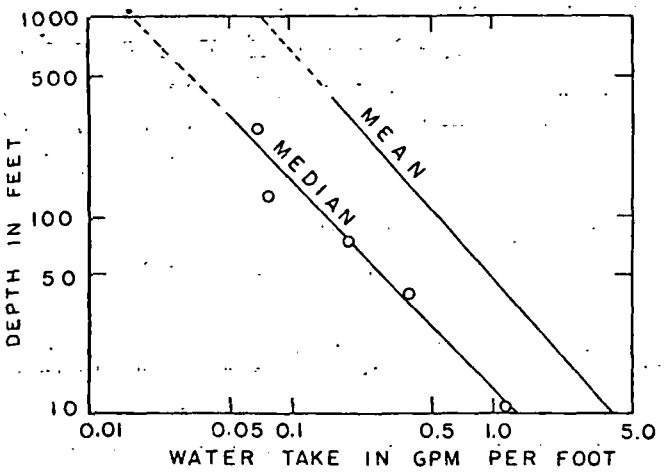

Fig. 5. Water-injection rates, or water take, related to depth in granitic rocks of California. Diagram based on data from 412 tests.

laneous rocks as well as the granitic rocks, Figure 7. This trend is lacking in data from amphibolite. The reason for this may be the fact that many data were from deep holes at the Oroville Dam site specifically drilled to intersect deeper fractured zones, which were presumably more permeable than the normal rock.

3. Frequency distributions of yield and water take are skewed strongly to the right, Figures 8 and 9. Mean values are between 2.0 and 3.5 times as large as the median values. The yields or water-take values, which are exceeded in only ten percent of the tests are five to ten times larger than the mean values. The ratio of mean to median values tends to be constant throughout all depths studied.

Optimum Depth of Wells

The optimum depth of wells in crystalline rocks is determined largely by economic factors provided the position of water-bearing zones cannot be predicted by geological or geophysical means. The first step in an economic analysis is to compare the cost of developing well water with the cost of water from other sources. Inasmuch as the amount of water produced per foot of well diminishes rapidly with depth,

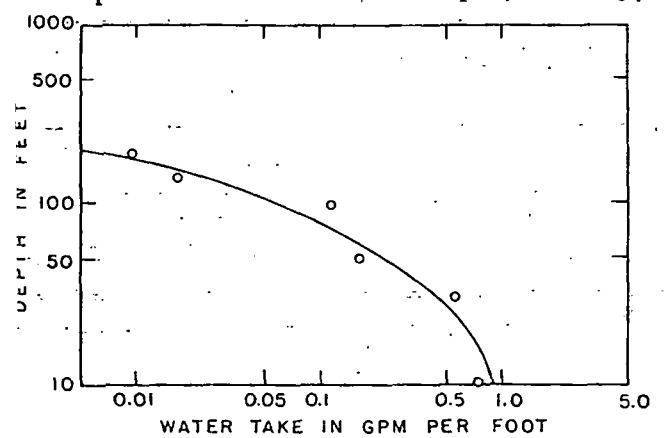

Fig. 6. Median water take in miscellaneous rock types in California. Diagram based on data from 494 tests in serpentine, slate, phyllite, gabbro, and other rocks.

the unit cost of water increases as a well is deepened. This relationship is shown by the two curves in Figure 10. Important assumptions used in making the curves were a well construction cost of $10.00 per foot, a power rate of 2 cents per KWH, an interest rate of 6 percent, and a well life of 30 years. Depth-yield relations similar to crystalline rocks of eastern United States and an average depth to the water table of 30 feet were also assumed. Although different curves should be constructed for each region of interest because of variations in economic and geologic factors, the general shape of all such curves is probably quite similar.

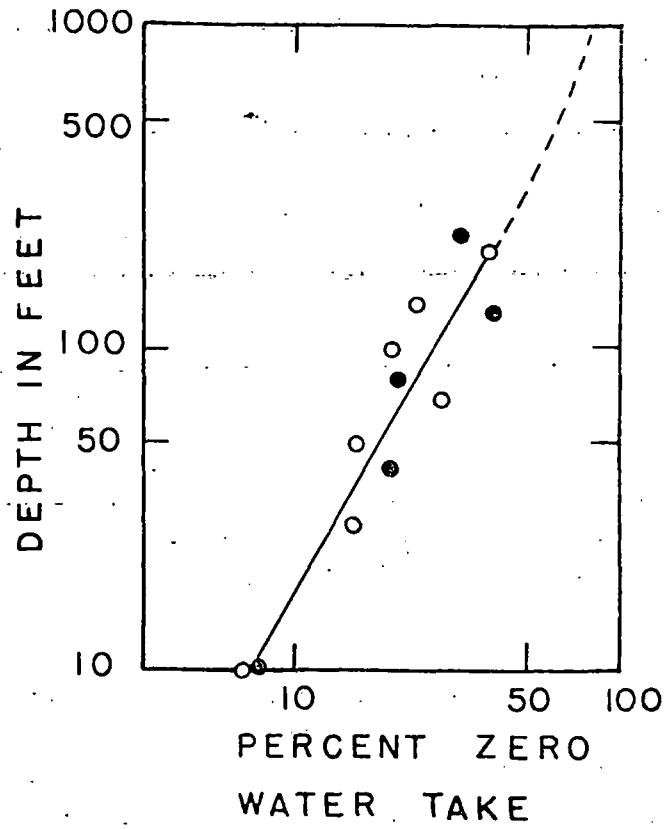

Fig. 7. Percent of tests having zero water take in granitic rocks, shown by black dots, and miscellaneous rocks, shown by open circles.

A fixed unit cost has been assumed for water from sources other than wells. This is commonly true of small amounts obtained from municipal supplies but may not be true of larger volumes. The straight lines in Figure 10 show the cost of various amounts of water per unit time for different unit charges. It can be seen that, under the assumed conditions, well water will be always more expensive than other water at 5 cents per 1000 gallons but always cheaper than water at 50 cents per 1000 gallons. Between these extremes, the choice should be based on a study of economic factors.

The manner in which Figure 10 can be used to assist in determining the optimum depth of wells will be given by the following hypothetical example. A city has a choice of either drilling a large number of wells or importing water at a fixed rate of 20 cents per 1000 gallons. From the mean curve in Figure 10 it is

determined that well water will be cheaper only if the depths of wells are generally less than 350 feet. The maximum economic advantage is gained for each well at the pumping rate which gives the greatest horizontal separation between the mean yield curve and the 20-cents line. This pumping rate is about 19 gpm which can be obtained at a depth of about 150 feet, which can be considered the optimum depth.

The foregoing example is correct only if a large number of wells are to be drilled. In such a case, a few wells which have high yields will compensate for the wells which are failures or which produce only a small amount. If a single well is to be drilled, the most likely, or median, yield is of most interest. As an example, if a small dairy wishes 20 gpm, the median yield curve of Figure 10 would indicate that it is unlikely that this amount of water can be obtained from a single well at a reasonable cost. Although

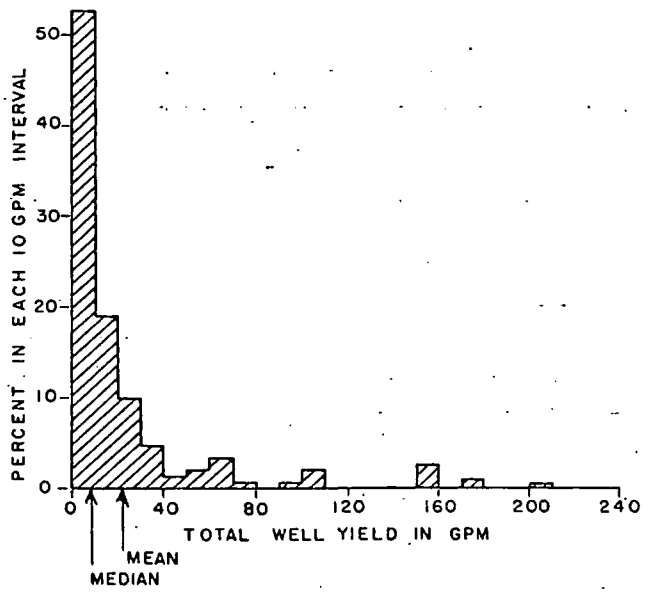

Fig. 8. Frequency distribution of yields of 239 wells in crystalline rocks of the Sierra Nevada. Data from wells of various depths have been grouped together. Of the total number, 8.4 percent were "dry holes" and 16.3 percent had yields of less than 1.0 gpm.

representing a different region, Figure 8 would suggest that there would be only one chance in four of obtaining the desired water from a single well. A very good chance exists, however, for the development of the water from 5 wells having depths of from 40 to 80 feet. The expected cost of this water is less than 15 cents per 1000 gallons. Of the five wells drilled, one would probably be a failure, three might produce 2 gpm each, and the other well might produce 15 gpm. The total production would be 21 gpm; the average, or mean, yield would be 4.2 gpm; but the most likely, or median, yield of a single well would be only 2 gpm.

One of the most frequently encountered problems in drilling in crystalline rocks is that of abandoning a well which has failed to encounter water. Experience has shown that there is always a chance of finding water at a greater depth, so the tendency is to take a

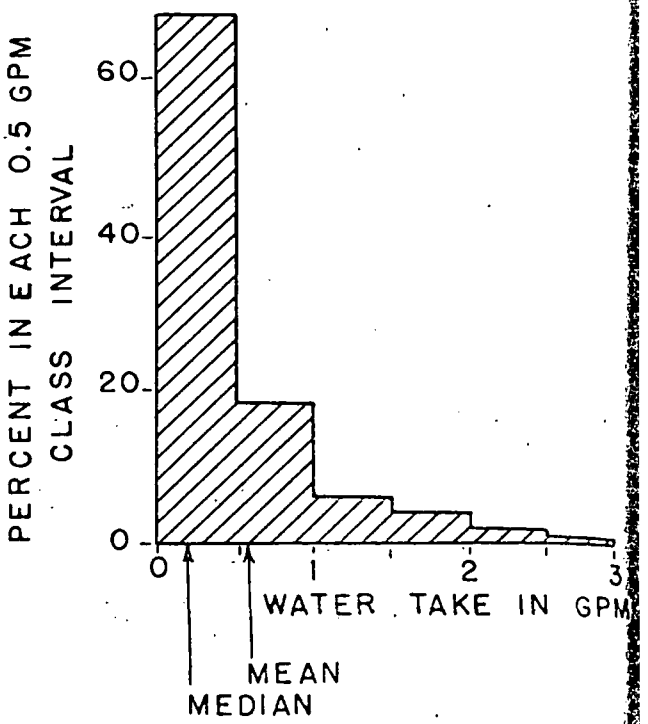

Fig. 9. Frequency distribution of water take of 62 tests the 81 to 100 ft. depth interval at the Oroville dam California. Zero water take was reported for 14 percent the tests.

chance and continue the same hole until water found or until there is no money left with which drill. As indicated in Figure 7, however, the chance of encountering water-bearing zones diminish rapidly with depth. Theoretically, the problem could be solved if data of the type shown in Figure 9 were available for all depth zones. On the basis of information gathered thus far, it would seem best to anticipate the problem before drilling by budgeting money for several relatively shallow exploration holes rather than spending the money in a single deep well. For domestic or stock wells which need to produce less than 2 gpm, the optimum depth is a short distance

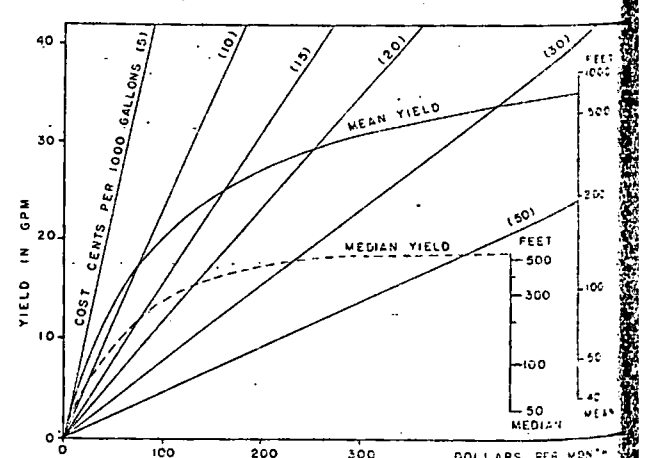

Fig. 10. Curved lines show cost of developing ground water in crystalline rocks of eastern United States under assumptions stated in the text. Straight lines indicate cost of water at fixed rates, such as might be delivered from city water supply. Yields in gallons per minute (gpm) for continuous use.

below the water table, a distance only great enough to allow for drawdown due to pumping and to accommodate seasonal water-level fluctuations. Thus, in planning domestic wells in an area in which the water table is near the surface, three adequately spaced holes only 60 feet deep would appear to be a far better means to search for ground water than a single hole 240 feet deep. Nevertheless, cost of preparing drilling sites, limitations of available space, and distance to points of use will determine the feasibility of drilling more than one hole.

Discussion and Summary

Aesthetic considerations, biological and chemical purity of water, local zoning regulations, and a large number of other factors which cannot be treated in simple economic or geologic analyses are commonly important in making decisions concerning water-well drilling. For this reason, the entire process of making the decisions will probably never be fully formalized. In a similar problem with oil-well drilling, Grayson (1960) has pointed out, however, that even though many steps will always remain qualitative, some type of formal approach is desired to minimize the possibility of serious errors. The present authors have attempted to give some quantitative expression to only one decision making step in one class of water-bearing material. It is our hope that the entire decision making process will be analyzed eventually. For the present, the following conclusions can be useful.

1. The water-bearing characteristics of most crystalline rocks are primarily controlled by weathering and structure. Rock type alone is commonly of secondary importance.

2. In the absence of geological and geophysical guidance, drilling in crystalline rocks encounters highly variable amounts of water. In unweathered rock, from 5 to 15 percent of the wells are failures, median yields are less than 8 gpm, and roughly 10 percent will have yields of 50 gpm or more.

3. Water production per foot of well decreases rapidly with an increase in well depth. This decrease is roughly ten-fold between depths of 100 and 1000 feet.

4. The optimum depth of water wells in crystalline rocks is determined largely by economic factors unless the geologic structure is known in detail.

5. Although a detailed economic study was not made, rough estimates suggest that the depth of single domestic wells should be less than 150 to 250 feet and wells of larger production should be less than 600 feet. In many places the optimum depth of domestic wells will be less than 100 feet.

Acknowledgements

Part of the present study was completed while the authors were employed by Carroll E. Bradberry and Associates, who are subcontractors to Hazleton-Nuclear Science Corporation under Contract No. AT (29-2)-1229 with the Nevada Operations Office of the U. S. Atomic Energy Commission. Much of the material in this report was taken from a report prepared under this contract which is concerned with an evaluation of radiologic contamination of ground water by nuclear testing. The authors are grateful to Robert L. Nevin of Carroll E. Bradberry and Associates and John V. A. Sharp and Maxwell K. Botz of Hazleton-Nuclear Science Corporation for helpful discussions of many of the ideas contained in this paper.

References

Crosby, W. O. 1881. On the absence of joint-structure at great depths, and its relations to the forms of coarsely crystalline eruptive masses. Geol. Mag. (Decade 2). 8.

Davis, S. N. and J. L. Turk. 1963. Some hydrogeologic characteristics of crystalline rocks. Private Report. Hazleton-Nuclear Science Corp. HNS-38.

Grayson, D. J., Jr. 1960. Decisions under uncertainty, drilling decisions by oil and gas operators. Harvard Business Sch., Boston.

Jahns, R. H. 1943. Sheet structure in granite, its origin and use as a measure of glacial erosion in New England. Jour. Geology. 51.

Lachenbruch, A. H. 1961. Depth and spacing of tension cracks. Jour. Geophys. Research. 66.

LeGrand, H. E. 1962. Perspective on problems of hydrogeology. Geol. Soc. America Bull. 73.

Smith, B. L. 1962. Geology of the Jersey Central Power and Light Company Yard Creek Storage Project, northern New Jersey. A paper presented to the Houston meeting of the Geol. Soc. America, Nov. 14, 1962.

Stewart, J. W. 1962. Water-yielding potential of weathered crystalline rocks at the Georgia Nuclear Laboratory. U. S. Geol. Survey Prof. Paper 450-B.

Turk, J. L. 1963. The occurrence of ground water in crystalline rocks. Stanford University, Student M.S. Report.

Wahlstrom, E. E. and V. Q. Hornback. 1962. Geology of the Harold D. Roberts Tunnel, Colorado: west portal to station 468 + 49. Geol. Soc. America Bull. 73.

INTERNATIONAL INFORMATION COLLECTED ON PERMEABILITY AND CAPILLARITY

A task group on permeability and capillarity of soils, representing Committee D-18 (Soils for Engineering Purposes), American Society for Testing and Materials, was established in 1962 to assemble information on research and methodology for the permeability and capillarity of soil and rock materials. The present objective of this task group is to collect information on equipment and procedures currently used throughout the world, to summarize current and past research, and to promote needed research for the future.

A detailed questionnaire has been prepared and distributed to universities, federal and state government agencies, and commercial organizations in the engineering, agricultural, and geologic disciplines in the United States and foreign countries. Anyone who did not receive a questionnaire, may do so by contacting the chairman of the task group: A. I. Johnson, Chief, Hydrologic Laboratory, U. S. Geological Survey, Denver, Colorado.

Hydrometallurgy, 6 (1980) 121—133
Elsevier Scientific Publishing Company, Amsterdam — Printed in The Netherlands

ORE LEACHING MODEL WITH PARTIAL DECOMPOSITION OF ROCKS. I. THEORETICAL PREDICTIONS

F. LETOWSKI

Institute of Inorganic Chemistry and Metallurgy of Rare Elements, Technical University, 50-370, Wrocław (Poland)

(Received January 9th, 1979; accepted in revised form January 23rd, 1980)

ABSTRACT

Letowski, F., 1980. Ore leaching model with partial decomposition of rocks. I. Theoretical predictions. *Hydrometallurgy*, 6: 121—133.

A theoretical model of rock leaching is derived for the simultaneous reaction of two components at different rates accompanied by disintegration of the rock. The model has been developed for the acid leaching of copper sulphide minerals in rocks that contain carbonate minerals. The rate controlling step is assumed to be diffusion through the elementary sulphur layer adhering to liberated sulphide particles.

INTRODUCTION

Considerable interest in hydrometallurgical metal winning processes, particularly in the winning of copper from ores, has led in recent years to a number of mathematical models which have been developed for these processes. At least three kinetic acid leaching models were developed for low-grade porphyry ores containing copper sulphides and particularly chalcopyrite: an "in situ" ore leaching model (Bartlett, 1973), a heap leaching model (Roman et al., 1974) and a mixed kinetics model (Braun et al., 1974; Madsen et al., 1975). A kinetic ammonia leaching model of ores containing native copper and chalcocite was also developed (Hockings and Freyberger, 1976). Finally, Roach and Prosser (1978) presented a universal model describing the chemical treatment of low-grade materials, based on the transportation of liquid or gaseous reactants through porous lumps. Of the other attempts to describe leaching processes mathematically one could mention the leaching models for pure minerals described by Habashi (1970), the geometrical leaching model for polydispersed materials (Neumann, 1964) and the leaching model for nonporous particles (Loveday, 1975). However, their application is limited as a rule to the high-grade materials.

The kinetic model which allows for the effect of chemical decomposition of secondary ore components on the leaching yield of the main component is pre-

0304-386X/80/0000—0000/$02.25

sented in this paper. This case occurs during acid leaching of copper sulphide ores from sedimentary deposits containing some carbonate gangue in the form of dolomite, calcite or magnesite.

It may be expected that in acid solutions the rate at which large pores are generated by decomposition of, for instance, dolomite will be high enough that penetration of the reagent to the interior of a lump of ore is a secondary factor determining leaching rate. In extreme, the lump may disintegrate and expose the copper minerals before they have reacted to any extent.

Studies were therefore initiated to determine conditions under which the costs involved in sulphuric acid consumption by the decomposition of dolomite might be compensated by the elimination of ore crushing and grinding in order to increase the access of the leaching agent to the surface of the copper sulphides and to replace the crushing process with the chemical decomposition of certain deposit components (Letowski, 1978).

Part II of this paper describes laboratory tests on the model derived in Part I (Letowski and Augustowska, 1980).

BASIC CONSIDERATIONS*

The model in question is concerned with ore leaching in an acid ferric sulphate solution. Ore components were divided into three groups:

(1) copper sulphides which consume an oxidant — ferric sulphate — during the leaching process;

(2) carbonates, mainly dolomite, which consume sulphuric acid during the leaching process;

(3) inert components.

The assumptions that define the model result from the following conditions in the leaching process:

(1) The decomposition of carbonates proceeds more rapidly than the simultaneous leaching of exposed copper minerals;

(2) As soon as the carbonates are fully decomposed the ore lumps disintegrate into smaller fragments;

(3) The extent to which the copper minerals are exposed to the reagent depends on the carbonate content of the ore; the insoluble components still partly block the surfaces.

The following deviations from real conditions were assumed:

(1) The model of an ore fragment of mass m_0 is a sphere with radius R_0 of the same mass and the same mass percentages of components. The factor σ which is greater than unity, relates real ore fragments to those of the model and is defined as the ratio of the real fragment surface area to that of a sphere of the same mass and density;

(2) In all unreacted ore fragments the distribution of all components is uniform;

*Definitions of the symbols used are given at the end of the paper.

(3) Copper sulphide particles are spherical grains with initial radius r_0, uniformly distributed in the ore fragment with initial radius R_0; the correlation between the model and actual condition being described by the factor σ_z defined as for the entire ore fragment;

(4) In the first approximation the sizes of all copper sulphide particles in an ore fragment are replaced by the average size of particles $\bar{r}_0$.

Additional assumptions defining the model are as follows:

(1) Decomposition of carbonates and leaching of copper proceeds with constant sulphuric acid and ferric sulphate concentrations in the leaching solution which may be readily achieved in a continuous process; the acid concentration is high enough for the hydrolytic precipitation of iron(III) from the solution to be ignored;

(2) The gypsum resulting from decomposition of dolomite and calcite does not block the sulphide surface to a significant extent. Owing to its appreciable solubility it is expected to crystallize out beyond the decomposition zone of the carbonates;

(3) The blocking effect of elementary sulphur, formed as a product of leaching of the sulphide, is assumed to control the rate of reaction of the exposed surfaces of the sulphide minerals.

The geometrical model of an ore fragment under leaching is presented in Fig. 1.

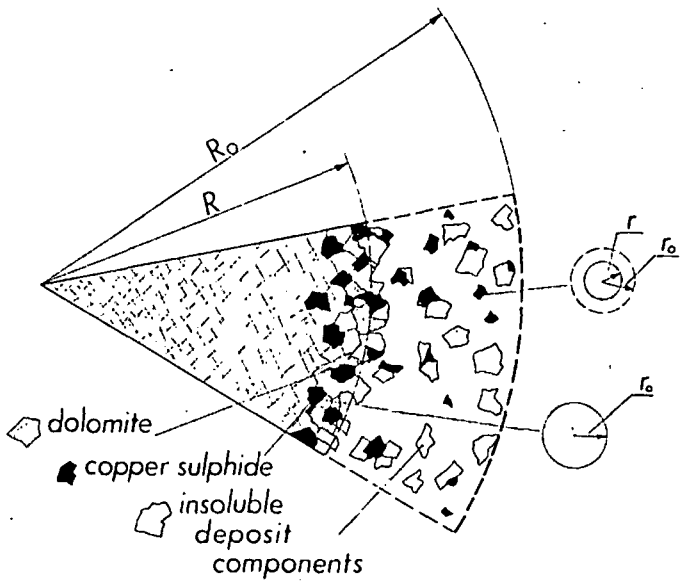

Fig. 1. Geometric model of an ore fragment under leaching.

THE EFFECT OF DOLOMITE DECOMPOSITION ON THE DEGREE OF COPPER LEACHING

According to the assumption of the model where $R_0 \gg r_0$, the degree of copper leaching α, is given by:

$$\alpha = (m_{Cu_0} - m_{Cu})/m_{Cu_0} \tag{1}$$

where m_{Cu} is the unleached mass of copper and m_{Cu_0} the initial mass of copper in the ore fragment. α depends on the degree of exposure of copper sulphide particles β which is the same as the degree of decomposition of the carbonates

$$\beta = \frac{n_0 - n}{n_0} = \frac{m_{d_0} - m_d}{m_{d_0}} \tag{2}$$

where n and m_d are the number of copper sulphide particles and mass of carbonate minerals in the unreacted core of radius R, respectively, and n_0 and m_{d_0} are the same values in the unleached ore fragment.

Since the mass of decomposed carbonates is $(4/3)\pi\rho g_d(R_0^3 - R^3)$ the degree of exposure of copper sulphides may be presented as a function of radius R of the unreacted core.

$$\beta = 1 - (R/R_0)^3 \tag{3}$$

On the other hand, the degree of dispersion of copper minerals expressed by the number of sulphide particles in the ore fragment, n_0, is the ratio of the total copper content in the ore fragment to the copper content in one sulphide particle and is equal to

$$n_0 = \frac{\frac{4}{3}\pi R_0^3 \rho g_{Cu}}{\frac{4}{3}\pi r_0^3 \rho_z x_{Cu}} = \left(\frac{R_0}{r_0}\right)^3 \frac{1}{G} \tag{4}$$

where the factor typical of a given type of ore, G, is equal to

$$G = \rho_z x_{Cu}/\rho g_{Cu} \tag{5}$$

The balance of leached copper may be described by the equation:

$$m_{Cu_0} - m_{Cu} = \tfrac{4}{3}\pi R_0^3 \rho g_{Cu} - \left[\tfrac{4}{3}\pi R^3 \rho g_{Cu} + \tfrac{4}{3}\pi \rho_z x_{Cu} \sum_{i=1}^{i=n_0-n} r_i^3\right] \quad \text{for } \tau_i \leq t \tag{6}$$

where the first term on the right-hand side is the initial copper content in the ore fragment and the expression in brackets is the sum of the copper mass left in the unreacted core and the mass of unleached copper left in $n_0 - n$ grains exposed during a time τ_i equal to, or smaller than the leaching time t.

After substituting the respective terms of eqn. (6) into expression (1) and,

after taking eqns. (2), (4) and (5) into account, the degree of copper leaching is

$$\alpha = \left[1 - \left(\frac{R}{R_0}\right)^3\right] \left[1 - \frac{\sum_{i=1}^{n_0-n} r_i^3}{(n_0 - n)\bar{r}_0^3}\right] \tag{7}$$

According to expression (3), eqn. (7) gives the relation between the degree of conversion of soluble deposit components β (i.e. carbonates in this case) and the degree of copper leaching α

$$\frac{\alpha}{\beta} = 1 - \frac{\sum_{i=1}^{n_0-n} r_i^3}{(n_0 - n)\bar{r}_0^3} \quad \text{for all } \tau_i \leqslant t \tag{8}$$

Values of α and β for all leaching times t are obtained experimentally. The ratio α/β can also be expressed in terms of mean values $\bar{r}_0$ and $\bar{r}$

$$\alpha/\beta = 1 - (\bar{r}/\bar{r}_0)^3 \tag{9}$$

where $\bar{r}$, the so-called "mean radius" of exposed grains of copper sulphides after leaching time t, is related to the sizes, r_i, of copper sulphide grains after an exposure time τ_i by means of the following relationship:

$$\bar{r}(t) = \left[\frac{\sum_{i=1}^{i=n_0-n} r_i^3}{n_0 - n}\right]^{1/3}_{(\tau_i \leqslant t)} \tag{10}$$

LEACHING PROCESS EQUATION

As in the case of the dissolution of pure mineral particles where, depending on leaching conditions, the Valensi, Jander or Ginstling—Brounsthein—Crank equations may be applied (Habashi, 1970) as well as in the other leaching models for low-grade raw materials mentioned in the introduction, the dependence of the degree of ore leaching on time may be derived with sufficient accuracy from the simplified Fick equation where the transportation of reactants or products is expressed by flux I perpendicular to the leached surface:

$$I = -\frac{\mathrm{d}m_{\mathrm{Cu}}}{\mathrm{d}t} = \left(\sum_{i=1}^{n_0-n} S_i\right) D \frac{\mathrm{d}c}{\mathrm{d}y_i} \tag{11}$$

where $-\mathrm{d}m_{\mathrm{Cu}}/\mathrm{d}t$ is the change in copper mass in the solid phase during leach-

of radii R and $\bar{r}$:

$$m_{Cu} = \tfrac{4}{3}\pi R^3 \rho g_{Cu} + \tfrac{4}{3}\pi \bar{r}^3 (n_0 - n)\rho_z x_{Cu} =$$

$$= \tfrac{4}{3}\pi \rho g_{Cu} \left[R^3 + (R_0^3 - R^3)\left(\frac{\bar{r}}{\bar{r}_0}\right)^3 \right] \tag{16}$$

Thus, a change in the mass of unleached copper is the following function of changes in R and $\bar{r}$:

$$dm_{Cu} = \frac{4\pi\rho g_{Cu}}{\bar{r}_0^3} [(\bar{r}_0^3 - \bar{r}^3)R^2 dR + (R_0^3 - R^3)\bar{r}^2 d\bar{r}] \tag{17}$$

Bearing in mind that according to eqn. (11) $dm_{Cu} = -I\,dt$ and substituting eqns. (15) and (17) for dm_{Cu} and I, the basic equation describing a change in the ore fragment size, R, and in the sizes of copper sulphide particles, $\bar{r}$, during the leaching process is

$$-\frac{4\pi\rho g_{Cu}}{\bar{r}_0^3} [(\bar{r}_0^3 - \bar{r}^3)R^2 dR + (R_0^3 - R^3)\bar{r}^2 d\bar{r}] =$$

$$= \frac{4\pi(R_0^3 - R^3)(1-p)\sigma_z D(c - c_i)\bar{r}}{G\bar{r}_0^2(\bar{r}_0 - \bar{r})}\,dt \tag{18}$$

This equation should be integrated within the appropriate limits of changes in R and $\bar{r}$ and time t:

$$\frac{(\bar{r}_0 - \bar{r})}{\bar{r}\bar{r}_0}(\bar{r}_0^3 - \bar{r}^3)\int_{R_0-\epsilon}^{R} \frac{R^2 dR}{R_0^3 - R^3} + \int_{\bar{r}_0}^{\bar{r}} \bar{r}\,d\bar{r} - \frac{1}{\bar{r}_0}\int_{\bar{r}_0}^{\bar{r}} \bar{r}^2 d\bar{r} =$$

$$= -\frac{(1-p)\sigma_z D(c - c_i)}{G\rho g_{Cu}} \int_0^t dt \tag{19}$$

The lower integration limit of the first integral is shifted by the amount of the value ϵ. This parameter characterizes the copper sulphide surface area accessible to the leaching agent as soon as the leaching process begins, corresponding to the fraction of ore fragment surface occupied by copper sulphides. Since, however, integration is carried out not as a function of surface area but of radius R,

$$\epsilon = R_0 \sqrt{g_{Cu}} \tag{20}$$

and this is the hypothetical change in radius R which would lead to the same degree of surface exposure as that occurring in the unleached ore fragment. In this case the corrected degree of sulphide surface exposure β is

$$\beta = 1 - R^3/(R_0 - \epsilon)^3 \tag{21}$$

ing, dc/dy_i is the gradient of oxidant concentration in the diffusion layer y_i, and $\sum_{i=1}^{n_0-n} S_i$ is the sum of all exposed sulphide surfaces through which the reactants are transported. D is the diffusion coefficient of the leaching agent in the reaction zone which in this case is probably limited to the diffusion layer y at the boundary of the solution and copper sulphide phases. In the case of a porous diffusion layer its thickness may vary as the reaction proceeds. In the case under consideration $y_i = r_{0i} - r_i$.

The exposed sulphide average surface area $\sum \bar{S}$, equal to the real sum $\sum_{i=1}^{n_0-n}$ is given by:

$$\sum \bar{S} = 4\pi \bar{r}^2 (1-p)(n_0 - n)\sigma_z \tag{12}$$

where p is the fraction of copper sulphide surface accessible for the leaching agent, depending on the degree of its masking by the insoluble part of the deposit. Since $n = n_0(1-\beta)$, taking eqns. (3) and (4) into account, one obtains the exposed surface area as a function of the radii R and $\bar{r}$ of the unreacted core and liberated sulphides:

$$\sum \bar{S} = 4\pi \bar{r}^2 (R_0^3 - R^3)(1-p)\sigma_z / G\bar{r}_0^3 \tag{13}$$

Under constant leaching conditions the flux of copper transported from unit surface area of a given sulphide is constant. Because $\sum \bar{S} = \sum_{i=1}^{n_0-n} S_i$, on substituting expression (13) for $\sum \bar{S}$ into eqn. (11) and allowing for the fact that for average grains

$$dy = d(\bar{r}_0 - \bar{r}) = -d\bar{r} \tag{14}$$

one obtains the relationship which, after integration within the reactant concentration limits in the bulk solution, c, and in the reaction zone, c_i, and also within the limits of the change in dimensions of copper sulphide particles from $\bar{r}_0$ to $\bar{r}$, leads to determination of the flux I

$$I = \frac{4\pi(R_0^3 - R^3)(1-p)\sigma_z D(c - c_i)\bar{r}}{G\bar{r}_0^2(\bar{r}_0 - \bar{r})} \tag{15}$$

According to the balance of leached copper (6) and relationships (4), (5), (3) and (10), the mass of unleached copper may be described by the function

and the lower integration limit of this integral may be represented by the function of the mass fraction of copper in the ore:

$$R_0 - \epsilon = R_0(1 - \sqrt{g_{Cu}}) \tag{22}$$

After solving eqn. (19) and after substituting α and β from relationship (9) the final equation may be derived

$$1 - \frac{2}{3}\frac{\alpha}{\beta} - \left(1 - \frac{\alpha}{\beta}\right)^{2/3} + \frac{2}{3}\frac{\alpha}{\beta}\left[\left(1 - \frac{\alpha}{\beta}\right)^{-1/3} - 1\right] \ln\left(1 + \frac{\beta}{A-1}\right) = kt \tag{23}$$

where the constant, k, is:

$$k = 2(1-p)\sigma_2 D(c - c_i)/\bar{r}_0^2 \; Gpg_{Cu} \tag{24}$$

and A is a factor depending on copper content in the ore:

$$A = (1 - \sqrt{g_{Cu}})^{-3} \tag{25}$$

DISCUSSION OF THE KINETIC EQUATION

Fig. 2 shows a number of curves $\alpha = f(kt)$ determined from eqn. (23) for various ratios α/β and various copper concentrations in the ore (g_{Cu}) related to the parameter A according to eqn. (25).

Generalising discussion of the leaching model with decomposition of deposit components and extending the interpretation of eqn. (23) to other cases, it can be seen that the variable which determines the leaching rate of the sulphide minerals $\alpha = f(t)$ is the leaching rate of the carbonate minerals $\beta = f(t)$.

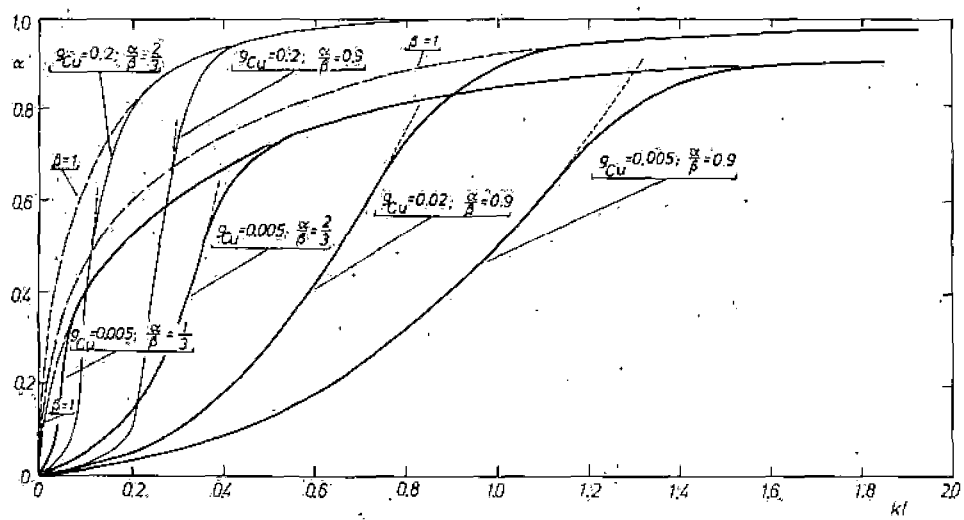

Fig. 2. Effect of the α/β ratio on the degree of copper leaching α for various copper concentrations in the raw material (g_{Cu}) as a function of kt.

In addition, the leaching rate α depends on the concentration of the sulphide minerals in the ore, included in rate constant k and in parameter A, and it also depends on other values typical of a given ore, represented by the rate constant k.

As the ratio α/β increases, the nature of the curves shown in Fig. 2 is changed since the leaching rate of the sulphide minerals is inhibited by the relatively slow decomposition of deposit components.

If β is much greater than α, it may be assumed with a certain degree of approximation that for all times t, β achieves a maximum value of 1. This is equivalent to rapid decomposition of the ore fragment, and the leaching process itself may be interpreted as the leaching of ore crushed down to sizes depending on the relative content of insoluble gangue components. In a specific case where, for instance, the carbonate concentration is so high that after its decomposition all copper sulphides would be exposed ($1 - p \approx 1$), the leaching rate is determined by the diffusion of reactants through the maximally extended sulphide surface and eqn. (23) is reduced to the form

$$1 - \tfrac{2}{3}\alpha - (1-\alpha)^{2/3} + \tfrac{2}{3}\alpha[(1-\alpha)^{-1/3} - 1] \ln \frac{A}{A-1} = kt \qquad (26)$$

This equation corresponds to curves in Fig. 2 determined for $\beta = 1$ and for various copper concentrations in the ore (g_{Cu}). During the leaching process the total decomposition of a gangue component being leached more rapidly is achieved earlier than that of the main component and it is therefore practically impossible to maintain a constant α/β ratio. For this reason the curves describing the leaching process for various α/β ratios turn gently into curves characteristic of $\beta = 1$ in the final stage of leaching.

On the other hand, if the degree of conversion of deposit components for all times t is approximately equal to the degree of leaching of the main component and $\alpha = \beta$, then the leaching rate is determined by the velocity of the spherical front shifting from R_0 to R and eqn. (23) is reduced to the form

$$\ln\left(1 + \frac{\alpha}{A-1}\right) = \tfrac{1}{2}(1 - 3kt) \qquad (27)$$

If $\beta < \alpha$ it is necessary to allow for the dominating effect of diffusion inhibition through a porous bed. Such a situation is contrary to the assumptions of the model presented in this paper. This condition is reflected in the model developed by Madsen et al. (1975) and the model of Roach and Prosser (1978).

The most important differences in the model described in this paper and that of the model of Roach and Prosser are as follows:

(1) In the geometrical assumption of the model of Roach and Prosser spherical grains of uniform size of reactive minerals randomly distributed in the ore lump are exposed to contact with leaching solution by cylindrical pores of uni-

$$\int_{R_0-\epsilon}^{R} \frac{R^2 dR}{R_0^3 - R^3} = -\frac{1}{3} \ln \frac{R_0^3 - R^3}{R_0^3 - (R_0 - \epsilon)^3} \tag{30}$$

Since according to eqn. (21) and eqn. (20)

$$R^3 = (R_0 - \epsilon)^3(1 - \beta) = [R_0(1 - \sqrt{g_{Cu}})]^3(1 - \beta) \tag{31}$$

the solution of integral (30) is the relationship

$$\int_{R_0(1-\sqrt{g_{Cu}})}^{R} \frac{R^2 dR}{R_0^3 - R^3} = -\frac{1}{3} \ln \left(1 + \frac{\beta}{A - 1}\right) \tag{32}$$

where A is a factor depending on the copper content of the ore according to relationship (25). Calculation of the other integrals in eqn. (19) yields the equation:

$$-\frac{(\bar{r}_0 - \bar{r})}{\bar{r}\bar{r}_0} \frac{(\bar{r}_0^3 - \bar{r}^3)}{3} \ln \left(1 + \frac{\beta}{A - 1}\right) + \frac{1}{2}(\bar{r}^2 - \bar{r}_0^2) - \frac{(\bar{r}^3 - \bar{r}_0^3)}{3\bar{r}_0} = -\frac{(1 - p)\sigma_z D(c - c_i)t}{G\rho g_{Cu}} \tag{33}$$

which, after being ordered and putting $(\bar{r}_0^3 - \bar{r}^3)/3\bar{r}_0$ before the bracket, after solving with respect to α and β using eqn. (9), results in the final equation (23).

LIST OF SYMBOLS

A	parameter depending on the copper content in the ore, $A = (1 - \sqrt{g_{Cu}})^{-3}$
c, c_i	leaching agent (ferric sulphate) concentration in the bulk solution and in the reaction zone
D	diffusion coefficient of the leaching agent in the reaction zone y
G	coefficient typical of a given type of ore, $G = \rho_z x_{Cu}/\rho g_{Cu}$
g_d, g_{Cu}	mass fraction (content) of carbonates or copper in the ore
I	flux of reactant or leaching products
k	rate constant
m_0, m_{d_0}, m_{Cu_0}	initial quantity of unleached ore and initial quantity of carbonates and copper in the ore
m, m_d, m_{Cu}	mass of ore, carbonates and copper in the ore at time t
n_0, n	number of copper sulphide particles with average radius $\bar{r}_0$ or $\bar{r}$ in an ore fragment with radius R_0 or R, respectively
p	coefficient related to the masking of the copper sulphide surface by the insoluble component of the deposit, equal to the fraction of surface inaccessible for the leaching agent

form size arranged in an orthogonal three-dimensional interconnected network. The general Roach and Prosser equation may be presented in the following form according to their terminology:

$$1 - \tfrac{2}{3}\frac{\phi}{\theta} - \left(1 - \frac{\phi}{\theta}\right)^{2/3} = \frac{2M'CD_{\text{eff}}t}{\theta\rho\alpha n'R^2} \tag{28}$$

where ϕ is recovery or proportion of the reactive phase (minerals) leached from the ore lump, and θ is ultimate recovery or proportion of reactive phase eventually accessible. Parameter θ does not depend on the leaching time and it is constant during the process.

(2) In the geometrical assumption of the model described in this paper spherical grains of uniform size of the main reactive phase (minerals) uniformly distributed in the ore lump are blocked by the accompanying reactive phase and by insoluble ore components. Because the rate of decomposition or leaching of the accompanying reactive phase (in this case dolomite) is more rapid than the rate of leaching of main reactive phase (in this case copper sulphides), the main reactive minerals are liberated during the leaching process.

The ratio α/β in eqn. (23) corresponds to the ϕ/θ ratio in eqn. (28). In contradiction to the parameter θ, which is constant during leaching, the degree of exposure of grains of main reactive minerals (relationship (2)) changes during the leaching process. This results in the final equation (23).

One can easily observe that the first three terms of eqn. (23) related to the diffusion contribution (Madsen et al., 1975; Letowski, 1978) correspond to the left-hand term of eqn. (28). Other terms in the left hand of eqn. (23) are related to the degree of exposure of the grain surfaces of the main reactive component which depends on the degree of conversion of another reactive component.

APPENDIX

In order to solve the first integral in eqn. (19) it was resolved into simple fractions:

$$\int \frac{R^2 dR}{R_0^3 - R^3} = \tfrac{1}{3}\int \frac{dR}{R_0 - R} - \tfrac{2}{3}\int \frac{R\,dR}{R^2 + RR_0 + R_0^2} -$$

$$- \frac{R_0}{3}\int \frac{dR}{R^2 + RR_0 + R_0^2} \tag{29}$$

and then typical solutions were used replacing the function arctg R with the first term of a series expansion. Taking the integration limits into consideration, this integral was calculated

R_0 radius of the unleached ore fragment

R radius of the unreacted ore fragment core at time t

r_{0j} radius of the copper sulphide grains of a given grain-size grade j in the unleached ore fragment

$\bar{r}_0$ average radius of copper sulphide particles in the unleached ore fragment, $\bar{r}_0 = \sum_j r_{0j} x_j$

r_i radius of ith grain of copper sulphide leached at $\tau_i \leqslant t$

$\bar{r}$ average radius of unreacted core of copper sulphide grains during the leaching process, $\bar{r}(t) = \left[\sum_{i=1}^{i=n_0-n} r_i^3/(n_0-n) \right]^{1/3}_{(\tau_i \leqslant t)}$

$\sum_{i=1}^{n_0-n} S_i$ sum of surface areas of copper sulphide particles i accessible to the leaching agent

$\sum \bar{S}$ sum of surface areas of copper sulphide particles with average radius $\bar{r}$ accessible to the leaching agent, $\sum \bar{S} \equiv \sum_{i=1}^{n_0-n} S_i$

t leaching time of ore fragment

y, y_i reaction zone: thickness of liquid diffusion layer or thickness of porous diffusion layer of solid product of the sulphide leaching reaction at the phase boundary solution-copper sulphide

x_{Cu} mass fraction (content) of copper in the sulphide

x_j mass fraction of copper sulphide in a given grain-size grade j

α degree of copper leaching

β degree of carbonate decomposition

σ, σ_z sphericity coefficients: ratio of the actual ore fragment surface or actual copper sulphide particle surface to the surface area of a sphere with the same mass and density

ρ, ρ_z densities of ore and copper sulphides

τ_i leaching time of copper sulphide particle i equal to or smaller than time of ore fragment leaching t, $\tau_i \leqslant t$

Note: Explanation of the symbols used in eqn. (28) are provided by Roach and Prosser (1978).

REFERENCES

Bartlett, R.W., 1973. A combined pore diffusion and chalcopyrite dissolution kinetics model for in situ leaching of a fragmented copper porphyry. International Symposium on Hydrometallurgy, Chicago, 1973. AIME, New York, pp. 331–374.

Braun, R.L., Lewis, A.E. and Wadsworth, M.E., 1974. In-place leaching of primary sulphide ores: laboratory leaching data and kinetics model. Metall. Trans., 5: 1717—1726.

Habashi, F., 1970. Principles of Extractive Metallurgy. Vol. I. Gordon and Breach, New York.

Hockings, W.A. and Freyberger, W.L., 1976. Laboratory studies of in situ ammonia leaching of Michigan copper ores; In J.C. Yannopoulos and J.C. Agarwal (Eds.), Extractive Metallurgy of Copper, Vol. 2, AIME, New York, pp. 873—906.

Letowski, F., 1978. Hydrometallurgy of domestic copper raw materials. Pr. Nauk. Inst. Chem. Nieorg. Metal. Pierwiastkow. Rzadkich Politech. Wroclaw, 36: 3—168. (in Polish).

Letowski, F. and Augustowska, R., 1980. Ore leaching model with partial decomposition of rocks: II. Laboratory tests. Hydrometallurgy, 6: 135—146.

Loveday, B.K., 1975. A model for the leaching of non-porous particles. J. S. Afr. Inst. Min. Metall., 76(2): 16—19.

Madsen, B.W., Wadsworth, M.E. and Groves, R.D., 1975. Application of a mixed kinetics model to the leaching of low grade copper sulfide ores. Trans. Soc. Min. Eng. AIME, 258 (March): 69—74.

Neumann, L., 1964. A study on the dissolution kinetics of polydisperse solids by the method of a geometrical model. Collect. Czech. Chem. Commun., 29: 2094—2113.

Roach, G.I.D. and Prosser, A.P., 1978. Prediction of rates of chemical processes for treatment of low-grade materials: theory and tests for mass-transfer controlled reactions. Trans. Inst. Min. Metall., Sect. C: Mineral Process Extr. Metall., 87: C129—C138.

Roman, R.J., Benner, B.R. and Becker, G.W., 1974. Diffusion model for heap leaching and its application to scale-up. Trans. Soc. Min. Eng. AIME, 256 (Sept.): 247—256.

Zechstein Ore

Hydrometallurgy, 6 (1980) 135—146
Elsevier Scientific Publishing Company, Amsterdam — Printed in The Netherlands

ORE LEACHING MODEL WITH PARTIAL DECOMPOSITION OF ROCKS. II. LABORATORY TESTS*

F. LETOWSKI and R. AUGUSTOWSKA

Institute of Inorganic Chemistry and Metallurgy of Rare Elements, Technical University, 50-370, Wrocław (Poland)

(Received June 22nd, 1979; accepted in revised form January 23rd, 1980)

ABSTRACT

Letowski, F. and Augustowska, R., 1980. Ore leaching model with partial decomposition of rocks. II. Laboratory tests. *Hydrometallurgy*, 6: 135—146.

A kinetic leaching model with partial decomposition of the ore components has been applied to the acid leaching of a dolomitic sulphide copper ore. By means of the model the rate constants for the leaching of uncrushed ore lumps (> 0.65 cm) were determined from measurements of the fraction of copper leached and the simultaneous decomposition of dolomite. The experimental results appeared to be in good agreement with the theoretical leaching model equation. The use of the model in assessing the contributions of various rate controlling factors in the leaching process was demonstrated.

INTRODUCTION

Penetration of an acid leaching agent deep into an ore lump, facilitated by decomposition of dolomite, makes possible rapid exposure of the sulphide copper minerals without any need for comminution of the ore by grinding. A kinetic model of such a leaching process (Letowski, 1980) is described by the following equation:

$$1 - \frac{2}{3}\frac{\alpha}{\beta} - (1 - \frac{\alpha}{\beta})^{2/3} + \frac{2}{3}\frac{\alpha}{\beta}[(1 - \frac{\alpha}{\beta})^{-1/3} - 1]\ln(1 + \frac{\beta}{A-1}) = kt \qquad (1)$$

where α and β are the fraction of copper leached and dolomite decomposed, respectively, A is the parameter depending on copper content of the ore, g_{Cu}:

$$A = (1 - \sqrt{g_{Cu}})^{-3} \qquad (2)$$

and k is the leaching process rate constant defined as

$$k = \frac{2(1-p)\sigma_z D(c - c_i)}{r_0^2 G \rho g_{Cu}} \qquad (3)$$

*Part I: Letowski, 1980.

0304-386X/80/0000-0000/$02.25

The meaning of the symbols in this equation is as follows: p is the fraction of copper sulphide surface inaccessible to the leaching agent, and depends on the degree of masking by the insoluble part of deposit, σ_z is the sphericity coefficient which expresses the ratio between the actual surface area of the sulphide and the spherical surface of the same mass and density, D is the diffusion coefficient of the leaching agent in the reaction zone, c and c_i are the leaching agent concentrations in the bulk solution and in the reaction zone, respectively, r_0 is the mean copper sulphide grain radius in the unleached ore fragment, and G is the coefficient typical of a given type of ore defined by:

$$G = \rho_z \, x_{Cu} / \rho \, g_{Cu} \tag{4}$$

where ρ and ρ_z are the densities of the ore and copper sulphides in the ore, respectively, and x_{Cu} is the mass fraction of copper in the sulphide.

The first three terms of eqn. (1) denoted by X, i.e.

$$1 - \frac{2}{3}\frac{\alpha}{\beta} - (1 - \frac{\alpha}{\beta})^{2/3} = X \tag{5}$$

are related to transportation through a porous layer to the unreacted copper sulphide surface and the expression denoted by Y, i.e.

$$\frac{2}{3}\frac{\alpha}{\beta}\,[(1 - \frac{\alpha}{\beta})^{-1/3} - 1\,]\,\ln(1 + \frac{\beta}{A - 1}) = Y \tag{6}$$

is related to the development of the sulphide surface accessible to the leaching agent.

The expression $\ln(1 + \beta/(A - 1))$ describes the effect of the copper content of the ore (eqn. (2)) and the effect of the degree of dolomite decomposition expressed as a function of a change in the radius of the ore fragment during leaching from R_0 to R

$$\beta = 1 - (R/R_0)^3 \tag{7}$$

on the copper leaching process.

EXPERIMENTAL

Leaching tests were carried out with two fractions of solid slate copper ore lumps received from the Lower-Silesian Zechstein sedimentary deposits. The leaching process was performed continuously at 22—25°C in glass columns filled with ore fragments of specific grain size fractions. The leaching solution was recirculated in a closed circuit, the columns being fed from the bottom. The volumes of the solutions were selected so that the reactant concentration changes during the experiments might be regarded as insignificant with no effect on the rate constant k.

The main ore components and the compositions of leaching solutions are

summarized in Table 1; other experimental conditions are presented in Table 2.

Variations of copper and magnesium concentrations in the leaching solutions in columns I and II are presented in Table 3 while the corresponding variations in iron(II) and iron(III) concentrations are presented (typically for the coarser ore fraction, i.e. column I) in Fig. 1.

TABLE 1

Specification of ore and composition of the leaching solution.

Ore	
Mass fraction of copper, g_{Cu}	0.0468
Mass fraction of dolomite, g_d	0.1411
Mass fraction of chalcocite, Cu_2S	0.044
Mass fraction of bornite, Cu_5FeS_4	0.016
Mass fraction of chalcopyrite, $CuFeS_2$	0.004
Ore density, ρ (kg/dm³)	2.64
Leaching solution	
H_2SO_4 concentration (g/dm³)	50.0
Fe(III)* initial concentration (g/dm³)	12.0

Sulphuric acid consumption for decomposition of dolomite, 0.15 kg H_2SO_4/kg ore.

*In the form of $Fe_2(SO_4)_3$.

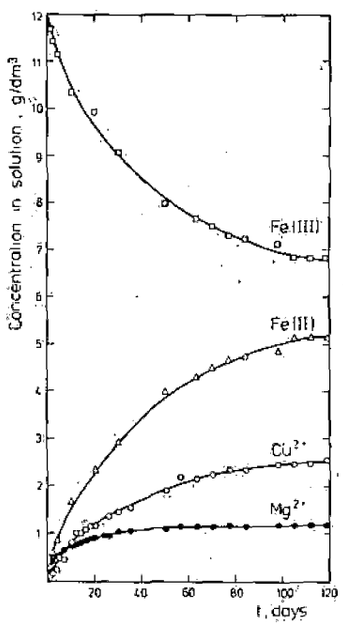

Fig. 1. Variations in solution concentrations during leaching of the ore fraction of a mean radius R_0 = 1.35 cm in column I (Table 3).

TABLE 2

Specification and conditions of laboratory ore leaching tests

Specification	Column I	Column II
Mass of ore, m (kg)	1.297	1.306
Fraction (ore fragment size) (cm)	2.4—3.4	1.0—1.4
Number of ore fragments, n	47	490
Average radius of ore fragments, R_0* (cm)	1.35	0.65
Column size, dia. × height (cm × cm)	6.8 × 54	6.8 × 54
Volume of leaching solution (dm^3)	15	15
Flow rate ($m^3 s^{-1} \times 10^3$)	3.67	3.67
Duration of tests, t (days)	120	90

*Average radius of ore fragments in a given fraction was determined from the relationship $R_0 = (3\ m\ \rho\ n/4\pi)^{1/3}$ where m = ore mass; ρ = ore density; n = number of ore fragments in the column.

TABLE 3

Variations of copper and magnesium concentrations in leaching solutions as a function of leaching time, t

Column I, R_0 = 1.35 cm			Column II, R_0 = 0.65 cm		
t (days)	Concentration (g/dm^3)		t (days)	Concentration (g/dm^3)	
	$[Cu^{2+}]$	$[Mg^{2+}]$		$[Cu^{2+}]$	$[Mg^{2+}]$
1	0.085	0.186	1	0.286	0.285
2	0.135	0.415	2	0.289	0.602
4	0.225	0.520	4	0.450	0.838
5	0.482		5	0.610	
7	0.440	0.652	10	1.202	1.150
10	0.800	0.737	12	1.320	1.160
12	1.010	0.740	14	1.450	1.170
14	1.020	0.810	16	1.480	1.180
16	1.080	0.840	18	1.602	1.195
18	1.160	0.880	20	1.750	1.220
20	1.175	0.920	24	1.780	1.240
24	1.336	0.960	26	1.860	1.240
26	1.355	0.960	48	2.340	1.245
30	1.460	1.040	50	2.422	1.260
35	1.560	1.062	56	2.540	1.288
50	1.922	1.090	63	2.526	1.302
56	2.182	1.140	70	2.580	1.300
63	2.164	1.162	77	2.620	1.300
70	2.250	1.170	84	2.678	1.302
77	2.340	1.184			
84	2.362	1.184			
98	2.464	1.184			
105	2.470	1.184			
112	2.480	1.184			
119	2.560	1.184			

CALCULATIONS

The plots of α and β determined from the data summarized in Tables 2 and 3 are presented for both experiments in Fig. 2.

The rate constants, k, were determined graphically by approximating the left-hand side of eqn. (1) to a straight line function of the leaching time (Fig. 3). The values of k determined by this method are: for a mean ore fragment radius $R_0 = 1.35$ cm., $k = 3.8 \times 10^{-3}$, and for the finer fraction, $R_0 = 0.65$ cm., $k = 4.8 \times 10^{-3}$.

Zechstein ore

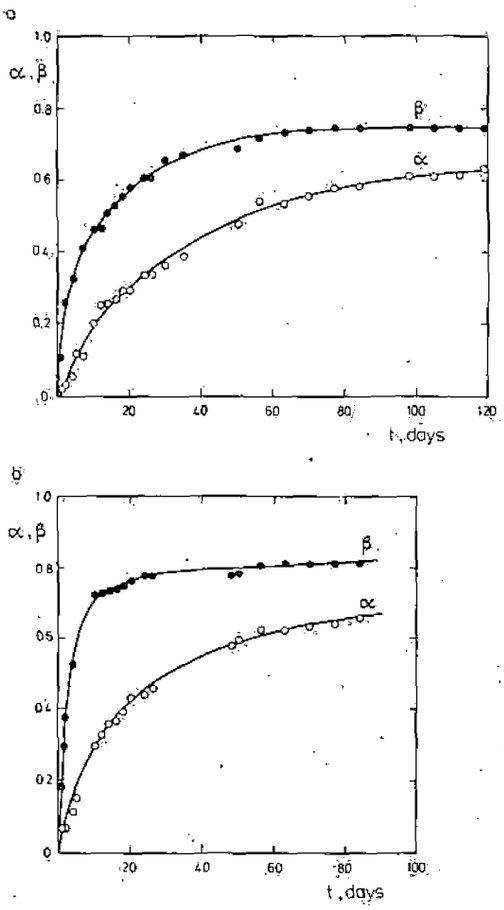

Fig. 2. Degree of copper leaching α and degree of dolomite decomposition β during leaching tests: (a) column I, $R_0 = 1.35$ cm; (b) column II, $R_0 = 0.65$ cm.

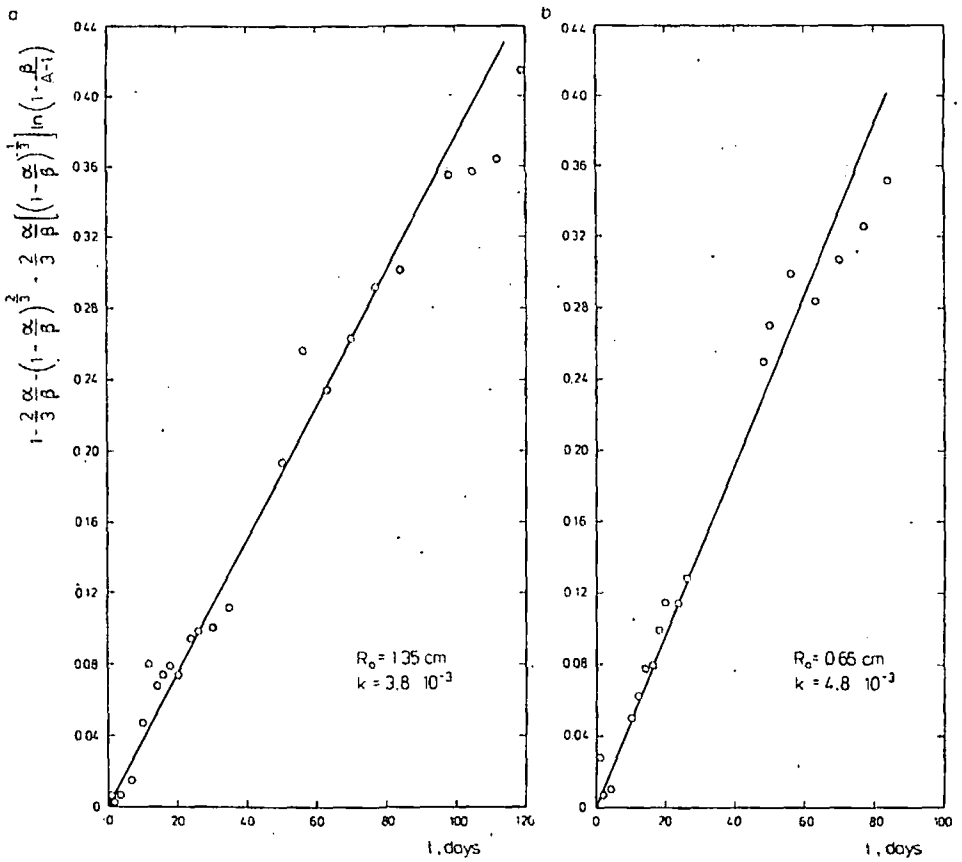

Fig. 3. Graphical determination of the rate constant k according to eqn. (1): (a) column I, R_0 = 1.35 cm; (b) column II, R_0 = 0.65 cm.

DISCUSSION OF RESULTS AND CONCLUSIONS

It may be readily proved (Letowski, 1980) that

$$\frac{\alpha}{\beta} = 1 - (\bar{r}/\bar{r}_0)^3 \qquad (8)$$

where $\bar{r}_0$ is the mean copper sulphide grain radius in an unleached ore fragment and $\bar{r}$ is the mean radius of the unreacted cores of copper sulphide grains during leaching of the ore fragments.

The mean radius $\bar{r}$ is equal to the sum of the radii r_i of sulphide grains for which time of exposure τ_i is equal to or shorter than time of leaching t (Letowski, 1980).

Since for the same type of ore the sizes of copper sulphide grains should not depend on the degree of fineness of the ore fragment size then the plot

$\alpha/\beta = f(t)$ for both fractions under investigation should coincide on one curve. This relationship is presented in Fig. 4. The slight spread of the α/β ratios for leaching the ore fragments of the mean radius R_0 = 0.65 cm and 1.35 cm indicates that the experiments performed were accurate.

On the other hand, variations in the contributions of the rate inhibiting factors related to diffusion (X), and surface development (Y), should be different for both fractions (Fig. 5).

Inhibition of the leaching reaction owing to diffusion through a porous layer exceeds that resulting from limited surfaces development in the initial stages of the leaching process. For the finer fraction (R_0 = 0.65 cm) the contribution of the latter factor and the decomposition reaction rate of

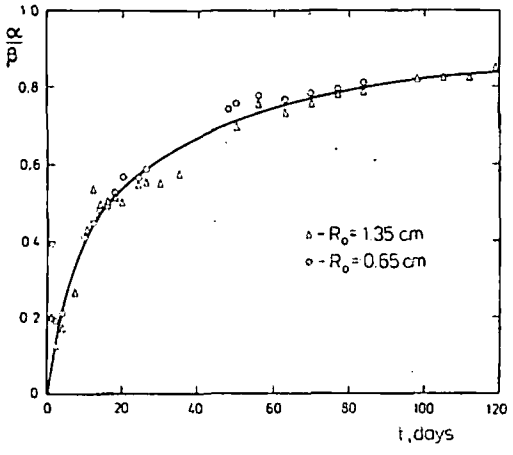

Fig. 4. Variations in the α/β ratio during leaching.

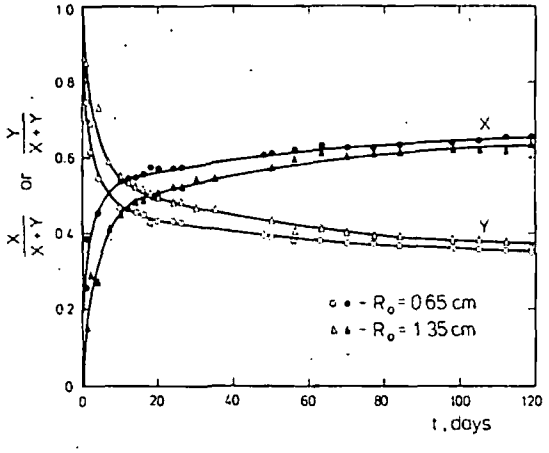

Fig. 5. Contribution of the diffusion factor (X) and surface development factor (Y) to inhibition of the leaching process rate according to eqns. (5) and (6).

copper sulphides become comparable with inhibition due to the transportation of reactants to the reaction zone within 7 days but for the coarse fraction (R_0 = 1.35 cm) only after 19 days of leaching. This means that for larger ore fragments the leaching process is controlled more by the transport conditions to the reaction zone than by surface development. In the latter stages of the leaching process diffusion inhibition contributes about 35% to control of the leaching rate and inhibition related to limited development of the sulphide surface accessible to the leaching agent contributes about 65%.

The results of the experiments indicate the following deviations of actual leaching processes from the assumptions of the model:

(1) The rate constant varies slightly depending on the ore fragment size.

(2) Plots of $\beta = f(t)$ presented in Fig. 2 demonstrate that in the final leaching stage the decomposition of dolomite becomes inhibited at 70--80%. In effect the measured points for leaching periods exceeding 60—100 days do not satisfy the model equation (1) with sufficient accuracy and in Fig. 3 these points can be seen to deviate considerably from the straight line towards lower values of k.

The reasons for these deviations may be attributed to the variability of certain parameters included in the constant k (eqn. (3)) which were not expected when eqn. (1) was derived (Letowski, 1980).

The solid decomposition product of dolomite is gypsum which may be accumulated as a reaction product directly in its zone of formation, or may crystallize from the solution beyond the reaction zone. An attempt is made to account for the deviations from the model in terms of these possibilities.

In the former case this could lead to a decrease in the decomposition rate of dolomite as leaching proceeds or even to complete masking of the dolomite surface. In that case the surface fraction of exposed copper sulphides equal to $(1 - p)$ would not be constant owing to more rapid decomposition of dolomite.

In the latter case, if gypsum were to crystallize from solution beyond the reaction zone then in the course of leaching it might impede the transport conditions through the layer so that it would be necessary to allow for variations in the diffusion coefficient D. However, although the decomposition rate of dolomite in sulphuric acid and ferric sulphate solutions is of the same order as the decomposition rate of chalcocite and is higher than the dissolution rate of other copper sulphides (Table 4), the decomposition rate of dolomite is more inhibited than the leaching reactions of copper sulphides.

Under such circumstances it is considered more probable that the source of the deviations observed is the masking of the dolomite surface by gypsum in the course of the leaching process.

The mass of decomposed dolomite $m_{d_0}\beta$ is equal to $I_d S t$ where I_d is the dolomite decomposition rate (g cm^{-2} s^{-1}), S the dolomite contact surface with solution and t the time in which a conversion ratio of β is reached.

$$m_{d_0}\beta = I_d S_t \tag{9}$$

TABLE 4

Decomposition rates of dolomite in sulphuric acid and initial dissolution rates of copper sulphides in ferric sulphate solutions

Mineral	Leaching agent	Concentration	Temp. (°C)	Rate of dissolution (g cm^{-2} s^{-1})	Reference
Dolomite	H_2SO_4	6%	20	1.72×10^{-5}	Letowski (1979)
Chalcocite	$Fe_2(SO_4)_3$	3—6 g Fe(III)/dm^3	20—30	1.8—2.8×10^{-5}	Mulak and Niemieck (1969), Letowski (1979)
Covellite	$Fe_2(SO_4)_3$	for conc. of Fe^{3+}	25	$\sim 10^{-7}$	Mulak (1971)
Bornite	$Fe_2(SO_4)_3$	higher than about	25	6.1×10^{-7}	Dutrizac and MacDonald (1974a)
Chalcopyrite	H_2SO_4, O_2	0.1 *M*	20	5.8×10^{-10}	Lewis and Braun (1973)

Since the initial dolomite mass m_{d_0} in the ore fragment is $(4/3)\pi R_0^3 \rho g_d$ and the surface area S, according to the spherical geometry and eqn. (7), is $S_0(1-\beta)^{2/3}$ where S_0 is the initial ore fragment surface area occupied by dolomite and $S_0 = 4\pi R_0^2 \sigma g_d(1-\rho)$, on substituting these relationships into eqn. (9) one obtains an expression which makes possible calculation of the time t within which the ore fragments of initial radius R_0 will reach the conversion ratio of β:

$$\frac{\beta}{(1-\beta)^{2/3}} R_0 = at \tag{10}$$

where

$$a = 3I_d(1-p)\sigma/\rho \tag{11}$$

Coefficient a may be determined from experimental data (Table 3) for both ore fractions from the formula $[\beta/(1-\beta)^{2/3}]R_0 = f(t)$. This function is presented in Fig. 6. It is approximately linear in the initial stage of leaching and the directional coefficient a is about 0.10 up to t = 14 days. For longer leaching times, probably because of variations in the $(1-p)$ factor, a no longer remains constant but gradually decreases reaching a value of 0.015 after 80 days of leaching. These variations may be attributed to the dolomite masking by gypsum formed in the reaction with sulphuric acid. It must be expected that if a sulphate-free leaching solution (e.g. HCl + $FeCl_3$) were applied, the factor $(1-p)$ would be approximately constant.

A possible effect of variations in reactant concentrations in the leaching solution on the constant k should also be considered (eqn. (3)). The conditions of the experiments were selected so that this effect would be constant during the leaching process. In compliance with the experimental conditions (Tables 1 and 2) the maximum change in H_2SO_4 concentrations accompanying the complete decomposition of dolomite did not exceed 13 g/dm^3, but the concentration of ferric sulphate decreased considerably during leaching (Fig. 1). However, according to many authors (Thomas and Ingraham, 1967; Kopylov and Orlov, 1969; Mulak and Niemiec, 1969; Dutrizac et al., 1969; Dutrizac and MacDonald, 1974a,b; Ugarte and Burkin, 1975; Ferreira and Burkin, 1975) the effect of changes in Fe^{3+} concentration on the copper sulphide leaching rate is secondary for $[Fe^{3+}] >$ 0.1 M, i.e. in solutions containing more than about 6 g/dm^3 of Fe(III). Since the ferric ion concentration during the experiments always exceeded that value, concentration changes observed should not affect the rate constant k.

From eqn. (10) and from the coefficients a determined from experiments with the fraction of ore fragments of mean radius R_0 = 1.35 cm, the expected changes in the degree of dolomite decomposition were calculated for other sizes of the leached ore fragments and presented in Fig. 7. A comparison of the curve calculated in this way for R_0 = 0.65 cm with the points obtained during experiments in column II exhibits certain differences which appear after the leaching time exceeding 40 days and did not result from the assumed model.

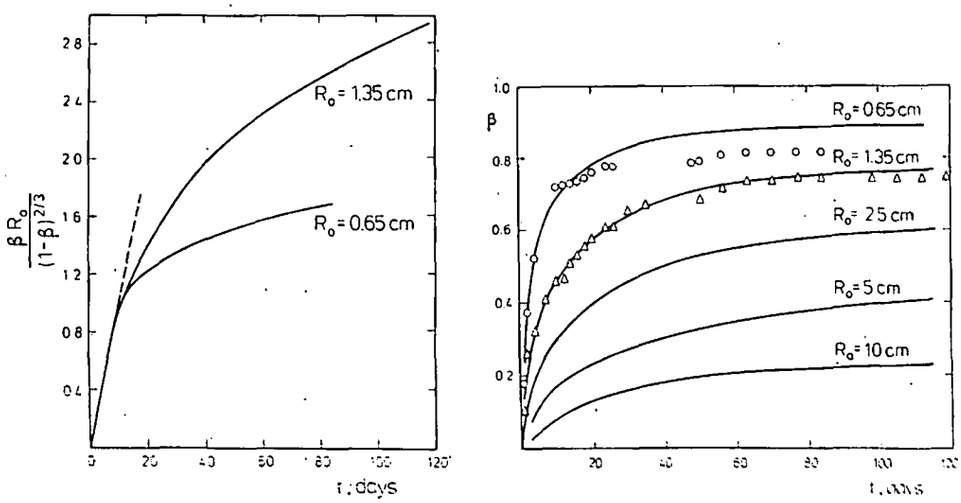

Fig. 6. A plot of $[\beta/(1-\beta)^{2/3}]R_0$ versus leaching time t for $R_0 = 1.35$ cm, and $R_0 = 0.65$ cm.

Fig. 7. Effect of the ore fragment size R_0 on the degree of dolomite decomposition β as a function of the leaching time t.

An attempt to describe the laboratory leaching tests presented in this paper on the basis of the theoretical leaching model with partial decomposition of the rock suggests its possible practical application, the more so as the deviations of the experimental results from theoretical assumption have been elucidated in the discussion presented. It is possible to expect that by applying the model for interpretation of other leaching cases and by determining the nature and magnitudes of experimental deviations from the theoretical model it would be possible to identify equally clearly the course of the leaching process.

VALIDITY OF THE MODEL

It should be noted that although the agreement between the experimental data and the predictions of the model are good except in the latter stages of leaching, this in itself does not establish the physical validity of the model. In order to do so it would be necessary to determine the values of the parameters k and a independently by minerological examination of the ore both before and during the course of leaching. Such a study should also confirm whether gypsum precipitation is in fact the cause of the deviations from the predictions of the model observed during the later stages of the process and whether an impenetrable layer of gypsum does form to prevent reaction of the acid with the dolomite.

Nevertheless the model is a useful means of predicting the effect of various leaching conditions and of indicating the relative importance of the various factors that might control the leaching rate.

REFERENCES

Dutrizac, J.E. and MacDonald, R.J.C., 1974a. Ferric ion as a leaching medium. Miner. Sci. Eng., 6(2): 59—100.

Dutrizac, J.E. and MacDonald, R.J.C., 1974b. Kinetics of dissolution of covellite in acidified ferric sulphate solution. Can. Metall. Q., 13(3): 423—33.

Dutrizac, J.E., MacDonald, R.J.C. and Ingraham, T.R., 1969. The kinetics of dissolution of synthetic chalcopyrite in aqueous acidic ferric sulphate solutions. Trans. Metall. Soc. AIME, 245: 955—959.

Ferreira, R.C.H. and Burkin, A.R., 1975. Acid leaching of chalcopyrite. In A.R. Burkin (Ed.), Leaching and Reduction in Hydrometallurgy. The Institution of Mining and Metallurgy, London, pp. 54—66.

Kopylov, G.A. and Orlov, A.I., 1969. Rates of bornite and chalcocite dissolution if ferric sulphate, Tr. Irkutsk. Politechn. Inst. (Rus.), 46: 127—132.

Letowski, F., 1979. Hydrometallurgy of domestic copper raw materials, Pr. Nauk. Inst. Chem. Nieorg. Metal. Pierwiaskow. Rzadkich Politech. Wroclaw, 36: 3—168 (in Polish).

Letowski, F., 1980. Ore leaching model with partial decomposition of rock. I. Theoretical predictions, Hydrometallurgy, 6: 121—133.

Lewis, A.E. and Braun, R.L., 1973. Nuclear chemical mining of primary copper sulphides. Trans. Soc. Min. Eng. AIME, 254: 217—254.

Mulak, W., 1971. Kinetics of dissolving polydispersed covellite in acidic solutions of ferric sulphate. Roczn. Chem., 45: 1417—1424.

Mulak, W. and Niemiec, J., 1969. Kinetics of cuprous sulphide dissolution in acidic solutions of ferric sulphate. Roczn. Chem., 43: 1387—1394.

Thomas, G. and Ingraham, T.R., 1967. Kinetics of dissolution of synthetic covellite in aqueous acidic ferric sulphate solutions. Can. Metall. Q., 6: 153—165.

Ugarte, F.J. and Burkin, A.R., 1975. Mechanism of formation of idaite from bornite by leaching with ferric sulphate solution. In A.R. Burkin (Ed.), Leaching and Reduction in Hydrometallurgy. The Institution of Mining and Metallurgy, London, pp. 46—53.

OXIDATION OF MOLYBDENUM BY NITRIC ACID

UDC 669.283

I. P. Smirnov, V. I. Zyurkalov, and N. I. Chuikina

A study was made in the present work of molybdenite oxidation by nitric acid [1-5] in the presence of other sulfides and of their effect upon the kinetics of the process. The subject of study was molybdenite powder -0.1 + 0.074 mm in size containing 94% Mo. The added sulfides were of the same size.

A weighed portion of molybdenite (0.1-0.3 g) was placed in a glass vessel, to which 1200 ml of a solution of acids of specified concentration were added. The solution was mixed mechanically at 600 rpm. Provision was made to isolate the gas phase produced from the surrounding atmosphere. The process temperature was kept constant with an accuracy of ± 0.5° C. The oxidation-reduction potential of the solution was monitored continuously, and the solution molybdenum concentration was measured periodically. The instant of molybdenite addition to the solution heated to the necessary temperature was taken as the start of the process.

The sulfuric and nitric acid concentrations in the solution were each kept at the 50 g/liter level in studying the effect of temperature upon the speed of molybdenite oxidation.

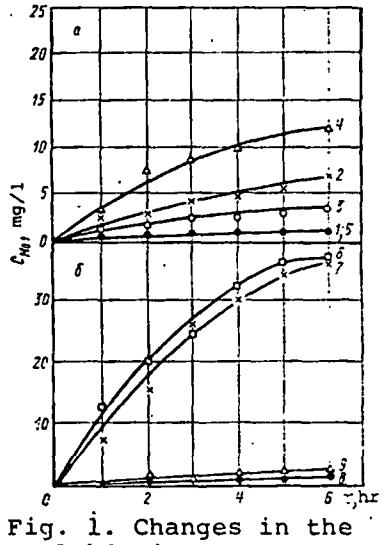

Fig. 1. Changes in the molybdenite concentration in time at 80° C with various additives, g/liter: 1) without additives; 2) 1 FE(III); 3) 0.5 $CuFeS_2$; 4) 0.5 FeS_2; 5) 0.5 FeS_2 + 20 $CO(NH_2)_2$; 6) 2 FeS_2; 7) NO_2 (gas); 8) 2 ZnS; 9) 50 H_2SO_4 + 2 $Ce(SO_4)_2$.

Oxidation of molybdenite by nitric acid in a sulfuric acid medium begins at 70-80° C and proceeds at low speeds (Fig. 1). Addition of sulfides (pyrite and chalcopyrite) increases the speed of molybdenite dissolution, pyrite having the more effective action.

Experiments in which nitrogen peroxide was passed through the [illegible] ut to confirm that oxides of ni[illegible] pyrite and chalcopyrite were ad[illegible] idation was achieved as when py[illegible] lb, curves 6 and 7).

th[illegible] rite is present, the effect of wh[illegible] because the oxides of nitrogen [illegible]g to the following reactions:

$$[illegible]O_2 + 5N_2 + 4H_2O. \quad (1)$$

$$+ 7/2N_2 + 4H_2O \quad (2)$$

and curve 5 (see Fig. 1a) coincides with curve 1, which is for oxidation by nitric acid alone.

It is interesting to note that there was no acceleration of molybdenite oxidation when molybdenite and sphalerite were oxidized together (see Fig. 1, curve 8). Sphalerite obviously dissolves according to the following reactions:

$$ZnS + 2HNO_3 = Zn(NO_3)_2 + H_2S\uparrow. \quad (3)$$

$$ZnS + H_2SO_4 = ZnSO_4 + H_2S\uparrow. \quad (4)$$

The hydrogen sulfide which evolves reacts with the nitric acid without forming oxides of nitrogen:

$$8HNO_3 + 5H_2S = 4N_2 + 5H_2SO_4 + 4H_2O. \quad (5)$$

The experiments confirmed that the oxides of nitrogen formed by the decomposition of nitric acid act as oxidizing agents for molybdenite.

Increasing the pyrite consumption increases the molybdenite oxidation speeds considerably. The oxidation speed obtained by passing nitrogen peroxide through the solution is achieved with a pyrite consumption of 3 g.

Raising the temperature when pyrite is added increases the speed of molybdenite oxidation substantially (Fig. 2). The presence of pyrite shifts the temperature at which oxidation begins. With a pyrite consumption of 2 g, oxidation begins at 30° C and proceeds more rapidly than oxidation by nitric acid alone at 80° C. At 80° C the speed of molybdenite oxidation in the presence of pyrite is dozens of times greater than without pyrite.

Thus it was established that addition of pyrite to solutions containing nitric acid caused the acid to decompose and intensified the process of molybdenite decomposition.

When nitrogen peroxide was passed through the sulfuric acid solution, the molybdenite oxidation speeds were of the same order as when pyrite was added (see Fig. 2). It is quite probable that nitrogen peroxide serves as the direct oxidizing agent. The reaction of molybdenite oxidation by nitric acid is in the kinetic region, and the apparent activation energy is 20-26 kcal/mole [1,3]. When nitrogen peroxide is passed through the sulfuric acid solution, the apparent activation energy reaches 20.5-23.6 kcal/mole when the temperature changes from 60 to 80° C. It falls to 4-4.5 kcal/mole with a further increase in temperature, to 90° C. Diffusion limitations are imposed upon the molybdenite oxidation process under these conditions.

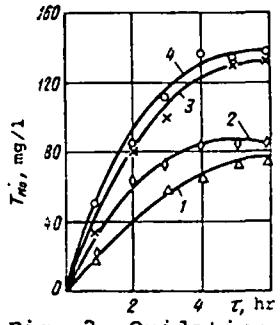

Fig. 2. Oxidation of molybdenite in the presence of pyrite (2,3) and with nitrogen peroxide blowing (1,4): T_{Mo} = concentration. Temperature, °C: 1,2) 70; 3,4) 80.

The oxidation of molybdenite by nitric acid with addition of pyrite is in the mixed diffusion-kinetic region. The apparent activation energy when the temperature changes from 60 to 90° C is 8-9 kcal/mole.

The speed of molybdenite oxidation by oxygen in an alkaline medium is determined by the heterogeneous reaction on its surface [6]. The oxygen is adsorbed (chemisorption) on the sulfide surface, which is covered by a monomolecular layer of oxygen consisting of 1 mole O_2 to each mole of molybdenite. The chemical mechanism of sulfide oxidation in an acid medium is probably more complex. The products of molybdenite oxidation are molybdate and sulfate ions MoO_4^{2-} and 2 SO_4^{2-} [5], i.e., 9 atoms of O_2 are required for one atom of Mo. It was proved in [7-9] that molybdenite is oxidized by annexation of an oxygen atom, with formation of molybdenum oxysulfide and subsequent replacement of sulfur atoms by oxygen atoms.

$$MoS_2 + {}^1/_2O_2 \rightleftarrows MoOS_2. \quad (6)$$

$$MoOS_2 + 1{}^1/_2O_2 \rightleftarrows MoO_2S + SO_2. \quad (7)$$

$$MoO_2S + {}^1/_2O_2 \rightleftarrows MoO_3 + SO_2. \quad (8)$$

Molybdenite can be regarded as a p-type semiconductor [8] which can maintain "strong" chemisorption of nitrogen peroxide and which has marked donor-acceptor properties. Formation of a "strong" bond between the surface and the sorbed particle leads to an increase in the reactive capacity of the latter.

Thus the following molybdenite oxidation mechanism may be suggested.

1. Adsorption of nitrogen peroxide at active centers on the molybdenite surface:

$$MoS_2 + NO_2 \rightarrow MoS_2 \ldots NO_2aq. \quad (9)$$

2. Reaction between molybdenite and nitrogen peroxide, forming oxy compounds:

$$MoS_2 \ldots NO_2aq \rightarrow MoOS_2 + NO\uparrow. \quad (10)$$

3. Oxidation of molybdenum oxy compounds:

$$MoOS_2 + 5NO_2 \rightarrow MoO_2S + SO_4^{2-} + 5NO\uparrow. \quad (11)$$

$$MoO_2S + 5NO_2 \rightarrow MoO_3 + SO_4^{2-} + 5NO\uparrow. \quad (12)$$

4. MoO_3 dissolves in the solution.

Molybdenite is oxidized and dissolved at constant speed. This is typical of processes taking place at active centers (caused by defects in the crystalline structure) and not over the whole surface; this is proved by the straightness of the sectors in the molybdenum concentration-time curves (see Fig. 1). When all the active centers are occupied, the curves showing changes in the speed of molybdenite oxidation in time are almost parallel to the abscissa.

CONCLUSIONS

1. Pyrite has the greatest effect upon the speed of molybdenite oxidation: it is readily oxidized by nitric acid, causing the latter to decompose forming oxides of nitrogen.

2. Oxidation begins at 30° C in the presence of pyrite, and increases in speed as the temperature rises and pyrite consumption increases.

3. The apparent activation energy values for the reactions were found. It was demonstrated that addition of pyrite shifts the reaction into the diffusion-kinetic region.

4. A chemical mechanism for the reaction of molybdenite oxidation by nitric acid was suggested. It was demonstrated that oxidation takes place at active centers on the mineral surface.

REFERENCES

1. N. N. Sobinyakova and G. A. Ivantsova, Mineral Raw Materials, 1961, Issue 2, 206-209; 1966, Issue 13, 70-64.

2. A. N. Zelikman, Molybdenum, Moscow, Metallurgizdat, 1970, 440 pages, illustrated.

3. O. V. Fedulov, B. I. Taranenko, V. D. Ponomarev, et al., in: Metallurgy and Concentration, Alma-Ata, Vol. 2, 1966, 86-94.

4. S. S. Smirnov, The Oxidation Zone in Sulfide Deposits, Moscow, Academy of Sciences of the USSR, 1951, 330 pages, illustrated.

5. D. M. Yukhtanov and K. D. Leont'eva, Tsvetnye Metally, 1953, No. 6, 30-33.

6. J. Forward, Metallurgical Reviews, 1960, 5, No. 18, 1021-1027.

7. A. E. Mikhailov, Geochemistry, Moscow, Gosgortekhizdat, 1962, 212 pages, illustrated.

8. F. F. Vol'kenshtein, Electron Theory of a Catalyst in Semiconductors, Moscow, Fizmatgiz, 1960, 187 pages, illustrated.

9. A. A. Opalovskii and V. E. Fedorov, Uspekhi Khimii, 1966, 35, No. 3, 427-459.

UDC 669.2

ANKB-1,
solutions
copper de

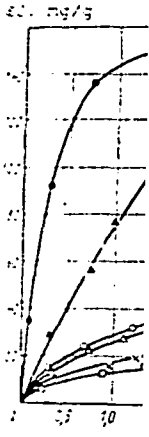

Fig. 1. R
of ion-e
saturati
per to c
centrati
tion: 1)
2) KB-2
op. 180;
50b; 5)
6) AMF-5
Solution
tion, g/
NH_3; 80-
SO_4^{2-}; Na
cations

4. Amph
aminophen
5. Amph
polymer a
2.2 ml/g.
Polymer
structure
and ANKB-
The res
tion prop
that of A

A. N. Ze

A. G. Kh
Siberian
1973, 55

K. M. Ol
Moscow,

OREGON'S MINERAL DEVELOPMENTS - 1980

BY

JERRY J. GRAY AND HOWARD BROOKS

OREGON DEPARTMENT OF GEOLOGY
AND MINERAL INDUSTRIES

PRESENTED AT THE DECEMBER, 1980
86TH NORTHWEST MINING ASSOCIATION
CONVENTION, SPOKANE, WASHINGTON

This paper is not intended to give a complete summary of the mineral happenings in Oregon for 1980. It is intended to give a glimpse of Oregon's total mineral spectrum through the use of 55 slides. Some major mineral developments will be left out because no slides were available. For those interested, a much more complete analysis will be published in the Department's "Oregon Geology" during the early part of 1981.

The presentation of this paper will be a little different than in previous years. In past years the paper was separated into three sections, energy minerals, metals and nonmetals. Last year's speaker noticed that when the nonmetal section of the paper was reached, a good quarter of the audience walked out. So this year the paper is arranged as a trip across the state, starting with the northwest then moving south to the southwest, crossing to the center of the state, and then over to the northeast corner of the state. Therefore, anybody that wants to miss the nonmetals section will need to pop in and out like a yo-yo.

In 1979 the Mist gas field was the star of the show and remains so for 1980. SLIDE 1 gives a location map for the Mist area.

Oregon's first and only gas field was the site of continued drilling activity during 1980. Since the beginning of the year, one drilling rig has been continuously active, drilling wells for American Quasar Petroleum and for the partnership of Reichhold, Diamond Shamrock, and Northwest Natural Gas Company.

Within the area shown on the map , Reichhold and its partners drilled two producers this year as well as eleven dry holes and six dry redrills. The redrills consisted of directional holes drilled from the surface location of an existing straight hole.

TECHNICAL REPORT N-72-6

OPERATION MINE SHAFT

MINERAL ROCK EVENT, FAR-OUT GROUND MOTIONS FROM A 100-TON DETONATION OVER GRANITE

by

D. W. Murrell

April 1972

Sponsored by U. S. Army Engineer Division, Huntsville
Project SX30223

Conducted by U. S. Army Engineer Waterways Experiment Station, Vicksburg, Mississippi

ARMY-MRC VICKSBURG, MISS.

THE CONTENTS OF THIS REPORT ARE NOT TO BE USED FOR ADVERTISING, PUBLICATION, OR PROMOTIONAL PURPOSES. CITATION OF TRADE NAMES DOES NOT CONSTITUTE AN OFFICIAL ENDORSEMENT OR APPROVAL OF THE USE OF SUCH COMMERCIAL PRODUCTS.

ABSTRACT

The objectives of this study were to measure all ground motions in the outrunning region produced by the Mineral Rock Event of Operation Mine Shaft. The Mineral Rock Event was a duplication of the Mine Ore Event of the same series, and was a 100-ton sphere of TNT placed with the center of gravity 0.9 charge radius (about 7.2 feet) above the ground surface.

Accelerometers and velocity gages were installed from 200 to 500 feet from ground zero at depths of 2, 10, and 18 feet. Time histories of all successfully recorded gages are presented in Appendix A along with integrals of each record.

The outrunning acceleration data were partially obscured by a cable noise problem. This noise was blast overpressure-induced and unfortunately was present during the significant outrunning motion onset, i.e., before airblast arrival at the gage locations. Although these data are limited, they are discussed along with the outrunning velocity data. Airblast-induced motions are treated in detail.

Vertical airblast-induced accelerations were found to attenuate rapidly with distance and depth from the maximum downward acceleration of 32 g's at the 200-foot range and 2-foot depth. These accelerations were correlated with overpressure, and, for the 2-foot depth, acceleration-to-overpressure ratios averaged 0.2 g/psi, which is considerably less than for a similar detonation over soil.

Vertical particle velocities also attenuated with distance and depth from the maximum value of 1.3 ft/sec at the 200-foot range and 2-foot depth. Horizontal velocities followed much the same pattern, with a peak value of 2 ft/sec at the same location. Outrunning motion was noted on all horizontal velocity gage records. For the vertical component, outrunning motion was not apparent at the 250-foot range, but was of significant magnitude at the 500-foot range.

Vertical downward displacements of a high confidence level were limited to the 250-foot range and were found to be 0.0060 to 0.0075 foot. Horizontal displacements were successfully computed from acceleration and velocity records, and at the 250-foot range were three to four times as large as the vertical displacements.

PREFACE

This report describes an experiment conducted by the U. S. Army Engineer Waterways Experiment Station (WES) as a part of Operation Mine Shaft. This study was sponsored by the Research Branch of the Huntsville Division, U. S. Army Corps of Engineers (HND). Operation Mine Shaft itself was conducted under the auspices of the Defense Nuclear Agency (DNA), with the WES having direct technical supervision.

This study, designated Project SX30223, was conducted under the supervision of Messrs. G. L. Arbuthnot, Jr., Chief, Nuclear Weapons Effects Division, L. F. Ingram, Chief, Physical Sciences Branch and Technical Director for Mine Shaft, and J. D. Day, Chief, Blast and Shock Section. Project personnel were Messrs. D. W. Murrell, Project Engineer and author of this report, W. M. Gay, C. M. Wright, and F. L. Switzer, all of the Blast and Shock Section, and Messrs. L. T. Watson, F. P. Leake, B. E. Beard, G. H. Williams, and C. E. Tompkins of the Instrumentation Services Division, WES.

The author acknowledges the able assistance rendered by the WES Concrete Division personnel, under Mr. D. M. Walley, who performed the grouting work, and Soils Division personnel, under Mr. Henry McGee, who drilled all instrument holes.

COL Levi A. Brown, CE, and COL Ernest D. Peixotto, CE, were Directors of WES during the investigation and the preparation of this report. Mr. F. R. Brown was Technical Director.

CONTENTS

CONVERSION FACTORS, BRITISH TO METRIC UNITS OF MEASUREMENT

British units of measurement used in this report can be converted to metric units as follows.

Multiply	By	To Obtain
inches	25.4	millimeters
feet	0.3048	meters
miles	1.609344	kilometers
pounds	0.4535924	kilograms
ounces	23.34952	grams
tons (2,000 pounds)	0.907185	megagrams
pounds per square inch	6.894757	kilonewtons per square meter
pounds per cubic foot	16.0185	kilograms per cubic meter
feet per second	0.3048	meters per second

CHAPTER 1

INTRODUCTION

1.1 OBJECTIVE

The objective of this study was to obtain and analyze ground motion measurements in the outrunning region for a high explosive (HE) surface burst over rock.

1.2 BACKGROUND

Rational design of missile launch and control systems requires knowledge of the free-field response of geological media to explosions which produce significant loadings of the ground surface. The phenomenon of outrunning ground motion is not well understood, and very little experimental data are available for design purposes. The Mine Shaft Series presented an excellent opportunity to supplement the meager amount of empirical data on hand. A rather limited program was undertaken on the first two events, Mine Under and Mine Ore (Reference 1), and the results suggested that a more ambitious program on Event Mineral Rock would be worthwhile. The charge weights and geometries for these events are given in Table 1.1.[1] While scaling of data from these HE tests to the nuclear case is less than exact, results of explosive tests can be extremely useful in verification of calculational techniques which are being developed for predicting ground shock from nuclear explosions.

1.3 GROUND MOTION PREDICTIONS

Since the amplitude and frequency ranges of instrument systems are limited, reasonably accurate predictions of ground shock phenomena are imperative for maximum data recovery and integrity. Theoretical prediction techniques currently available for above-ground detonations were developed primarily for superseismic ground shock in alluvial-type soils,

---

[1] A table of factors for converting British units of measurement used in Table 1.1 and elsewhere in this report to metric units is given on page 8.

and extension of these to a hard rock environment was not deemed appropriate. Consequently, gage and rccording system set ranges were selected on the basis of the limited far-out data acquired on Events Mine Ore and Mine Under and extrapolations of the close-in data from the Mine Ore Event (Reference 1). Predictions of peak motions for the parameters to be measured, i.e., horizontal acceleration (AH), vertical acceleration (AV), horizontal velocity (UH), and vertical velocity (UV), were made and are listed in Table 1.2 for the locations of interest.

TABLE 1.1 EVENTS IN WHICH OUTRUNNING MOTION DATA HAVE BEEN OBTAINED AT THE CEDAR CITY TEST SITE

Event	Date of Detonation	Yield	Charge Radius	Height to Center of Charge
		tons TNT	feet	feet
Mine Under	22 Oct 68	100	8	14.2
Mine Ore	12 Nov 68	100	8	7.2
Mineral Rock	8 Oct 69	100	8	7.2

TABLE 1.2 GROUND MOTION PREDICTIONS

Peak predicted values are downward (negative) values for vertical motions and outward (positive) values for horizontal motions. AV--vertical acceleration; AH--horizontal acceleration; UV--vertical velocity; UH--horizontal velocity.

Distance	Depth	Peak Predictions			
		AV	AH	UV	UH
feet	feet	g's	g's	ft/sec	ft/sec
200	2	25	25	a	a
	18	12	12	a	a
250	2	18	18	0.3	0.7
	10	13	13	0.2	0.5
	18	8	8	0.1	0.2
300	2	10	10	a	a
	10	7	7	a	a
	18	4	4	a	a
400	2	5	5	a	a
	10	3	3	a	a
	18	2	2	a	a
500	2	3	3	0.06	0.14
	10	2	2	a	a
	18	1	1	a	a

[a] Not measured.

CHAPTER 2

PROCEDURE

2.1 DESCRIPTION OF TEST SITE AND EVENT

The site of the Mine Shaft Series was in the Three Peaks area of southwestern Utah, roughly 8 miles northwest of Cedar City. The Mineral Rock Event was a 100-ton TNT sphere whose radius was approximately 8 feet and whose center of gravity was 7.2 feet (0.9 charge radius) above the ground surface. The event was detonated on 8 October 1969.

The test site itself was an iron-rich intrusion covered with a thin layer of sandy silt and somewhat weathered rock having a maximum surface relief of approximately 4 feet (Reference 2).

A detailed presentation of the rock properties is found in Reference 3. Briefly, the rock was classified as a tonalite according to the system of Shand (Reference 4), and results of laboratory analysis of the rock indicated a specific gravity of 2.6, a laboratory specimen compression wave velocity of 13,000 ft/sec, a porosity of 5.0 percent (relatively high compared to granite, dolomite, etc.), and nonlinear hysteretic stress-strain behavior. Refraction seismic surveys (Reference 5) conducted in the field showed generally lower seismic velocities than were obtained with the laboratory specimen. These lower velocities were found to be related to the direction of the major joint systems, which occurred predominately in a north-south direction. Seismic velocities of 9,700 to 12,200 ft/sec were observed on traverses parallel to the jointing (north-south), and from 8,000 to 9,400 ft/sec transverse to the joints (east-west).

2.2 INSTRUMENTATION LAYOUT

Thirty-six ground motion gages were installed for this project, including 28 accelerometers and 8 particle velocity gages. These gages were installed at 14 locations ranging from 200 to 500 feet from ground zero (GZ) and at depths of from 2 to 18 feet. The gage layout is presented in Table 2.1 and is shown graphically in Figure 2.1.

All gage locations were along a single radial line which lay roughly E 10° S of GZ. This line was an extension of the easterly gageline

instrumented for the close-in measurement program (Reference 6) which covered the region from 40 to 110 feet from GZ. Actual gage locations were varied slightly from a true radial in order to maintain, as closely as possible, the desired distance from GZ and yet to locate the gages in a reasonably competent outcrop of rock which required a minimal removal of overburden.

The system of gage identification used in this report was designed to be self-explanatory, listing in order the distance from GZ, the gage depth, and gage type and orientation. The code consists of a three-digit number giving the horizontal distance in feet, a one- or two-digit number giving the depth below surface in feet, and a two-letter code indicating the gage type and orientation. Gage types are broken down into accelerometers, coded as A, and velocity gages, represented by U. V represents vertical and H horizontal for the gage orientation. Thus for example, Gage 250-10-AH was a horizontal accelerometer located 250 feet from GZ and at a depth of 10 feet.

2.3 INSTRUMENTATION

2.3.1 Gages and Calibration. Of the 28 accelerometers installed for this study, 18 were Endevco Model 2262 semiconductor strain gage types, 8 were Statham Model A69TC gages, and 2 were Consolidated Electrodynamics Corporation (CEC) Model 4-202 strain gage models. The Endevco gages are undamped and have a natural frequency of 31 kHz. The Statham and CEC gages are damped to 0.7 times critical and have natural frequencies of 230 to 500 Hz, depending on range.

The particle velocity gages were a commercially available CEC version of the Sandia Corporation Model DX-B (Reference 7). This gage, developed under a Defense Atomic Support Agency (now Defense Nuclear Agency) contract, is a greatly overdamped mechanically integrating accelerometer. With various modifications for individual users, it is the "standard" particle velocity gage for ground shock measurements, and has proved reliable on a number of field experiments.

All gages were calibrated in-house at the U. S. Army Engineer Waterways Experiment Station (WES). All accelerometers were calibrated

statically on a spin table with proper cable lengths attached. Calibration resistors were then selected for each gage which gave an output of known acceleration when shunted across an arm of the bridge circuit.

The velocity gages were calibrated by allowing the seismic mass (a pendulum) to swing through its arc under the pull of gravity. A calibration curve was produced with a slope of 1 g for horizontal gages and 2 g's for vertical gages. Calibration resistors were selected which, when shunted, gave an output equivalent to a known velocity.

Calibration resistors were manually shunted, and outputs were recorded just prior to shot time, in case of failure of the automatic stepping circuit. At 30 seconds before shot time, all resistors were again shunted, this time automatically.

2.3.2 Recording System. Signal conditioning equipment for the accelerometers consisted of operational amplifiers designed and fabricated by WES. These amplifiers are solid state units having a frequency response of 0 to 10 kHz.

CEC 1-113B (System D) carrier-demodulator amplifiers were used with velocity gages. These units have a frequency response of 600 Hz when terminated with the design load of roughly 70 ohms (a galvanometer). On the Mineral Rock Event, however, the System D's were used to feed a tape driver amplifier, which is a high-impedance load, cutting the frequency response to about 100 Hz.

All data were recorded on CEC VR-3300 FM magnetic tape recorders. Twelve channels of data were recorded on each machine, along with a reference track and IRIG B time code.

All signal conditioning and data recording equipment was housed in two recording vans located some 3,000 feet from GZ. These vans were parked behind timber and earth revetments to provide protection from airblast and ejecta. Figure 2.2 shows the recording van area; the view is toward GZ and the protective revetments can be seen in the background.

2.3.3 Data Reduction. All data recorded in the field were of analog form on FM magnetic tape. These were digitized at the rate of 24 kHz on an analog-to-digital converter at WES. The digital data were then processed through a GE 400 digital computer which performed integrations and, where

necessary, baseline corrections, and were then plotted automatically by an on-line plotter.

2.4 FIELD OPERATIONS

Field operations for this project began immediately following the Mineral Lode Event, which was detonated on 5 September 1969. All field operations, benefited by good weather and working conditions, proceeded smoothly, and the project was ready on 29 September 1969, 10 days preshot.

2.4.1 Instrument Cables. Cable runs of 50-pair telephone-type cable were used for 2,700 feet from the recording van area toward GZ. These cables had been installed for Events Mine Under and Mine Ore and were found to be serviceable. About 300 feet from GZ, a junction box was installed, and additional multipair cable was run to the far-out motion gageline where a second junction box was installed. From this point, individual four-conductor cable was run to each gage. All individual gage cables destined for a given location were then bundled together and were protected by pipe insulation of 1/2-inch wall thickness. Cables between junction boxes and between the second junction box and instrument holes were placed in trenches 12 to 18 inches deep in the soil overburden. Where subsurface rock prevented this, the cable was bedded in dry sand and covered with sandbags and native material.

2.4.2 Gage Installation. All ground motion gages scheduled for a particular location were installed in a single aluminum canister. The canister was constructed of 5-inch-outside-diameter by 1/2-inch-wall-thickness aluminum tubing, with end caps of 1/2-inch aluminum plate. The bottom end cap had an aluminum gage mounting block welded in place. A placement stem was attached to the top cap. Canisters were potted with paraffin after gage installation to dampen gage mount vibration and seal out moisture. Overall canister length, not counting placement stem, was 10 inches, and weight was 17 pounds 2 ounces, giving a density of 171 pcf. This compares favorably with the average rock density of 162 pcf.

Figure 2.3a shows a canister bottom cap and gage mounting block with two velocity gages and two accelerometers installed. Figure 2.3b shows a typical assembled canister with placement stem attached.

Gage canisters were set in place using an aluminum placement tool, the bottom section of which contained a threaded coupling to fit the placement stem. After placement and orientation of a canister, grout designed to match the density and sonic velocity of tonalite was pumped until the canister was just covered. The grout was then allowed to set, the placement tubing was removed, and grout was pumped to a point just below the next canister location. The installation procedure was then repeated for this location.

TABLE 2.1 GROUND MOTION GAGE LAYOUT

X denotes AV, AH; Y denotes AV, AH, UV, UH.
AV--vertical acceleration; AH--horizontal acceleration; UV--vertical velocity; UH--horizontal velocity.

Horizontal Distance	Gage Array at Indicated Depth		
	2 feet	10 feet	18 feet
feet			
200	X		X
250	Y	Y	Y
300	X	X	X
400	X	X	X
500	Y	X	X

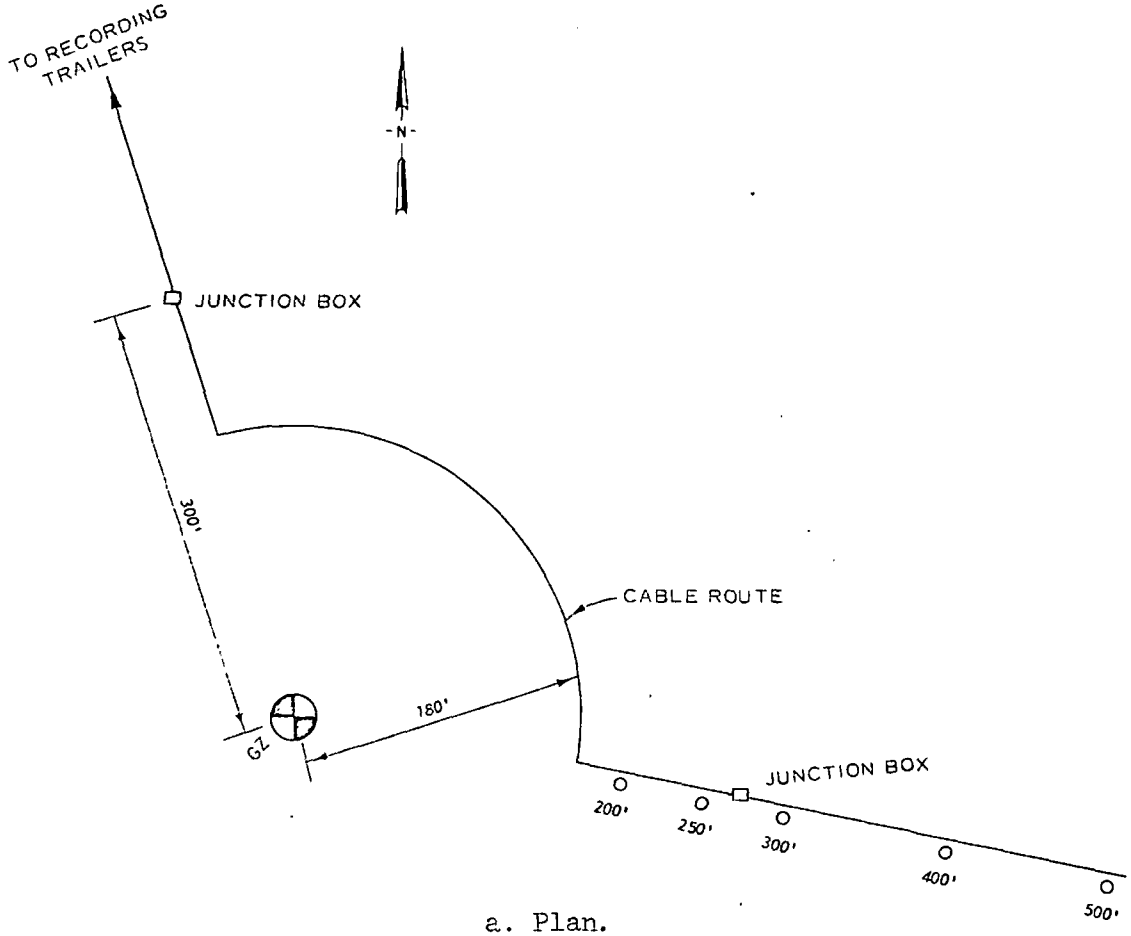

a. Plan.

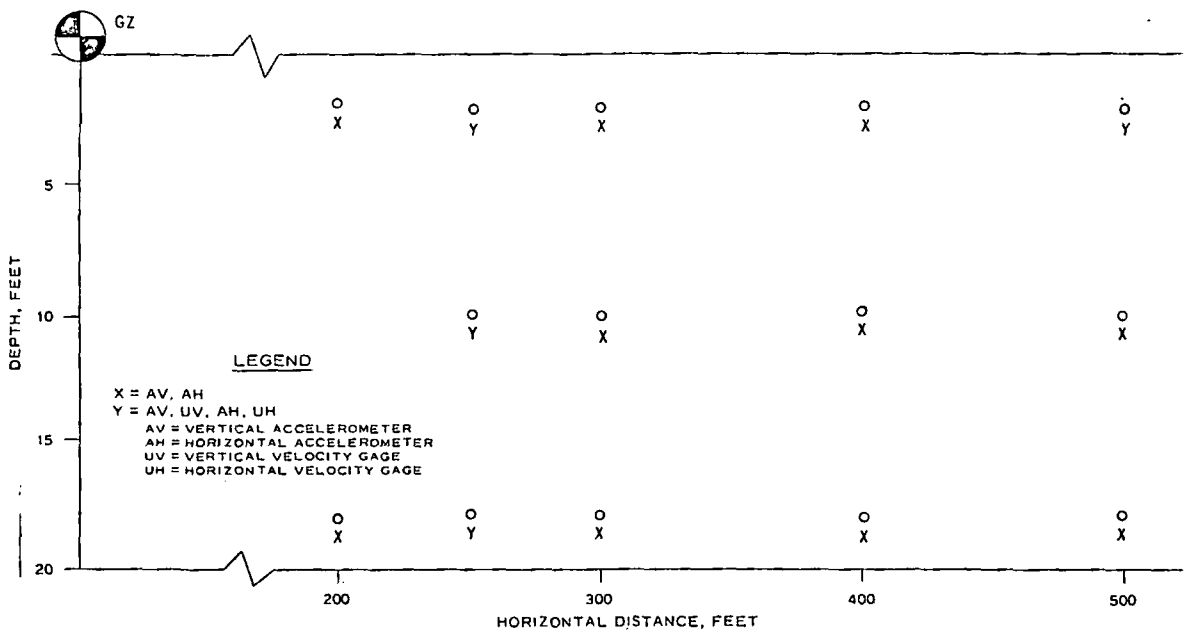

b. Section.

Figure 2.1 Gage layout.

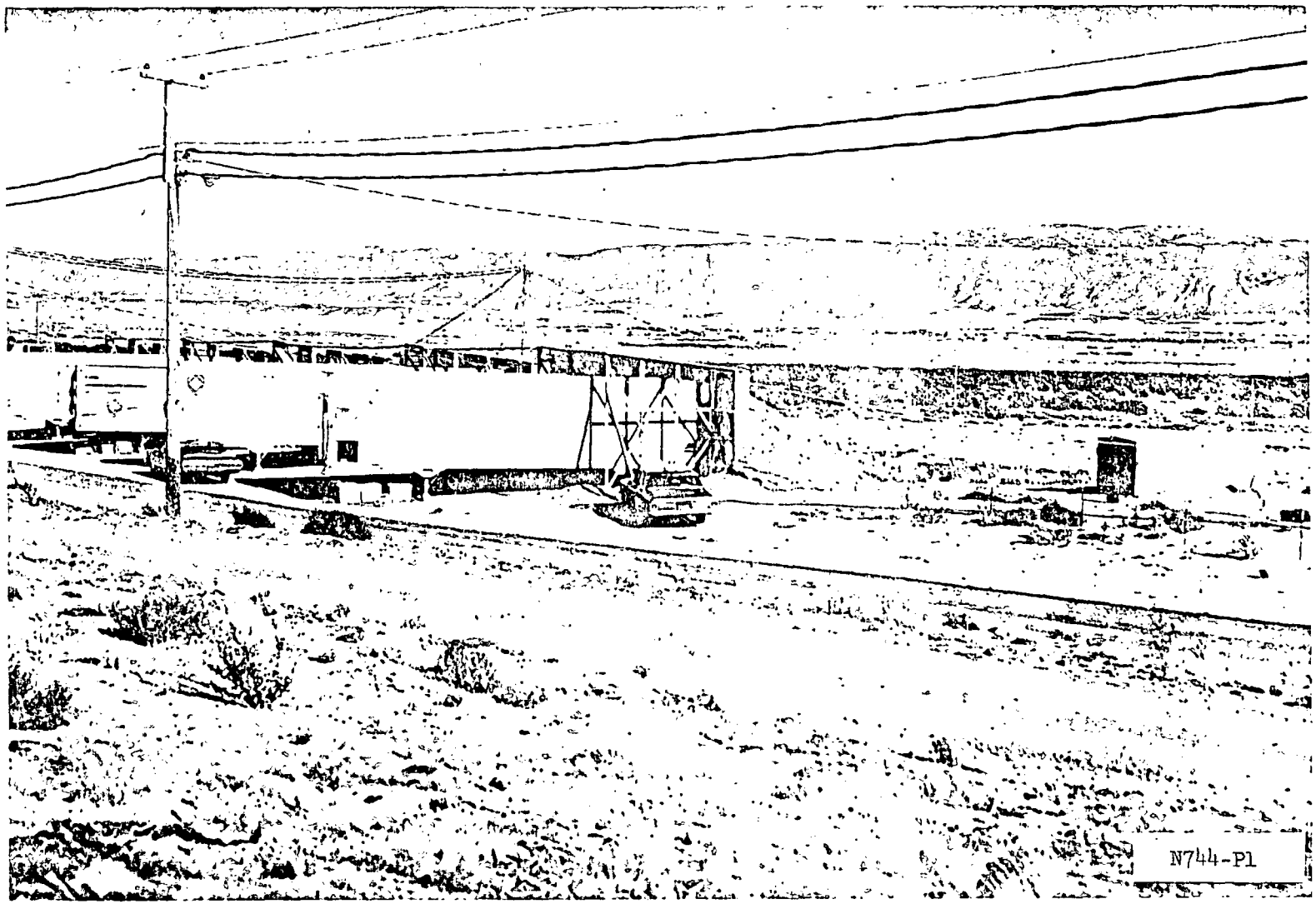

Figure 2.2 Recording van area.

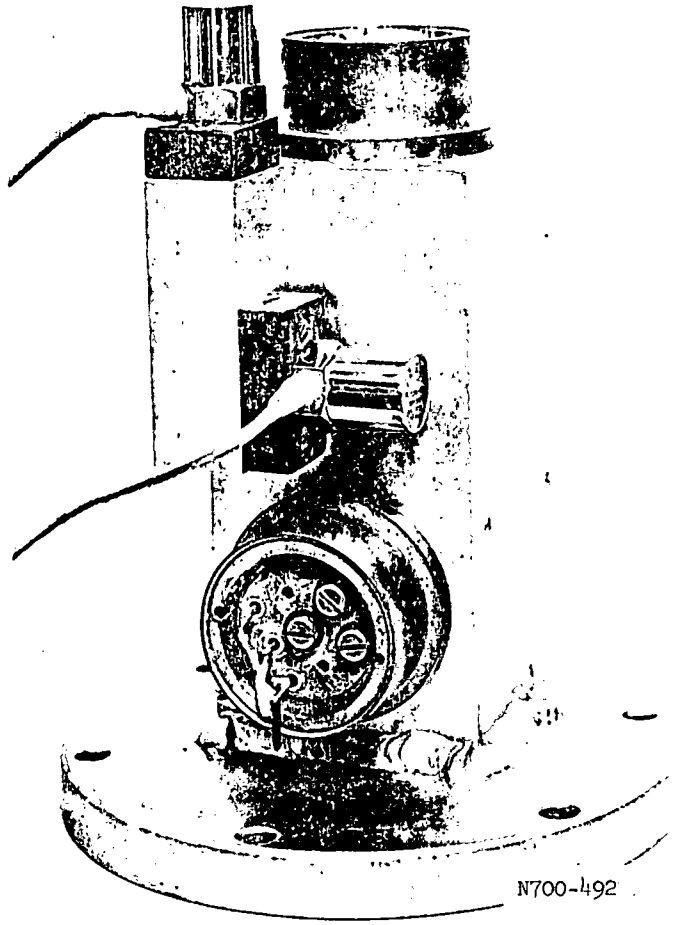

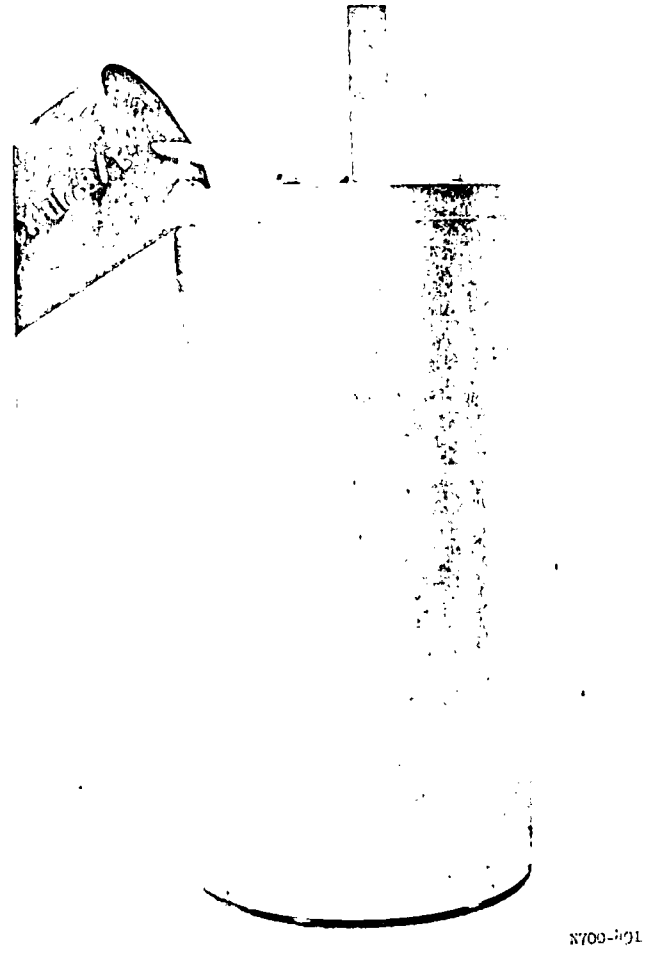

a. Gage mount and gages.

b. Assembled gage canister.

Figure 2.3 Typical gage canister assembly.

CHAPTER 3

RESULTS

3.1 INSTRUMENT PERFORMANCE

All gages checked out satisfactorily after installation, and all were operational at shot time. Start signals were received at shot time, and calibration and recording equipment operated as programmed. The Detonation Zero pulse was received and recorded on all tape machines.

Of the 36 gages installed for the Mineral Rock Event, 34 responded to the ground shock. No data were received from Gages 500-2-UH and 500-10-AV. Seven particle velocity gages operated successfully and yielded data of excellent quality. The 27 accelerometers, however, were affected by electrical noise at 20 msec after detonation. This noise persisted for about 15 msec, and primarily affected records from the 300- and 400-foot ground ranges. Attempts to remove the noise by digital filtering were unsuccessful since the noise was within the frequency band of the ground shock data itself.

Some of the noise was removed by beginning data processing only after onset of the noise. Data processing was begun at 25 msec after detonation for data from the 300-foot range, at 35 msec for the 400-foot range, and at 45 msec for the 500-foot range. These times were selected in order to skip as much noise as possible yet insure that little or no data were lost. That no real, or at least measurable, data were thus removed is borne out by the shock arrival time of 29 msec for the horizontal velocity gage at the 250-foot range and 18-foot depth. The minimum arrival at the 300-foot range would then be about 33 to 34 msec, or well after data processing had begun. This procedure substantially improved the quality of record integrations by removing a large portion of the noise-induced baseline shift. Some effects of this noise are still present in the first and second integrals, however.

It is worth noting that onset of the noise coincides with airblast arrival at the portions of the gage cable line which lie closer to GZ than the gageline itself (see Figure 2.1). Since the pressures encountered could alter somewhat the electrical characteristics of the cable, the noise

was possibly shock generated. It remains unresolved, however, why the velocity data were not affected, since the ac carrier system should be more sensitive to capacitive changes induced by squeezing than the dc accelerometer circuits.

The 34 successfully recorded time histories are presented in Appendix A along with first and second integrals. The label in the upper right-hand corner of each record lists the event, gageline direction (east), and gage identification code, plus computer and data recall information. Marked on each record with an arrow labeled "AB" is the airblast arrival time at the surface above the gage.

Peak values of measured parameters and integrals are presented in Table 3.1.

3.2 ARRIVAL TIMES

Arrival times of ground motion were unfortunately obscured by noise except for four of the velocity gages and the two accelerometers at the 200-foot range and 18-foot depth. Arrival times for these gages are listed in Table 3.1. Both of the accelerometers showed initial response at 16.8 msec after detonation, indicating arrival of outrunning ground shock (the airblast arrived at this point some 24 msec after detonation). The average ground shock transmission velocity was 12,000 ft/sec to the 200-foot range, and is in fair agreement with the 13,000 ft/sec determined by laboratory compression wave velocity tests. Initial motion was detected on the horizontal velocity gages at the 250-foot range at 29, 30, and 32 msec for the 18-, 10-, and 2-foot depths, respectively, while airblast arrival at this point was about 40 msec, again indicating the presence of outrunning motion. Average shock transmission velocity from GZ to Gage 250-18-UH was then 8,500 ft/sec, which is considerably less than that calculated for the 200-foot station.

Outrunning motion was also noted at Gage 500-2-UV, where the arrival time was 62.4 msec, giving a transmission velocity of 8,000 ft/sec. The difference may be attributed, at least in part, to the difficulty in picking accurate arrival times for the velocity gages, which exhibit low

initial motions and long rise times. It is worth noting also that the 8,000- to 8,500-ft/sec velocities are in good agreement with data obtained on field seismic tests which reported velocities much less than those obtained on the laboratory specimens. It is also possible that rock jointing, which caused lower seismic velocities in the east-west direction than in the north-south direction, was locally most severe beyond the 200-foot range.

Figure 3.1 is a plot of airblast-induced-motion arrival times at the 2-foot depth and, where obtained, outrunning arrival times versus distance. The airblast-induced-motion arrival times are noted to agree well with the predicted airblast arrival itself and serve to substantiate the airblast predictions since arrival times for airblast were not reported beyond the 320-foot distance.

3.3 ACCELERATION

As mentioned previously, all acceleration channels were subjected, to some degree, to an extraneous electrical noise during the early portion of the ground motion. This noise obscured the outrunning ground motion and, at the 200- and 250-foot ranges, was superposed on the airblast-induced motions. Fortunately, the airblast-induced signals at these locations were of considerably greater amplitude than the noise signals. This can be seen from the first two traces in Figure 3.2. At the 300-foot and 400-foot stations, initiation of data processing was delayed, thus eliminating most of the noise. This process was used also at the 500-foot range; however, at this location signal amplitude was small enough that the noise is still quite apparent. The waveforms seen in Figure 3.2 are characteristic of near-surface vertical accelerograms in rock, i.e., a sharp downward spike of very short rise time (generally less than 1 msec) followed by oscillations and/or an upward pulse.

The record of Gage 500-2-AV shows a fairly well developed outrunning waveform, although the early portion is obscured. After noise cessation at about 105 msec, the oscillatory, relatively long-period pulse of outrunning motion is evident, with the downward spike at airblast arrival superposed at 153 msec. The downward acceleration due to airblast is noted to be of

larger magnitude and shorter duration than the immediately preceding outrunning signal. This was consistent throughout the array. Figure 3.3 is a plot of peak downward vertical acceleration versus distance for all three depths instrumented. Four vertical acceleration peaks measured at the 2-foot depth on Event Mine Ore are included, and are generally in good agreement with the Mineral Rock data.

Peak downward accelerations at the 2-foot depth are noted to attenuate rapidly with increasing distance. This suggests the use of a correlation based on downward acceleration-to-overpressure ratios, which has also been found effective for accelerations in soil (Reference 8). Figure 3.4 is a plot of this ratio versus overpressure for the five stations instrumented. Overpressures used in computing the ratios are listed in Table 3.2 (Reference 9).

For the first four stations, 200, 250, 300, and 400 feet, the downward acceleration-to-overpressure ratios are 0.16, 0.14, 0.24, and 0.20 g/psi, respectively. At the 500-foot range, the ratio drops off to 0.10, in contrast to the pattern of increasing ratios at lesser overpressures usually observed in soil. The 0.2-g/psi average ratio for the first four locations is considerably lower than the figure of 0.6 to 1.0 g/psi for similar pressure ranges noted for 100-ton detonations over soil (Reference 8). This is consistent with elastic theory, which gives an inverse relationship between acceleration and seismic velocity for a constant rise time of stress. The difference is not as great as the 10-fold difference that the seismic velocity ratio would suggest.

Attenuation of peak downward vertical acceleration with depth is also apparent from Figure 3.3 and is consistent throughout the horizontal array. Peak values at the 18-foot depth ranged from 22 to 38 percent of those at the 2-foot depth. This is in marked contrast to data in soil, where accelerations at a depth of 17 feet average about 7 percent of near-surface (1.5-foot) data. This fact emphasizes the effectiveness of an alluvial soil, such as encountered on the Distant Plain Series, as a filter of high-frequency motions, even though near-surface accelerations are larger at similar overpressures in soil.

Peak horizontal accelerations are plotted versus distance in Figure 3.5. The peak values plotted are peak outward accelerations neglecting apparent noise peaks. In most cases, the peak values can be attributed to passage of the airblast, with two obvious exceptions being Gages 500-2-AH and 500-10-AH. At these locations, the acceleration signature was dominated by an outrunning motion of both greater magnitude and considerably longer duration than the airblast-induced motion. A rapid attenuation with distance is again apparent, and, for the 2-foot depth, is about the same in rate as was noted for vertical accelerations. The peak horizontal accelerations themselves, however, are consistently only 40 to 60 percent of the vertical peaks.

Horizontal accelerations also attenuate sharply with depth. Most of the attenuation appears to occur in the upper 10 feet of rock, with generally only a small difference in peak values at 10- and 18-foot depths. This is in contrast to vertical measurements, where data at the 18-foot depth were consistently well below those at the 10-foot depth.

3.4 PARTICLE VELOCITY

The number of particle velocity gages installed for this project was unfortunately small, especially in view of the high quality data yielded. Integrals of acceleration records, especially the early portions, are somewhat suspect due to the noise problem. See, for example, the first integral of Gage 300-10-AH (Figure A.20) where integration of the noise produced a relatively spurious and erroneous initial velocity.

Figure 3.6 shows, for comparison, the three vertical velocity records from the 250-foot ground range. These records are typical of vertical velocities in the superseismic region, and indicate an absence of measurable vertical outrunning ground shock at this location. The records are characterized by an initially downward pulse of width which increases with depth, followed by an upward motion of nearly uniform duration. Also shown in Figure 3.6 is a composite vertical velocity record constructed from close-in data (Reference 6) from Mineral Rock which was obtained at distances of 40 to 110 feet from GZ. It is emphasized that the amplitudes indicated on the composite record are meaningless, even as a relative

indicator, since the amplitudes of various portions of the record are dependent on location. A striking similarity in wave shape is present, however, indicating that predominant features of the ground shock persist throughout the range of instrumentation. Of interest here is the increased width of the initial downward pulse for the far-out data, which follows the pattern set on close-in measurements. The initial downward pulse, for example, was only of 1.8-msec duration at the 40-foot range, and had increased to 4.8 msec at 110 feet, both at the 2-foot depth (Reference 6). The duration of this pulse had increased to 16 msec at the 250-foot location. The subsequent upward and downward oscillation does not appear to have been affected by either depth or distance and retained a nearly uniform period of 140 msec at all distances and depths instrumented for both close-in and far-out programs.

In contrast to the apparently superseismic waveforms of Figure 3.6, the outrunning vertical velocity of Gage 500-2-UV is shown in Figure 3.7. Here the motion is initially upward and is oscillatory, with the downward airblast-induced pulse superimposed on the outrunning motion at about 155 msec. The outrunning motion is both larger and of longer period than the airblast-induced pulse at this location, and the wave shows significant oscillation well beyond the airblast arrival. Since this record indicates that significant vertical outrunning motion was present at this range, it would be expected that similar motions would be observed at the 250-foot stations at corresponding times, i.e., about 30 msec. It is also apparent that the magnitudes and frequencies are well within the capability of the velocity gage. Significant horizontal outrunning motion was observed at the 250-foot range, as will be discussed later, so it must be concluded that the outrunning pulse, though present, had not developed a measurable (relative to airblast motion) vertical component at the 250-foot range.

Peak downward vertical particle velocity is plotted versus distance in Figure 3.8. Shown here are the four vertical velocity measurements along with integrals of vertical acceleration records. In all cases where velocity was measured directly, the peak downward motion was considerably less than that obtained from integrated accelerations. This is in keeping with results from previous tests, although the low-frequency response of the

velocity gage amplifiers, as used on this experiment, probably aggravated the problem.

For the most part, downward velocities plotted in Figure 3.8 are associated with passage of the airblast above the point in question, although outrunning motions no doubt exert some influence on the peaks. Phasing of the airblast relative to outrunning motion was important at Stations 500-2 and 500-18. For example, at Station 500-2, the airblast pulse was superposed on an upward cycle, and no net downward motion resulted. Peak downward motions for this station are consequently not associated with the airblast.

Vertical velocities, as did accelerations, attenuated sharply with distance, at about the same rate for the 2-foot depth as the airblast overpressure. Downward velocities at the 2-foot depth correlate well with pressure, and velocity-to-overpressure ratios range from 0.012 to 0.023 ft/sec/psi. This ratio is again less than has been observed for alluvial soils where ratios in this pressure region are about 0.05 ft/sec/psi (Reference 8).

Attenuation of the downward velocities with depth is less regular than was found for accelerations, and at the 300- and 400-foot ranges the deeper motions are greater than the shallow ones. This can probably be attributed, at least in part, to integration of noisy data. The three directly measured velocities at the 250-foot range, for example, do exhibit a decrease in amplitude with increasing depth, as might be expected. This reinforces their credibility, at least in relation to each other.

An average fit to the close-in velocity data is also shown in Figure 3.8. Most of the data fall in reasonable proximity to an extension of the close-in data, although several points appear to be rather high. It is clear that no gross anomalies in magnitudes are present, and this is in turn an indicator of data reliability.

Figure 3.9 shows horizontal particle velocity-time histories for the 250-foot range. The first of these, for the 2-foot depth, is marked by two features which depart from the pattern set by the two deeper stations. First is the double peak on the first outward pulse which was not noted at the deeper locations; however, it did appear on the acceleration integral

also (Figure A.7). The second anomalous occurrence is the series of fairly significant peaks at 160 to 180 msec after detonation. This was not apparent to any extent on the integrated acceleration, and is thought to be a gage malfunction. The remaining two records show a single smooth outward pulse of similar duration. The last plot on Figure 3.9 is a composite horizontal velocity waveform constructed from close-in data (Reference 6). The amplitude is again arbitrary. The period of this pulse averaged 50 msec, which appears slightly shorter than on the far-out data, although the difference is not great.

Figure 3.10 presents peak outward horizontal velocities versus distance for both direct measurements and integrals. Much better agreement is immediately noted between peak values obtained by the two methods than was found for vertical data. This follows the trend noted for close-in measurements and is probably due to the lower frequencies (longer initial pulses) for horizontal data which the velocity gages are better able to follow.

Attenuation with range is similar to that found for vertical data, and follows a projection of close-in measurements quite well. As a result, there appears to be approximately a one-to-one correspondence between horizontal and vertical peaks, at least within the data scatter. Attenuation with depth, although apparent, is not pronounced, and again is concentrated in the upper 10 feet of rock.

3.5 DISPLACEMENT

Vertical displacement peaks, as can be seen from Table 3.1, show considerable disparities between second integrals of acceleration and first integrals of velocity, and even between measurements at the same ground range. Consequently, no plot of vertical displacement versus distance was constructed. The three integrals of velocity measurements at the 250-foot range did produce displacements which were very consistent among themselves, ranging from 0.0060 foot at 18-foot depth to 0.0075 foot at 2-foot depth. This precision, together with the generally typical velocity waveforms from which they were derived, lends credence to the data at this point.

Peak horizontal displacements are plotted versus distance in

Figure 3.11, and with two readily apparent exceptions, plot nicely with a regular attenuation pattern. Very little attenuation with depth is seen in Figure 3.11, with a notable example being the data at 250-foot range where all six data points (three velocity integrals, three acceleration second integrals) all fall between 0.020 and 0.028 foot. The horizontal peak displacement values all seem to fall somewhat above the average fit to close-in data. It should be kept in mind, however, that the representative fit to the close-in data is an average, and data scatter would encompass the far-out peaks.

Using the data at the 250-foot range as representative values, it is seen that horizontal displacements at this range are three to four times larger than the vertical. Since peak velocities exhibited a one-to-one correspondence, the difference can be attributed to the longer durations of the horizontal particle velocities. This, in turn, is brought about by the fact that horizontal airblast and outrunning velocity pulses reinforce each other (both outward), thus tending to lengthen outward pulse duration, while destructive interference may occur in vertical displacements depending on placing of the airblast and outrunning signals.

TABLE 3.1 PEAK GROUND MOTION DATA

AV--vertical acceleration; AH--horizontal acceleration; UV--vertical velocity; UH--horizontal velocity. Positive motion is upward for vertical and outward for horizontal.

Distance	Depth	Gage Type	Arrival Time	Acceleration		Velocity		Displacement	
				Positive	Negative	Positive	Negative	Positive	Negative
feet	feet		msec	g's	g's	ft/sec	ft/sec	feet	feet
200	2	AV	--	23	32	0.14	1.4	a	0.03
		AH	--	16.4	19.2	1.9	0.48	0.059	b
	18	AV	16.8	4.9	7.1	0.37	0.88	a	0.016
		AH	16.8	4.8	2.4	1.4	0.52	0.04	b
250	2	AV	--	8.9	15.6	0.34	1.2	a	0.016
		UV	--		--	0.27	0.72	0.002	0.0075
		AH	--	10.0	3.0	1.4	0.50	0.028	b
		UH	32.0	--	--	1.2	0.40	0.026	b
	10	AV	--	3.1	4.0	0.26	1.2	a	0.052
		UV	--	--	--	0.28	0.43	0.002	0.007
		AH	--	3.2	2.2	0.96	0.42	0.027	b
		UH	30.0	--	--	0.85	b	0.026	b
	18	AV	--	2.2	2.8	0.39	0.62	0.005	0.012
		UV	--	--	--	0.28	0.34	0.003	0.006
		AH	--	4.6	1.8	0.76	0.15	0.023	b
		UH	29.0	--	--	0.60	0.22	0.019	b
300	2	AV	--	10.4	12.0	0.42	0.59	0.017	0.003
		AH	--	6.6	6.0	0.72	0.76	0.023	b
	10	AV	--	2.4	4.2	0.51	0.72	a	0.017
		AH	--	2.4	2.2	0.66	0.43	0.019	b
	18	AV	--	1.4	2.6	0.25	0.56	a	0.015
		AH	--	1.7	1.4	0.62	0.53	0.022	b
400	2	AV	--	6.0	6.0	0.34	0.42	0.001	0.006
		AH	--	2.4	2.5	0.48	0.35	0.014	b
	10	AV	--	3.0	2.4	0.70	0.72	0.014	0.018
		AH	--	1.4	1.1	0.22	0.40	0.009	0.008
	18	AV	--	2.0	1.5	0.38	0.59	0.001	0.014
		AH	--	0.88	1.0	0.18	0.62	0.007	0.019
500	2	AV	--	2.80	1.4	0.19	0.16	0.003	0.007
		UV	62.4	--	--	0.12	0.12	0.002	0.003
		AH	--	0.58	0.49	0.32	0.05	0.022	b
		UH	--	c	--	--	--	--	--
	10	AV	--	c	--	--	--	--	--
		AH	--	0.58	0.60	0.48	0.10	0.034	b
	18	AV	--	0.60	0.56	0.25	0.13	0.008	b
		AH	--	0.66	0.52	0.14	0.22	0.005	b

[a] No positive peak.
[b] No negative peak.
[c] No data.

TABLE 3.2 AIRBLAST OVERPRESSURES

Distance	Pressure	Remarks
feet	psi	
200	190	Predicted value
250	115	Airblast Line 1 (North)
300	49	Adjacent to ground shock instrument hole
400	30.3	Adjacent to ground shock instrument hole
500	15.0	Adjacent to ground shock instrument hole

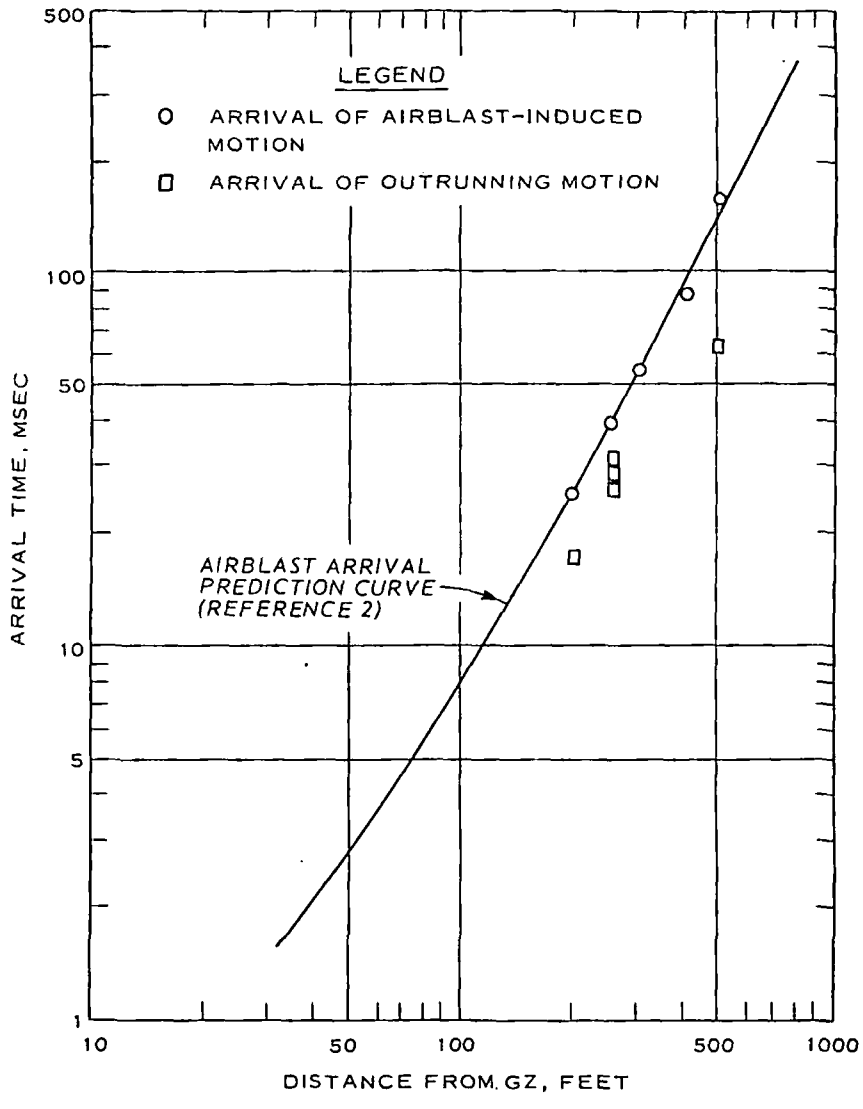

Figure 3.1 Motion arrival times at 2-foot depth.

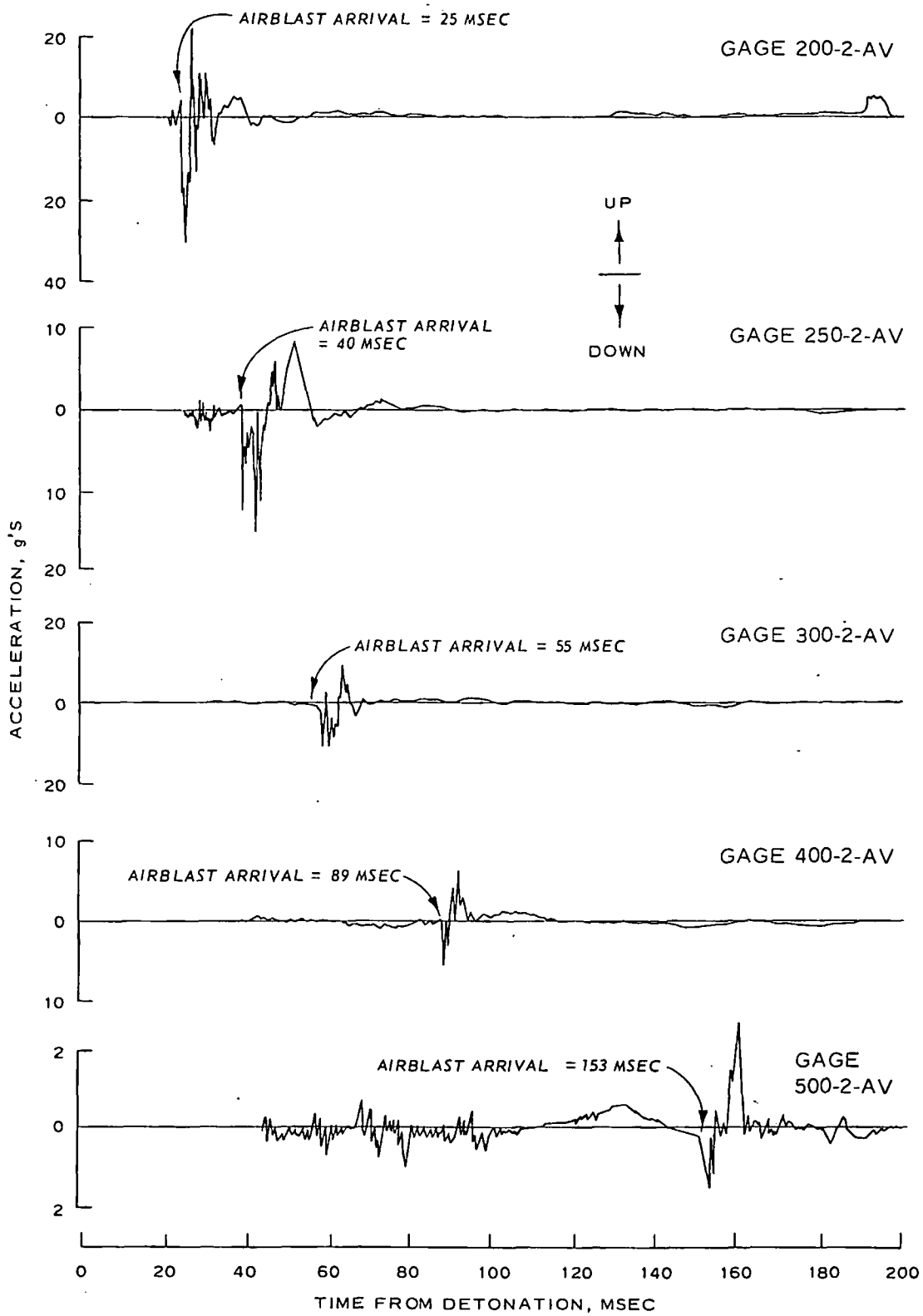

Figure 3.2 Vertical acceleration histories, 2-foot depth.

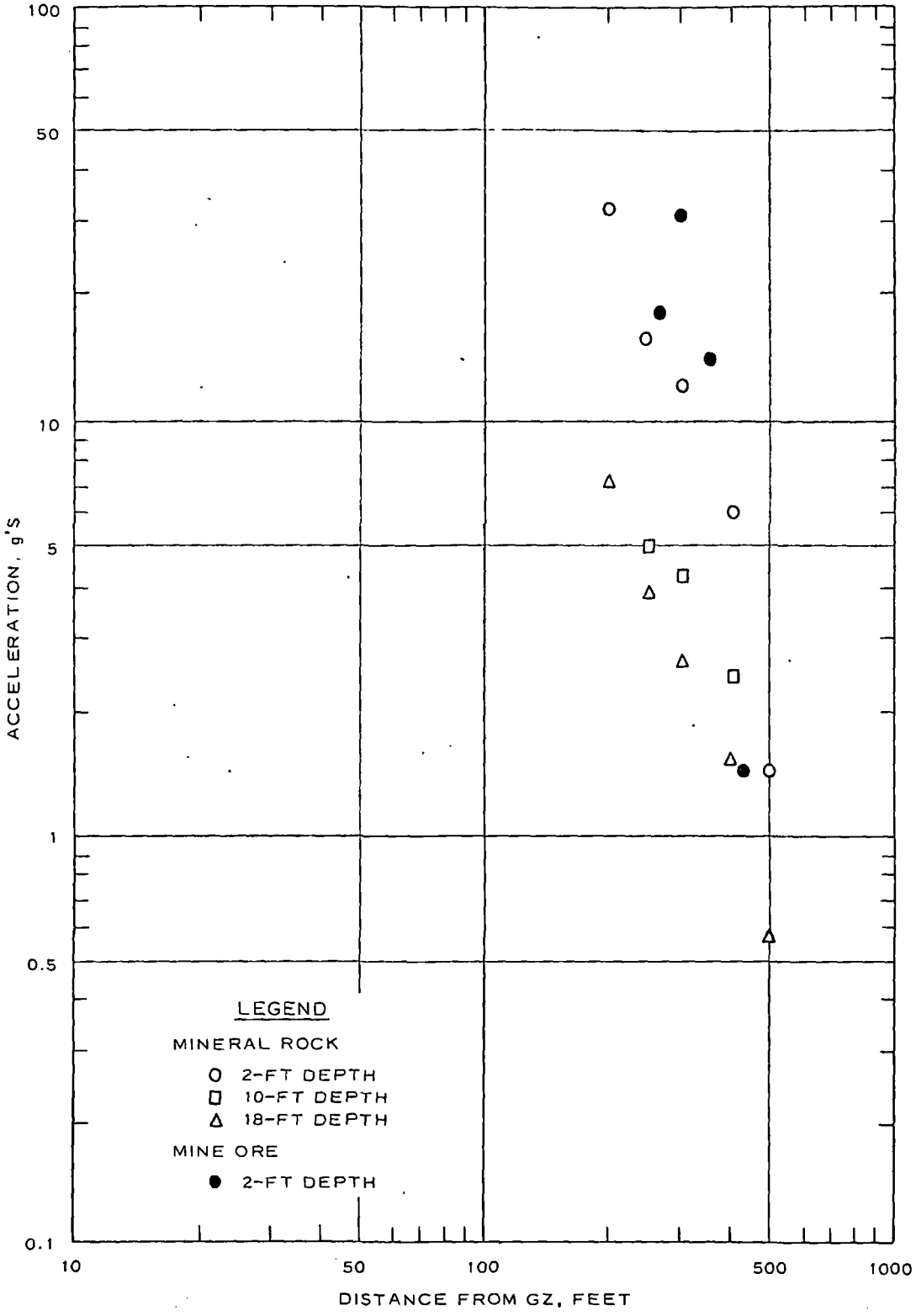

Figure 3.3 Peak downward vertical acceleration versus distance.

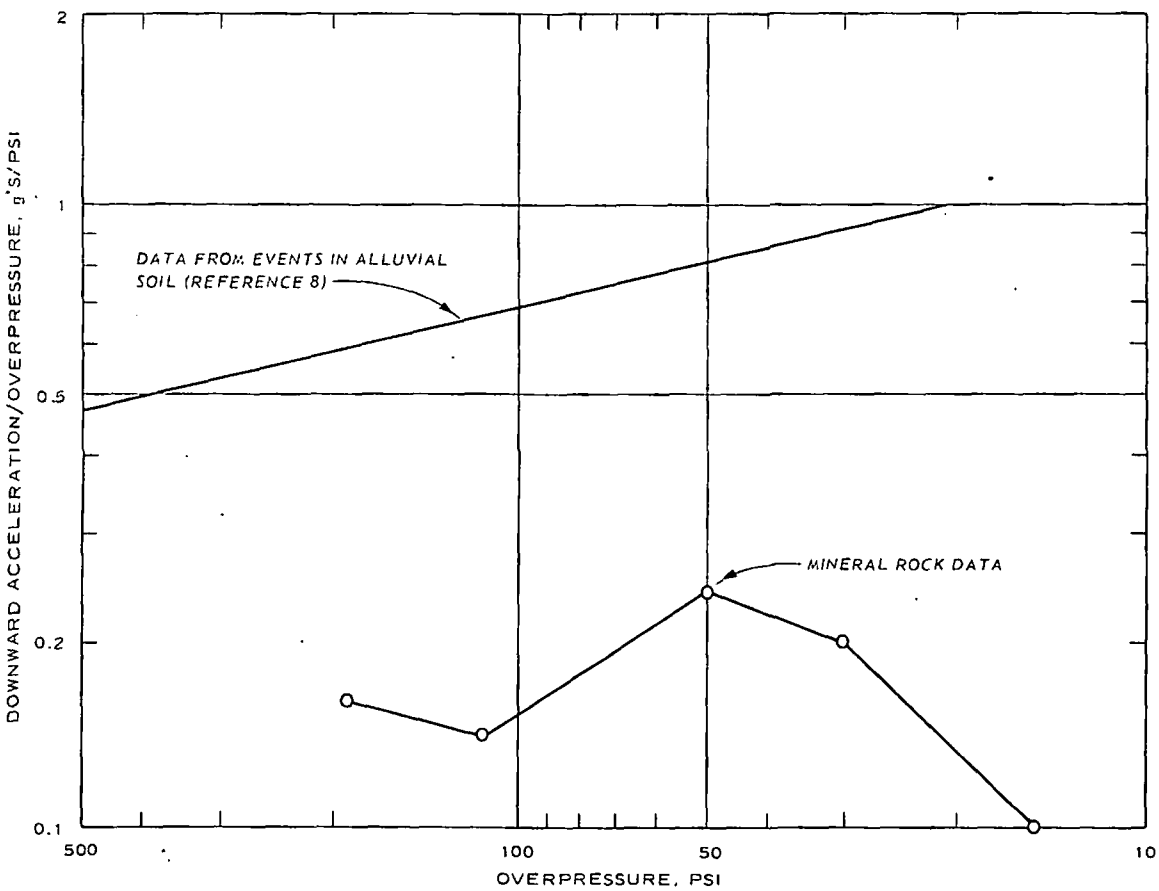

Figure 3.4 Acceleration-to-overpressure correlation.

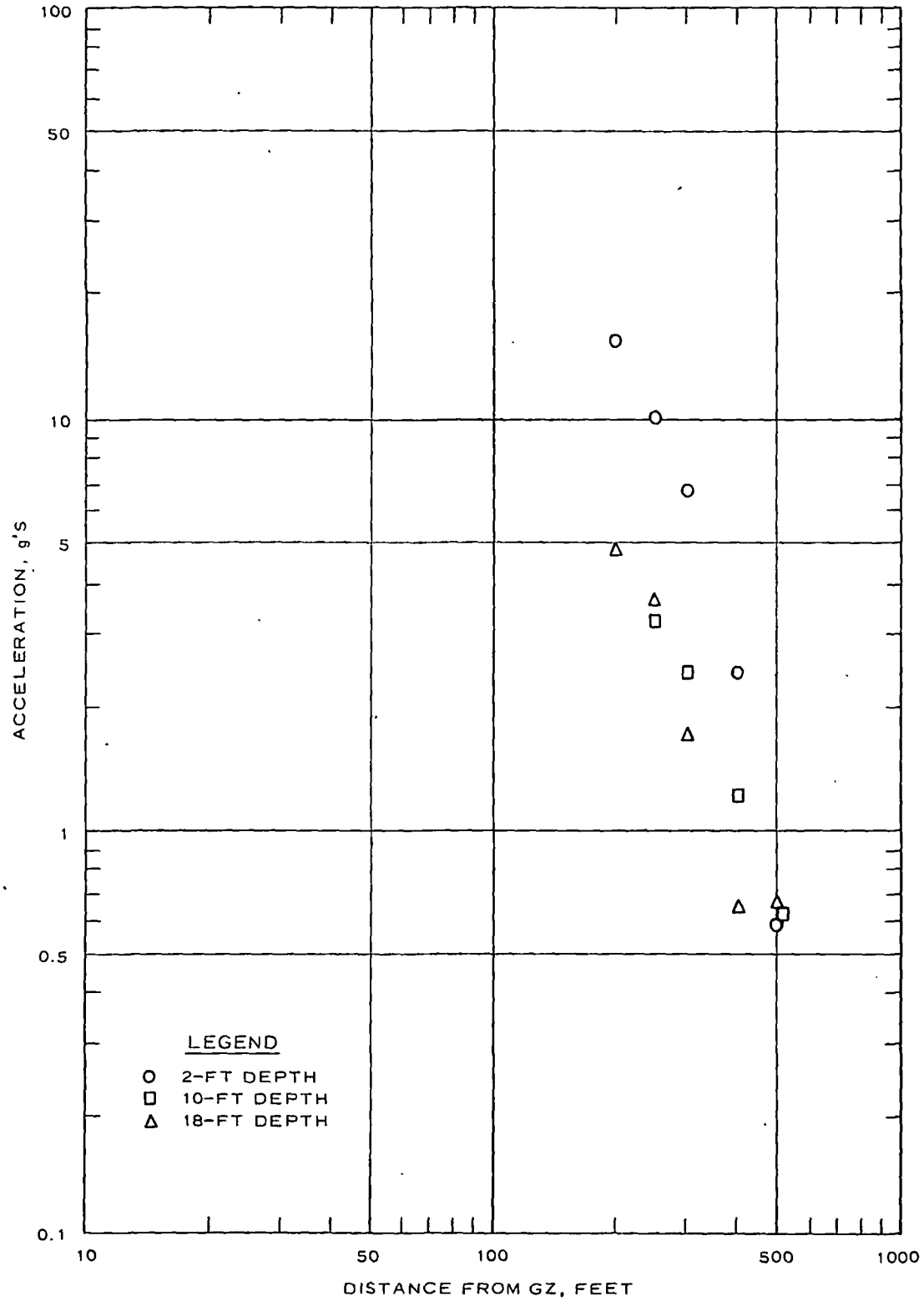

Figure 3.5 Peak horizontal (outward) acceleration versus distance.

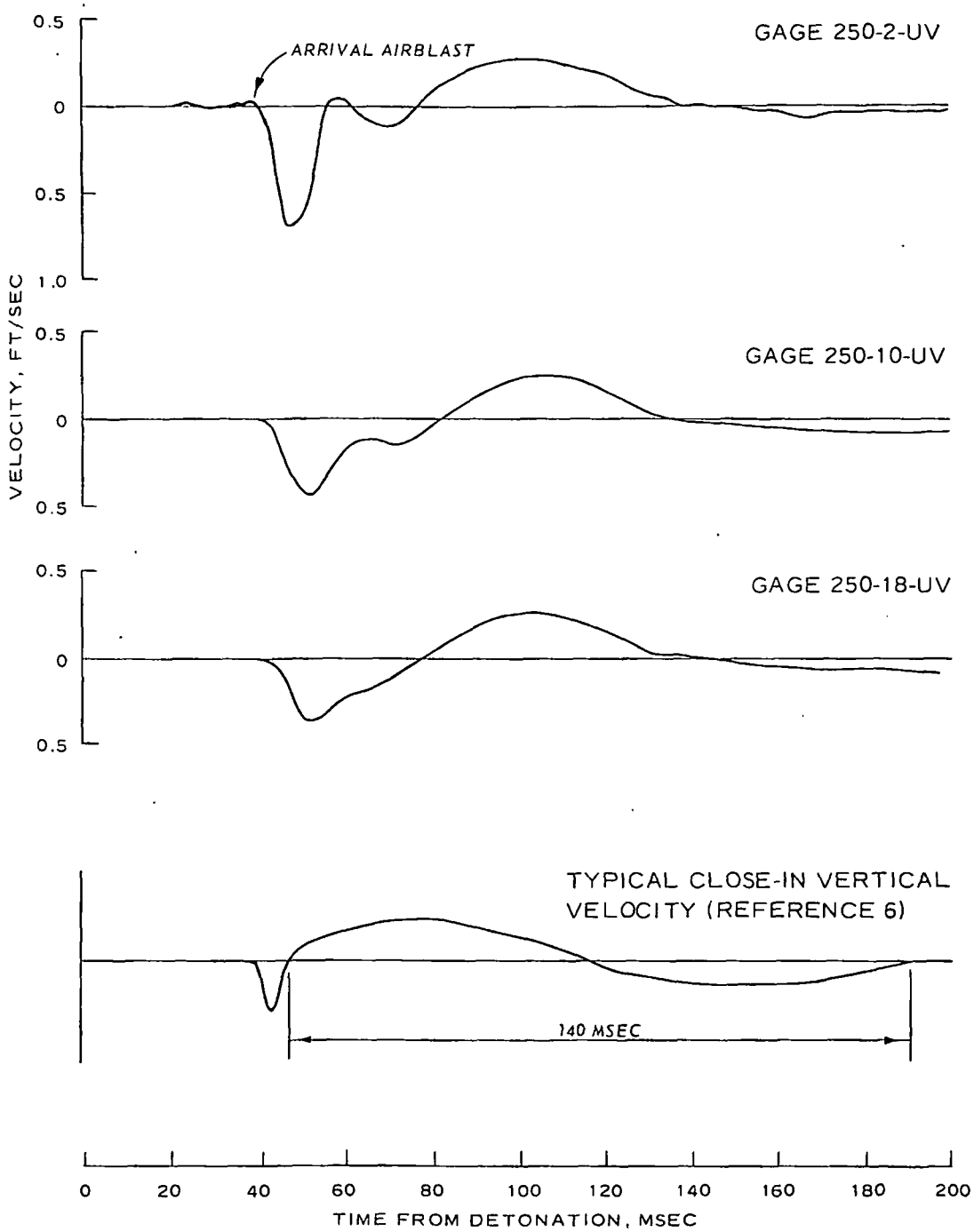

Figure 3.6 Vertical velocity histories, 250-foot range.

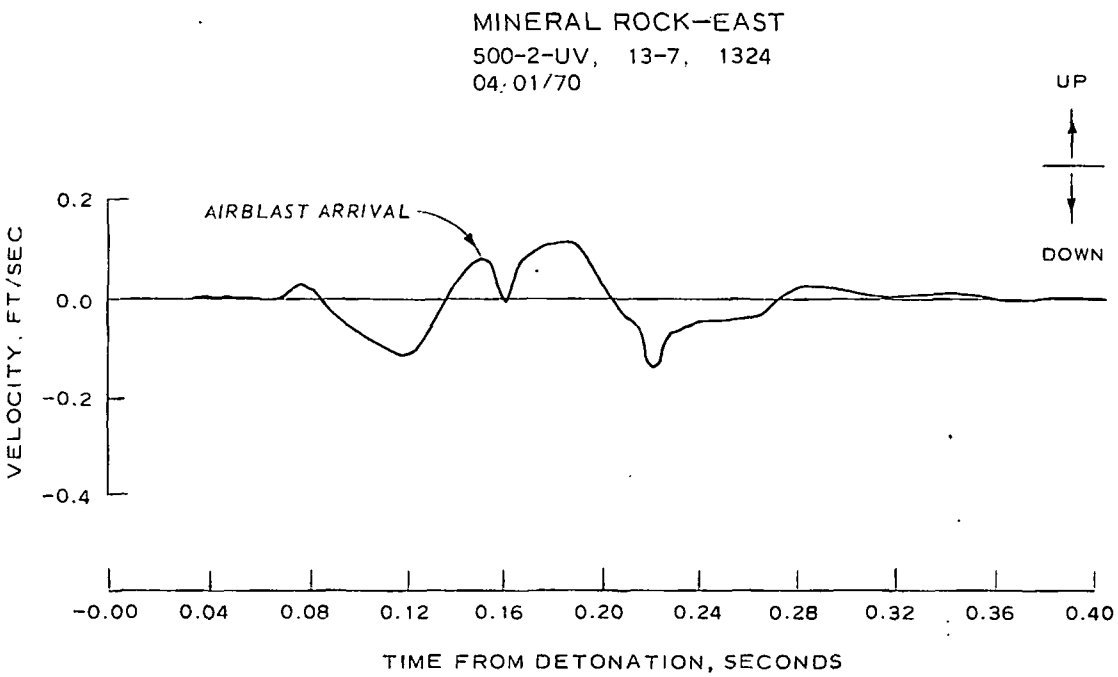

Figure 3.7 Outrunning vertical velocity waveform.

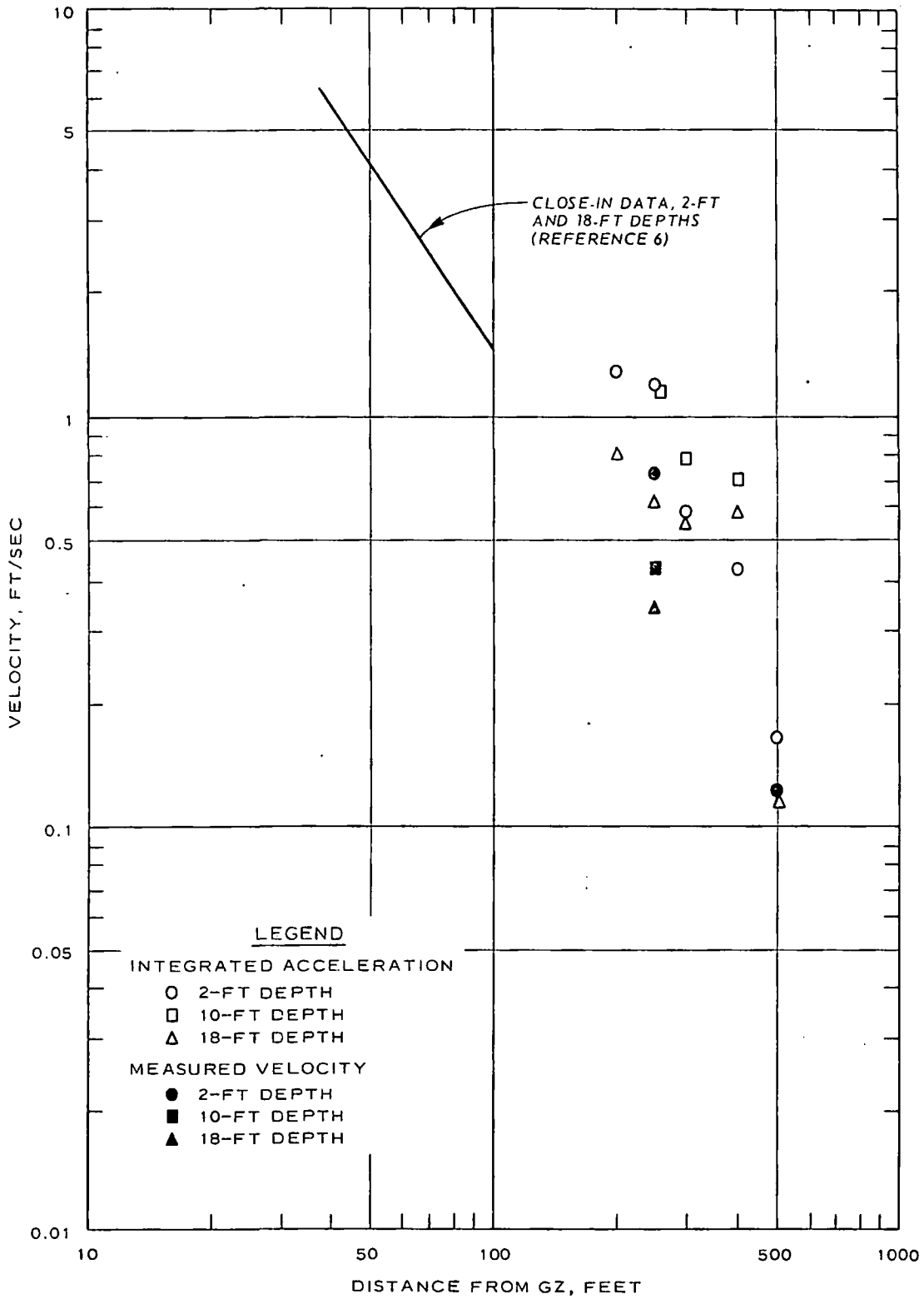

Figure 3.8 Peak downward (airblast-induced) vertical velocity versus distance.

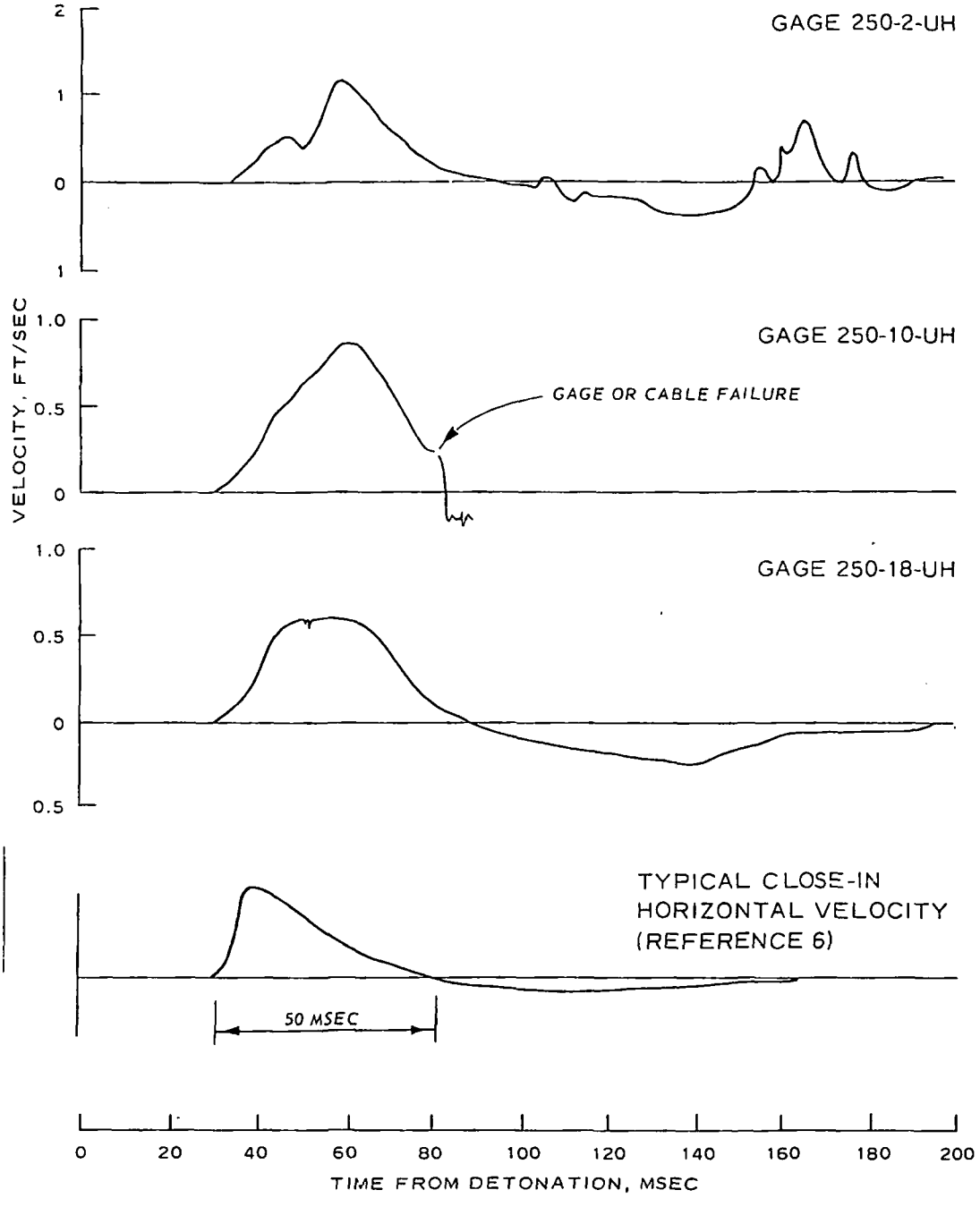

Figure 3.9 Horizontal velocity histories, 250-foot range.

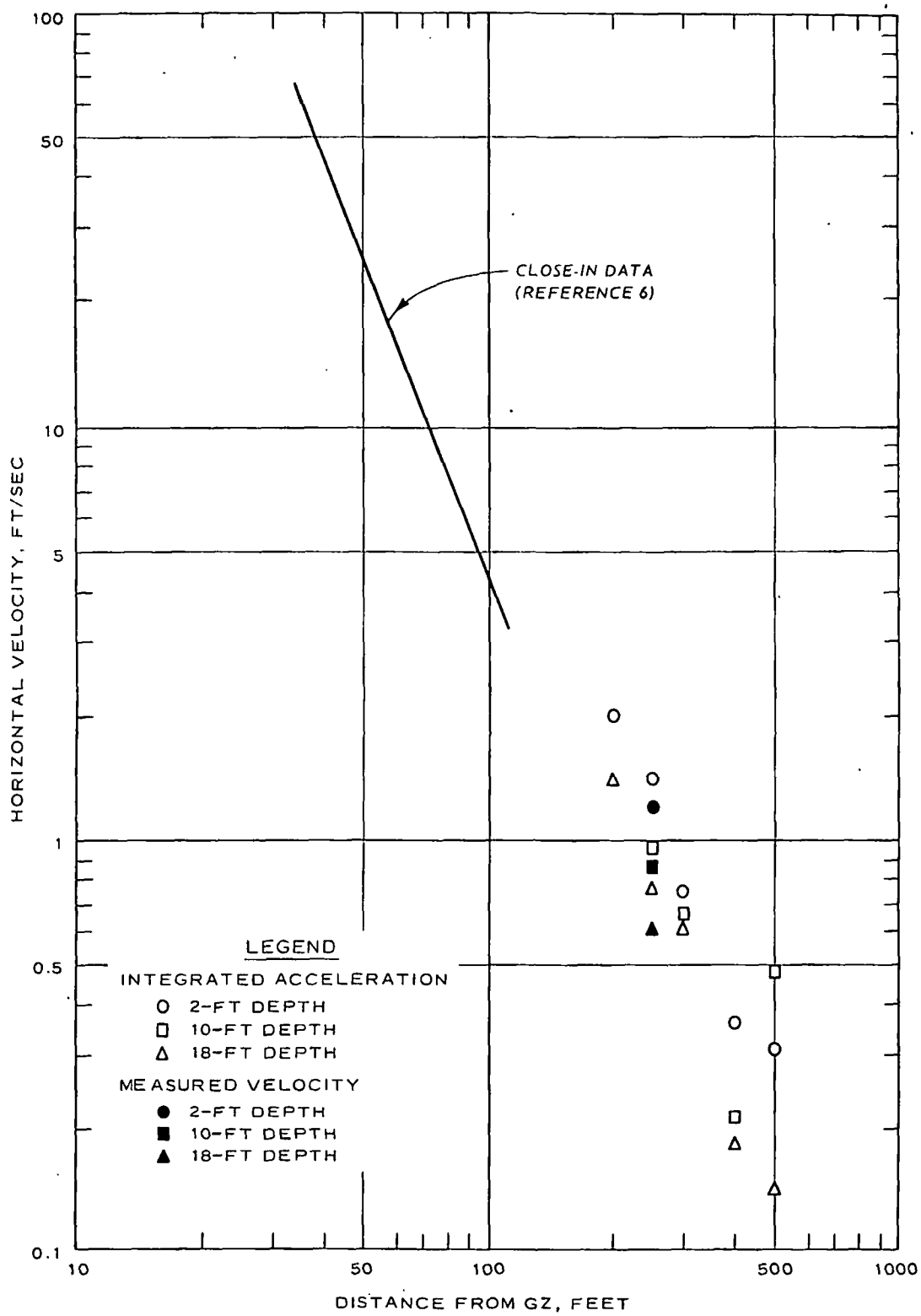

Figure 3.10 Peak horizontal particle velocity versus distance.

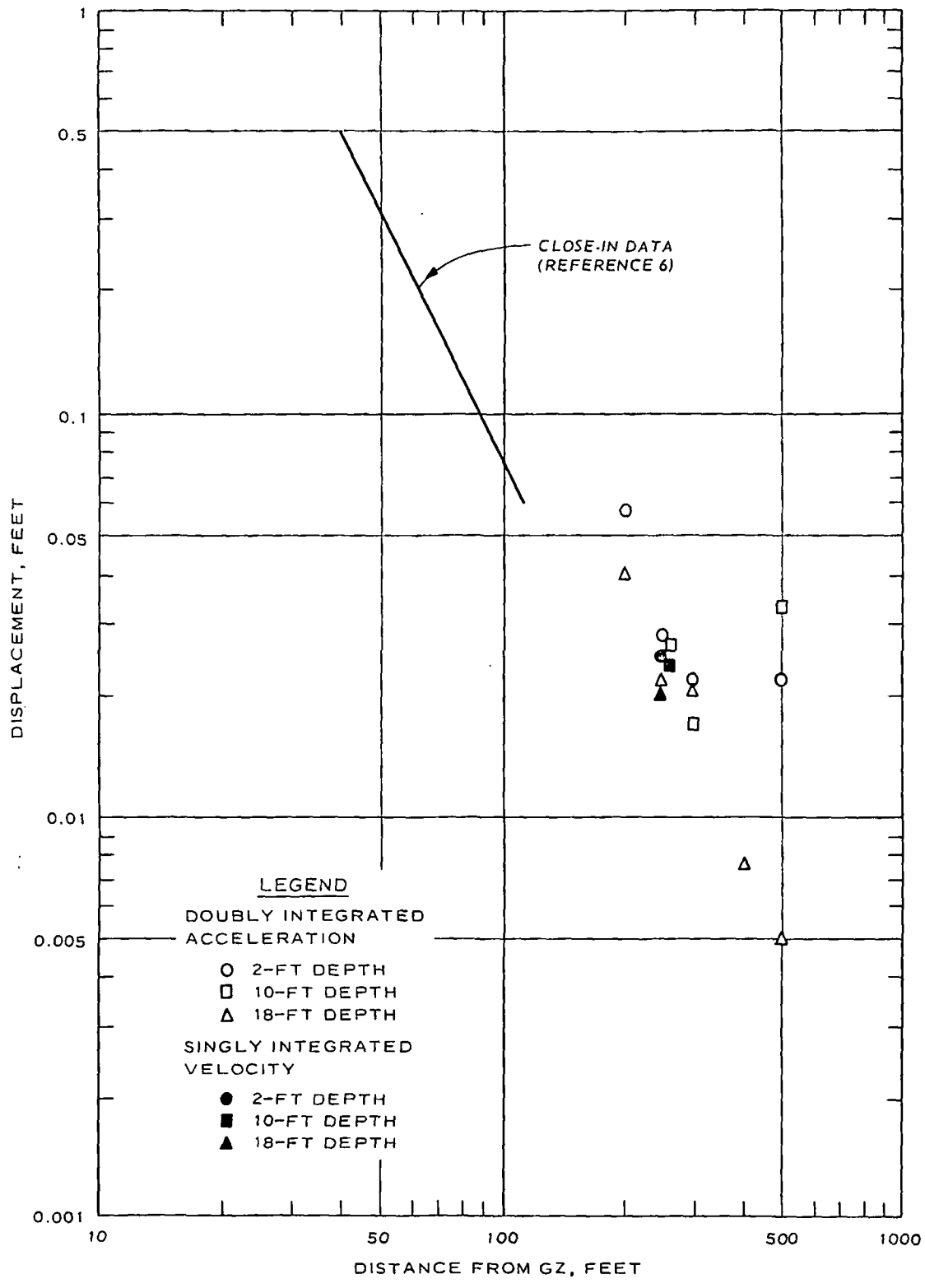

Figure 3.11 Peak horizontal displacement versus distance.

CHAPTER 4

CONCLUSIONS AND RECOMMENDATIONS

4.1 INSTRUMENT PERFORMANCE

All 36 gages installed for this project were operable at shot time, indicating successful installation insofar as gage or cable damage was concerned. All channels calibrated properly, and recording systems operated correctly as programmed. Two gages (one accelerometer and one velocity gage) produced no readable output and are considered to have failed at shock arrival. The remaining 27 accelerometers were all subjected to a strong electrical noise signal at 20 msec after the detonation. This time was noted to correspond to shock arrival at the nearest approach to GZ of the cable line, and the noise was attributed to shock effects on the cable itself, even though considerable cable protection precautions had been taken. The seven operable velocity gages were not affected.

With the exception of the pressure-induced cable noise, the 34 successfully recorded gages showed good response. The relatively low-frequency response of the velocity gage-System D amplifier system caused some problems in comparing vertical data with acceleration integrals.

Gage and recording system set ranges were sufficiently accurate that good signal amplitude was obtained on all channels. All signals were well above normal system background noise, yet no channels were driven out of band.

4.2 MOTION MEASUREMENTS

Peak downward airblast-induced vertical accelerations were found to attenuate sharply with both distance and depth from the maximum value of 32 g's at the 200-foot range and 2-foot depth. Vertical airblast-induced accelerations were noted to correlate well with overpressure, averaging about 0.2 g/psi for the 2-foot depth. This ratio is approximately one-fourth that for 100-ton detonations over soil.

Peak horizontal accelerations were also generally associated with passage of airblast and were approximately one-half the vertical peaks at the

2- and 10-foot depths; at the 18-foot depth, horizontal accelerations were about three-fourths the vertical.

Downward airblast-induced vertical velocities attenuated with distance and depth, although attenuation with depth was less regular than for accelerations. This is attributed partially to the noisy accelerograms which did not produce very reliable integrals. No measurable vertical outrunning velocity was noted at the 250-foot range. At the 500-foot range, however, the outrunning pulse had a significant vertical component of both greater magnitude and longer duration than the airblast-induced motion. Horizontal velocities followed much the same pattern as did the vertical, and over the range instrumented were roughly equal to vertical peaks. Horizontal velocities generally showed considerable outrunning motion, with the airblast-induced pulse superposed on a long-duration outward pulse. Relative velocity contributions of the two pulses were quantitatively indeterminate, although due to its duration, the outrunning (directly induced) motion would be the primary source of displacements.

Vertical displacement measurements of a high confidence level were limited to the 250-foot range. Very little attenuation with depth was noted, with displacements ranging from 0.0075 foot at the 2-foot depth to 0.0060 foot at the 18-foot depth. Horizontal displacements were successfully computed from both velocity and acceleration data. At the 250-foot range, they were three to four times as large as the vertical displacements.

4.3 RECOMMENDATIONS

Recommendations for future work fall into two categories: (1) changes or improvements in basic experiment design, and (2) changes in operational procedure.

Under the first of these, it is recommended that a larger percentage of channel space on future tests be devoted to velocity gages. This provides generally more reliable displacement data and, except where acceleration data itself is of vital importance, should be the primary instrumentation. Where accelerations are required, velocity gages provide excellent back-up data.

Additionally, instrument locations should be spread over as wide a

range of distance and depth as practical in order to adequately define attenuation patterns.

Under the second category, the cable protection methods used for Mineral Rock were apparently inadequate. Since pressure effects had not been noticed on prior tests, protection from ejecta missiles was uppermost in mind, and cables were adequately protected from this hazard. Pressure protection for future tests could be offered by more judicious (though more expensive) cable routing and by protection by encasing in pressure-proof material such as conduit.

APPENDIX A

MOTION-TIME HISTORIES

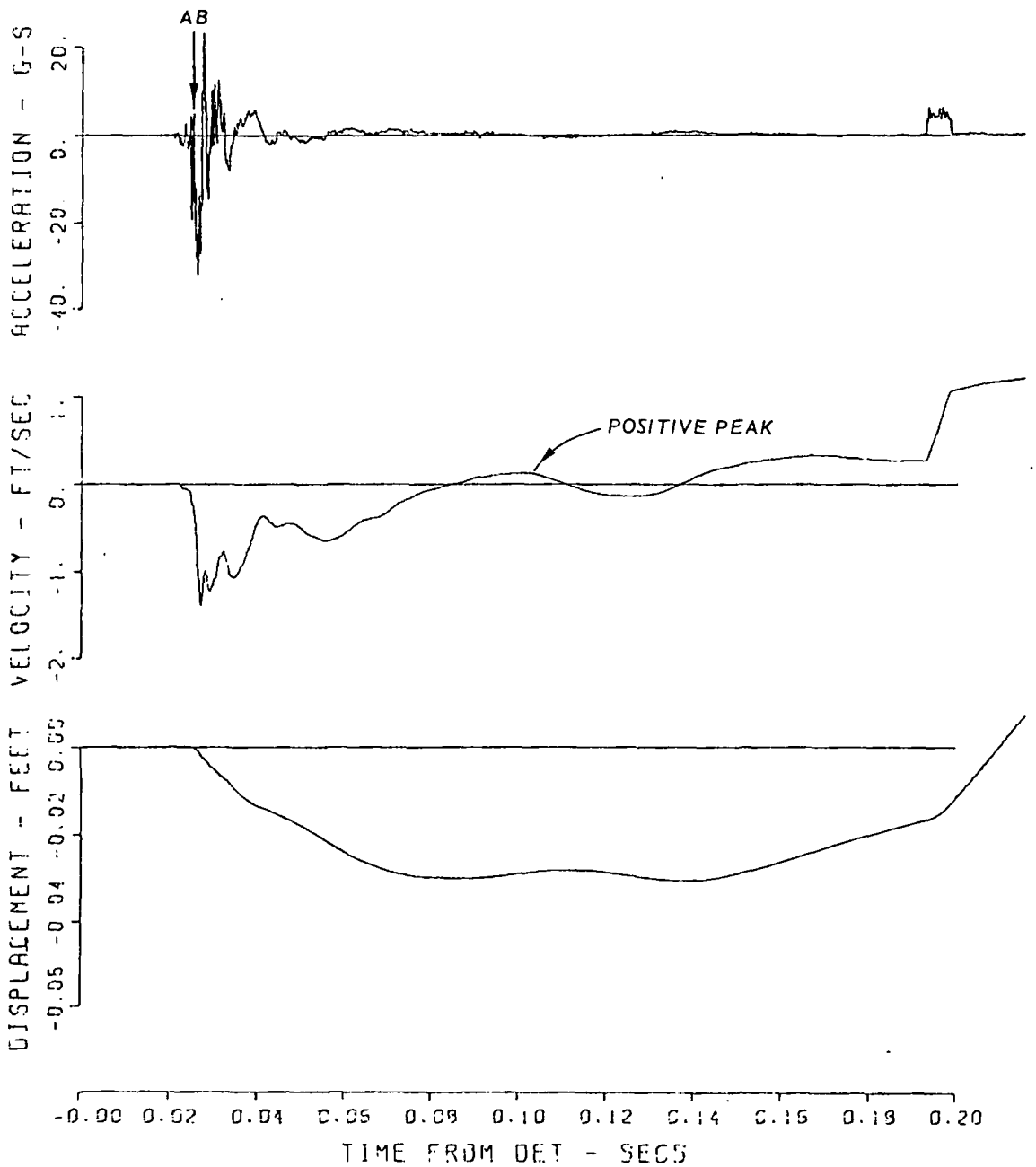

Figure A.1 Gage 200-2-AV.

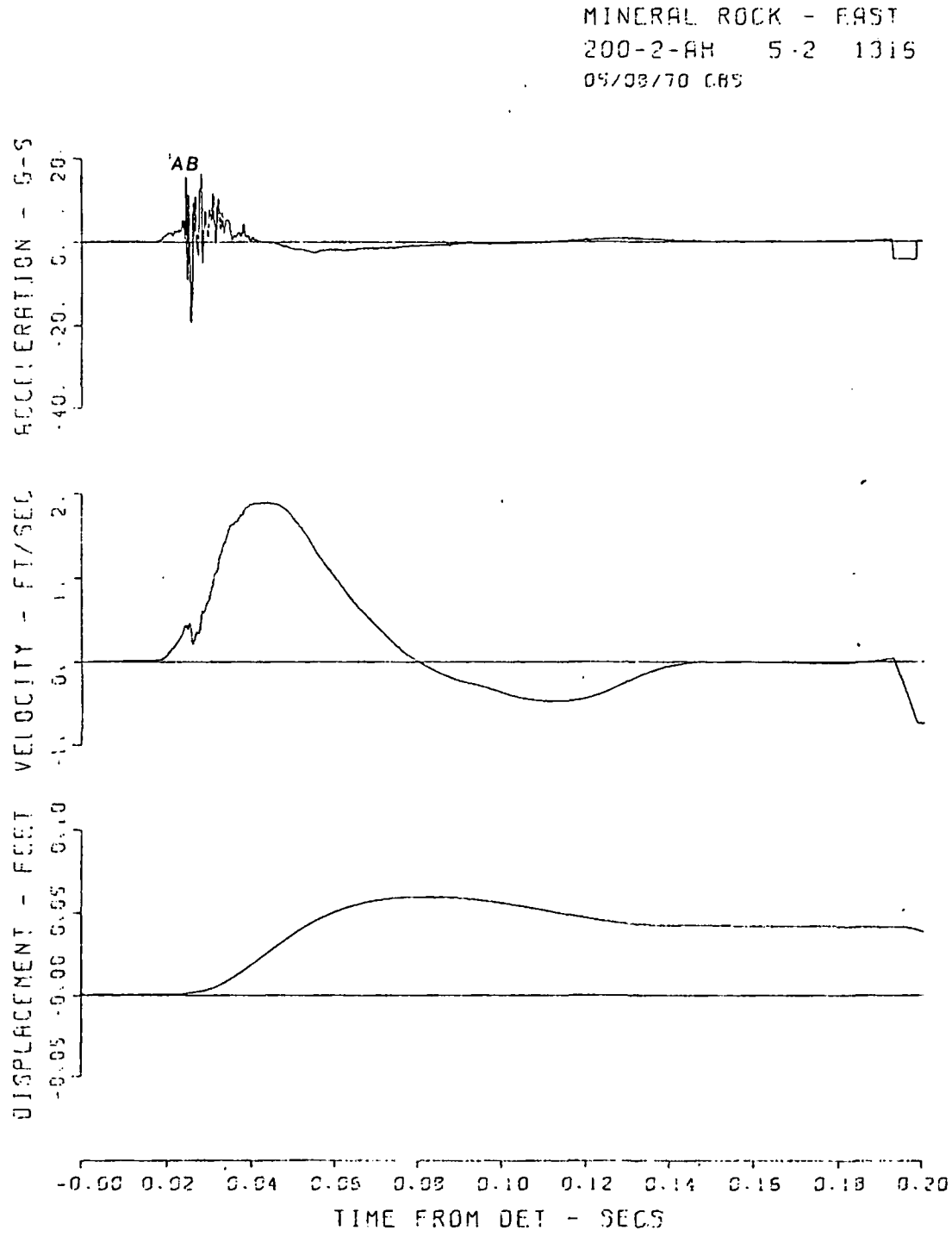

Figure A.2 Gage 200-2-AH.

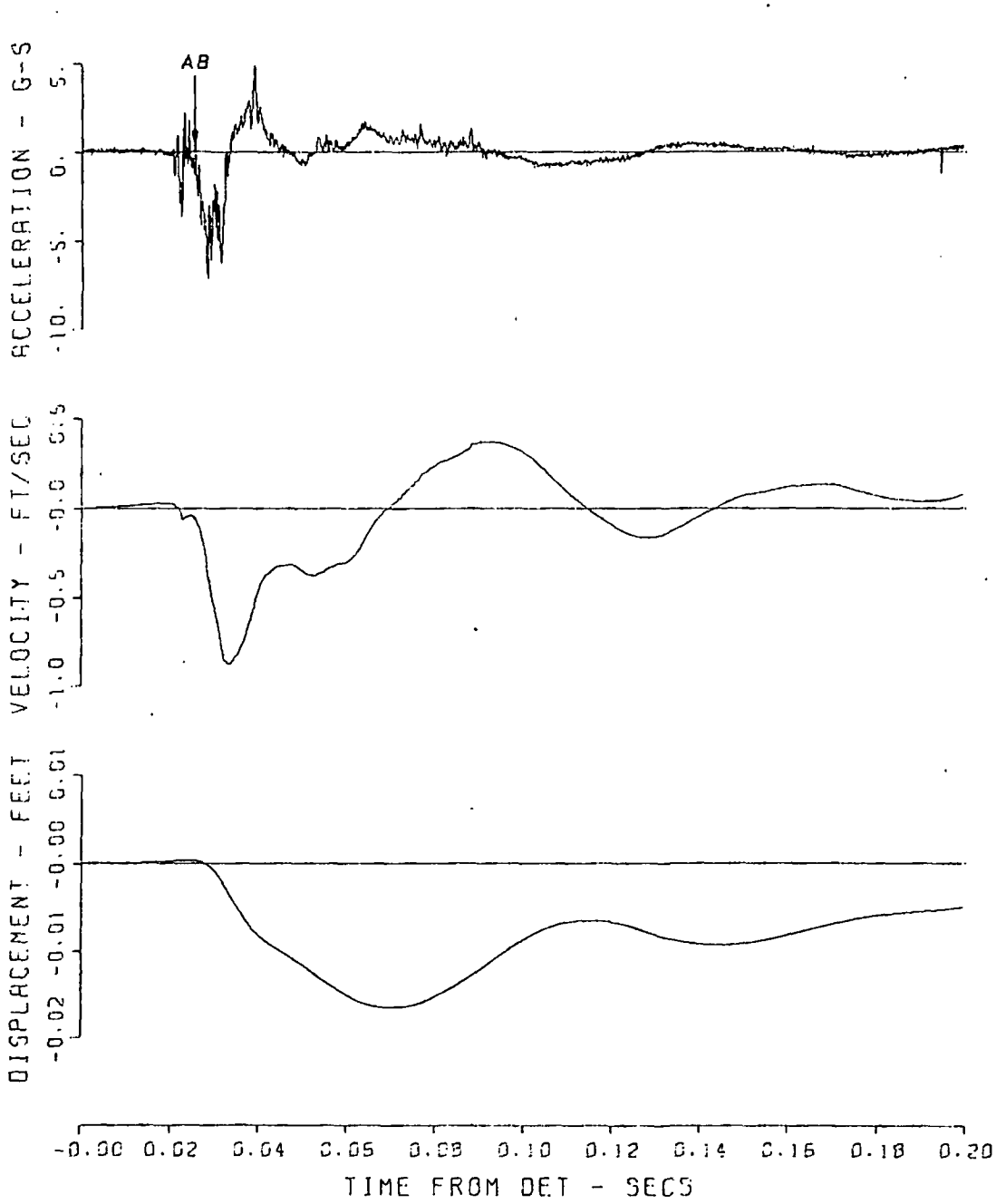

Figure A.3 Cage 200-18-AV.

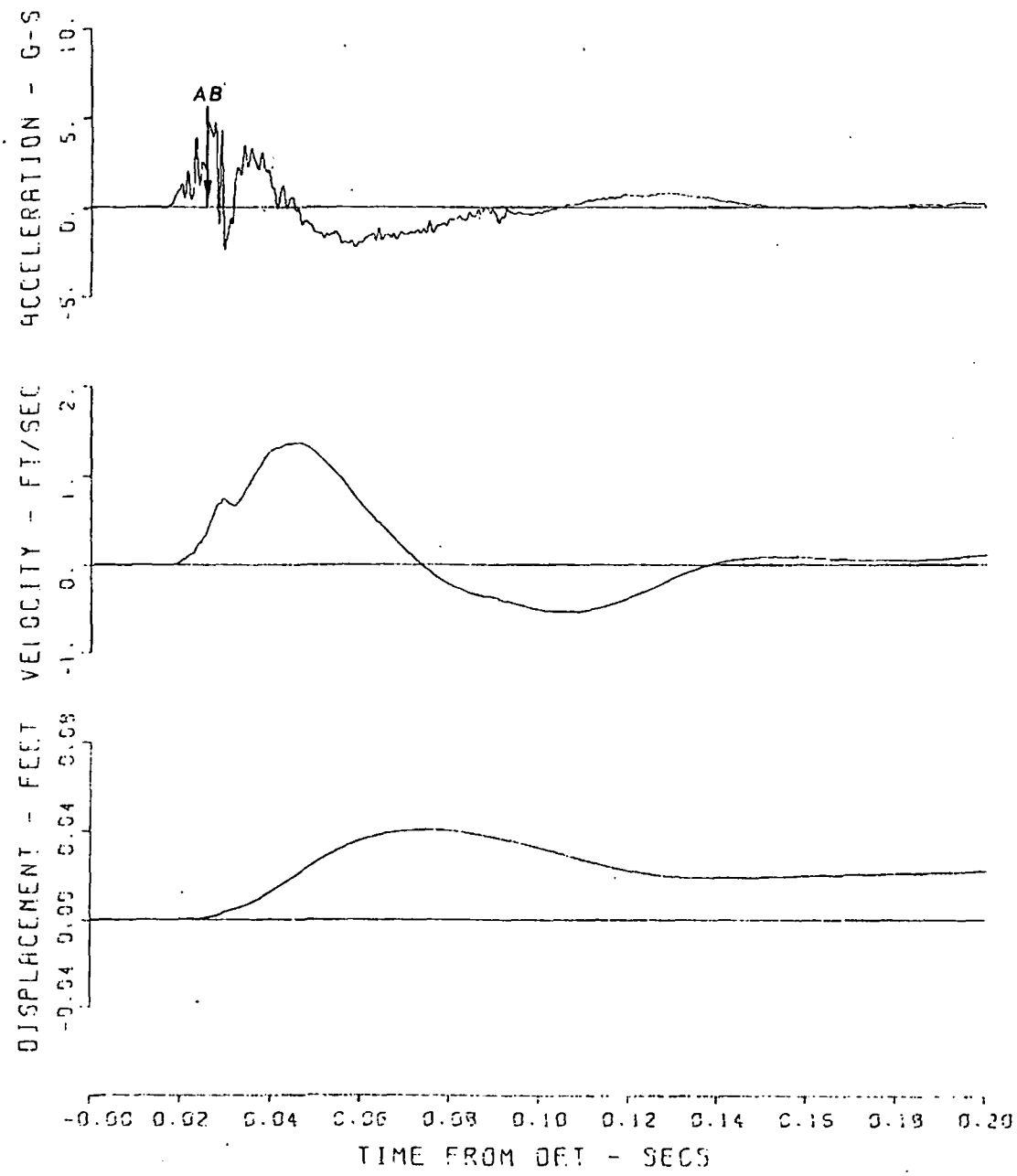

Figure A.4 Gage 200-18-AH.

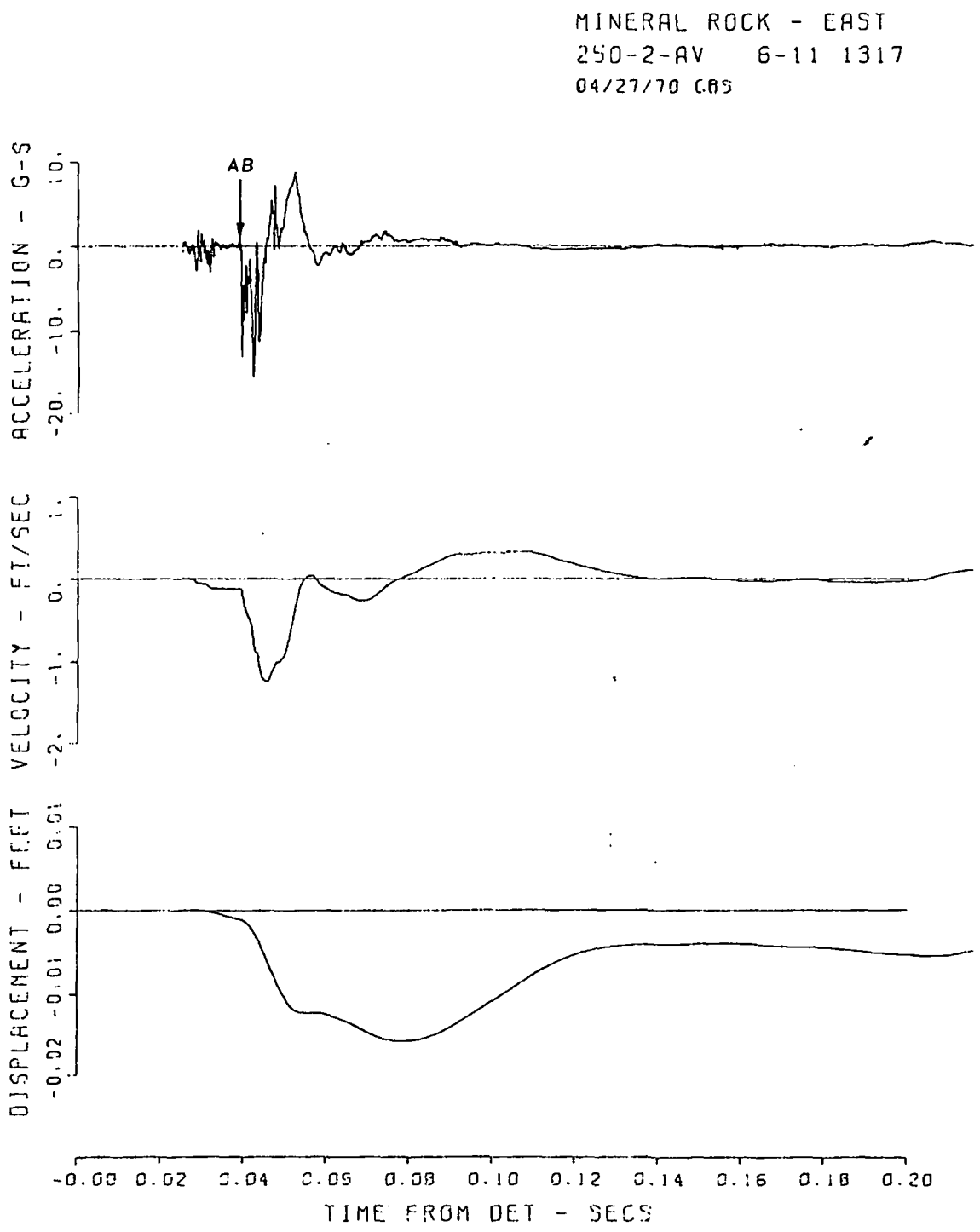

Figure A.5 Gage 250-2-AV.

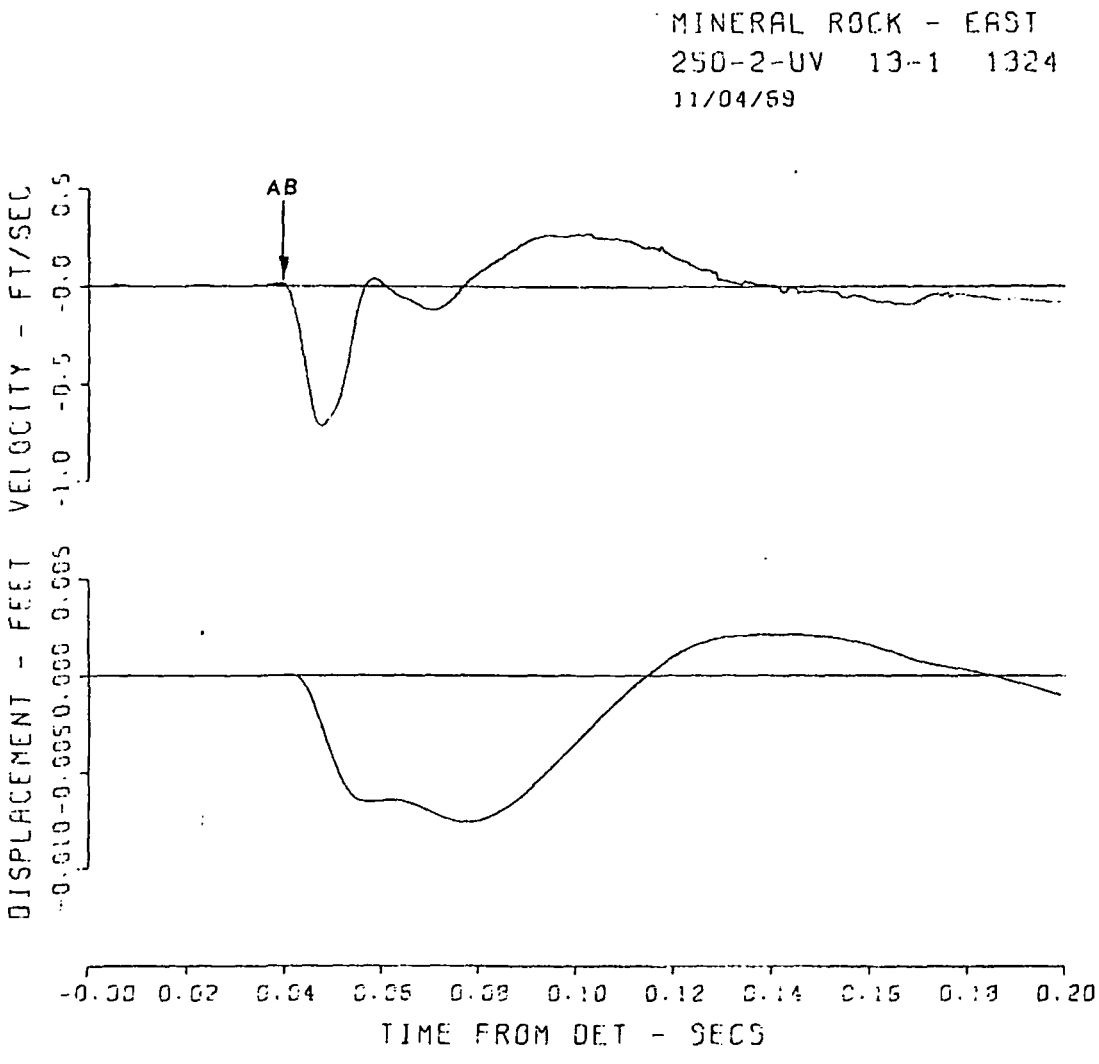

Figure A.6 Gage 250-2-UV.

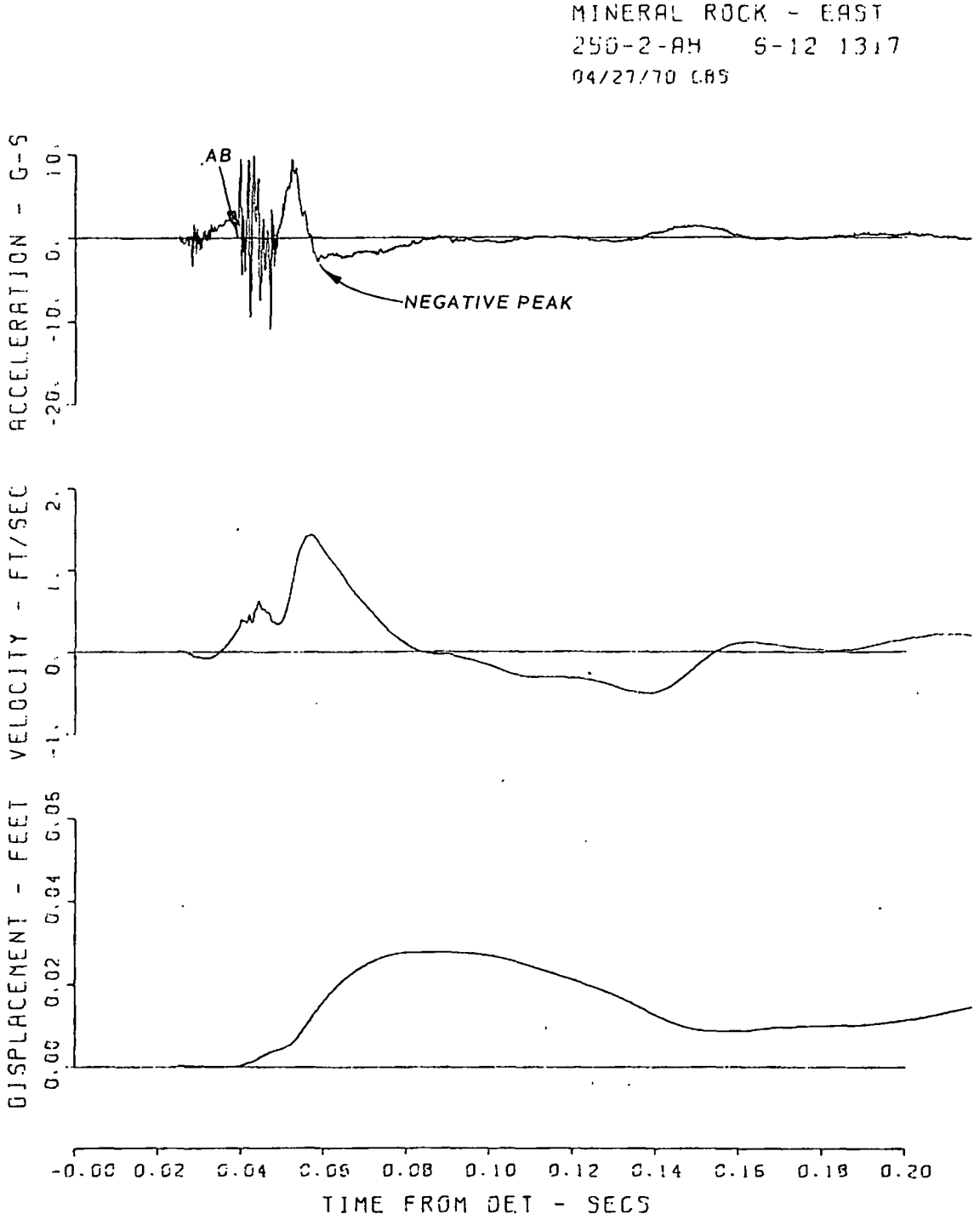

Figure A.7 Gage 250-2-AH.

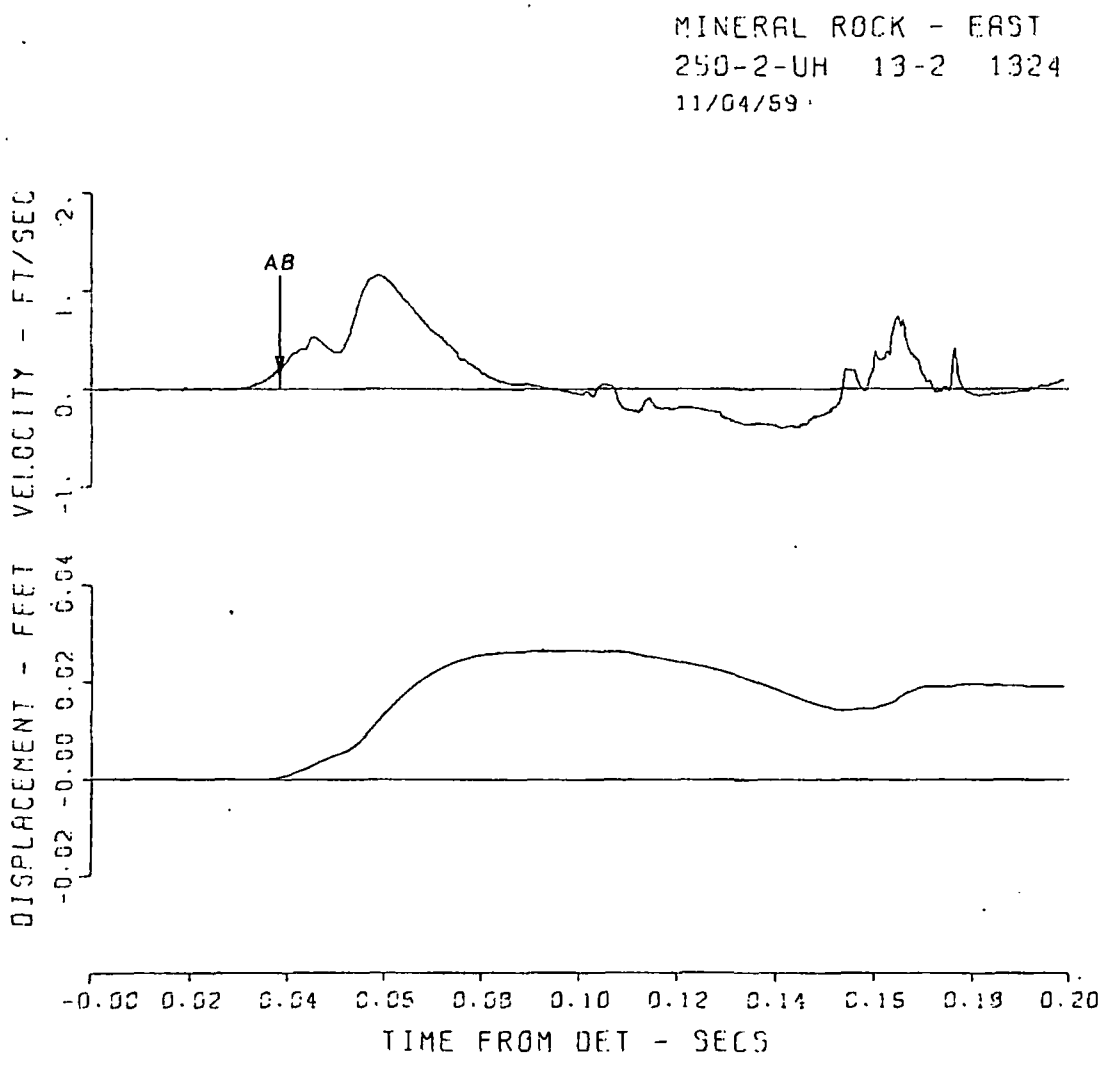

Figure A.8 Gage 250-2-UH.

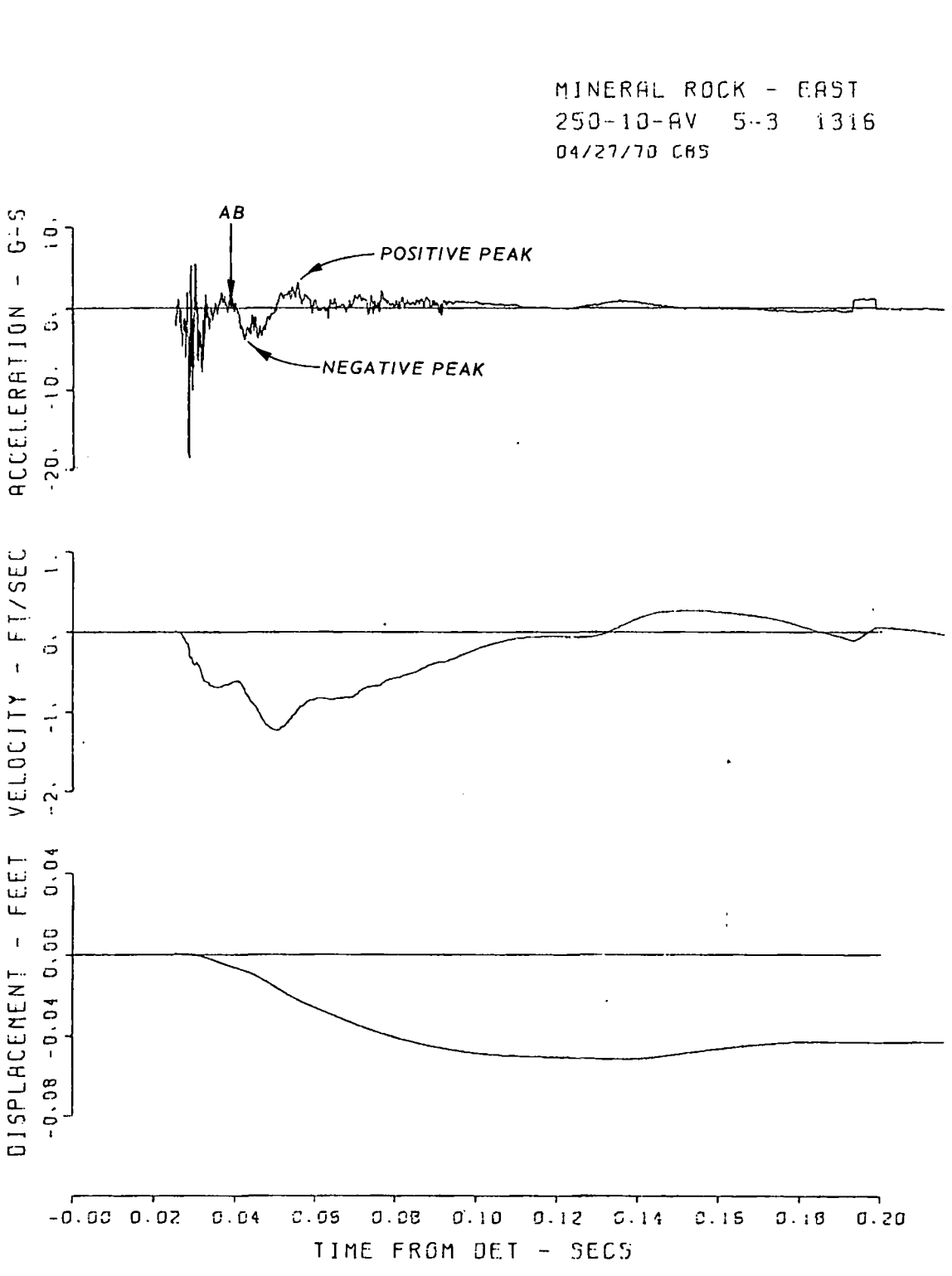

Figure A.9 Gage 250-10-AV.

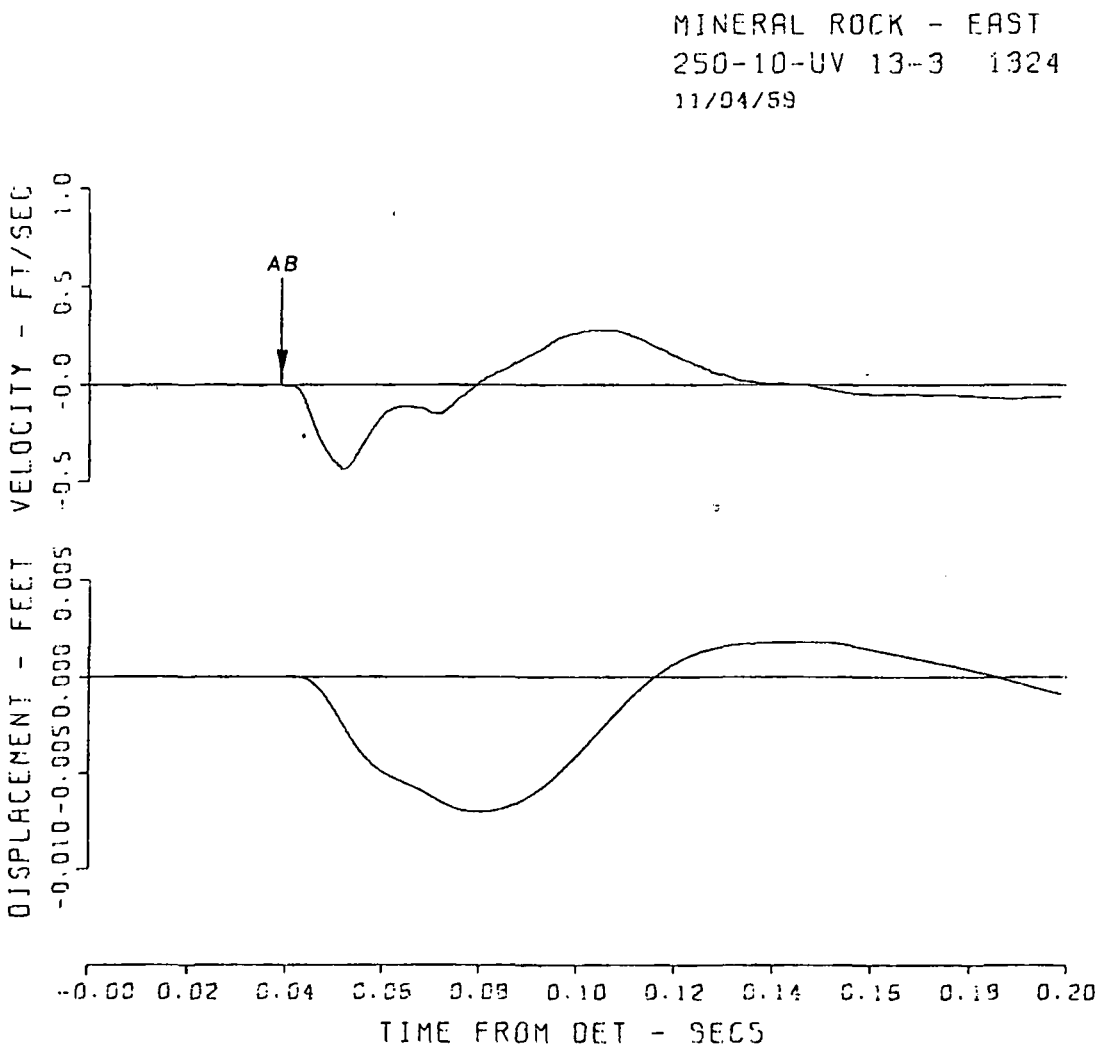

Figure A.10 Gage 250-10-UV.

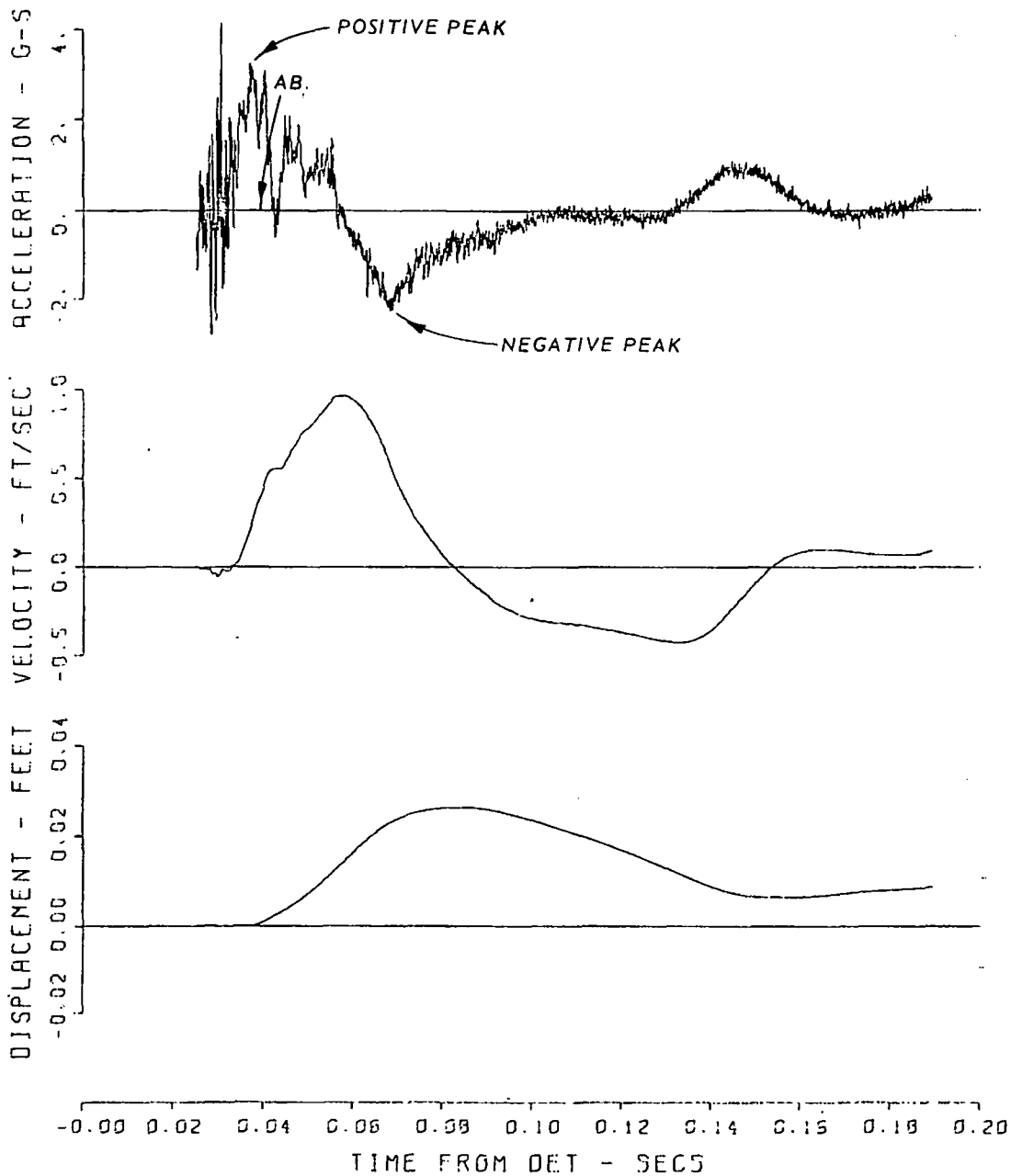

Figure A.11 Gage 250-10-AH.

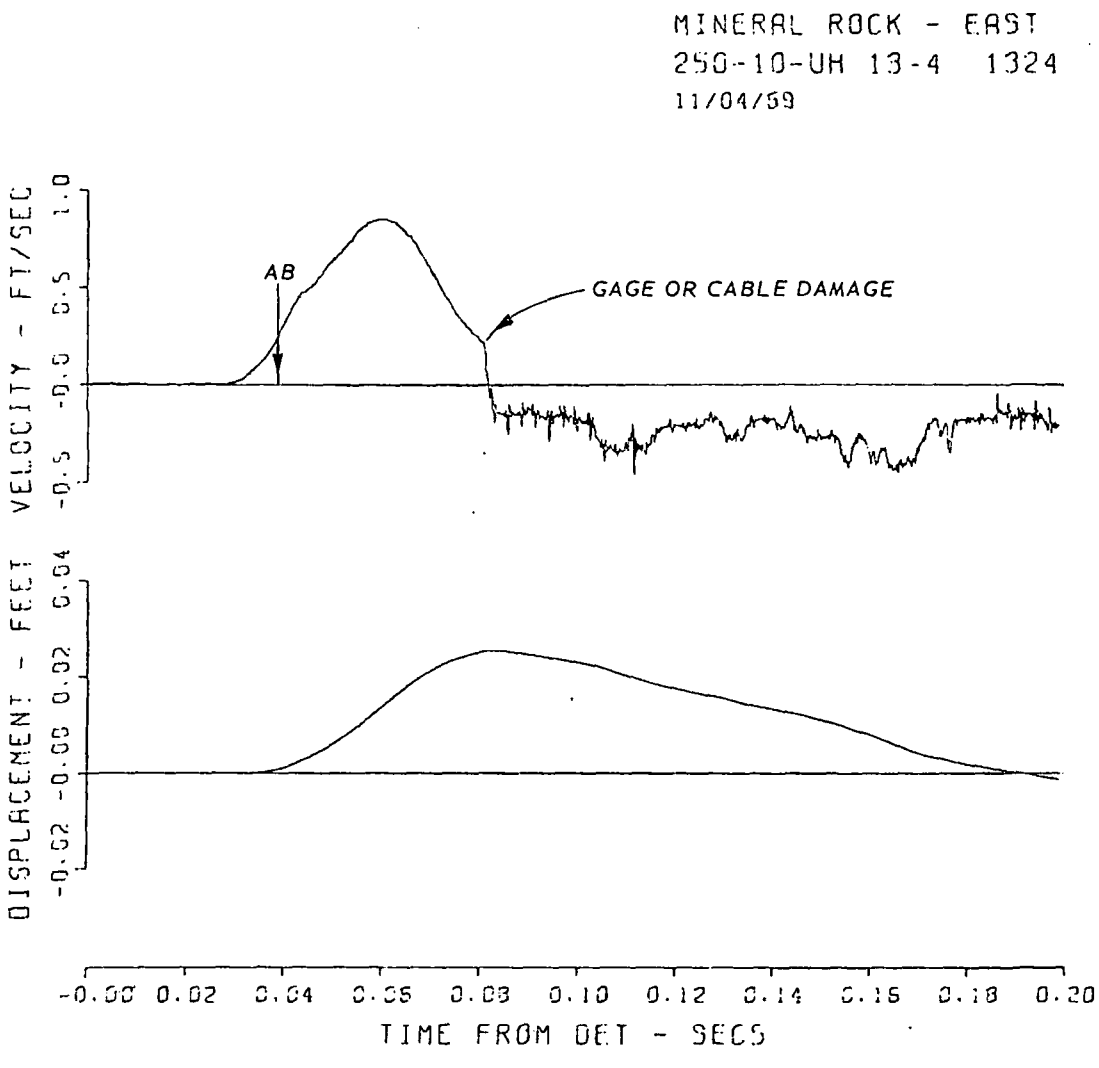

Figure A.12 Gage 250-10-UH.

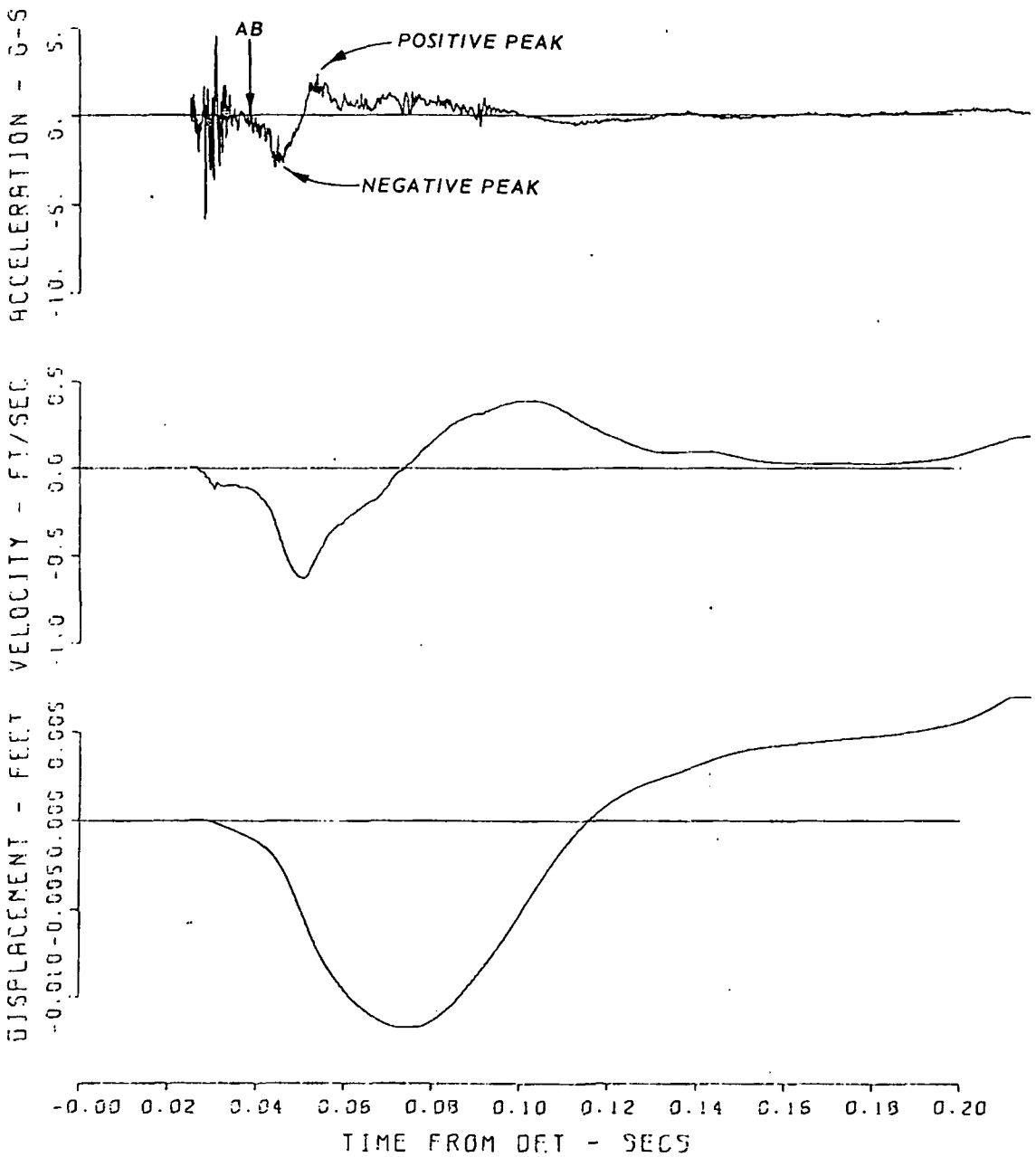

Figure A.13 Gage 250-18-AV.

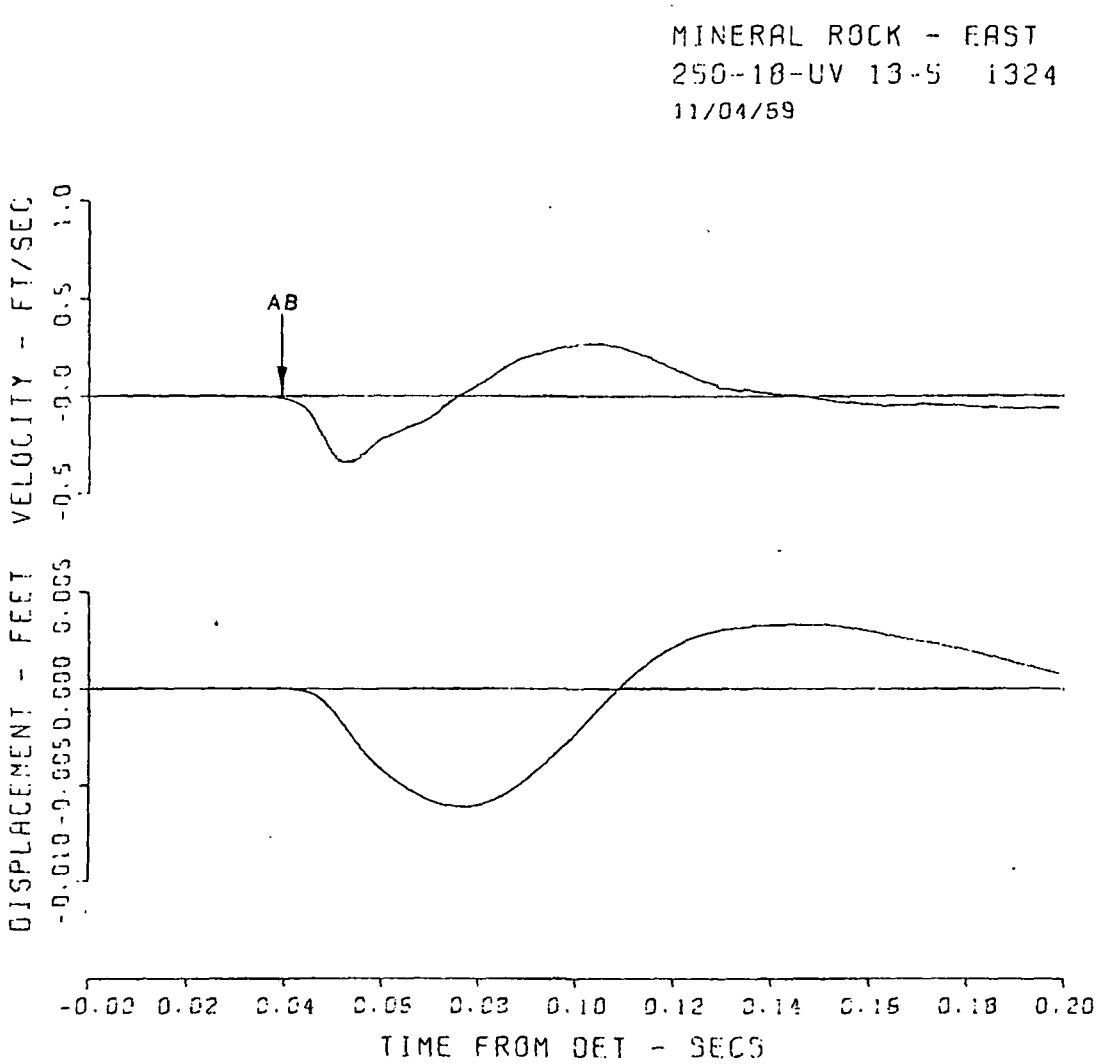

Figure A.14 Gage 250-18-UV.

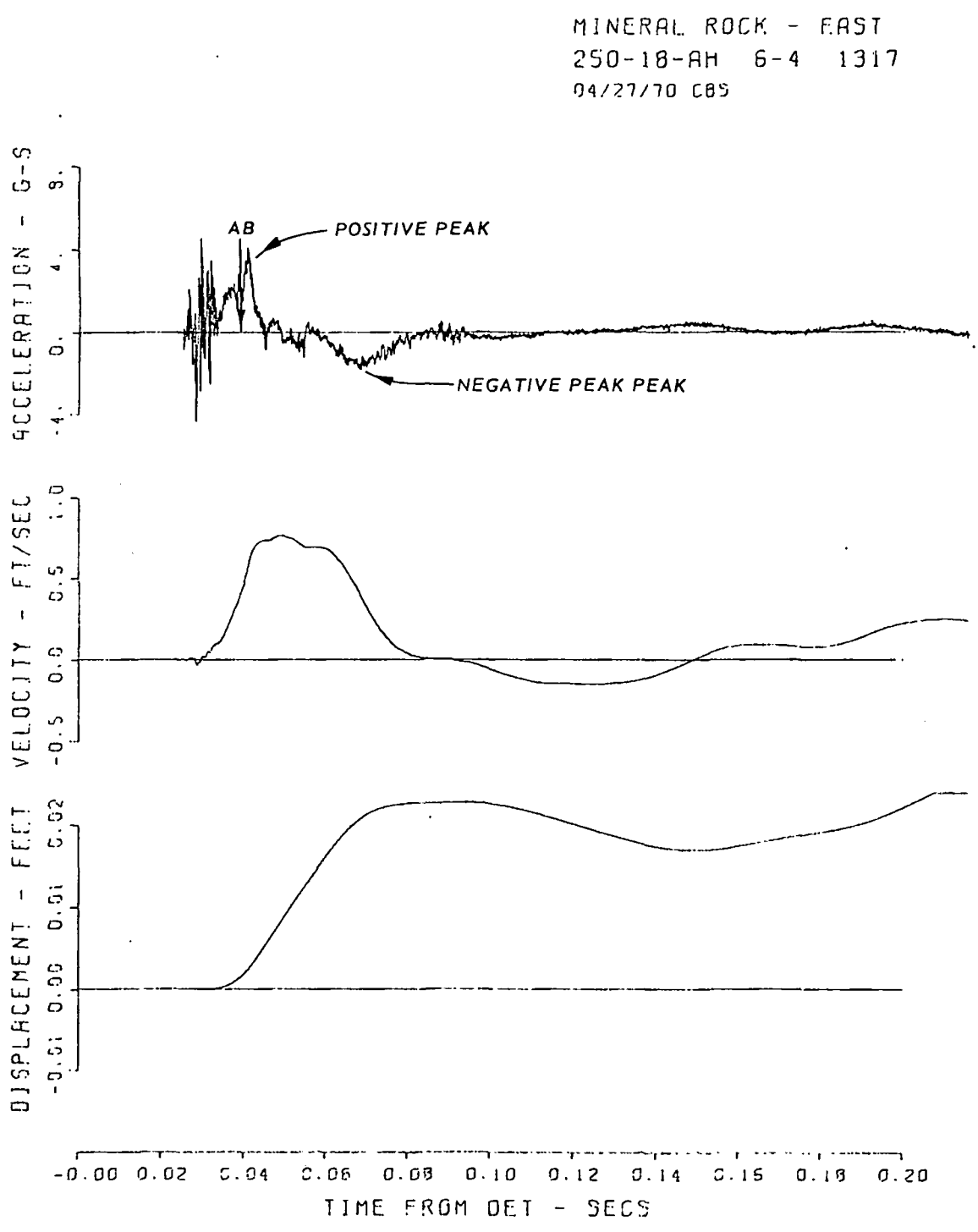

Figure A.15 . Gage 250-18-AH.

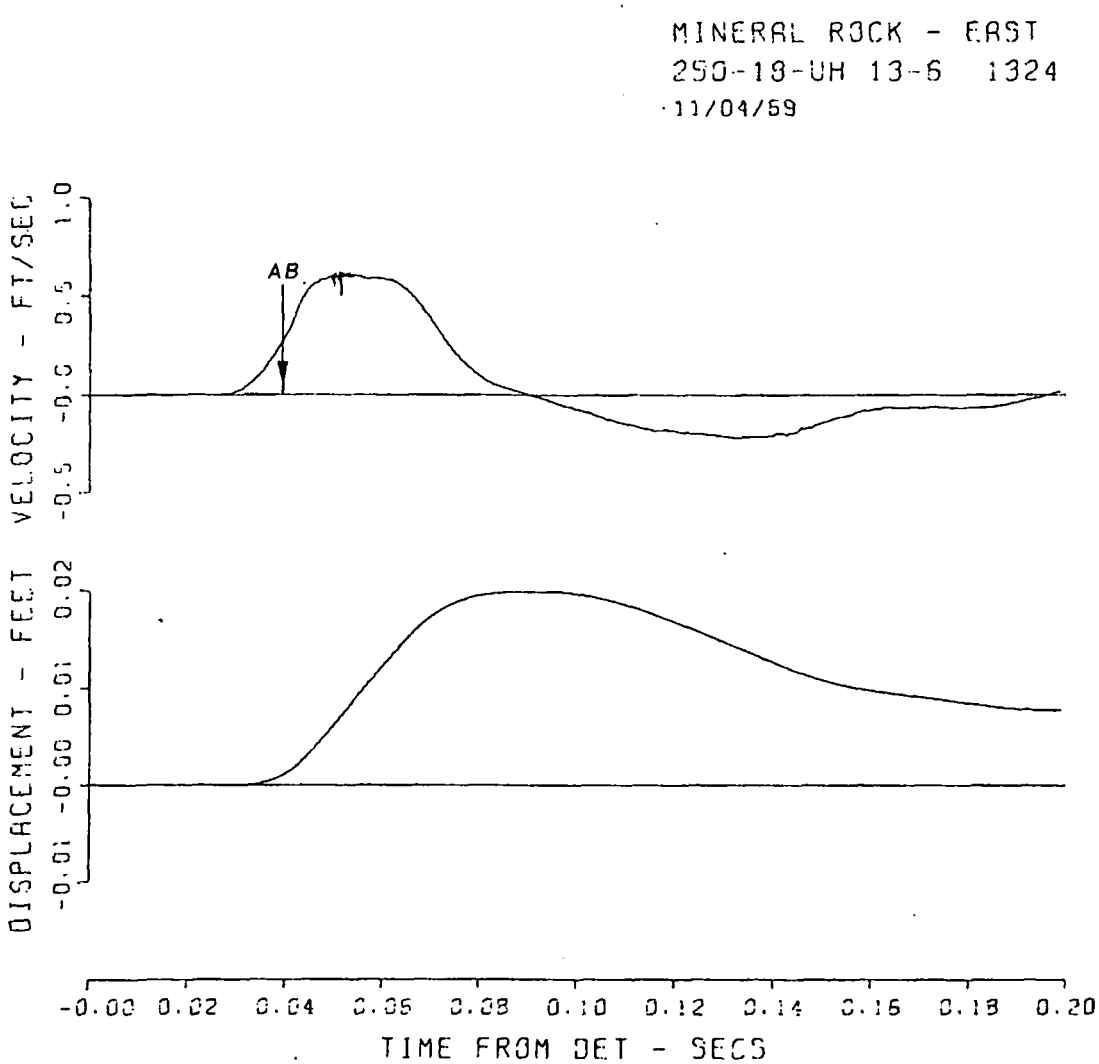

Figure A.16 Gage 250-18-UH.

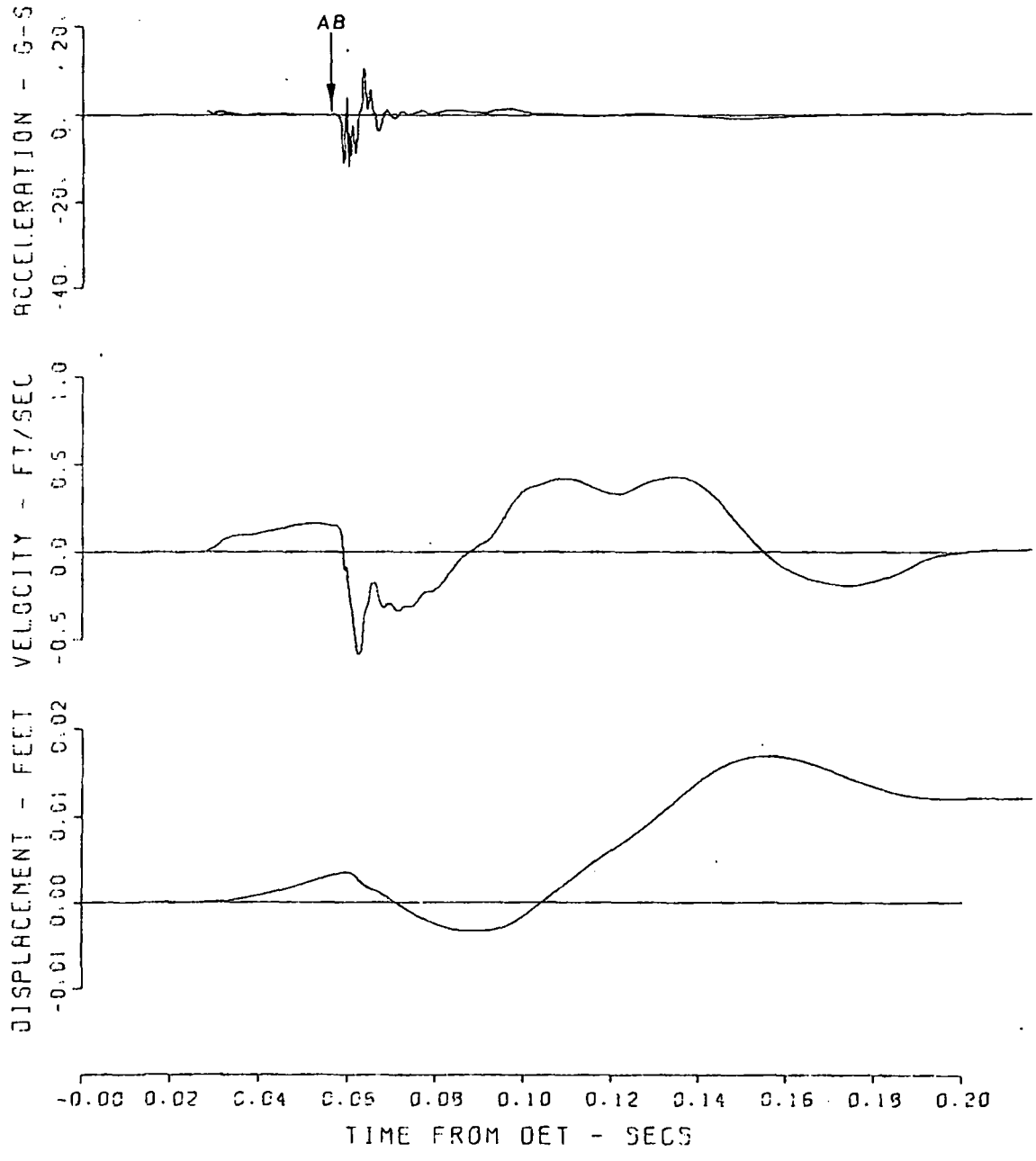

Figure A.17 Gage 300-2-AV.

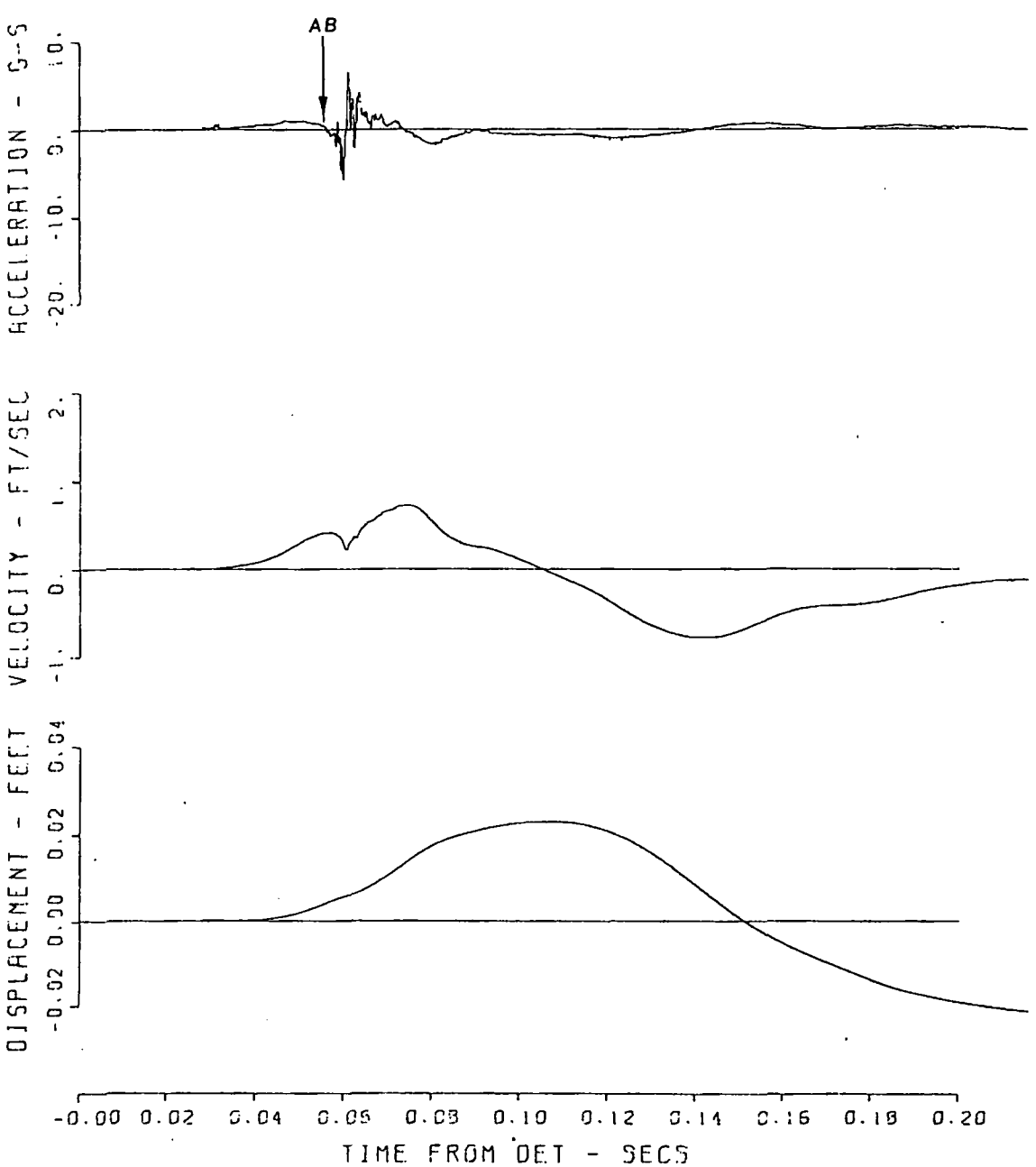

Figure A.18 Gage 300-2-AH.

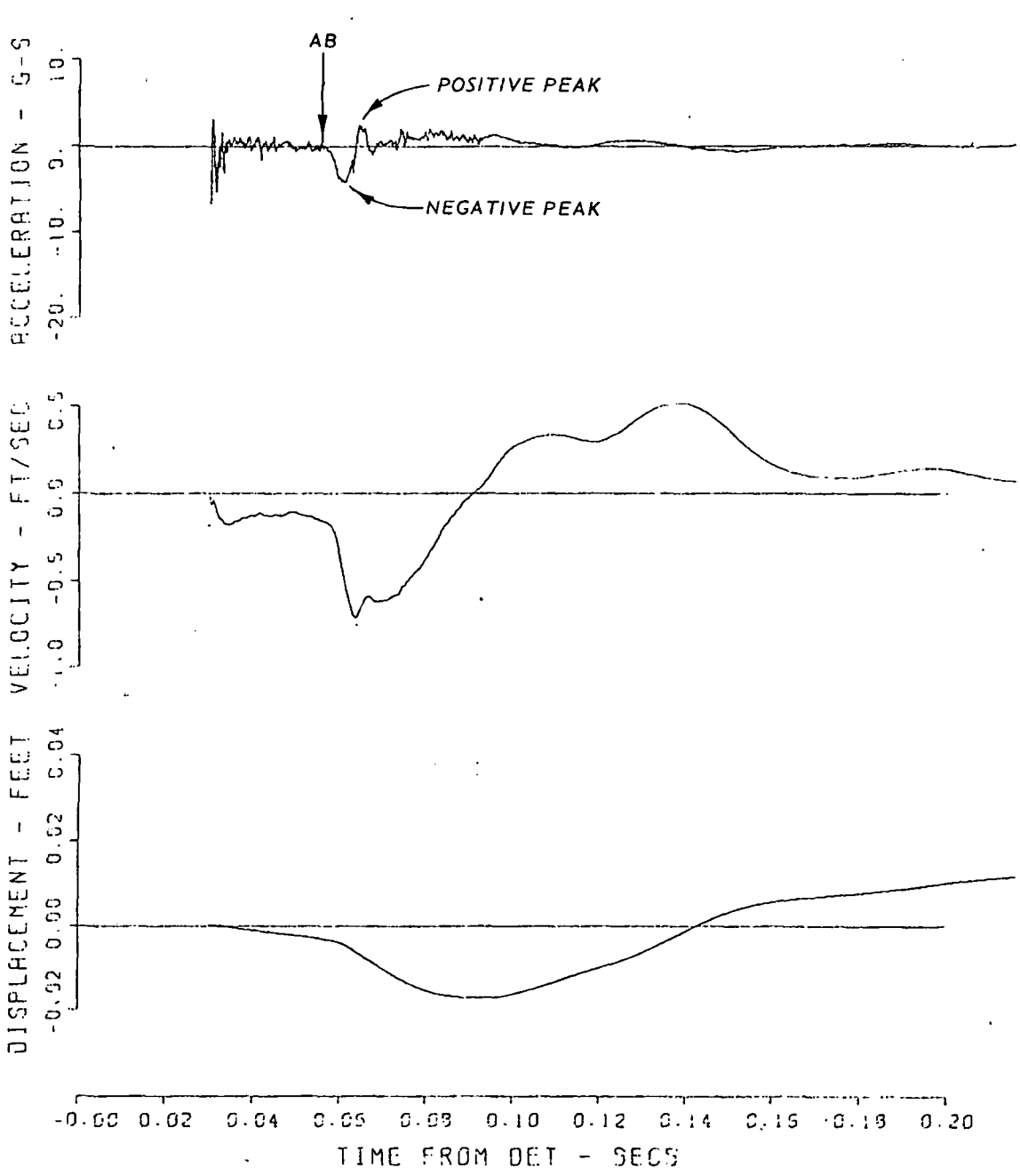

Figure A.19 Gage 300-10-AV.

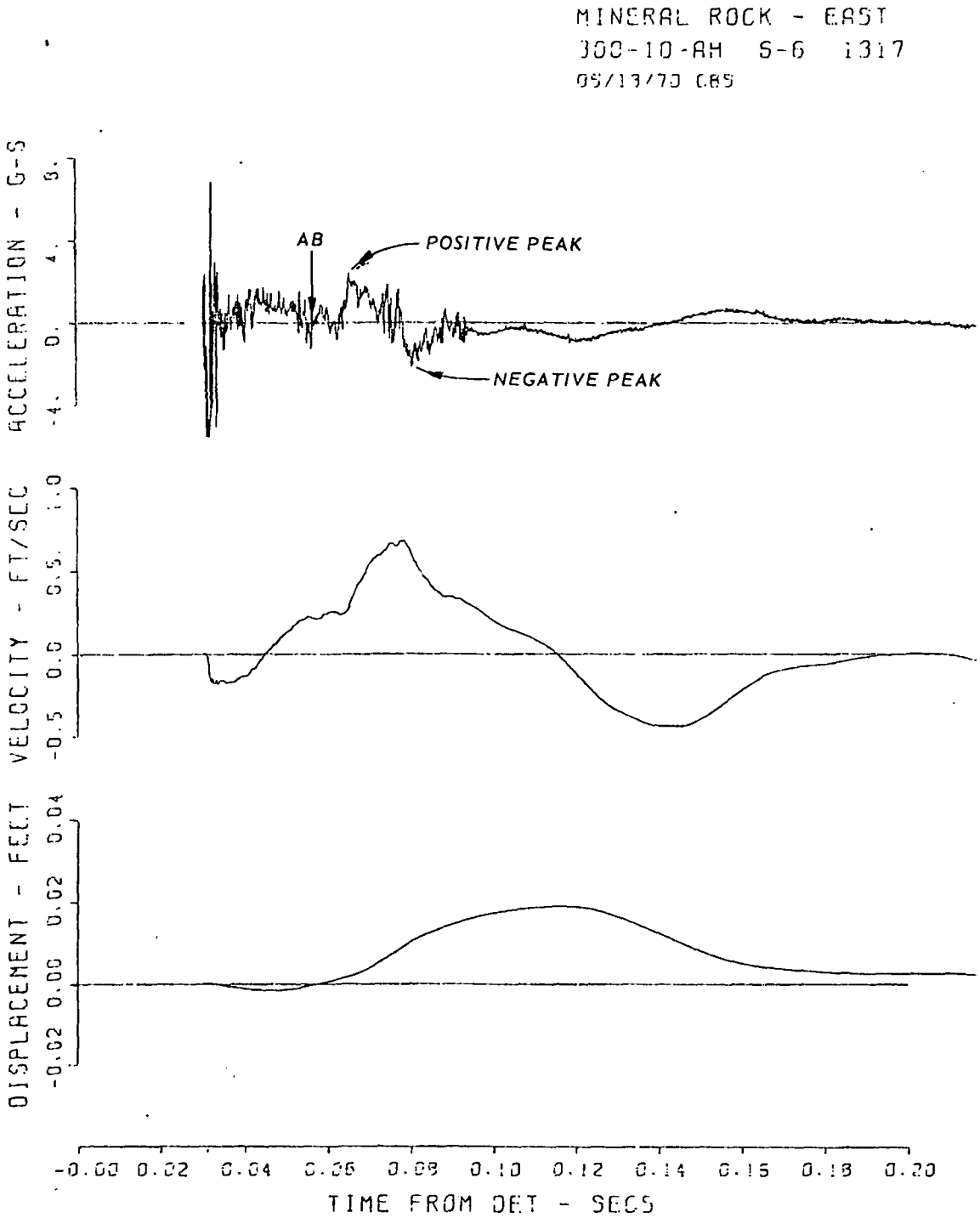

Figure A.20 Gage 300-10-AH.

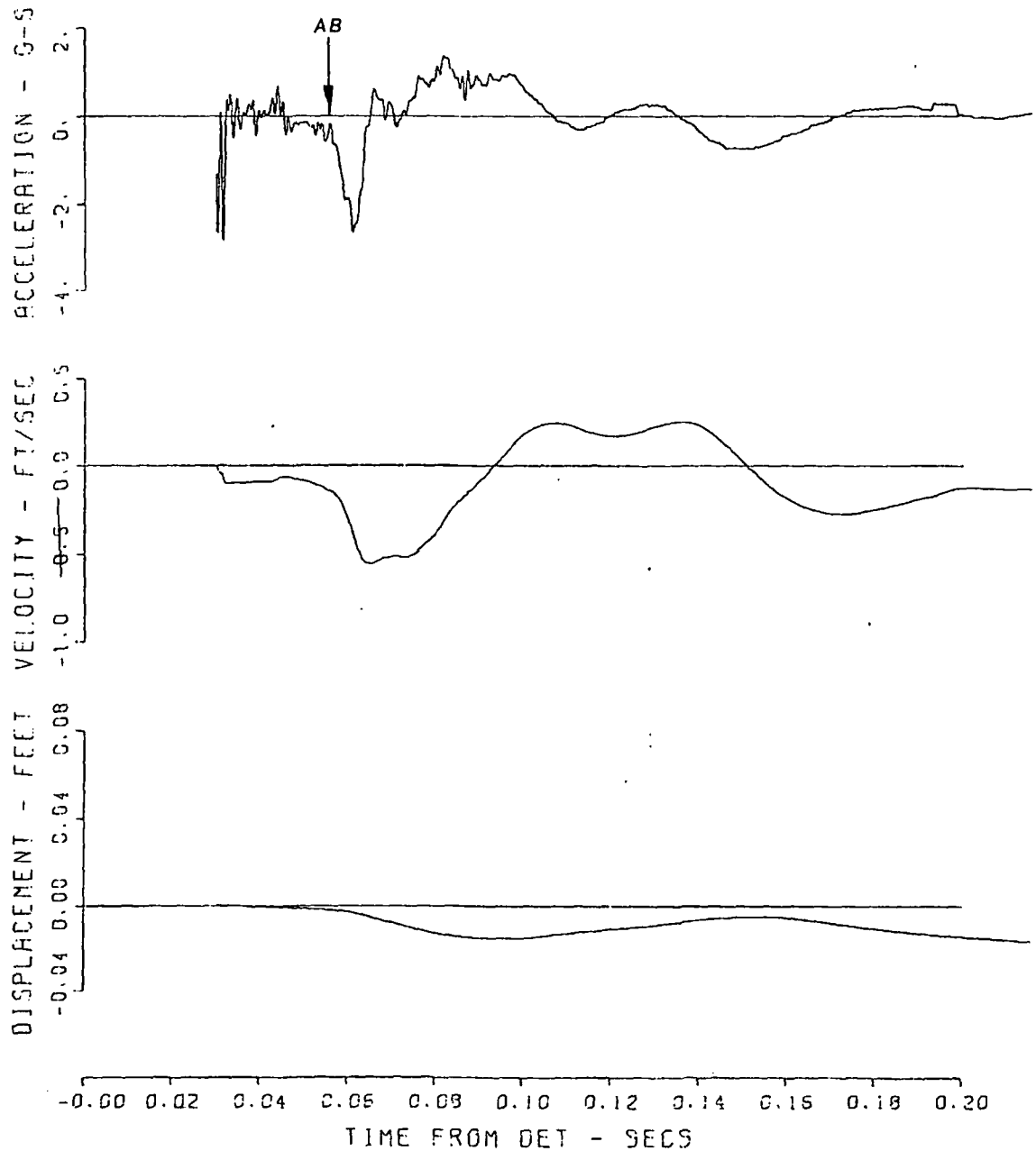

Figure A.21 Gage 300-18-AV.

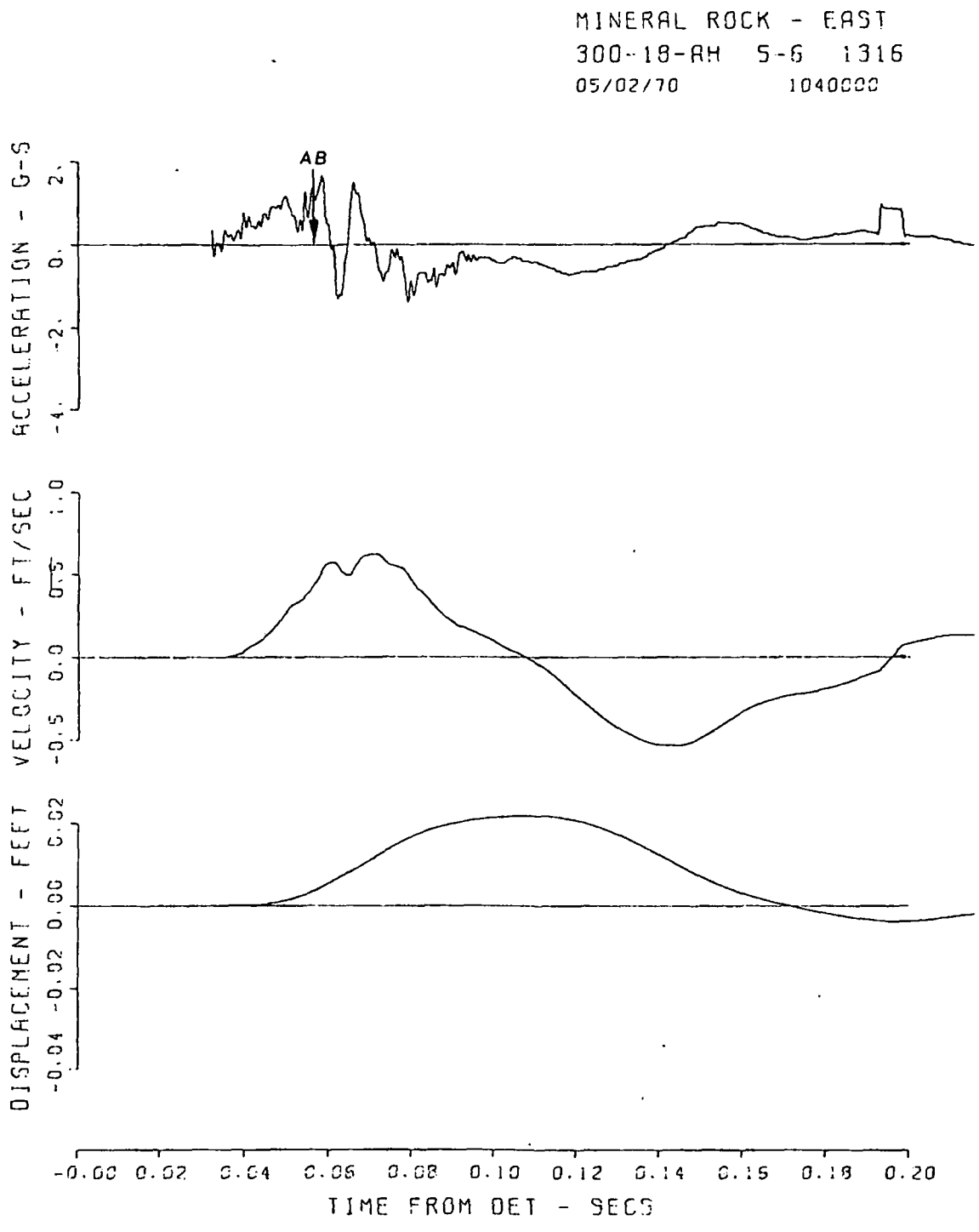

Figure A.22 Gage 300-18-AH..

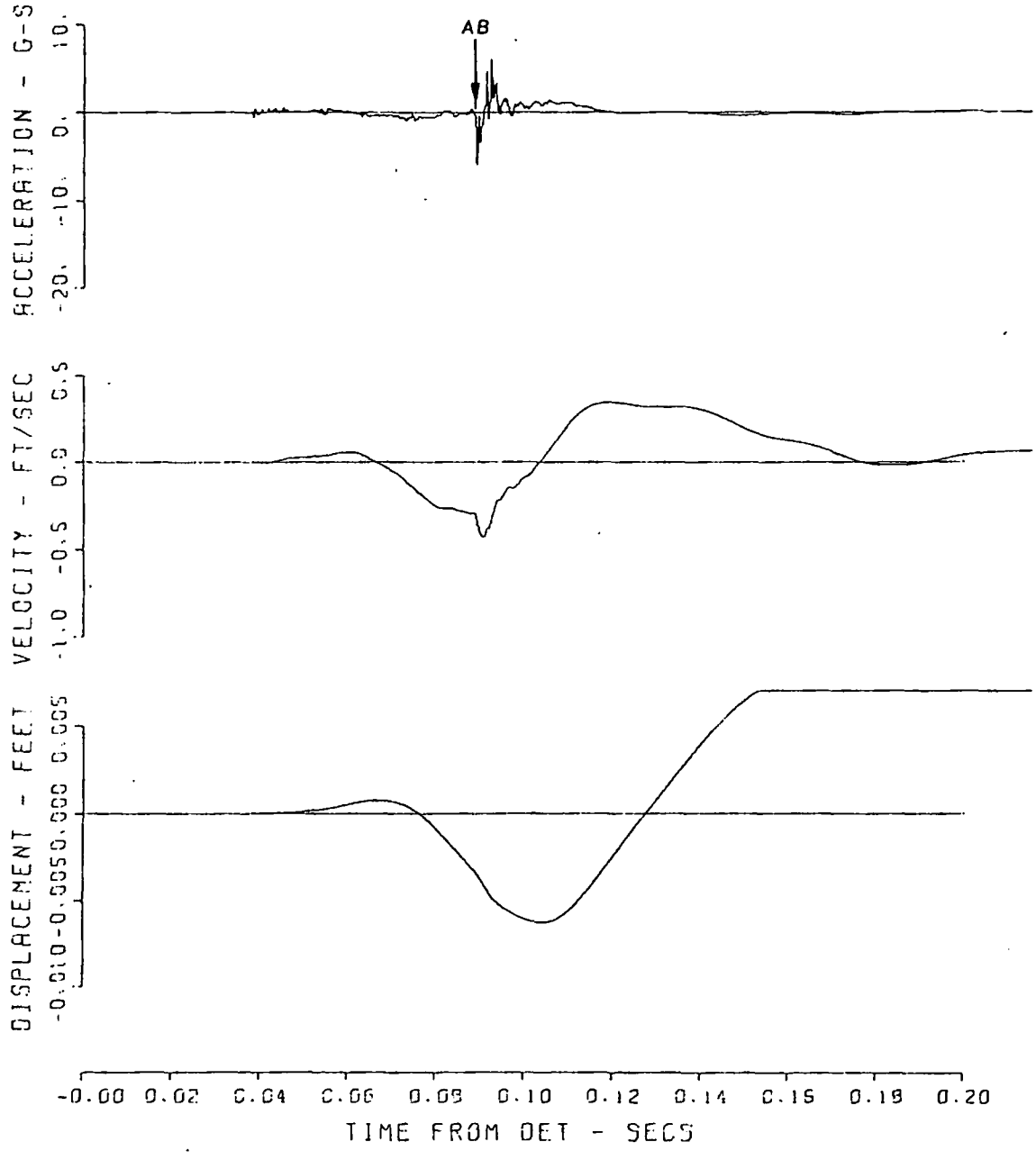

Figure A.23 Gage 400-2-AV.

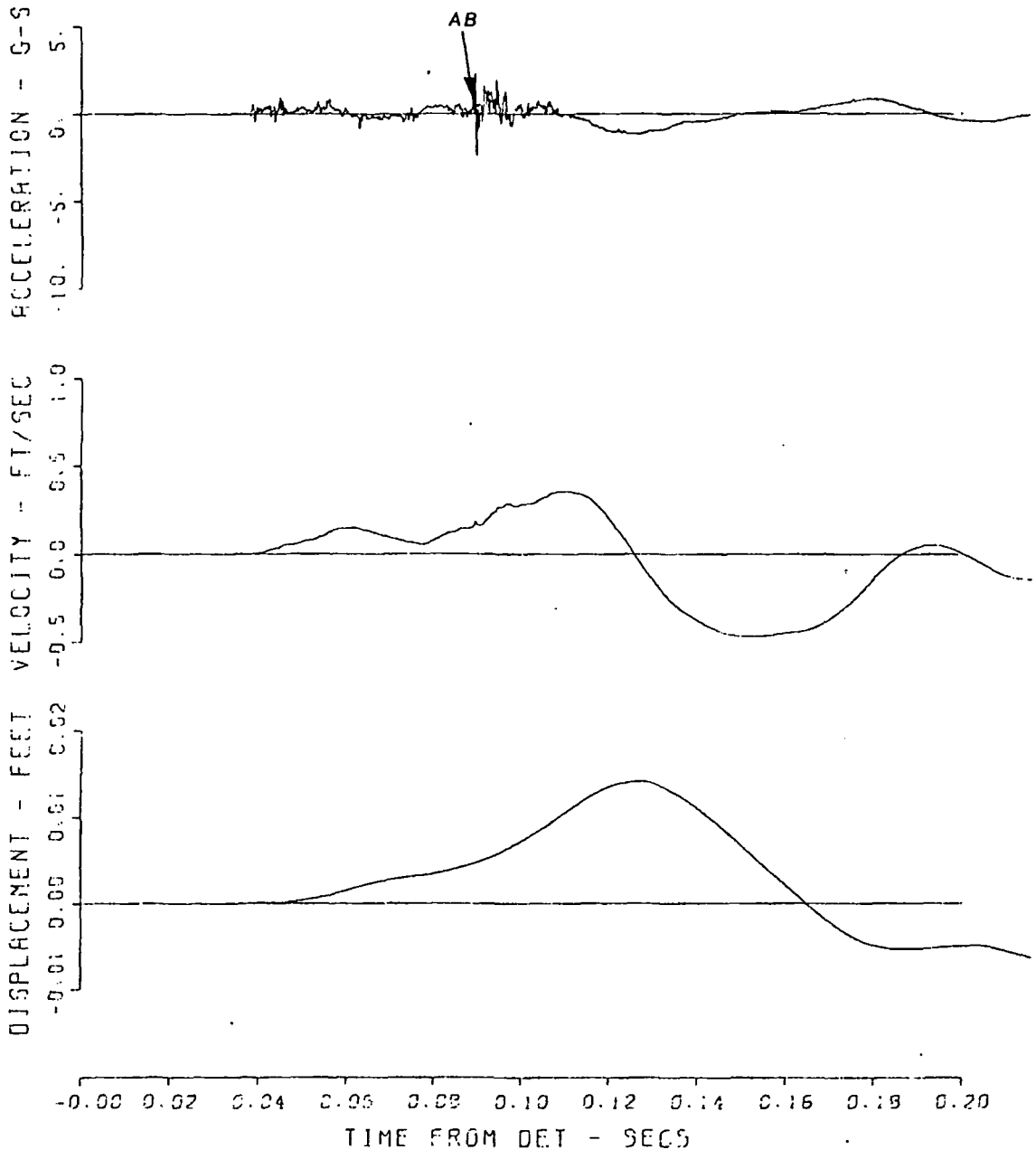

Figure A.24 Gage 400-2-AH.

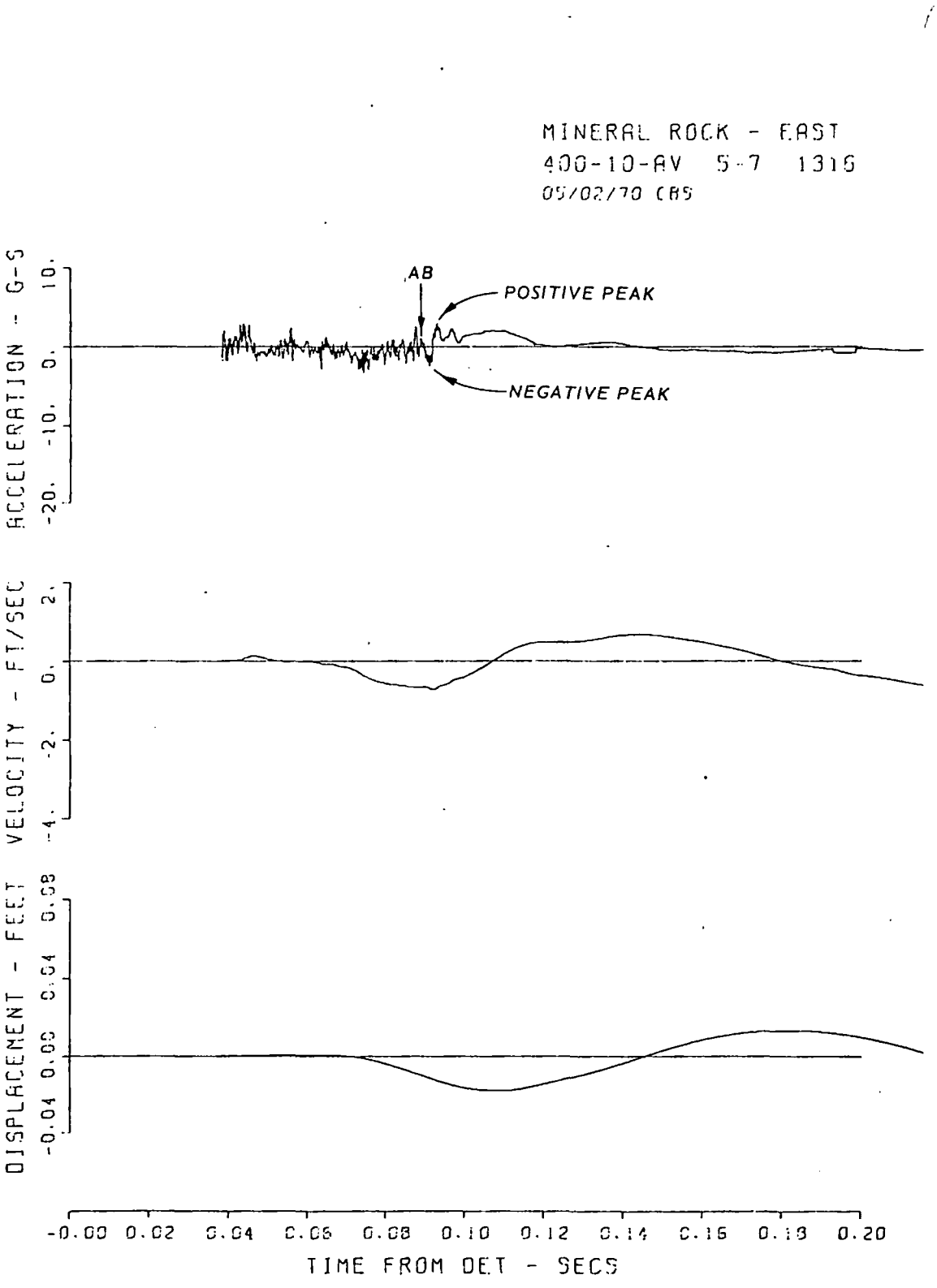

Figure A.25 Gage 400-10-AV.

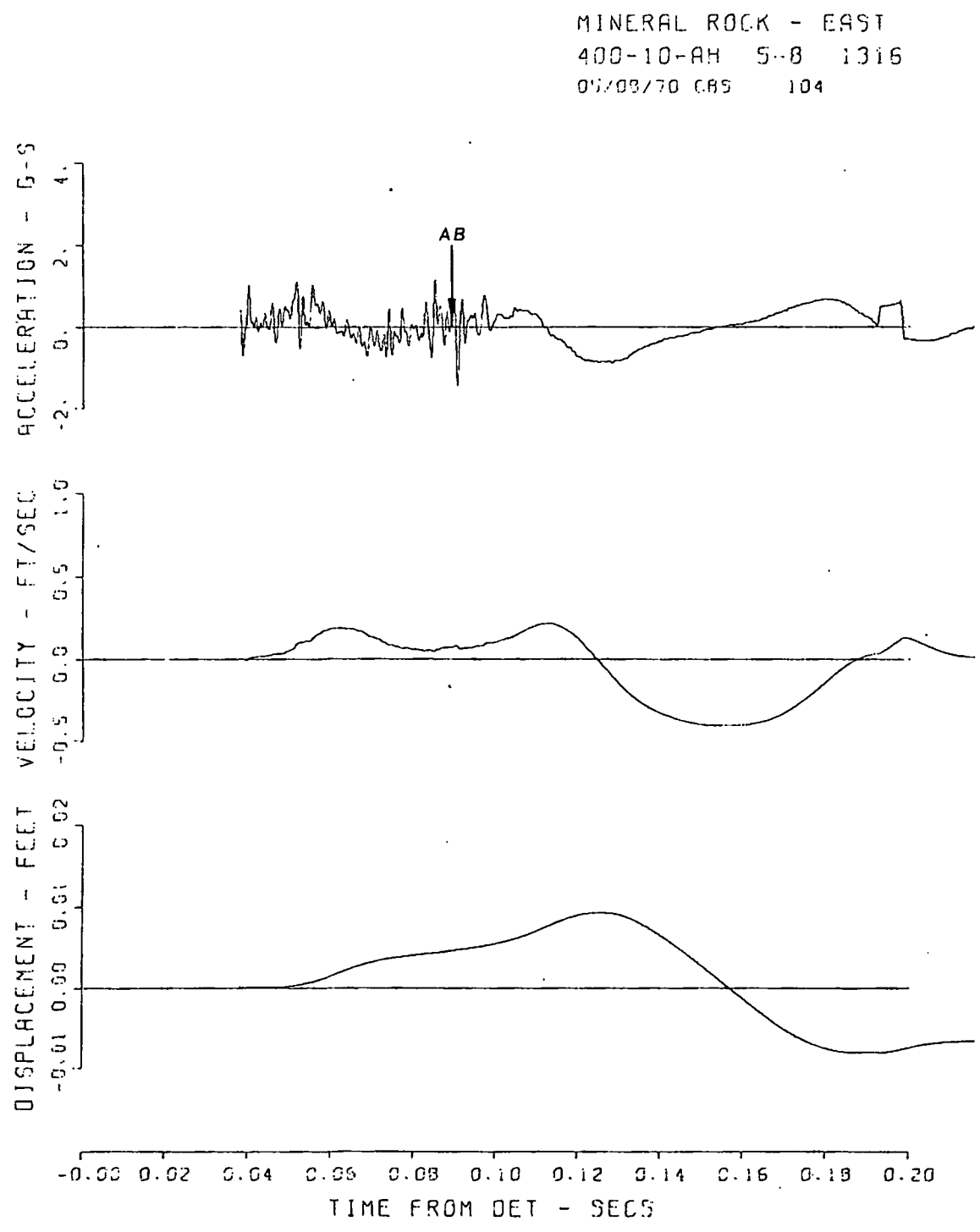

Figure A.26 Gage 400-10-AH.

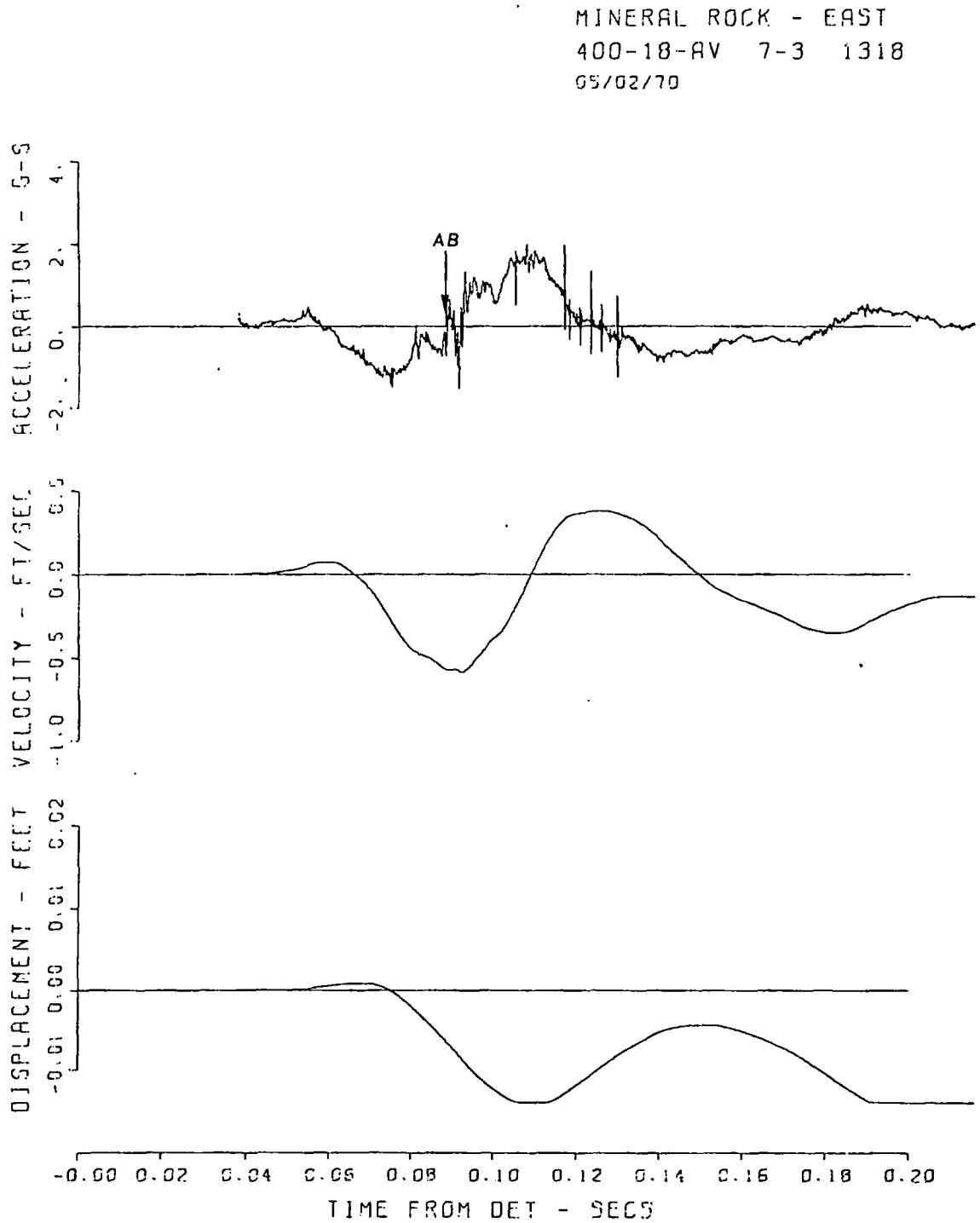

Figure A.27 Gage 400-18-AV.

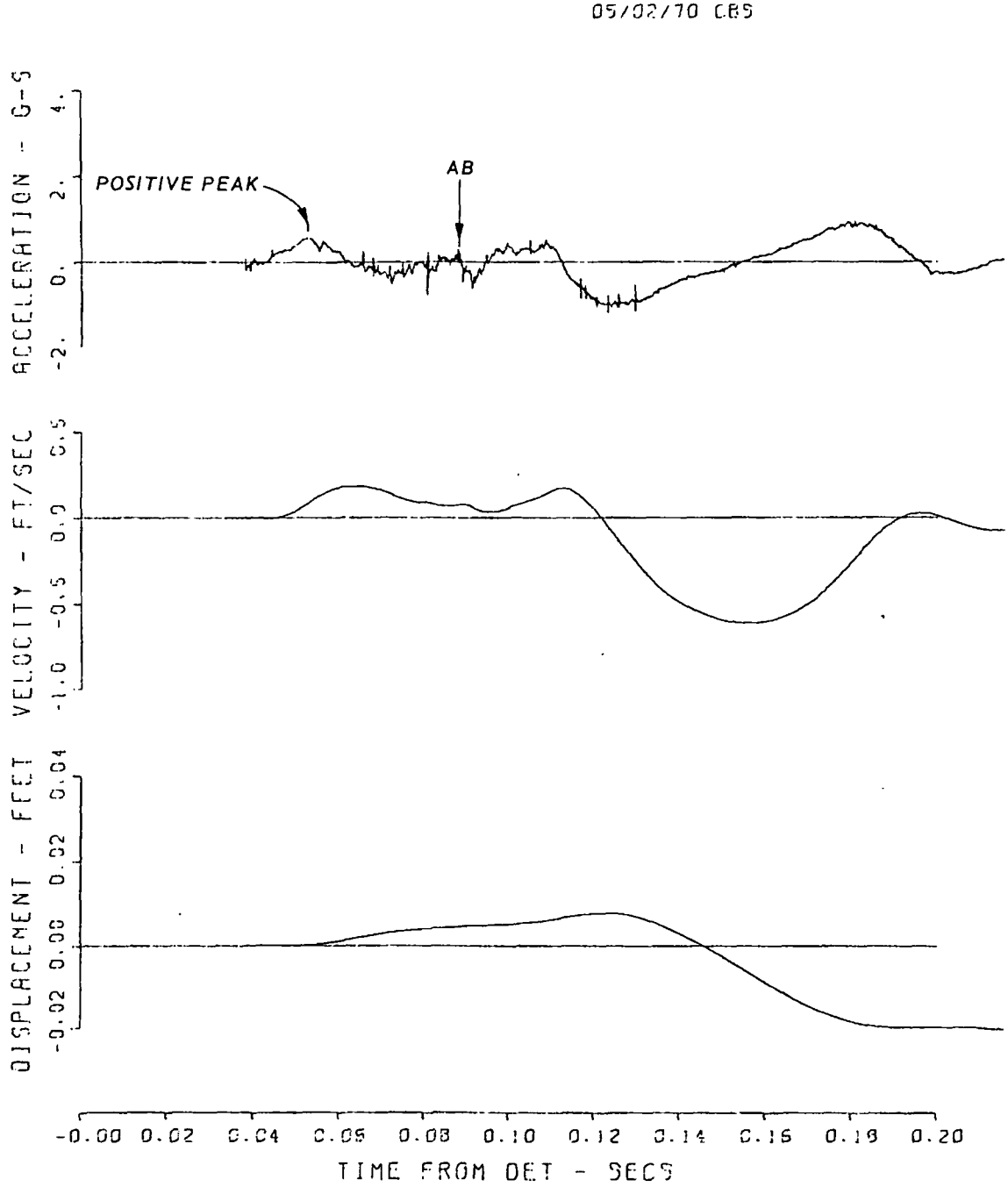

Figure A.28 Gage 400-18-AH.

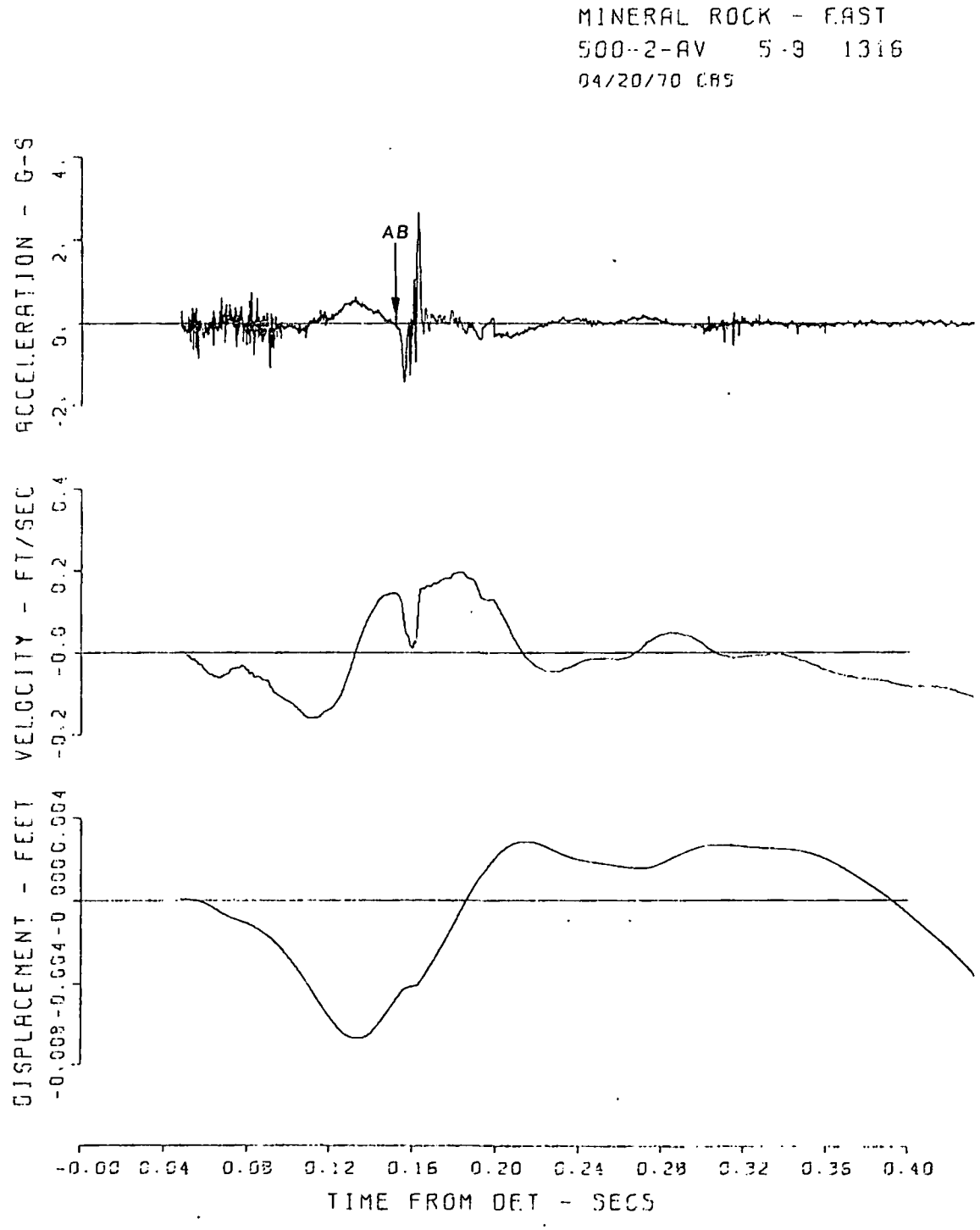

Figure A.29 Gage 500-2-AV.

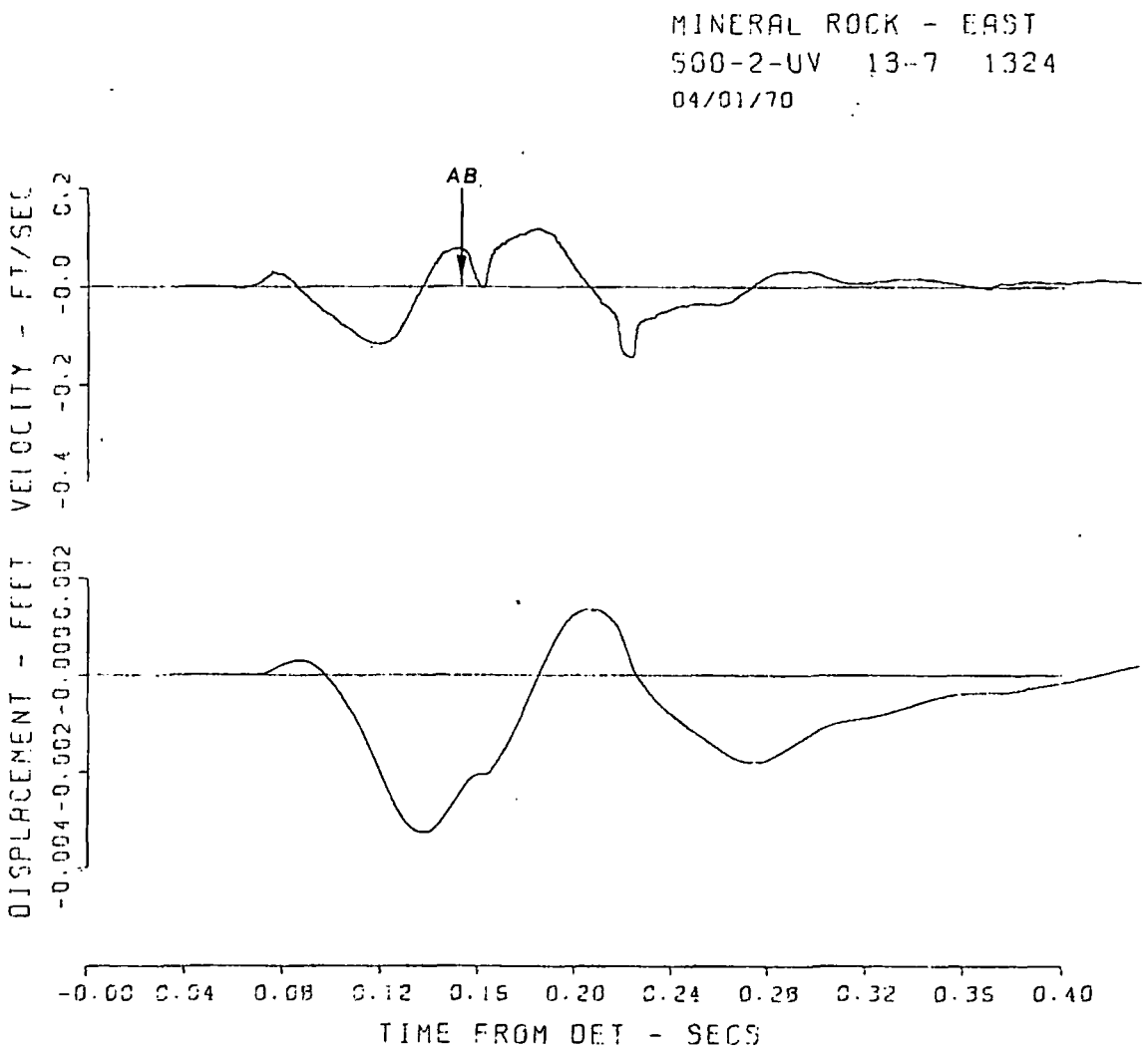

Figure A.30 Gage 500-2-UV.

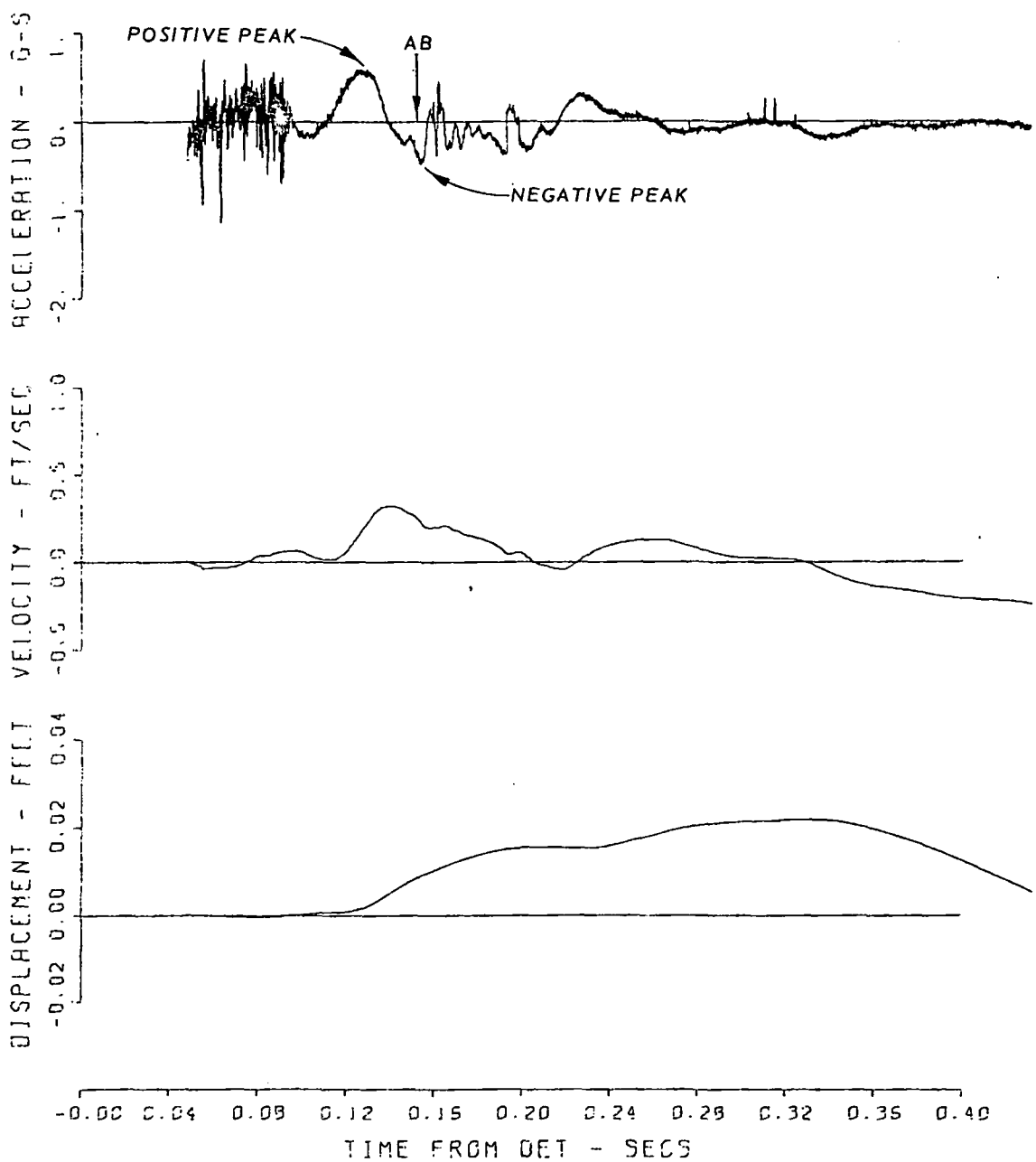

Figure A.31 Gage 500-2-AH.

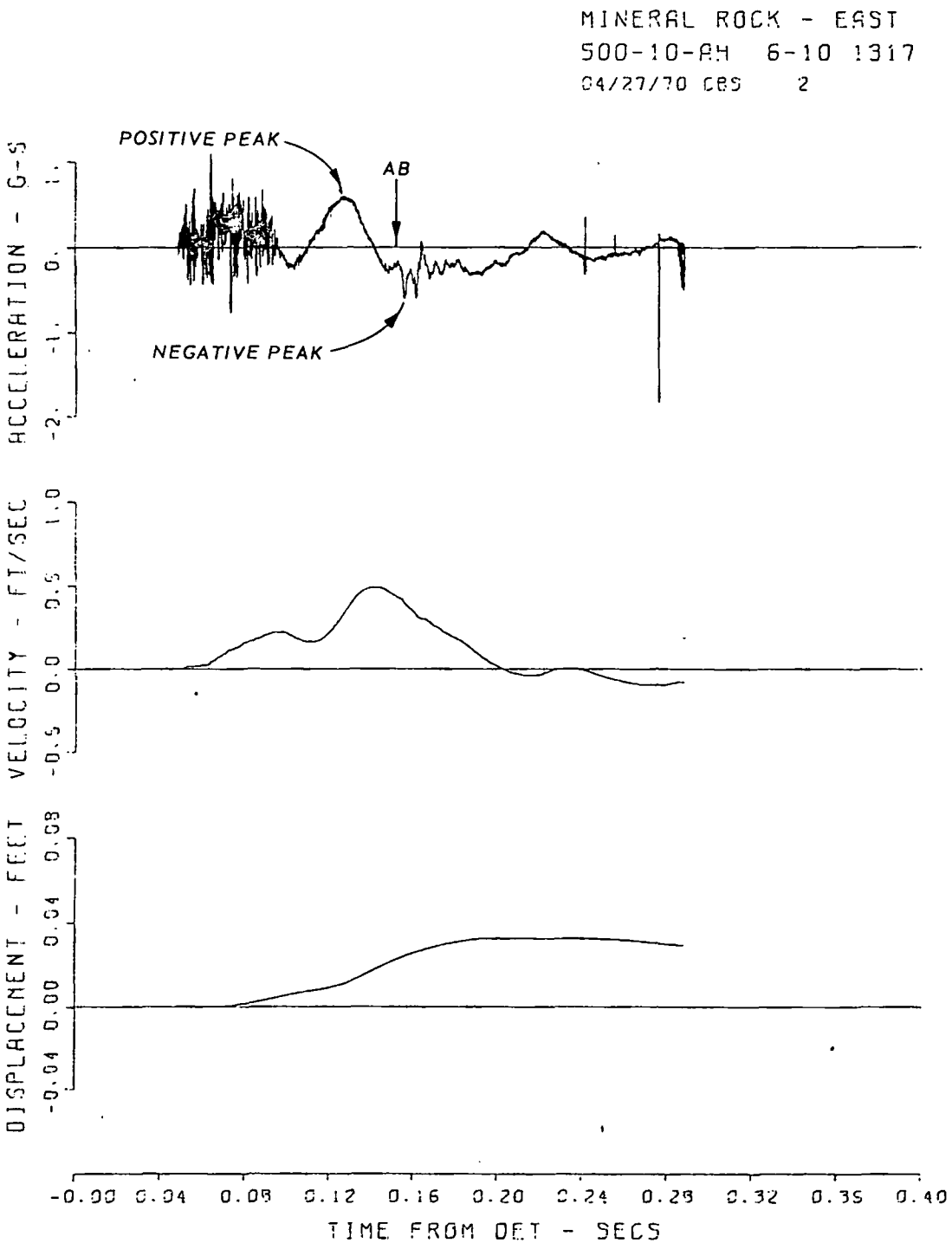

Figure A.32 Gage 500-10-AH.

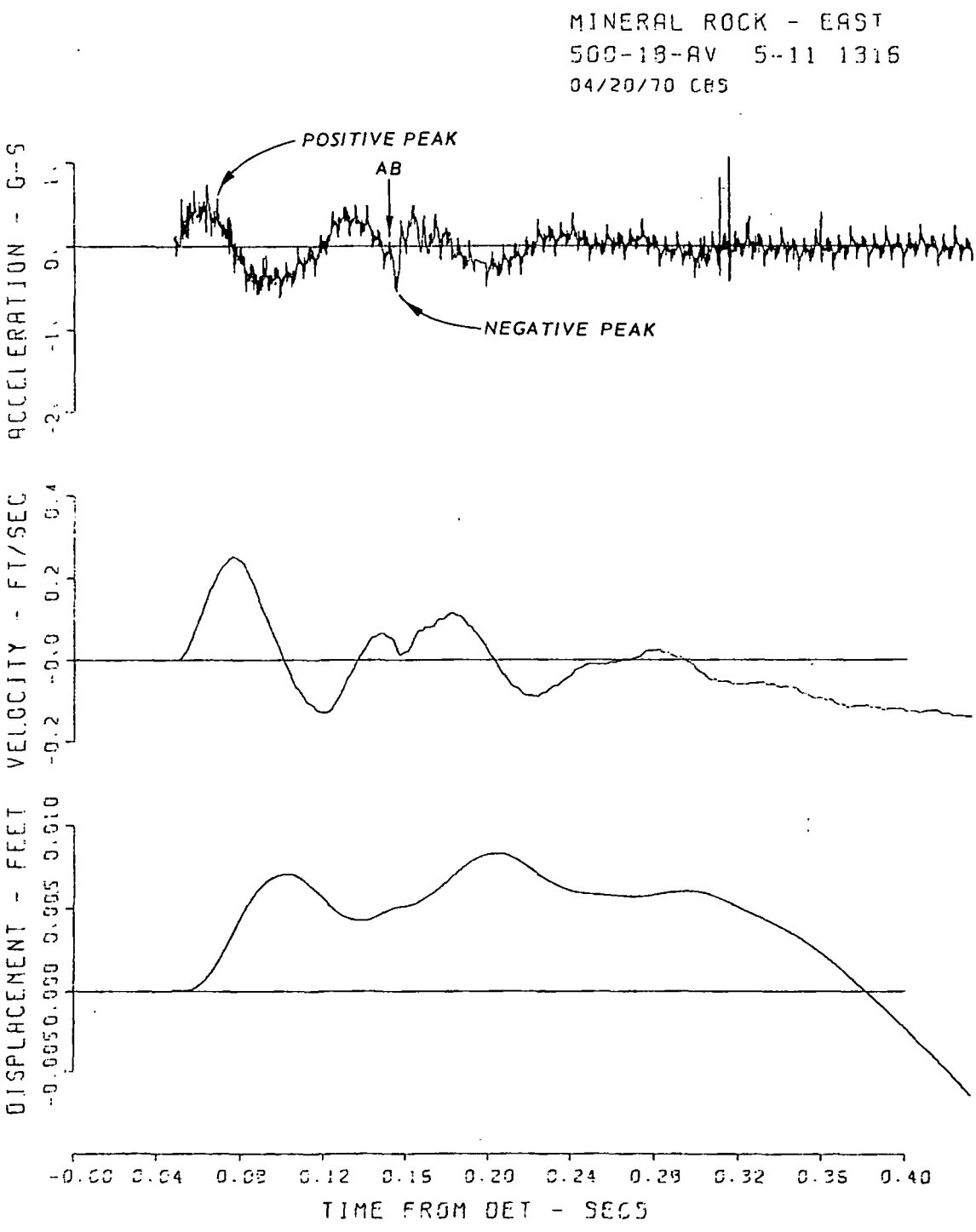

Figure A.33 Gage 500-18-AV.

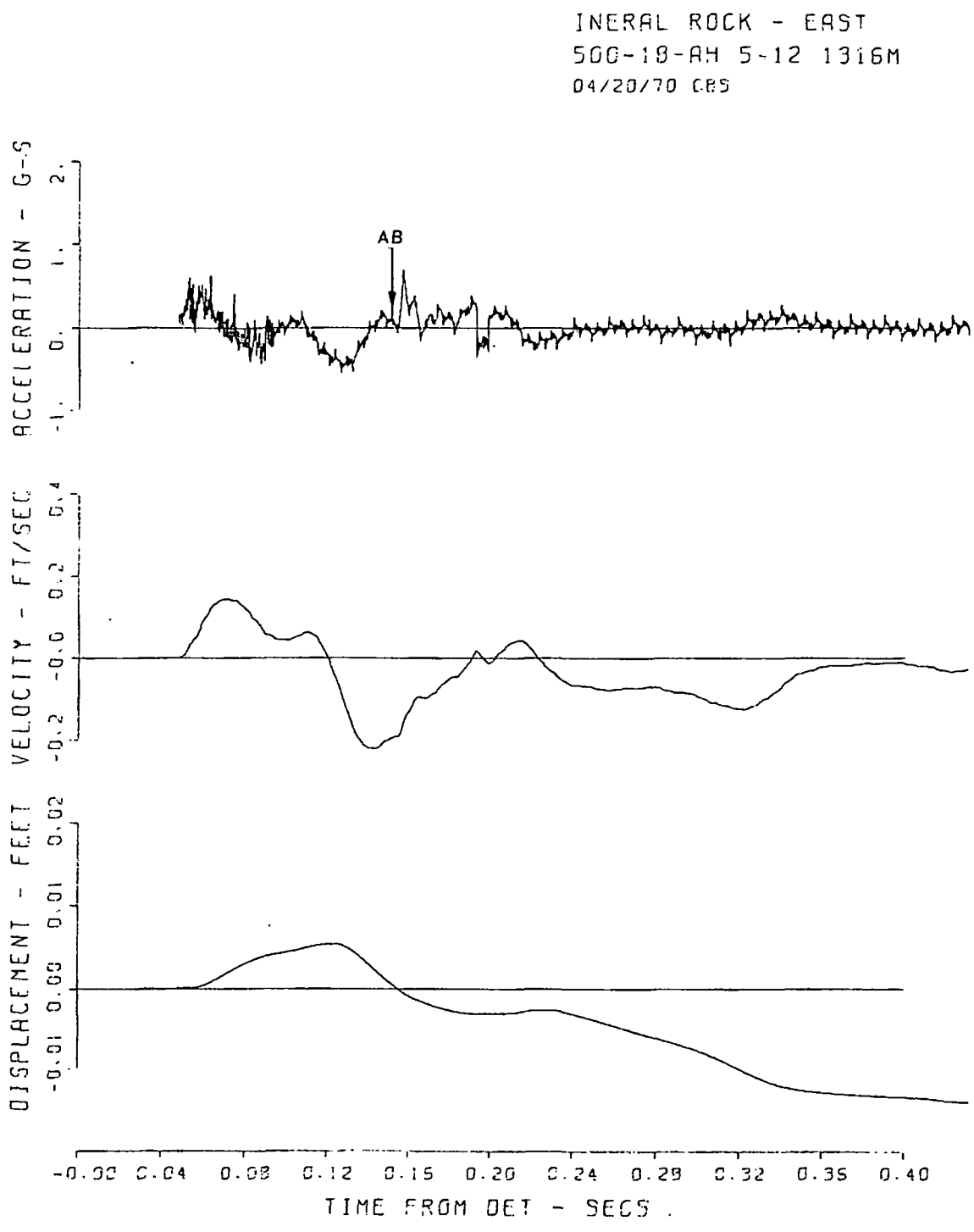

Figure A.34 Gage 500-18-AH.

REFERENCES

1. C. E. Joachim; "Mine Shaft Series, Events Mine Under and Mine Ore: Subtask SS222, Ground Motion and Stress Measurements"; Technical Report N-72-1, January 1972, U. S. Army Engineer Waterways Experiment Station, CE, Vicksburg, Mississippi; Unclassified.

2. L. F. Ingram and R. C. Holmes; "Mine Shaft Series, Events Mineral Lode and Mineral Rock; Technical, Administrative, and Operational Plan"; DASIAC Special Report No. 97, July 1969; Defense Atomic Support Agency, DASA Information and Analysis Center, Santa Barbara, California; Unclassified.

3. K. L. Saucier; "Properties of Cedar City Tonalite"; Miscellaneous Paper C-69-9, June 1969; U. S. Army Engineer Waterways Experiment Station, CE, Vicksburg, Mississippi; Unclassified.

4. S. J. Shand; "Eruptive Rocks; Their Genesis, Compaction, Classification, and Their Relation to Ore-Deposits, with a Chapter on Meteorites"; Third Edition, 1947; John Wiley and Sons, New York, N. Y.; Unclassified.

5. C. R. Kolb and others; "Operation Mine Shaft, Geological Investigation of the Mine Shaft Sites, Cedar City, Utah"; MS-2170, Miscellaneous Paper S-70-22, August 1970; U. S. Army Engineer Waterways Experiment Station, CE, Vicksburg, Mississippi; Unclassified.

6. D. W. Murrell; "Operation Mine Shaft, Event Mineral Rock; Ground Motions from a 100-Ton TNT Detonation over Granite"; MS-2160 (in preparation); U. S. Army Engineer Waterways Experiment Station, CE, Vicksburg, Mississippi; Unclassified.

7. J. W. Wistor; "An Extended Range Velocity Gage for Measurements in High Shock Environments"; Sandia Corporation Memorandum; Sandia Corporation, Albuquerque, New Mexico; Unclassified.

8. D. W. Murrell; "Distant Plain Events 6 and 1A, Project 3.02A, Earth Motion and Stress Measurements"; Technical Report N-70-14, September 1970; U. S. Army Engineer Waterways Experiment Station, CE, Vicksburg, Mississippi; Unclassified.

9. G. D. Teel; "Airblast Measurements from a 100-Ton TNT Detonation over Granite--Mineral Rock Event, Mine Shaft Series"; BRL Report No. 1502, October 1970; U. S. Proving Ground, Ballistic Research Laboratories, Aberdeen Proving Ground, Maryland; Unclassified.

DISTRIBUTION LIST FOR TECHNICAL REPORT N-72-6

Address	No. of Copies
Army	
Division Engineer, U. S. Army Engineer Division, Huntsville, P. O. Box 1600, West Station, Huntsville, Ala. 35807 ATTN: HNDED-R, Mr. Michael Dembo	50
Commanding General, U. S. Army SAFEGUARD System Command, P. O. Box 1500, West Station, Huntsville, Ala. 35807 ATTN: SSC-DH, Mr. Henry L. Solomonson SSC-H, Mr. Wallace Kirkpatrick	3 6
Commanding General, U. S. Army SAFEGUARD System Evaluation Agency, White Sands Missile Range, N. Mex. 88002 ATTN: SSEA-PBB	1
District Engineer, U. S. Army Engineer District, Omaha, 215 North 17th St., Omaha, Nebr. 68102 ATTN: MROED-SE, Mr. C. L. Hipp	1
Commanding General, U. S. Army Materiel Command, Washington, D. C. 20315 ATTN: AMCRD-BN	1
Office of the Secretary of the Army, Director of Civil Defense, Washington, D. C. 20310 ATTN: Mr. George Sisson	1
Commanding Officer, U. S. Army Combat Developments Command, Nuclear Agency, Fort Bliss, Tex. 79916	1
Director, U. S. Army Ballistic Research Laboratories, Aberdeen Proving Ground, Md. 21005 ATTN: Mr. George D. Teel Mr. J. Keefer Mr. J. Meszaros Mr. J. Mester	1 1 1 1
Director, U. S. Army Mobility Equipment R&D Center, Fort Belvoir, Va. 22060 ATTN: Mr. R. Medding Mr. E. Leland	1 1

Address	No. of Copies
Army (Continued)	
Director, U. S. Army Engineer Waterways Experiment Station, Explosive Excavation Research Office, P. O. Box 808, Livermore, Calif. 94550	1
U. S. Army Cold Regions Research and Engineering Laboratories, Hanover, N. H. 03725	
ATTN: Mr. Ted Vogel	1
Mr. North Smith	1
Chief of Engineers, Department of the Army, Washington, D. C. 20315	
ATTN: LTC Larry Russell, DAEN-MER-D	1
Mr. George O. Fellers	1
Mr. M. L. Martin, DAEN-MCE-D	1
Mr. G. W. Prescott, DAEN-CWE-G	1
Mr. C. F. Corns, DAEN-CWE-D	1
Dr. Larry Schindler, DAEN-MCE-D	4
Director, U. S. Army Construction Engineering Research Laboratory, P. O. Box 4005, Champaign, Ill. 61820	1
ATTN: Mr. John Healy	
U. S. Army Research Office, Arlington, Va.	
ATTN: Mr. Merrill Kreipke	1
Dr. V. Zadnick	1
U. S. Army Advanced Ballistic Missile Defense Agency, 1320 Wilson Blvd and Ft. Meyer Dr., Arlington, Va. 22209	2
ATTN: LTC Marvin Kortum	
U. S. Army Engineer Division, Missouri River, P. O. Box 103, Downtown Station, Omaha, Nebr. 68101	1
ATTN: Mr. E. G. Erikson	
Safeguard Systems Manager, Safeguard Systems Office, 1320 Wilson Blvd., Arlington, Va. 22209	1
ATTN: Dr. John Shea	
Navy	
Commander, Naval Ordnance Laboratory, White Oak, Silver Springs, Md. 20910	
ATTN: Mr. J. Petes	1
Dr. L. Rudlin	1

Address	No. of Copies
Navy (Continued)	
Commander, U. S. Naval Weapons Center, China Lake, Calif. 93555 ATTN: Mr. Hal Richey	1
Commanding Officer and Director, Naval Ship Research and Development Center, Washington, D. C. 20007 ATTN: Mr. E. Habib	1
Commanding Officer and Director, Naval Civil Engineering Laboratory, Port Hueneme, Calif. 93041	
ATTN: Dr. W. Shaw	1
Mr. J. Allgood	1
Mr. R. Seabold	1
Air Force	
Commander, Air Force Weapons Laboratory, Kirtland Air Force Base, N. Mex. 87117	
ATTN: WLIL	2
Dr. M. A. Plamondon	1
CPT Don Gage	1
Mr. R. Henney	1
Dr. Henry F. Cooper, Jr.	1
Commander, Air Force Rome Air Development Center, Griffiss AFB, N. Y. 13440 ATTN: Mr. R. Mair	1
Lookout Mountain Air Force Station, 8935 Wonderland Ave., Los Angeles, Calif. 90041 ATTN: Mr. K. Hackman	1
Space and Missile Systems Organization, Air Force Unit Post Office, Los Angeles, Calif. 90045	
ATTN: CPT M. Heimbecker	2
COL J. O. Putnam	2
COL W. T. Winter	2
LTC Jack Cahoon	2
Strategic Air Command, Offutt AFB, Nebr. 68113 ATTN: COL Conklin	1
Commanding General, White Sands Missile Range, N. Mex. 88002 ATTN: STEWS-TE-NT (Mr. J. Gorman)	1
Headquarters, U. S. Air Force, Washington, D. C. 20330 ATTN: AFRDQSN	1

Address	No. of Copies
AEC	
Asst Gen Mgr for Military Application, Atomic Energy Commission, Washington, D. C. 20545	3
Division of Technical Information Extension, U. S. Atomic Energy Commission, P. O. Box 12, Oak Ridge, Tenn. 37830	2
Director, Lawrence Radiation Laboratory, P. O. Box 808, Livermore, Calif. 94550 ATTN: Technical Library	10
Director, Los Alamos Scientific Laboratory, P. O. Box 1663, Los Alamos, N. Mex. 87544 ATTN: Document Control	2
Sandia Corporation, P. O. Box 5800, Kirtland AFB, N. Mex. 87115	
ATTN: Mr. A. W. Snyder (Org 5220)	1
Document Library	6
Mr. J. Reed	1
Dr. M. Merritt	1
Mr. W. R. Perret	1
Sandia Corporation, Livermore Laboratory, P. O. Box 969, Livermore, Calif. 94550 ATTN: Document Control FOR: Technical Library	3
Other Government	
Center of Astrogeology, 601 East Cedar Ave., Flagstaff, Ariz. 86001 ATTN: Dr. David Roddy	1
Denver Mining Research Center, Bldg 20, Denver Federal Center, Denver, Colo. 80228	
ATTN: Dr. L. A. Obert	1
Mr. Wilbur Duvall	1
Mr. Harry Nicholls	1
DOD	
Assistant to the Secretary of Defense (Atomic Energy), Washington, D. C. 20305 ATTN: LTC Luther B. Aull III	1
Commander, DNA, Kirtland AFB, N. Mex. 87115	
ATTN: ECDV	1
FCTG-5	1

Address	No. of Copies
DOD (Continued)	
Commander, Test Command, DNA, Kirtland AFB, N. Mex. 87115	
ATTN: TCDT-B	15
TCDA-T	1
Director, DNA, Washington, D. C. 20305	
ATTN: APSI	1
APTL	1
SPSS	5
Administrator, Defense Documentation Center, Cameron Station, Bldg 5, Alexandria, Va 22314 ATTN: Document Control	12
Director, Weapons Systems Evaluation Group, Washington, D. C. 20305	1
Director, Advanced Research Projects Agency, Washington, D. C. 20301 ATTN: Dr. Stan Ruby	1
Armed Services Explosives Safety Board, Nassif Bldg, Washington, D. C. 20315 ATTN: Mr. Russell Perkins	1
Defense Intelligence Agency, Washington, D. C. 20301	
ATTN: Mr. A. W. Holt, DIAAP-8B	1
DIAST-3	1
Director of Defense Research and Engineering, Washington, D. C. 20301	
ATTN: Asst. Director (Strategic Weapons)	1
Asst. Director (Nuclear Programs)	2
DOD Contractors	
Physics International Company, 2700 Merced St., San Leandro, Calif. 94557	
ATTN: Mr. F. M. Sauer	1
Mr. Joe Kochly	1
Dr. C. Godfrey	1
TRW Systems, Inc., One Space Park, Redondo Beach, Calif. 90278 ATTN: Mr. F. Galbraith	1

Address	No. of Copies
DOD Contractors (Continued)	
General Electric Company, TEMPO Center for Advanced Studies, 816 State St., Santa Barbara, Calif. 93102	
ATTN: DASIAC, Mr. Warren Chan	1
The Boeing Company, P. O. Box 3707, Seattle, Wash. 98124	
ATTN: Mr. G. D. Jones	1
Mr. H. Leistner	1
Kaman Aircraft Corporation, Nuclear Division, 1700 Garden of the Gods Road, Colorado Springs, Colo. 80907	
ATTN: Mr. D. Sachs	1
Mr. Dale Seacrist	1
Mr. Paul Ellis	1
University of Denver, Colorado Seminary, Denver Research Institute, University Park, Denver, Colo. 80210	
ATTN: Mr. J. Wisotski	1
URS Corporation, 1811 Trousdale Dr., Burlingame, Calif. 94010	
ATTN: Mr. K. Kaplan	1
Chief Superintendent, Defence Research Establishment, Suffield, Ralston, Alberta, Canada	2
IIT Research Institute, 10 West 35th Street, Chicago, Ill. 60616	
ATTN: Dr. Eliot Raisen	1
Dr. Ted Shiffman	1
Mr. Don Anderson	
Aerospace Corporation, P. O. Box 1308, San Bernardino, Calif. 92402	
ATTN: Mr. Sam Italia	1
Mr. Craig Smith	1
Dr. Mason Watson	1
TRW Systems Group, San Bernardino Operations, 600 E. Mill St., Bldg 527, Room 710, San Bernardino, Calif. 92402	
ATTN: Mr. Fred Pieper	1
Mr. J. Carpenter	1
Dr. Lieberman	1
Agbabian-Jacobsen Association, 8939 S. Sepulveda Blvd, Los Angeles, Calif. 90045	
ATTN: Dr. Jim Workman	1
Mr. Ray Anderson	1

Address	No. of Copies

DOD Contractors (Continued)

Applied Theory, Inc., 1010 Westward Boulevard, Los Angeles, Calif. 90024 ATTN: Dr. J. J. Trullio	1
Dr. Nathan M. Newmark, 1114 Civil Engineering Bldg, University of Illinois, Urbana, Ill. 61801	1
The Ralph M. Parsons Co., 617 West Seventh St., Los Angeles, Calif. 90017 ATTN: Mr. William C. Starrett	1
The Bechtel Corporation, P. O. Box 58587, Vernon Branch, Los Angeles, Calif. 90058 ATTN: Mr. John D. Duffin	1
Black and Veatch, 1500 Meadowlake Parkway, Kansas City, Mo. 64114 ATTN: Mr. Harry Callahan	1
The Boeing Company, P. O. Box 1470, Huntsville, Ala. 35807 ATTN: Mr. Don Schindler	1
The Boeing Company, P. O. Box 3999, Seattle, Wash. 98124 ATTN: Mr. P. A. Gomes	1
University of Illinois, Urbana Campus, 112 English Bldg, Urbana, Ill. 61801 ATTN: Dr. Alfred J. Hendron	1
Paul Weidlinger Associates, Consulting Engineers, 110 East 59th St., New York, N. Y. 10022 ATTN: Dr. M. Baron	1
The Rand Corporation, 1700 Main St., Santa Monica, Calif. 90406 ATTN: Dr. C. C. Mow	1
Bell Telephone Laboratories, Inc., Whippany Road, Whippany, N. J. 07981 ATTN: Mr. Lou Peralta	1

Unclassified
Security Classification

DOCUMENT CONTROL DATA - R & D

(Security classification of title, body of abstract and indexing annotation must be entered when the overall report is classified)

1. ORIGINATING ACTIVITY (Corporate author)	2a. REPORT SECURITY CLASSIFICATION
U. S. Army Engineer Waterways Experiment Station Vicksburg, Miss.	Unclassified
	2b. GROUP

3. REPORT TITLE

OPERATION MINE SHAFT, MINERAL ROCK EVENT, FAR-OUT GROUND MOTIONS FROM A 100-TON DETONATION OVER GRANITE

4. DESCRIPTIVE NOTES *(Type of report and inclusive dates)*

Final report

5. AUTHOR(S) *(First name, middle initial, last name)*

Donald W. Murrell

6. REPORT DATE	7a. TOTAL NO. OF PAGES	7b. NO. OF REFS
April 1972	89	9

8a. CONTRACT OR GRANT NO.	9a. ORIGINATOR'S REPORT NUMBER(S)
b. PROJECT NO. SX30223	Technical Report H-72-6
c.	9b. OTHER REPORT NO(S) *(Any other numbers that may be assigned this report)*
d.	

10. DISTRIBUTION STATEMENT

Approved for public release; distribution unlimited.

11. SUPPLEMENTARY NOTES	12. SPONSORING MILITARY ACTIVITY
	U. S. Army Engineer Division Huntsville, Alabama

13. ABSTRACT The objectives of this study were to measure all ground motions in the outrunning region produced by the Mineral Rock Event of Operation Mine Shaft. The Mineral Rock Event was a duplication of the Mine Ore Event of the same series, and was a 100-ton sphere of TNT placed with the center of gravity 0.9 charge radius (about 7.2 feet) above the ground surface. Accelerometers and velocity gages were installed from 200 to 500 feet from ground zero at depths of 2, 10, and 18 feet. Time histories of all successfully recorded gages are presented in Appendix A along with integrals of each record. The outrunning acceleration data were partially obscured by a cable noise problem. This noise was blast overpressure-induced and unfortunately was present during the significant outrunning motion onset, i.e., before airblast arrival at the gage locations. Although these data are limited, they are discussed along with the outrunning velocity data. Airblast-induced motions are treated in detail. Vertical airblast-induced accelerations were found to attenuate rapidly with distance and depth from the maximum downward acceleration of 32 g's at the 200-foot range and 2-foot depth. These accelerations were correlated with overpressure, and, for the 2-foot depth, acceleration-to-overpressure ratios averaged 0.2 g/psi, which is considerably less than for a similar detonation over soil. Vertical particle velocities also attenuated with distance and depth from the maximum value of 1.3 ft/sec at the 200-foot range and 2-foot depth. Horizontal velocities followed much the same pattern, with a peak value of 2 ft/sec at the same location. Outrunning motion was noted on all horizontal velocity gage records. For the vertical component, outrunning motion was not apparent at the 250-foot range, but was of significant magnitude at the 500-foot range. Vertical downward displacements of a high confidence level were limited to the 250-foot range and were found to be 0.0060 to 0.0075 foot. Horizontal displacements were successfully computed from acceleration and velocity records, and at the 250-foot range were three to four times as large as the vertical displacements.

DD FORM 1 NOV 1473 REPLACES DD FORM 1473, 1 JAN 64, WHICH IS OBSOLETE FOR ARMY USE.

Unclassified
Security Classification

14. KEY WORDS	LINK A		LINK B		LINK C	
	ROLE	WT	ROLE	WT	ROLE	WT
Detonation						
Explosion effects						
Granite						
Ground motion						
Mine Shaft (Series)						
Mineral Rock (Event)						

OPTIMUM NUMBER OF SPONTANEOUS-EVAPORATION STAGES WHEN LEACHING BAUXITES BY THE BAYER PROCESS

UDC 669.712.1

N. S. Mal'ts

Optimizing the production of alumina by the Bayer process depends on the apparatus and technology used to leach bauxites.

The optimum leaching process has to include facilities for varying the principal technological parameters for producing alumina by the Bayer process (concentrations and caustic modulus values of the recycled and aluminate solutions, the evaporated residue factor, and the number of red-mud washing stages, etc.) with a view to achieving the greatest possible technical and economic effects.

We know that the reliability of optimization calculations is governed by the correct selection, on a sound economic basis, of a quantitative evaluation of the quality of the employed solution (the optimality criterion), as well as by sufficiently complete mathematical description of the link between this criterion and the technology and equipment used in production, and the interconnection among these parameters.

It was shown earlier [1] that the requirements for the optimality criterion of the technological parameters used in the Bayer process are best satisfied by a complete economic index; this would be the sum of the heat and power consumed and the alkali consumed to compensate for its losses in the liquid phase of the discarded slurry. The fact that a sound basis was used to select this criterion of optimality for the principal technological parameters is proved by analyzing the components of the costs involved in producing alumina by the Bayer process. This analysis shows that the apparatus and technology are most effectively improved through effecting reductions in consumptions of heat, power, and soluble alkali, while retaining a high degree of alumina extraction from bauxite.

It is easy to prove that the specific outlays -- the sum of which was used as the optimality criterion for technological parameters of the Bayer process as a whole -- must also be included in the composite economic index for evaluating the optimality of the apparatus and the technology selected to leach bauxites.

Actually, the concentration of the recycled solution, and thus the concentration and caustic modulus of the autoclave slurry, are governed by the temperature of the leaching process; they depend on the system through which heat is regenerated from the leaching slurry and the method used to heat the slurry to the reaction temperature. The same technological parameters, coupled with the concentrations of the aluminate and the weak solution before evaporation (as well as its caustic modulus) in turn govern the heat and energy losses in the Bayer cycle, as well as consumptions for compensating losses of dissolved alkali in the discarded slurry.

The possible vaporization factor for the recycled solution (governed by its concentration, and accordingly the depression temperature) and the washing of the red mud depend on these parameters.

When the optimum apparatus and technology for leaching bauxite are selected, however, the optimality criterion cannot be limited solely by the sum of heat and energy consumptions as well as the expenditures made to compensate for alkali losses, since if this were so there would be no allowance made for capital outlays. Raising the leaching temperature and improving the system of regenerating heat from the leached slurry and heating the raw slurry call for considerable increases in capital outlay and in corresponding operating costs.

We therefore adopted the index of the sum C of reduced outlay figures per ton of bauxite processed as the optimality criterion for selecting the apparatus and technology to leach bauxites; this index includes the sum $C_1 + C_2$ of the heat and power consumption, the expenditures made to compensate for alkali losses with the liquid phase of the discarded slurry (C_3), and the normal expenditures in capital outlay C_4:

$$C = C_1 + C_2 + C_3 + C_4 \qquad (1)$$

Components $C_1 + C_2$ is the sum ΣQ of heat consumption in the Bayer cycle when leaching bauxite (Q_1) and vaporization of the recycled solution (Q_2), as related to the total amount G_b of processed bauxite, i.e.,

$$C_1 + C_2 = \frac{\Sigma Q}{G_b} \sigma_s, \qquad (2)$$

where σ_s - is the nominal cost per gcal steam.

Component C represents the losses by weight L_N of alkali (per ton of processed bauxite) from the liquid phase of the discarded slurry:

$$C_3 = L_N \sigma_N \qquad (3)$$

where σ_N - is the cost per ton of alkali in conversion to Na_2O.

Component C_4 allows for normal capital outlays per ton of processed bauxite:

$$C_4 = \frac{C_a \cdot V_{sl} \cdot 10^6}{8760 \cdot 160 \cdot 0.8} 0.31, \quad (4)$$

where C_a - is the nominal capital outlay corresponding to a single set of autoclaves with a productivity of 160 m^3/hr slurry, in million rubles; V_{sl} - the volume of fresh slurry, in m^3/t bauxites; 0.8 - the coefficient of equipment utilization; 0.31 - is a total coefficient, allowing for normal capital outlays (depreciation, repairs and maintenance, as well as equipment).

The quantities ΣQ, L_N, V_{sl}, and C_a -- included in Equations [2], [3], and [4] -- are associated with the principal apparatus-technology parameters of production and the bauxite composition by approximate mathematical-model equations.

The basic analytical expression for the link between the ΣQ, the heat consumption in the Bayer cycle, and the alkali losses from the liquid phase of the discarded slurry L_N with the apparatus-technological parameters of production; it is a component part of the mathematical description of the production system, as given in an earlier work [1].

With slight modifications, the mathematical model includes the equations for the link between heat and power consumption and the aqueous balance of the Bayer cycle with the system for the regeneration and utilization of heat during the autoclave leaching, given in an earlier work [2]. The approximate mathematical model also includes the regression equation: $A_{aut} = 1.286 N_{aut} + 0.7673 T_1 - 218.35$, obtained by the linear approximation of the data in Fig. 1 showing the connection between the solubility of Al_2O_3 in diaspore bauxites (SUBR) and the temperature T_1 and concentration N_{aut} in the autoclave-leaching region [3]. Within a leaching temperature of 220-260°C, it is permissible to make a linear approximation of the connection between the operating pressure P in an autoclave and the temperature; this is expressed by the simplified equation:

$$P = 0.5 T_1 - 8.8,$$

in which it is assumed that there is an excess pressure of 5 atm in the autoclaves and a solution depression of 15°C. An equation for the connection between the usefully employed heat from the heated vapor E and the temperature was similarly derived:

$$E = (710 - T_1) \cdot 10^{-3}$$

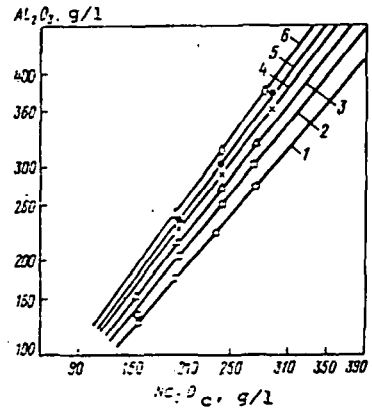

Fig. 1. Composition of equilibrium aluminate solutions in relation to temperature when leaching diaspore bauxites [3], °C: 1 - 200; 2 - 220; 3 - 240; 4 - 260; 5 - 280; 6 - 300.

The equation:

$$C_a = \frac{0.72}{40} P + \frac{0.061}{6} n_1 + \frac{f_1 \cdot 0.016}{200} + \frac{f_2 \cdot 0.016}{200} + \frac{0.2}{6} n_1$$

represents the relationship between the capital outlays C_a for a single autoclave battery with a capacity of 160 m^3/hr slurry to the operating pressure P in the autoclaves (or to T_1), the number of spontaneous-evaporation stages n_1, and the size of the heat-transfer surface necessary to heat the slurry in the spontaneous-evaporation system (f_1) and to heat the slurry with an external heat source (f_2) (the heating is conducted in tubular heat exchanges with a surface area of 200 m^2). The final term in this equation $\frac{0.2 n_1}{6}$ includes the increase in capital investment for the building and other equipment when the number of spontaneous-evaporation stages is increased to over six.

The optimum values for apparatus-technology parameters used in the leaching of bauxites, providing for minimum reduced specific outlays C, were determined with an electronic computer. The Δt values were successively fed into the computer (Δt was varied at 5°C intervals between 30° and 80°C), and the values of C and its components (C_1, C_2, C_3 and C_4) were calculated for the corresponding values of Δt, and the number of spontaneous-evaporation stages n_1.

The values of Δt and n_1, providing the minimum reduced specific outlays C are the optimum values, and are given in the Table for the bauxite-leaching temperatures T_1 under consideration and the varying values for steam costs σ_{st}. The cost of the paid for heat-content of the steam (taking into consideration the recycled condensate, it comes to 0.66 of the steam cost), depending on the region in which plans call for plant placement, may vary between 2 and 8 rubles per kcal.

Effect of Leaching Temperature and Cost of Steam for Heating on the Number of Spontaneous Evaporation Stages

T_l	σ_s	n_1	C_1	C_2	C_3	C_4	C	Δt	N_c
Heating with live steam, $\Delta t' = \Delta t$									
240	2	7	0,355	1,459	0,069	0,891	2,773	45	255
	3	7	0,443	1,824	0,069	0,891	3,680	45	255
	4	9	0,637	2,877	0,065	0,989	4,569	40	252
	5	12	0,705	3,543	0,062	1,135	5,444	35	249
	6	12	0,845	4,251	0,062	1,135	6,294	35	249
	7	16	0,855	4,884	0,059	1,330	7,127	30	246
	8	16	0,977	5,581	0,059	1,330	7,947	30	246
250	2	6	0,415	1,244	0,095	0,987	2,741	50	233
	3	6	0,623	1,866	0,095	0,987	3,571	50	233
	4	10	0,679	2,398	0,084	1,190	4,360	40	227
	5	13	0,849	2,998	0,084	1,199	5,126	35	225
	6	13	0,901	3,528	0,079	1,356	5,864	35	225
	7	17	0,911	4,033	0,075	1,566	6,584	30	222
	8	17	1,041	4,609	0,075	1,566	7,291	30	222
260	2	7	0,444	0,974	0,130	1,207	2,756	50	208
	3	7	0,667	1,462	0,130	1,207	3,466	50	208
	4	11	0,727	1,851	0,114	1,437	4,129	40	203
	5	14	0,804	2,250	0,107	1,608	4,768	35	200
	6	14	0,965	2,700	0,107	1,608	5,379	35	200
	7	17	1,125	3,150	0,107	1,608	5,990	35	200
	8	19	1,115	3,497	0,100	1,886	6,598	30	198
Heating with steam, without dilution, $\Delta t' = 0$									
240	2	4	0,523	1,254	0,073	0,838	2,693	60	222
	3	7	0,588	1,881	0,067	0,984	3,520	45	222
	4	7	0,784	2,508	0,067	0,984	4,343	45	222
240	5	9	0,871	3,135	0,064	1,082	5,152	40	222
	6	9	1,045	3,762	0,064	1,082	5,953	40	222
	7	12	1,067	4,389	0,060	1,229	6,745	35	222
	8	12	1,220	5,016	0,060	1,229	7,525	35	222
250	2	5	0,511	0,998	0,097	1,053	2,659	55	206
	3	6	0,697	1,496	0,091	1,105	3,391	50	206
	4	6	0,930	1,997	0,091	1,105	4,123	50	206
	5	10	0,930	2,496	0,081	1,313	4,820	40	206
	6	10	1,116	2,995	0,081	1,313	5,506	40	206
	7	13	1,139	3,494	0,077	1,470	6,180	35	206
	8	13	1,302	3,994	0,077	1,470	6,842	35	206
260	2	7	0,449	0,706	0,125	1,354	2,683	50	183
	3	7	0,748	1,059	0,125	1,354	3,286	50	183
	4	7	0,997	1,412	0,125	1,354	3,888	50	183
	5	11	0,997	1,764	0,110	1,578	4,449	40	183
	6	11	1,197	2,117	0,110	1,578	5,001	40	183
	7	14	1,222	2,470	0,103	1,746	5,540	35	183
	8	14	1,396	2,823	0,103	1,746	6,068	35	183
Heating with live steam and dilution within temperature of $\Delta t' = 40°C$									
240	2	4	0,478	1,438	0,080	0,766	2,763	60	252
	3	7	0,538	2,158	0,069	0,900	3,664	45	252
	4	7	0,717	2,877	0,069	0,900	4,562	45	252
	5	9	0,797	3,596	0,065	0,989	5,447	40	252
	6	9	0,956	4,315	0,065	0,989	6,325	40	252
	7	12	0,976	5,034	0,062	1,123	7,195	35	252
	8	12	1,105	5,754	0,062	1,123	8,054	35	252
250	2	6	0,424	1,199	0,094	1,009	2,726	50	227
	3	6	0,637	1,799	0,094	1,009	3,538	50	227
	4	6	0,849	2,398	0,094	1,009	4,350	50	227
	5	10	0,849	2,998	0,084	1,199	5,129	40	227
	6	10	1,018	3,597	0,084	1,199	5,898	40	227
	7	13	1,040	4,197	0,079	1,341	6,657	35	227
	8	13	1,188	4,796	0,079	1,341	7,405	35	227
260	2	7	0,454	0,925	0,129	1,234	2,743	50	203
	3	7	0,681	1,388	0,129	1,234	3,433	50	203
	4	7	0,908	1,851	0,129	1,234	4,123	50	203
	5	11	0,908	2,314	0,114	1,437	4,773	40	203
	6	11	1,090	2,776	0,114	1,437	5,417	40	203
	7	14	1,113	3,239	0,107	1,590	6,049	35	203
	8	14	1,272	3,702	0,107	1,590	6,670	35	203

Symbols: T_l - leaching temperature, °C; σ_s - cost of heating steam, in rubles/gcal; n_1 - number of spontaneous-evaporation stages; C_1 - C_4 - specific outlays, rub/tons of bauxites; Δt - temperature at which slurry is heated by external source of heat, °C; N - concentration of recycled solution, g/l.

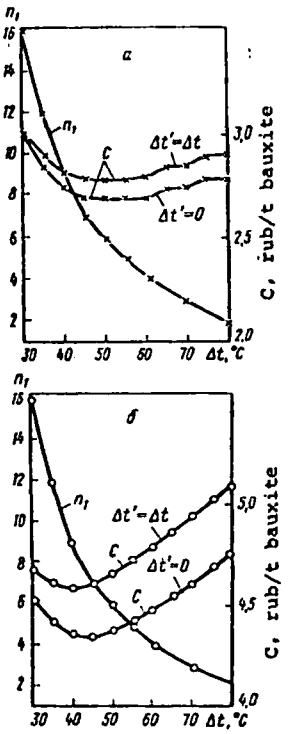

Fig. 2. Relationship of the number of spontaneous-evaporation stages (n_1) and the sum of reduced expenditures (C) to the temperature Δt to which slurry is heated by an external heat source at a leaching temperature of 240° C, and thermal power costing 2 rub/gcal (a) and 4 rub/gcal (b).

In an earlier paper [1], it was shown that with a fixed number of red-mud washing stages (5), and with the slurry heated to leaching temperatures without dilution ($\Delta t' = 0$)*, the optimum values for the concentration of the recycled solution are between 150 and 210 g/l Na_2O_c; therefore, in the calculations for leaching temperatures of 240, 250, and 260°C, the solution concentrations adopted for the reaction autoclaves (Naut) were respectively 210, 190, and 170 Na_2O_c. The modulus values of the aluminate solution following leaching, in relation to the

*$\Delta t'$ - temperature range for heating slurry with live steam (with dilution).

temperatures,were calculated from the equation showing the connection of the Al_2O_3 solubility with the temperature T_1 and the concentration N_{aut}. The other process parameters (Na, R, α_o, and n) were taken as fixed at a nominal level.

Depening on steam prices and leaching temperatures, the optimum number of spontaneous evaporation stages varies within 4 to 14 (see Table).

When heating the slurry with live steam is determined solely by the recuperative heating temperature ($\Delta t' = \Delta t$) and the cost of thermal power is high ($\sigma > 6$ rubles/gcal) the optimum number of spontaneous evaporation stages could be > 14.

When the cost of thermal power is < 4 rubles/gcal, and bears no relationship to the leaching temperature, the optimum number of spontaneous evaporation stages ($\Delta t' = 0.40°C$) is 4-7. This is connected with the effect of the capital investments and the operating costs (C_4) in the total specific outlay (C), although a decisive influence is exerted by the heat and power outlays ($C_1 + C_2$). We can see from the calculation results that where there is a thermal power cost of 2 rubles/gcal (Fig. 2a), the specific outlays are not extreme and the number of spontaneous evaporation stages can be varied within 3 to 9, with no appreciable economic loss. Where the thermal power cost is 4 rubles/gcal (Fig. 2b), there is a clear extreme area of optimum values, corresponding to 6-9 spontaneous-evaporates stages.

It is obvious that it is economically advisable to increase the leaching temperature -- particularly as the cost of thermal power rises.

For instance, the effectiveness of increasing the leaching temperature from 240°C to 260°C (using the variant $\Delta t' = 40°C$), where the thermal power costs 4 rubles/gcal, is about 0.44 rubles/ton of bauxite or about 1 ruble per ton of Al_2O_3. This calculation does not take account of the possibility of increasing the steam utilization factor when the concentration of the the recycled solution drops from 252 to 203 g/l Na_2O_3, nor does it take account of the increase in alumina extraction from bauxite as the leaching temperature is increased. Moreover, when the specific capital outlay is calculated, the same leaching time is employed for all of the considered temperatures; the possibility of substantially reducing the time as the process temperature is increased is not considered.

This confirms the progressive nature of the tendency toward increasing the temperature at which polyhydrate bauxites are leached.

CONCLUSIONS

It was shown that at the current cost of thermal power and the importance of capital and operating costs, the optimum number of spontaneous evaporation stages is 4-7. From an economic point of view, it is advisable to raise the temperature at which polyhydrate bauxites are leached to > 240°C.

1. N. S. Mal'ts. Tsvetnye Metally, 1966, No. 7, pp. 57-61
2. N. S. Mal'ts and V. A. Bernshtein. Tsvetnye Metally, 1967, No. 4, pp. 57-62.
3. N. N. Tikhonov, P. V. Yashunin, and S. I. Beneslavskii. Alumina Production. Collection No. 77, Leningrad, VAMI, 1971, pp. 5-8.

OCCIDENTAL MINERALS CORPORATION
A SUBSIDIARY OF OCCIDENTAL PETROLEUM CORPORATION

MIAMI PROJECT
918 LIVE OAK
MIAMI, ARIZONA

P. O. DRAWER A-G
MIAMI, ARIZONA 85539
(602) 473-4421

THE OXYMIN PROJECT AT MIAMI, ARIZONA

A SUMMARY OF A PRESENTATION MADE TO MIAMI, ARIZONA TOWN COUNCIL

September 12, 1977

HISTORY OF THE VAN DYKE COPPER DEPOSIT

The Van Dyke deposit is part of the Globe-Miami Copper District. A simplified map and cross-section are shown in Fig. 1. The first mining in the area, beginning about 1896, recovered ore from the outcrop where the copper minerals had oxidized into high-grade ore. Leaching began in the district in the early 1920's and has continued up to the present time. Leaching is the extraction of copper from rock through the percolating of a weak acid solution which dissolves the copper minerals. Leaching has accounted for a major part of production from the district. Unlike most of the other deposits in the district, the Van Dyke deposit does not outcrop. It is completely buried under the Gila Conglomerate and underlies part of the Town of Miami. Within the town limits, the deposit lies at a depth from 1,100 to 2,000 feet below the surface.

After signing an option for the Van Dyke property in 1968, OxyMin started its exploration program and by 1975, about 40 holes had been drilled throughout the deposit. This drilling delineated about 100 million tons of oxidized copper mineralization with an average grade of about one-half of one percent copper (0.5%).

IN-SITU LEACHING - WHY AND HOW

Due to the depth of the deposit, the low grade of the mineralization and the fact that a major portion of the deposit is under the Town of Miami, no conventional mining method, such as open pit or block caving, appears to be feasible. A modern mining method, in-situ (in-place) leaching through drill holes, however, offers considerable promise. In-situ solution mining means dissolving and

recovering the mineral values in the rock at great depths with solutions that are pumped down injection wells and pumped back up and out of recovery wells. The average copper mineral in hairline fractures is about five hundredths of an inch thick (0.05") or about as thick as a penny. A very minute amount of material, approximately 4 pounds leached from each ton of rock, will be removed. Because only this tiny fraction will be removed to the surface, no cavities will be formed. Collapse and surface subsidence is therefore impossible.

HOW OXYMIN HAS TESTED THE PROCESS

OxyMin in January, 1976, decided to start in-situ leach pilot testing through surface drill holes. Two holes were drilled to a little over 1000 feet in depth and 75 feet apart. As shown in Fig.2, the specific zone to be leach-tested was then hydrofractured with water and a fluid connection was established between the holes. Hydrofracing, or more properly, hydraulic fracturing, involves pumping water to the bottom of a cased well. When the fluid pressures from the water downhole exceed the rock pressure, the hairline fractures are opened slightly and thus form passages through which the fluid is circulated. Hydrofracturing, as used in the Van Dyke deposit, will extend the fractures a maximum of about 200 feet from the point of fluid injection.

After pressure testing with water to demonstrate the absence of casing leaks, weak sulfuric acid solution was then injected through one hole into a selected part of the copper oxide zone and retrieved up the other hole. Testing, to date, has proven the feasibility of in-situ leaching of this deposit. A very important result of the completed test is that it now appears that blasting is not necessary to increase permeability. The continuation of OxyMin's tests will not involve any underground detonation.

HAS IN-SITU LEACHING BEEN USED BEFORE?

In-situ solution mining operations under towns are not new at all. There are many present day examples of deposits being mined under towns at the same depths, or closer to the surface, than OxyMin's Van Dyke copper deposit. There are no commercial in-situ solution copper mining operations, but there are many successful commercial in-situ solution salt mining operations in existence today. In the

State of Michigan, there are at least five commercial in-situ solution salt mining operations below towns, at depths ranging from 900 to 3500 feet. There are two similar commercial in-situ solution salt mining operations in Ohio, and two in New York. One of the New York operations has been continuously operated for the past 70 years.

The objective of OxyMin is to apply some of the known and commonly used in-situ solution mining techniques to the Van Dyke property, so it will not be necessary to excavate large quantities of rock.

COMMERCIAL DRILLING WOULD BE UNDERGROUND

OxyMin anticipates in-situ solution leach mining from underground workings if further pilot test work proves the economic feasibility of commercial production. This would mean no noise, lights or vibration in the town. A vertical shaft will be sunk outside the town limits and a gridwork of nearly horizontal drifts will be driven below the town. The solution injection and recovery wells will be drilled and operated from the underground drifts, as shown in Fig.3.

The leach solutions will be weak sulfuric acid, the same as used by several other copper mining companies in this part of Arizona. The copper in the leach solutions will be recovered by a conventional solvent extraction and electrowinning plant built on the surface. The solutions from the plant which are then barren of copper will be recycled into the in-situ leaching circuit.

There will be no mill, dumps, tailings or smelter associated with this environmentally attractive and technically advanced operation. The shaft and the extraction plant will be the only sizable surface installations and they will both be outside the town limits.

WHAT ABOUT WATER?

Ground water for municipal supply in the Miami area is now obtained from several wells in the Central Heights area, about three miles northeast of the Van Dyke deposit (Fig. 4). They tap the upper sandstone layers of the Gila Conglomerate and yield moderate amounts of good quality water. Ground water from the alluvium in Bloody Tanks Wash, closer to the deposit, is not used for municipal supply, and has not been for several years except in extreme dry periods when it is added in fractional amounts to the Central Heights water. It is of poor quality, and exceeds several of the U.S. Public

Health Service recommended limits for domestic use.

OxyMin has constructed two wells for monitoring purposes in the alluvium of Bloody Tanks Wash in Miami. These wells are about 100 feet deep, and are located about 2500 feet downstream of the test site. These wells were specifically constructed so that representative ground water samples can be obtained by pumping from the alluvial aquifer in the Bloody Tanks Wash. Sampling from these wells has continued monthly since May, 1976, and will continue in the future. The factual data from these samples have been, and will continue to be, submitted to the Miami Town Council. The data indicate that no significant change in chemical constituents in the ground water has occurred during the pilot test leaching activities.

OxyMin has not conducted in the past, nor does it intend to conduct in the future, any operations that will impair the quality of the ground water within the Miami area. To this end, OxyMin will continue its hydrological evaluation and ground water monitoring programs throughout all phases of its operations.

THE QUESTION OF MINERAL RIGHTS

Development of mining operations in the Miami area and the development of the Town of Miami have historically coincided. Indeed, it was the mining activity that led to the establishment of the original Miami town site. The mineral estate was severed from the surface rights prior to creation of the surface estates and surface owners purchased the surface to a depth of forty feet.

Standardized deed restrictions, consistent with grant of the severed mineral estate, were incorporated in the surface deeds at the time the surface parcels were first offered in 1909 for sale to individual purchasers. In the language of the deeds, these restrictions absolve the mineral estate owners from liability to the surface owners in the event of subsidence resulting from mining operations conducted under them. During the development of the Town of Miami, the owner of the severed mineral estate and its lessees were conducting exploration, development and mining operations in, under and adjacent to the Town of Miami, commencing in 1916 and continuing to the present.

PROTECTION FOR LAND-OWNERS

The owners of the mineral estate, Van Dyke Copper Co. and Sho-Me Copper Co., are now willing to enter into agreements with the surface

estate owners requiring the mineral estate owner to compensate the surface owner for any damage that might be caused by mining operations conducted beneath the surface. OxyMin is willing to accept and assume such an agreement with respect to its operations. This proposal was first outlined to area residents, including members of the Town Council, at a meeting held 15 months ago in Miami. The binding effect of the agreement should assure the surface owners and any lending institutions that their property investment will continue to be secure. In addition, this agreement should permit those surface owners who might otherwise feel that their security was impaired to proceed with any surface developments or improvements that they might desire.

Compensation for damage would not be based upon some predetermined formula but rather upon an appraisal made at such time, if any, as surface damage occurs. OxyMin will soon make available to the surface owners a form of the agreement. Copies will be available at OxyMin's Miami office on Live Oak Street.

WHAT WILL HAPPEN IF OXYMIN GOES AHEAD

If OxyMin's further testing operations prove successful, full development will not only be compatible with the economic and environmental interests of the Town of Miami but will, in fact, be of substantial benefit to the entire Miami area. OxyMin anticipates that it will employ a work force of over 200 Miami area residents. The town's tax base will obviously benefit from such an operation as will the tax bases of the Miami School District and of Gila County. OxyMin reaffirms its willingness to work with the Miami community in an effort to achieve common goals. A common effort will provide a significant boost to the future stability and prosperity of the town and its residents.

If you have any questions about OxyMin's Miami project, please contact:

Bob Zache
Occidental Minerals Corporation
918 Live Oak Street
Miami, Arizona
(602) 473-4421

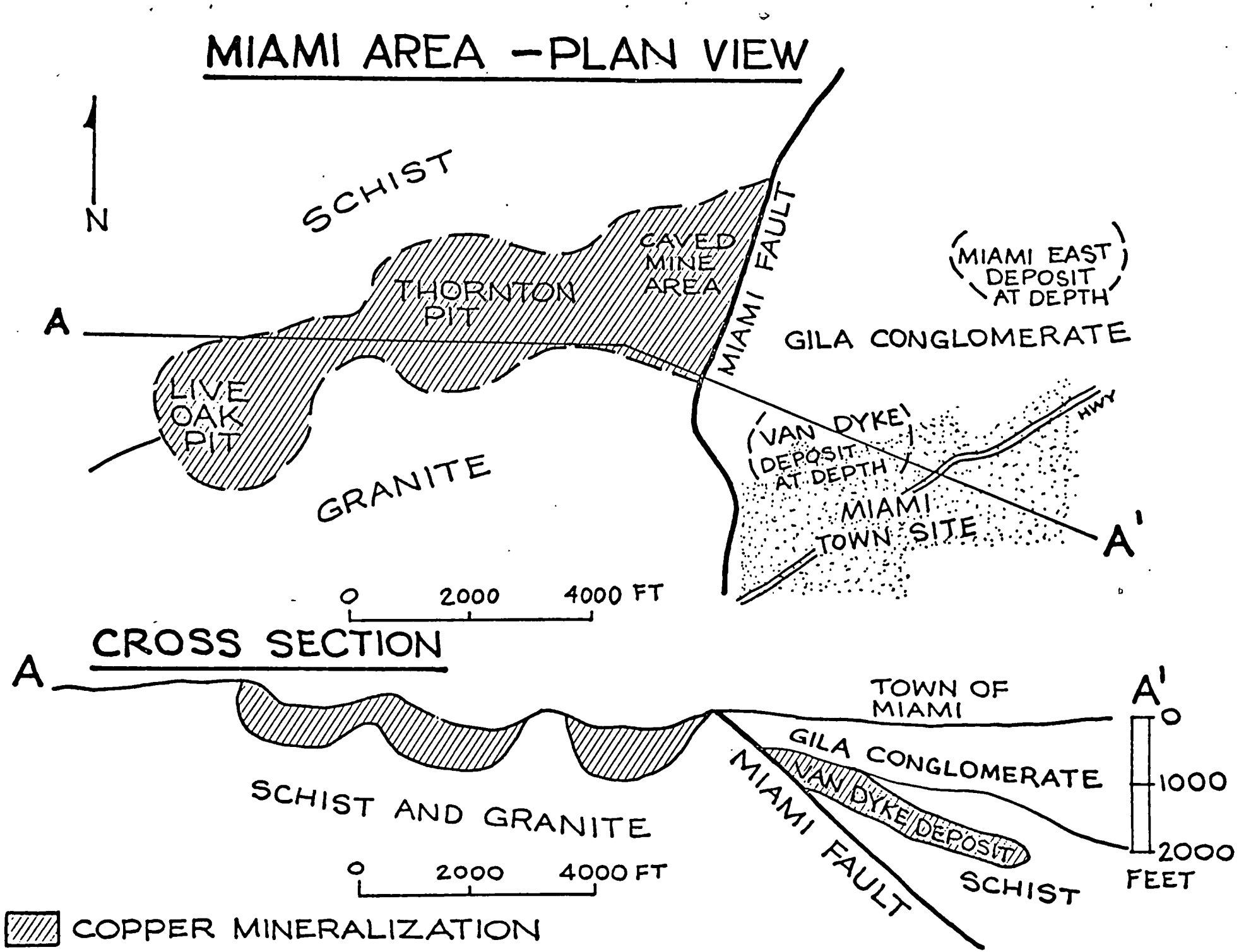
MIAMI AREA – PLAN VIEW
N
SCHIST
THORNTON PIT
CAVED MINE AREA
MIAMI FAULT
MIAMI EAST DEPOSIT AT DEPTH
A
GILA CONGLOMERATE
LIVE OAK PIT
GRANITE
VAN DYKE DEPOSIT AT DEPTH
HWY
MIAMI TOWN SITE
A'
0 2000 4000 FT
CROSS SECTION
A
TOWN OF MIAMI
A'
GILA CONGLOMERATE
VAN DYKE DEPOSIT
1000
2000
FEET
SCHIST AND GRANITE
MIAMI FAULT
SCHIST
0 2000 4000 FT
COPPER MINERALIZATION

FIG. 1

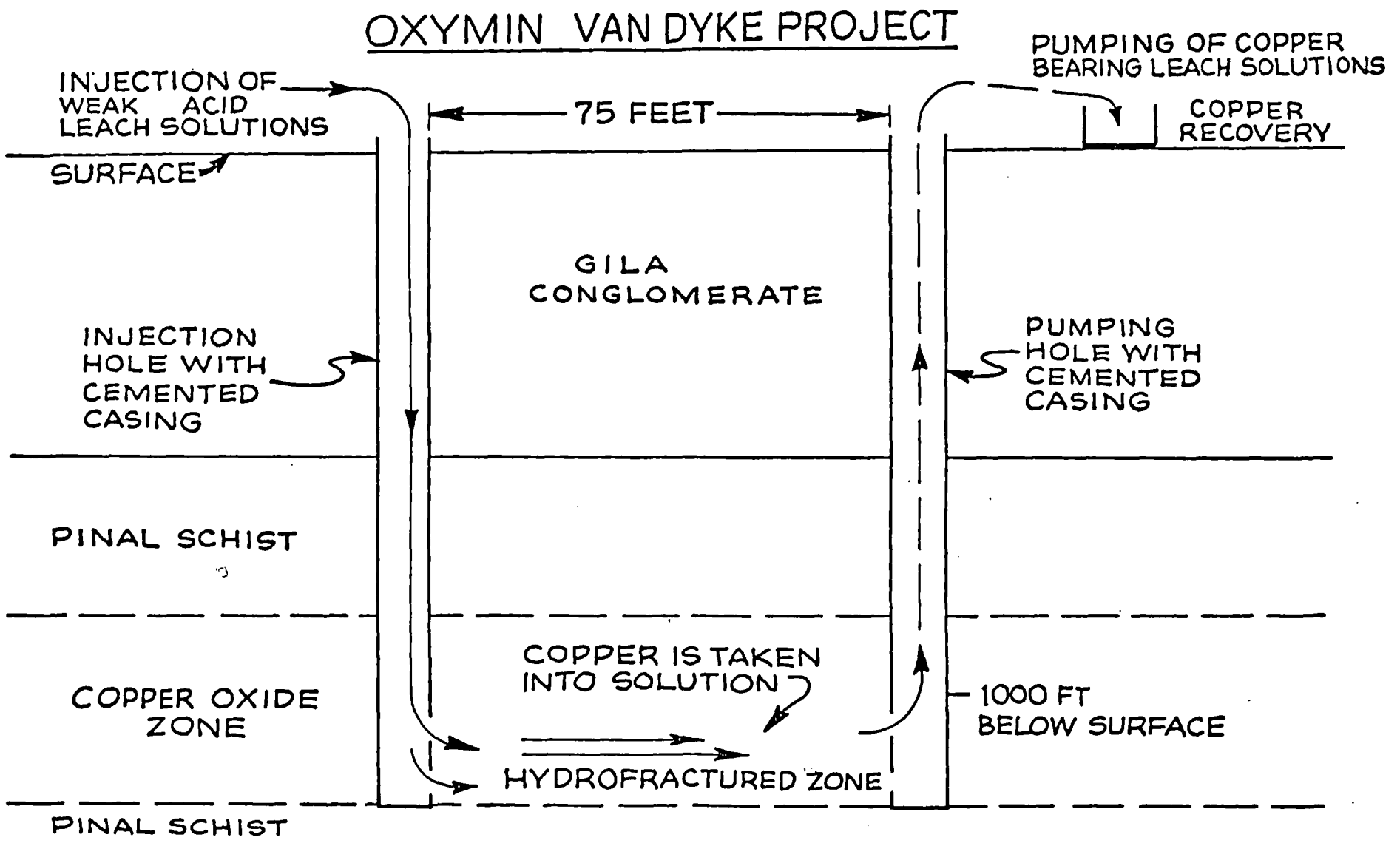

SCHEMATIC REPRESENTATION OF SOLUTION MINING TEST

FIG. 2

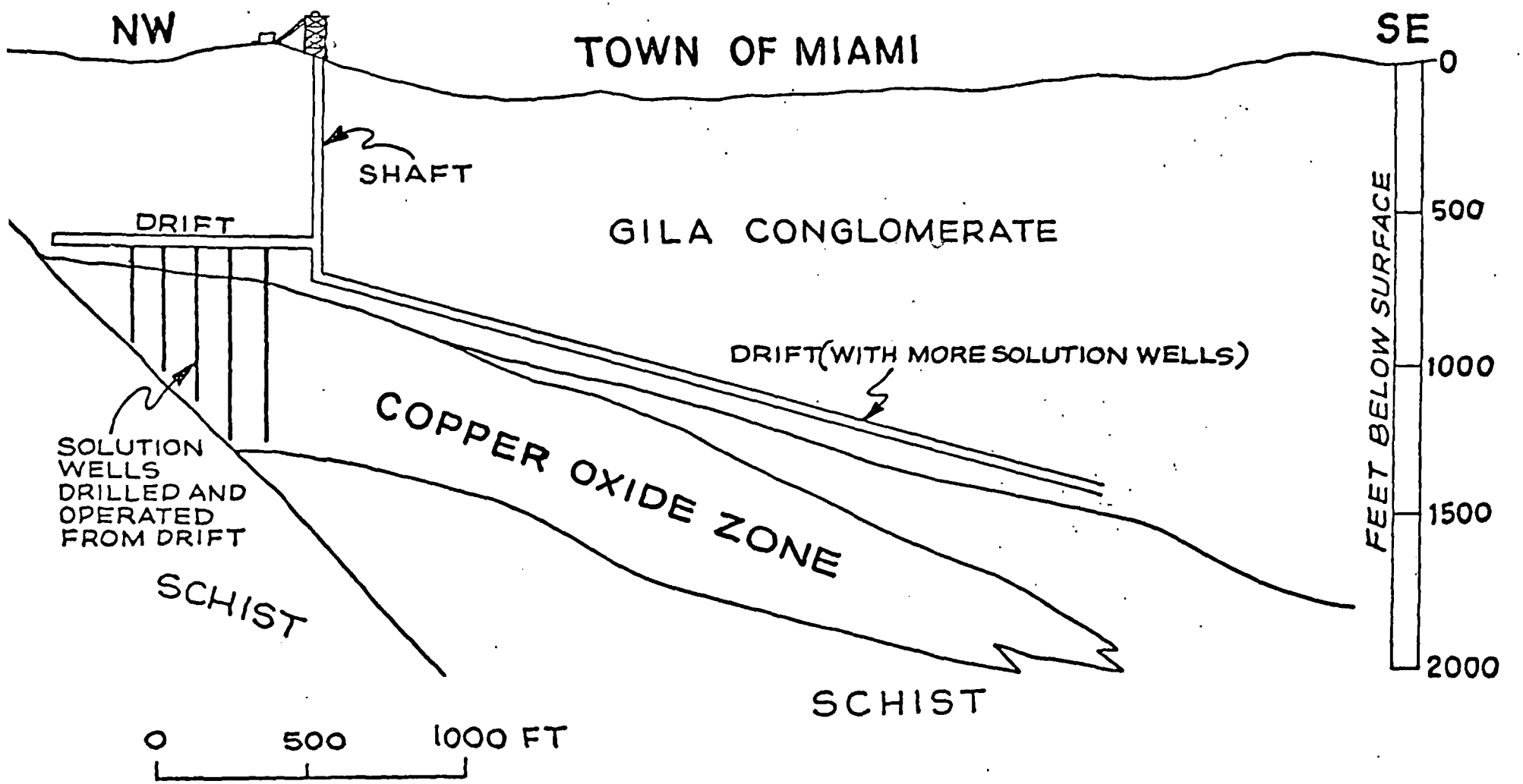

VERTICAL CROSS-SECTION THROUGH VAN DYKE DEPOSIT

FIG. 3

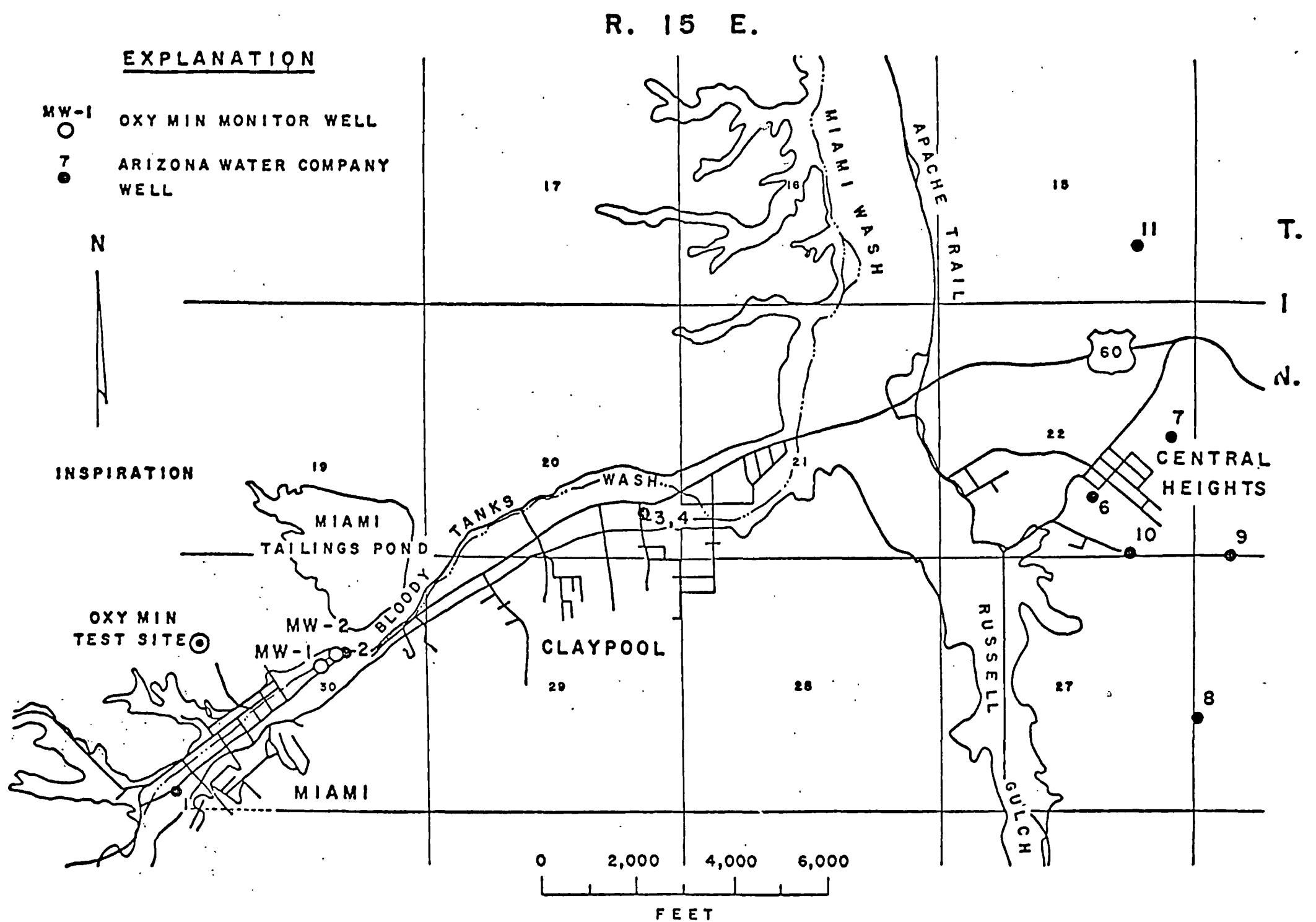

MAP OF MIAMI-CLAYPOOL AREA, ARIZONA

FIG. 4

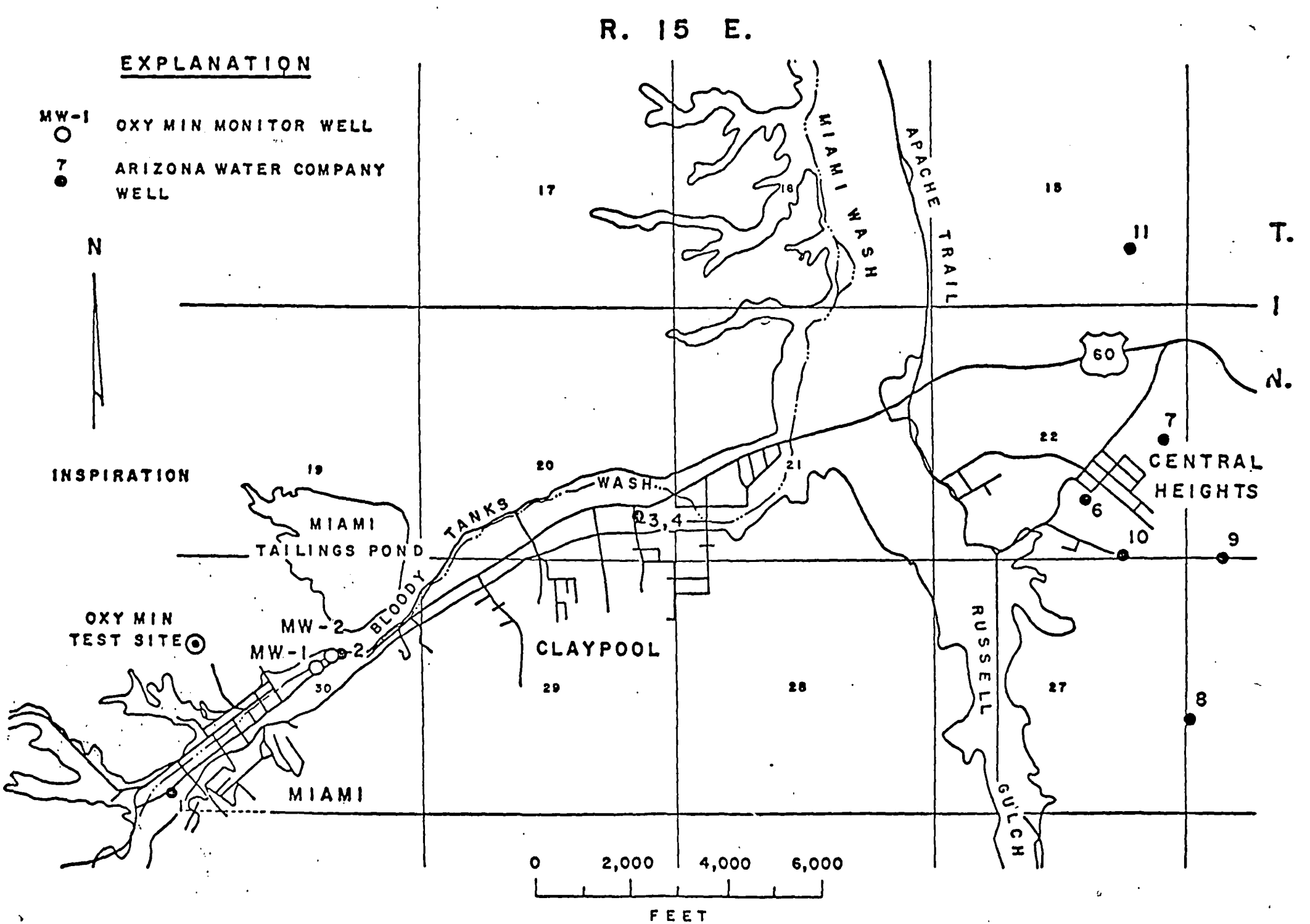

MAP OF MIAMI-CLAYPOOL AREA, ARIZONA

FIG. 4

OBSERVATIONS ON RECOMMENDED ELECTRODE ALLOYS

UDC 669.35:620.1

M. V. Zakharov, F. V. Korolev, and V. A. Ignat'ev

Choosing the best heat-resistant copper conductor alloys, including electrode alloys for centralized production, is a matter of vital importance. In our view this problem was not dealt with successfully in the paper by A. K. Nikolaev and his co-authors[1].

The authors took more than 20 different alloys for study, but most of the material given in the paper is indeterminate to say the least.

This affects the main points in the paper: alloy chemical composition, routines for hardening heat treatment and their validation, methods of research, the alloy physical and chemical properties produced, and finally the life of the alloys in welding machine contacts. Here are some examples.

1. Even the average chemical composition of the alloys studied is not given.
2. The hardening heat treatment for the alloys, namely the specific alloy aging routines, is not indicated.
3. The application of mechanical and heat treatment (quenching plus cold deformation plus aging) to the alloys studied is not clear, because this type of mechanical and heat treatment justifies itself only when copper alloy articles operate at moderate temperatures of the order of 200-400°C, not at 600-700°C as the authors state.
4. Although the operational life of electrode alloys on welding machines depends upon certain variables, the most important of them, provided that the necessary thermal conductivity is present, is heat resistance, i.e., the resistance of the alloys to creep. In this case creep in the alloys is made worse by the many thousand alternating electrode loading at high temperatures. This creep should have been assessed in the main alloys. At least the hardness and electrical conductivity of the tested alloys supplied for the machine should have been given.

The problems in assessing the operational life of the electrode alloys studied are not new. The alloys mentioned in the paper (see footnote 1), except for Br.K Kh Ko, have already been studied and tested by various authors, both at the All-Union Electric Welding Equipment Research Institute and at the plants, using both laboratory and plant heats. They have been tested both in the spot welding of steels and in other forms of resistance welding (seam welding, butt welding, etc.) and on other materials apart from steels. The results of this research have been discussed repeatedly at All-Union conferences. Comparative experimental data on the life of the alloys Mts5A (0.35% Cr + 0.2% Zr), Br.NBT (1.4% Ni + 0.3 Be + 0.1 Ti), and Mallory-328 (0.6% Cr + 0.05 Zr) in spot-welding low-carbon steel demonstrated the advantages of the Soviet alloy Br. NBT. Br. NBT alloy can be recommended for welding stainless steel and heat-resistant nickel and titanium alloys.

For spot-welding of low-carbon steels the authors recommend Br. Kh Tsr (0.4-1.0% Cr + 0.03-0.08% Zr), i.e., according to its average chemical composition, and Mallory-328 (0.65% Cr+ 0.04% Zr), although according to the authors' own experimental data their life was similar to that of Br.NBT (changes in D_{el} 0.8 and 0.8 mm respectively). Even the expensive English alloy MKB (2.5% Co + 0.5% Be) is noticeably inferior to the cheap Soviet alloy Br.NBT in spot and seam welding of various steels according to data from the All-Union Electric Welding Equipment Research Institute, in spite of the fact that MKB is made from pure metals. In our opinion this is due to the fact that MKB contains more beryllium than is required on the basis of the Cu-CoBe quasibinary section. Alloy MKB should have included only 0.40% Be on average instead of 0.5-0.6% Be, in order to be on the Cu-CoBe quasibinary section.

In our opinion Br. K Kh Ko alloy, which is recommended as having the longest life in welding stainless steel (see footnote 1), requires additional plant testing, for two reasons. Firstly, Br. K Kh Ko was given the optimum heat treatment. The chemical composition of Br. K Kh Ko was taken at the upper limit of alloying additions, and that of Br.NBT was taken at the lower limit.

Secondly, while having life values in welding stainless steel such as d_{el} 0.2 and 0.55 mm, the expensive Br. K Kh Ko alloy was considerably inferior to the cheap Br.NBT alloy in welding low-carbon steel ($d \approx$ 1.6 and 0.8 mm respectively). Accord-

[1] A. K. Nikolaev, F. S. Novik, V. M. Rozenberg, and S. K. Sliozberg, Tsvetnye Metally, 1974, No. 11, 53-59.

ing to recent findings by the authors themselves[2], after quenching at 1000°C, Br. K Kh Ko has a considerable amount of the ternary brittle chmical compound $Cr_3Co_5Si_2$ which is relatively insoluble in copper; hot forming of this alloy is therefore impossible without a line structure leading to anisotropy in properties and to corrosion.

There has been sufficient discussion of the problem of alloying electrode alloys, The most important fact is that the alloys with the longest lives (Br.NBT, Br. K KhN, Br. K Kh Ko) according to the authors' findings (see footnote 1) proved to be on the corresponding quasibinary sections.[3]

In our opinion, the universal Soviet alloy Br.NBT (1.6% Ni + 0.3% Be + 0.1% Ti). which is made from high-beryllium bronze production waste, must be recommended for all forms of resistance welding for stainless steel and heat resistant nickel and titanium alloys.

---

[2]N. I. Revina, A. K. Nikolaev, and V. M. Rozenberg, Nauchnye Trudy Institut Giprotsvetmetobrabotka, 1975, No. 48, 61-70.

[3]M. V. Zakharov, Tsvetnye Metally, 1974, No. 8, 63-67.

EDITORIAL NOTE

In the opinion of the metalworking section the paper by A. K. Nikolaev and others (Tsvetnye Metally, 1974, No. 11, 53-59) was of definite value in spite of certain faults.

The differences of opinion between the authors of that paper and M. V. Zakharov and others, the authors of the published observations, relate mainly to the evaluation of the alloys Br.NBT and Br. K Kh Ko.

Both alloys are produced mainly in the form of flat stock, and the technology for producing small-diameter rods (extrusion, drawing with intermediate annealings) in both alloys is laborious and far from perfect. Nevertheless there are Technical Specifications for these alloys and for 5 other electrode alloys, which will be replaced by a State Standard.

The answer to the question of advantages and disadvantages will apparently be found in prolonged practical use. The journal editorial board therefore regards continued discussion on this matter as undesirable in the immediate future.

Hydrometallurgy, 5 (1979) 67—93

OBSERVATIONS OF SOLUTION TRANSPORT, PERMEABILITY, AND LEACHING REACTIONS IN LARGE, CONTROLLED, COPPER-BEARING WASTE BODIES

L.E. MURR

Department of Metallurgical and Materials Engineering, New Mexico Institute of Mining and Technology, Socorro, New Mexico 87801 (U.S.A.)

(Received January 7th, 1979; accepted in revised form April 19th, 1979)

ABSTRACT

Murr, L.E., 1979. Observations of solution transport, peremability, and leaching reactions in large, controlled, copper-bearing waste bodies. *Hydrometallurgy*, 5: 67—93.

The leaching characteristics (waste-body temperature profiles, total daily oxygen consumption, and copper extraction as well as solution chemistry features) are compared for two vastly different, large (1.7×10^5 kg) low-grade, copper-bearing waste bodies. One column, a Kennecott-Santa Rita waste (0.36% total Cu) was primarily a chalcocite waste with little detectable acid consumption, requiring essentially no neutralization while the other column, a Duval-Sierrita waste (0.34% total Cu) was primarily a chalcopyrite waste with high acid consumers present in the host rock, and requiring a lengthy neutralization period. This latter column which measured 3.1 m in diameter, was appropriately scaled down with two smaller columns measuring 0.38 and 0.10 m in diameter, respectively. The initial permeability and drain-down characteristics are compared along with final permeabilities in the Kennecott-Santa Rita waste body (following the conclusion of leaching experiments). A post-leaching [Cl^-] tracer test conducted on the Kennecott-Santa Rita column suggests that, consistent with indications from permeability data, dead spaces occurred within the waste body and these features seem to have contributed to the leaching performance and characteristics. Scaling experiments were observed to accurately characterize and follow the neutralization of the Duval-Sierrita waste (as determined by monitoring effluent solution pH), but there was little correlation between copper extracted in the large Duval-Sierrita waste column (3.1 m diameter) and the smallest laboratory column (0.1 m diameter).

INTRODUCTION

It is well known that when the fluid flow characteristics in a system are known, it is possible to formulate heat and mass transfer phenomena from first principles [1]. In the absence of such data, it is necessary to construct mathematical models. Ultimately, however, such models must be verified by either the insertion of data or comparison with experimental observations.

Dump leaching of low-grade waste is a complicated process which involves the interrelationship of air convection, fluid transport, and bacterially-catalyzed reactions. These determine the dump heating which in turn influences the re-

actions. Permeability and variations of permeability will directly influence air convection and fluid transport, and can lead to irregularities in waste-particle consolidation which, over long periods of time, can alter dump properties and overall leaching performance. It is very difficult at present to differentiate between the effects of specific parameters characteristic of a leach dump on the leaching phenomena, especially rate of extraction, in the leaching of porphyry copper rock, particularly chalcopyrite wastes, even though several dump leaching models have been proposed which show considerable promise in scaling-up laboratory test data to expected field results [2—5]. The reason for this is the lack of scale data, the inability to perform large, controlled leaching studies, and the difficulty in performing experiments where the parameters alluded to above can be successfully distinguished and characterized.

As recently pointed out by Roman [6], research pertaining to solution flow in leach dumps has generally been neglected. Harris [7] has alluded to the phenomenon of bulk density convergence where the bulk density approaches that of the undisturbed rock where in principle compacted regions of a dump will act as a single "particle". Roman [6] has considered this briefly in terms of the solution flow path where at high bulk densities or regions of high bulk densities leach solution no longer surrounds each particle, but flow paths are effectively separated by these high-bulk-density "particle" regimes which lead to solution channeling. Roman [6] has shown a γ—γ log plot for a hole drilled into a leach dump at Kennecott's Chino operation in New Mexico which is indicative of two lithologic regimes based on the bulk density.

In describing a recent dump leaching model, Cathles and Apps [8] have demonstrated the importance of air convection, oxygen balance, and heat balance; including dump height and dump permeability. Some of these features have been demonstrated to be experimentally valid not only in practical (operating) leach dumps, but also in controlled, large-scale laboratory-type experiments [2].

The present experiments represent an attempt to gather some data pertinent to the dump leaching regime using large, controlled, waste-rock masses in insulated metal (stainless steel) tanks. This approach extends the limits of laboratory experiments to a scale commensurate with a large dump unit or model-unit, and allows for the monitoring and control of solution and air flow, heating effects, solution chemistry, and bacterial activity. The present paper presents some qualitative comparisons of two large waste bodies systematically leached over a 2-year period, along with some laboratory scaling of one of the waste bodies on smaller scales. This approach shows some promise in providing direct experimental evidence which not only provides a basis for existing models, but also new or extended models as well as illustrating a direct connection between permeability, transport, and attendant reactions in the dump leaching of low-grade, copper-bearing waste.

EXPERIMENTAL CONSIDE

The large-scale leachin
formed in two converted
inside diameter and 12.3
jacket separated from an
lite insulating layer. Acc
instrumentation was bro
through the inner stainle
the bottom of each tank
drilled with small 2.5 cm
pipe cross section of 4:1
through a line extending
the bottom of each tank
was placed above the ae
schedule 80 pipe were pl
sum moisture blocks wer
cumference of the inner
hand placed upon the ins
vated and dropped into t
leveling to randomly dist
until the level reached th
porous cup lysimeters fo
the port location, rock h
loading process continue
half, forming gutters) we
solution collection and a
PVC funnels were imbed
ly from the lysimeters. A
into the waste rock for p
analysis.

Solution was applied t
openings which provided
face. Solution entered th
a reservoir which allowed
diameter of 3 m, rotated

The solution circuit co
solution drained from th
or holding tanks into whi
for subsequent pumping
cells (iron scrap launders)
the pregnant solution of
tation, were normally in

Figure 1 illustrates the
facility described above,

EXPERIMENTAL CONSIDERATIONS

The large-scale leaching experiments to be described in this work were performed in two converted liquid-oxygen storage dewars which measured 3.1 m inside diameter and 12.3 m height. These tanks had an inside stainless steel jacket separated from an outer carbon (mild) steel wall by a 0.3 m thick perlite insulating layer. Access windows were cut into the outer steel wall and instrumentation was brought through these locations by attaching pipe fittings through the inner stainless steel jacket. An aeration system was provided at the bottom of each tank consisting of schedule 80 PVC pipe 1.5 m square, drilled with small 2.5 cm holes, with a total area of escape cross section to pipe cross section of 4:1. These aerators were connected to air compressors through a line extending out of the tanks. A drain line was also cut through the bottom of each tank. A 1 m high gravel bed, using quartzite rock (+2″), was placed above the aeration system and thermocouples imbedded in PVC schedule 80 pipe were placed at the top of the gravel beds. In one tank, gypsum moisture blocks were also placed in an array spaced 0.6 m from the circumference of the inner jacket, and approximately 0.5 m of waste rock was hand placed upon the instrumentation. Additional waste rock was then elevated and dropped into the tanks from an opening in the top, with frequent leveling to randomly distribute the rock size fractions. This was continued until the level reached the first access port location. Instrumentation, including porous cup lysimeters for the collection of solution samples, were placed at the port location, rock hand loaded over the instruments as before, and the loading process continued. In one tank PVC pipe half-sections (pipes cut in half, forming gutters) were placed at the access port locations to allow for solution collection and analysis, while in the other tank, 0.25 m diameter PVC funnels were imbedded near the center of the waste rock, displaced slightly from the lysimeters. Access pipes (5 cm diameter) also allowed for augering into the waste rock for periodic removal of small rock samples for bacterial analysis.

Solution was applied to the waste through a rotating arm with graduated openings which provided a uniform distribution of solution over the rock surface. Solution entered the arm through a slotted shaft which passed through a reservoir which allowed a pressure head to be maintained. The arm, having a diameter of 3 m, rotated at a speed of 1 rpm.

The solution circuit consisted of an underground holding tank into which solution drained from the copper-bearing waste body, a series of elevated surge or holding tanks into which solution was pumped from the underground tank for subsequent pumping to the solution distributor. A series of cementation cells (iron scrap launders) were placed just ahead of the surge tanks to strip the pregnant solution of its copper. Barren solution copper levels, after cementation, were normally in the range of 100—150 ppm copper.

Figure 1 illustrates the major design features of the large-scale leaching facility described above, showing the overall appearance of the waste rock tanks,

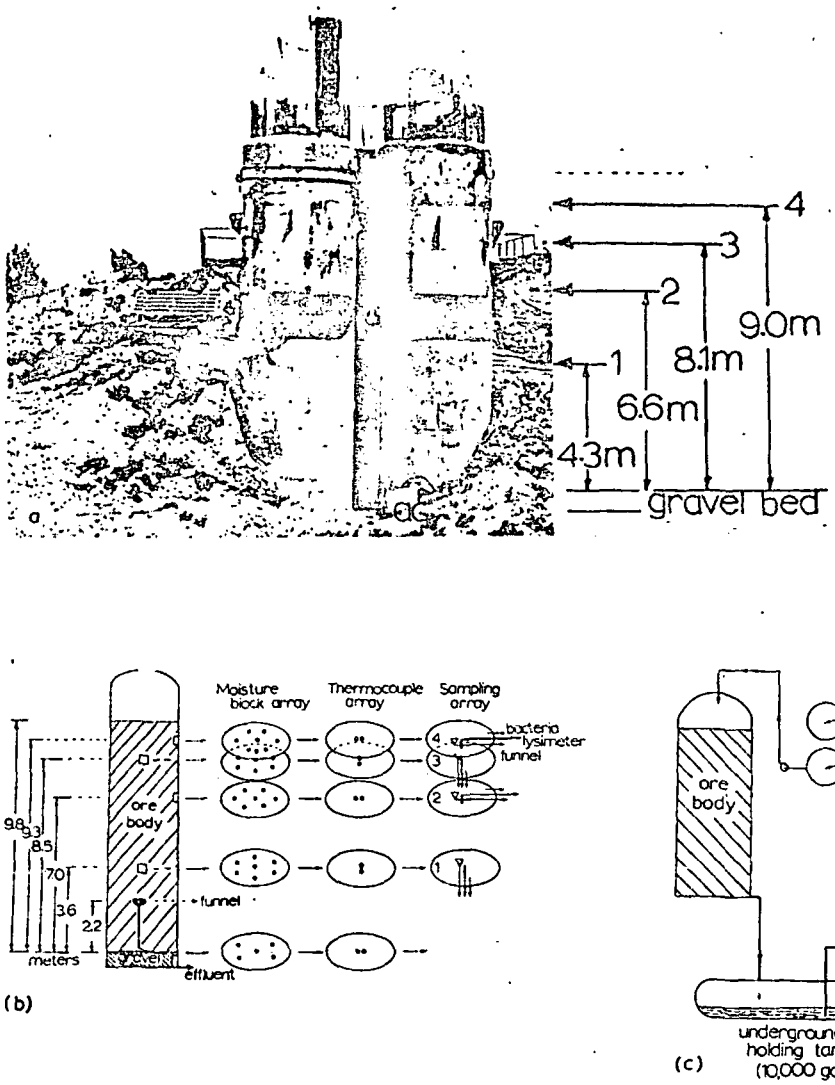

Fig. 1. Large experimental leach tank design and operational features (a) Physical view of the tanks. An air compressor is shown at (ac). One of two iron scrap launders utilized in the circuits is shown in the middle left of the photograph. (b) Schematic view of the sampling and instrumentation arrays in one of the experimental waste bodies (Duval-Sierrita). (c) Solution circuit schematic.

the placement of instrumentation, and the solution (leach) circuit. Table 1 shows for comparison the principal features and parameters of the two waste rock experiments. One column was filled with a Duval-Sierrita waste while the other was filled with a Kennecott-Santa Rita waste (copper-bearing rock). As shown in Table 1, there were fundamental differences not only in the rock

TABLE 1

Experimental waste-body a

Parameters	
Quartz (wt%)	
K-feldspar (wt%)	
Biotite (wt%)	
Dickite (wt%)	
Total Cu (wt%)	(
Non-sulfide Cu (Acid-soluble % of total Cu)	(
Chalcocite (wt%)	<(
Chalcopyrite (wt%)	<(
Pyrite (wt%)	-
Carbonate (wt%)	<(
Total SiO_2 (wt%)	
Total Fe (wt%)	5
Dry body bacteria: (cells/g)	
Total waste-body weight (kg)	1.6 x
Max-rock size (inches)	

size, but also in composi
chalcocite waste with so
ly a chalcopyrite waste,
consumers. The Duval-Si
Kennecott-Santa Rita hc
prone to decrepitation.
and transport properties.

Initial permeabilities
tanks and blowing air at
various locations. The ga
flow into and out of the
measured by plotting the
finding a representative s
column and the air viscos

Following the dry (wa
rated with water. The Ke
Mines (New Mexico) leac
body was saturated with
tank was allowed to drai
were monitored. Retaine
utilized on each waste co

TABLE 1

Experimental waste-body analysis and properties

Parameters	Kennecott-Santa Rita waste	Duval-Sierrita waste
Quartz (wt%)	68	29
K-feldspar (wt%)	2	38
Biotite (wt%)	2	5
Dickite (wt%)	—	5
Total Cu (wt%)	0.36	0.34
Non-sulfide Cu (Acid-soluble % of total Cu)	0.22	0.03
Chalcocite (wt%)	<0.3	—
Chalcopyrite (wt%)	<0.1	0.8
Pyrite (wt%)	~4	3.3
Carbonate (wt%)	<0.1	2
Total SiO_2 (wt%)	75	71
Total Fe (wt%)	5.6	2.7
Dry body bacteria: (cells/g)	10^3	<10
Total waste-body weight (kg)	1.6×10^5	1.7×10^5
Max-rock size (inches)	<4	6

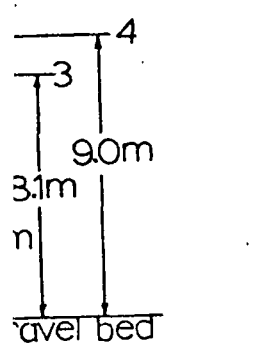

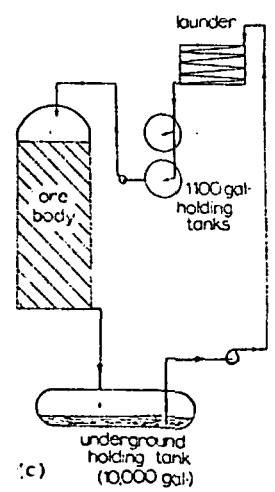

eatures (a) Physical view of
n scrap launders utilized in
Schematic view of the sam-
vaste bodies (Duval-Sierrita).

leach) circuit. Table 1
ameters of the two waste
al-Sierrita waste while
ste (copper-bearing rock).
nces not only in the rock

size, but also in composition. The Kennecott rock was characteristically a chalcocite waste with some chalcopyrite. The Duval rock was characteristically a chalcopyrite waste, with a high carbonate content (~2%) and other acid consumers. The Duval-Sierrita host rock was a very hard silicate while the Kennecott-Santa Rita host rock was an easily fragmented quartz monzanite prone to decrepitation. This produced some marked differences in permeability and transport properties.

Initial permeabilities were measured for the dry rock masses by sealing the tanks and blowing air at various rates of flow through the columns, vented at various locations. The gauge pressure was recorded at each flow rate when the flow into and out of the columns had equilibrated. Per meabilities were then measured by plotting the pressure in atmospheres versus the flow rate in ml/s, finding a representative slope, and then considering the distance through the column and the air viscosity in the standard Darcy equation.

Following the dry (waste) permeability measurements, each tank was saturated with water. The Kennecott waste column was saturated with Chino Mines (New Mexico) leach solution (tailings water) at pH 2.6. The Duval waste body was saturated with fresh water adjusted to pH 2.5 with H_2SO_4. Each tank was allowed to drain following saturation and the drainage characteristics were monitored. Retained water was also calculated. These procedures were utilized on each waste column but not simultaneously. The Kennecott experi-

ment was begun in late 1975 while the Duval experiment was begun in late 1976. Little neutralization was necessary in the Kennecott waste and the initial inundation brought out roughly 12% of the total copper (acid-soluble copper). No copper was solubilized during the Duval waste inundation and a considerable neutralization period was required.

The Duval column experiment was also followed with two smaller scale experiments. One involved a column run simultaneously at the large-tank test site [Fig.1(a)], while the other involved a laboratory-scale test conducted in the laboratory. The rock sizes and air and solution flow rates were scaled-down using a simple geometrical criterion based on the large waste-body diameter/height ratio. Since this ratio differed in the smaller scale versions by a factor 2 from the large-tank waste body, this factor was also considered in designing the smaller experiments. Table 2 shows the scaling data and other experimental parameters characteristic of these experiments.

All leaching experiments were conducted in intermittant solution application cycles (referred to in this work as flushes) where leach solution was normally applied for 48 h periods followed by several weeks of rest. Air was continuously forced through the waste using the aeration scheme described earlier, and the rest periods provided for oxidation to occur. The influent and effluent solutions were continuously monitored for Cu, Fe^{2+}, Fe^{3+}, pH and Eh. The total oxygen consumed was also monitored by measuring the oxygen level at the injection point and at the top of the waste body for a known air-flow (injection) rate. Bacterial activity was also monitored by a technique which determined the population or most probable number of microorganisms per

TABLE 2

Duval-Sierrita waste leaching scale-test data

Parameters	Large column	Medium column	Small column
Diameter, d (meters)	3.04	0.38	0.10
Waste-body height, h (meters)	9.75	2.64	0.69
d/h	0.290	0.145	0.145
Maximum particle (rock) size (inches)	6	0.75	0.20
Initial drain-down rate (l/min)	4	0.20	0.10
Initial onfluent solution (leach) Rate (l/min)	2	0.100	0.005
Initial air-flow rate (l/min)	17.5	0.875	0.044
Recovered/saturated solution	0.77	0.72	0.68
Waste-body weight (kg)	1.7×10^5	4.1×10^2	7.0

gram or ml of sample. T
where and these results

At the conclusion of
out the waste column w
tracer (as NaCl) was add
The [Cl^-] concentration
several influent flow rat
min B dye was flushed i
optical and U.V.). The c
each 0.6 m length photo
level. At this writing, thi
been entirely completed
[port 1 in Fig. 1(a)]. Th
paper was written.

RESULTS AND DISCUSSIC

As a matter of conven
lar to that described in t
the original wet and dry
from Fig. 2 that consider
regimes at the outset of l
cott column probably re
tions at access ports 1 an
the drain-down character
drain-down for the Kenn
solution channels while t
difference in the size frac
smaller size distribution t
shown in Fig.4 which illu
scaling experiment. Here
2), and the curves shrink
column draining flow rat
plot of the same, abbrevi

As indicated previously
tial neutralization while t
period. The neutralizatio
cording to Table 2), and s
acidified to various pH va
required make-up in the c
in Fig.5, that this phase o
as the effluent solution p
continuous solution appli
sizes) was essentially neut
ization for the large colur

gram or ml of sample. The details of this analysis have been described elsewhere and these results will not be presented in this paper [9].

At the conclusion of the Kennecott experiment, the permeabilities throughout the waste column were again determined as outlined above, and a [Cl^-] tracer (as NaCl) was added in pulses to the fresh water (Flush) solution (pH 6.8). The [Cl^-] concentration in the effluent was monitored along with the pH, at several influent flow rates. At the conclusion of this tracer test, 2 kg of Rhodamin B dye was flushed into the waste in order to act as a stain indicator (both optical and U.V.). The column was then systematically unloaded from the top, each 0.6 m length photographed, and sampled rigorously at each access port level. At this writing, this post-mortem or post-leaching procedure had not been entirely completed but the unloading had reached the first access port [port 1 in Fig. 1(a)]. The Duval column was still being leached when this paper was written.

RESULTS AND DISCUSSION

As a matter of convenience, the results will be treated in a chronology similar to that described in the previous section. Figure 2 shows for comparison the original wet and dry waste (ore) body permeabilities. It should be apparent from Fig. 2 that considerable differences existed in the copper-bearing waste regimes at the outset of leaching. The permeability discontinuity in the Kennecott column probably resulted from hand loading over the instrument locations at access ports 1 and 2 [Fig.1(a) and (b)]. Figure 3 shows for comparison the drain-down characteristics of the two waste columns. The more rapid drain-down for the Kennecott column is probably indicative of some initial solution channels while the difference in slope of the curves also reflects a difference in the size fractions; the Kennecott column having a significantly smaller size distribution than the Duval column (Table 1). This feature is also shown in Fig.4 which illustrates the drain-down rates for the Duval-waste scaling experiment. Here the rates are reduced with smaller size fraction (Table 2), and the curves shrink in the same proportion. The discontinuity in the large column draining flow rate shown in Fig.4 is averaged out in the corresponding plot of the same, abbreviated data in Fig.3.

As indicated previously, the Kennecott column required essentially no initial neutralization while the Duval column required an extensive neutralization period. The neutralization was also carefully scaled down (solution flow according to Table 2), and solution application was begun with fresh well water acidified to various pH values with H_2SO_4 and recycled, adding new water as required make-up in the circuit [Fig. 1(c)]. It is interesting to note as shown in Fig.5, that this phase of the Duval experiment scaled very closely in-so-far as the effluent solution pH could be monitored. Figure 5 shows that after continuous solution application for roughly 165 days, the Duval waste (at all sizes) was essentially neutralized. This was in some respects a superficial neutralization for the large column where it can be seen that the effluent pH values

were less than the influent pH values only after roughly 515 days of elapsed time from the start of neutralization. It can be noted in Fig.5 that air, at differing rates, was continuously forced through the large column, and appropriately scaled down as shown in Table 2 for the smaller columns (medium and small scales). Following the initial neutralization period (Fig.5), the solution was normally applied in flushes of 48 hours duration, followed by a rest period as indicated in Fig.5. The scaling of these leaches or flush periods ended with flush 8 (Fig.5).

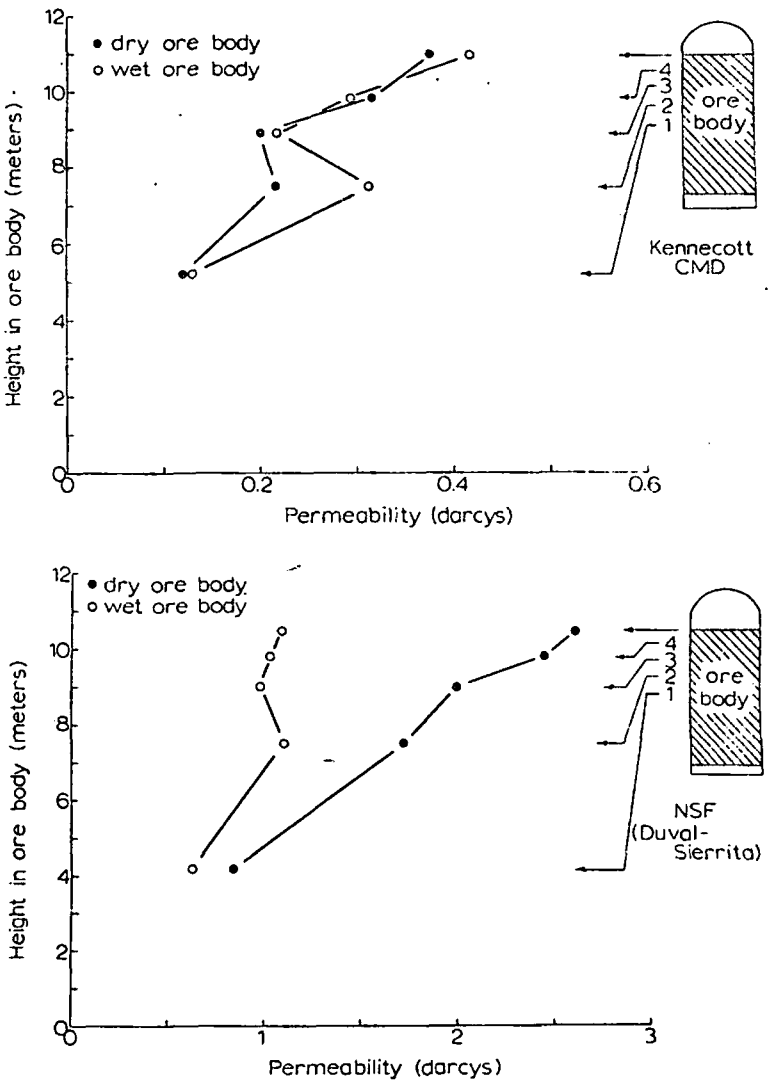

Fig.2. Comparison of initial dry and wet waste (ore) body permeability profiles.

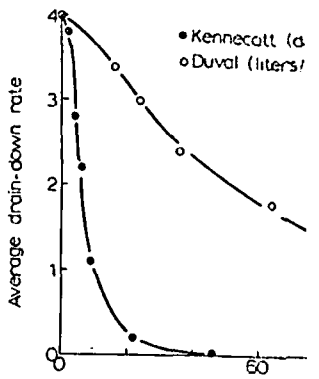

Fig.3. Comparison of initial waste column and the Duval

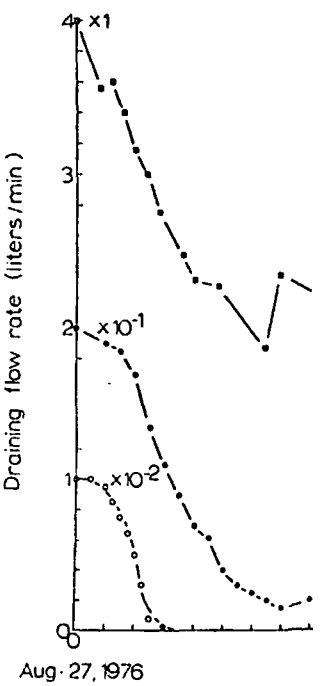

Fig.4. Initial scaling drain-do
Table 2 for scaling details).

ghly 515 days of elapsed
d in Fig.5 that air, at dif-
rge column, and appropriate-
olumns (medium and
iod (Fig.5), the solution
n, followed by a rest period
flush periods ended with

ennecott
CMD

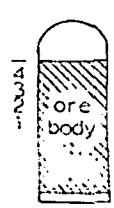

NSF
ival-
Sierrita)

rmeability profiles.

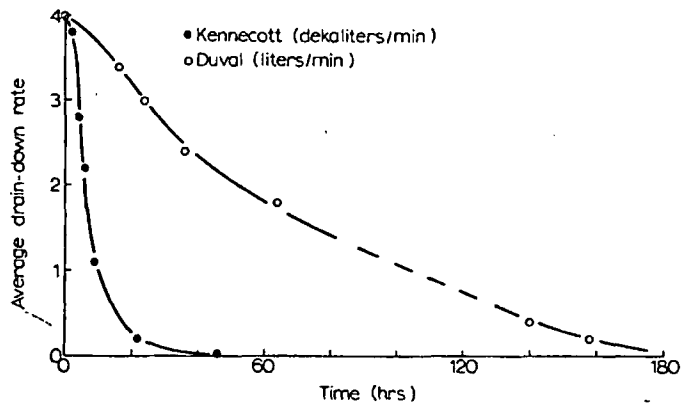

Fig.3. Comparison of initial drain-down rate characteristics for the Kennecott-Santa Rita waste column and the Duval-Sierrita waste column.

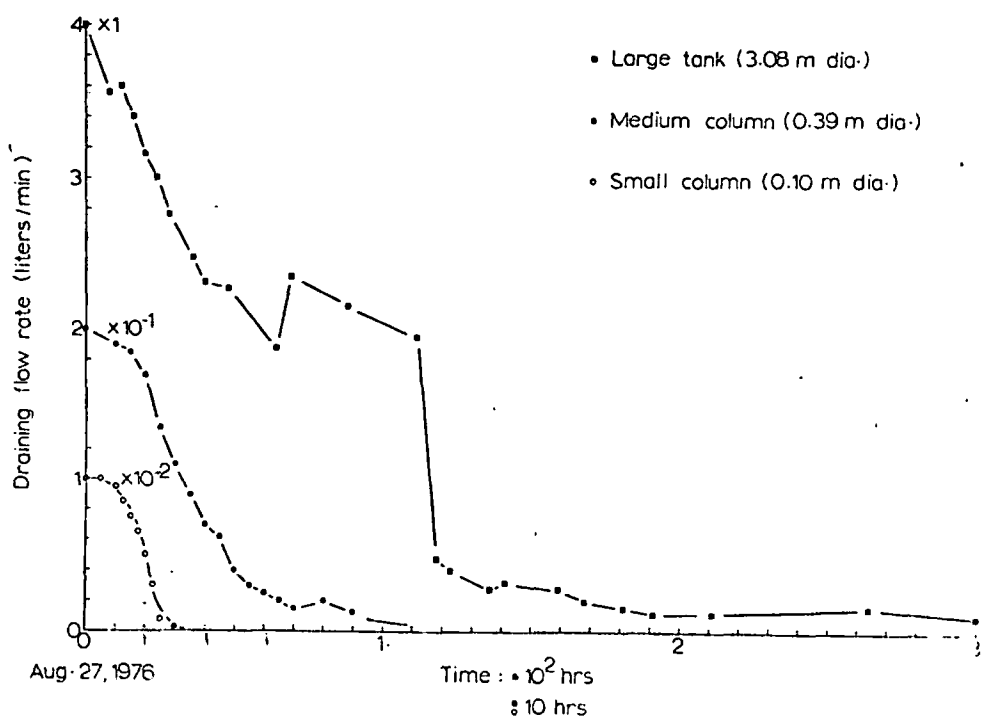

Fig.4. Initial scaling drain-down characteristics for the Duval-Sierrita waste material (see Table 2 for scaling details).

Figure 6 shows the leaching features in terms of copper extracted for the large Duval waste column and the smaller-scale columns as well as those of the Kennecott waste column for comparison. The flush periods and flush sequences for the Kennecott waste column are also indicated. In addition to the enormous difference in leaching characteristics shown on comparing these respective waste bodies, it can be observed from Fig.6(a) that in the large column, there is no measurable copper extraction until after the neutralization period shown in Fig.5. In addition, the scaling of the leaching or extraction of copper seems to be relatively ineffective, especially when comparing the small (laboratory) scale column experiment with the large (Duval) column experiment. This occurs in large part because of the particle size difference, the flow characteristics, and probably temperature. Figure 7 shows the smaller-scale (medium and small column) test temperatures. Since the laboratory temperatures were nearly constant (and consistently high), there was a definite temperature advantage aiding the copper leaching reactions in the laboratory. Figure 8 shows for comparison, the large waste column temperature profiles and the ambient test site temperatures over the total testing period to date. It can be readily observed that the Kennecott waste body temperature profiles are decidedly different from the Duval waste body temperature profiles, and this obviously must account in large part for the very marked differences in copper extraction. Figure 8 shows that to a large extent, the Duval waste body temperatures were controlled by the ambient annual cycle while the Kennecott waste column temperatures were in several cases independent of the ambient temperature. This is due in large part to bacterial catalysis which was much more effective in the Kennecott column than the Duval column as discussed previously [9]. Figure 9 shows, for comparison with Fig.8, the corresponding oxygen consumption data for the two large columns. The ambient annual temperature cycle is observed to influence these values also. It is of interest, however, to note in Fig.9(b), that the oxygen consumption in the Kennecott column does not decline with the abrupt temperature reduction after 300 days of elapsed time. This is due to the continuation of bacterial catalysis [9].

The decline in leaching at the end of the Kennecott experiment as indicated in Figs. 6, 8, and 9 is not really understood at this time although a combination of phenomena seem to be involved. For example, Fig.10 shows some of the changes which occurred during leaching (solution flushes), at the later stages of the experiment. The large difference in the effluent Fe^{2+} concentration is apparent along with the declining pH values. In addition, the draining (flow rate) tail seems shortened at the later flush (21) and the copper concentration corresponding to this tail is considerably reduced from the earlier flush (15). To a large extent these features are characteristic of the internal chemistry, etc. of the waste body which is indicated in some respects in lysimeter data tabulated in Fig.11. Figure 11 should be compared with Fig.8 as well.

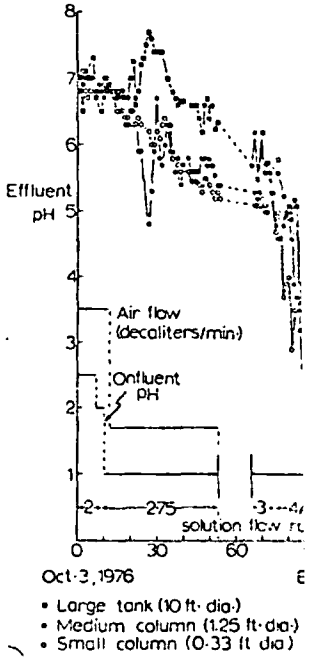

Fig.5. Duval-Sierrita leac

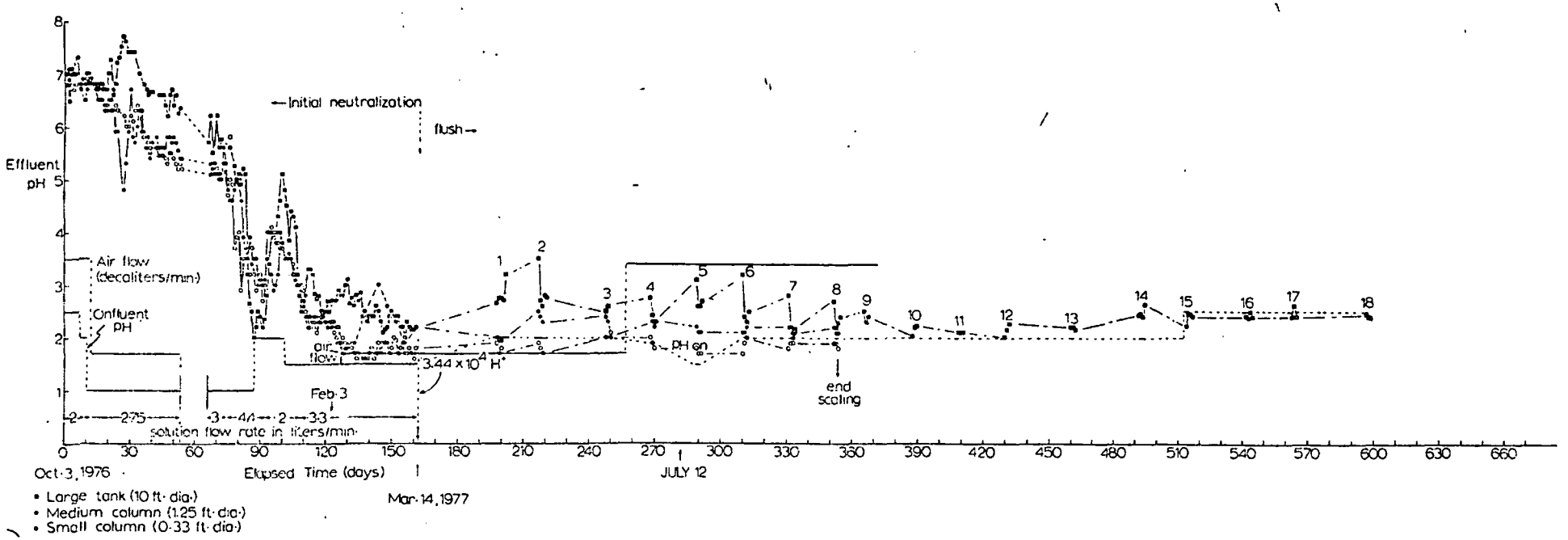

Fig. 5. Duval-Sierrita leach (solution flush) cycle-scaling data and waste-rock neutralization referenced to solution effluent pH. Onfluent pH valves are generally shown as dotted.

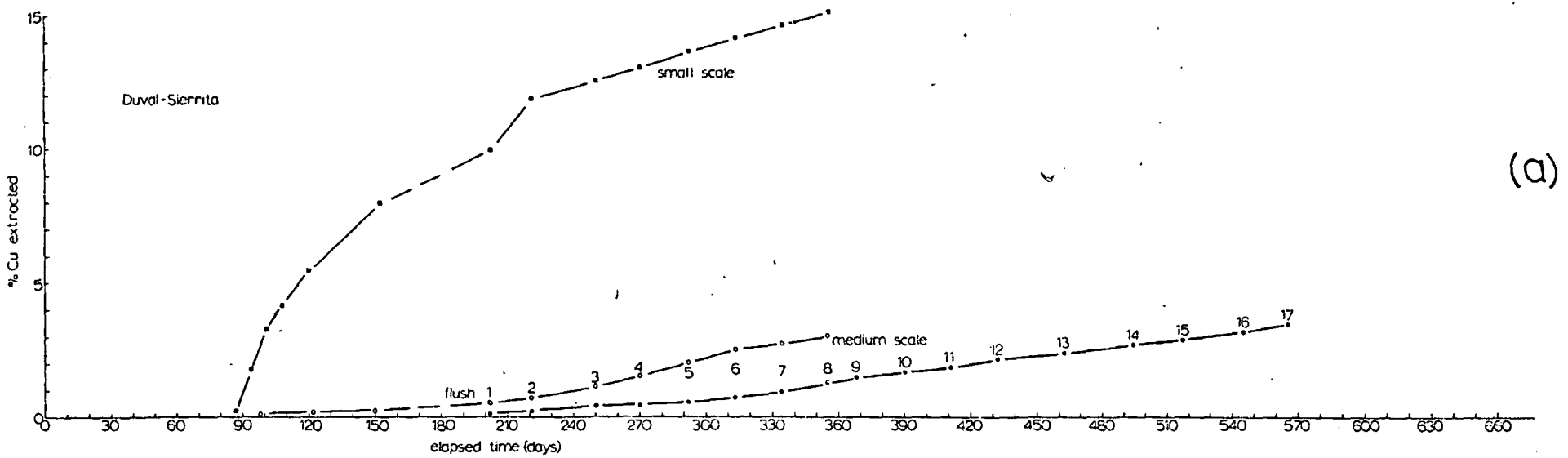

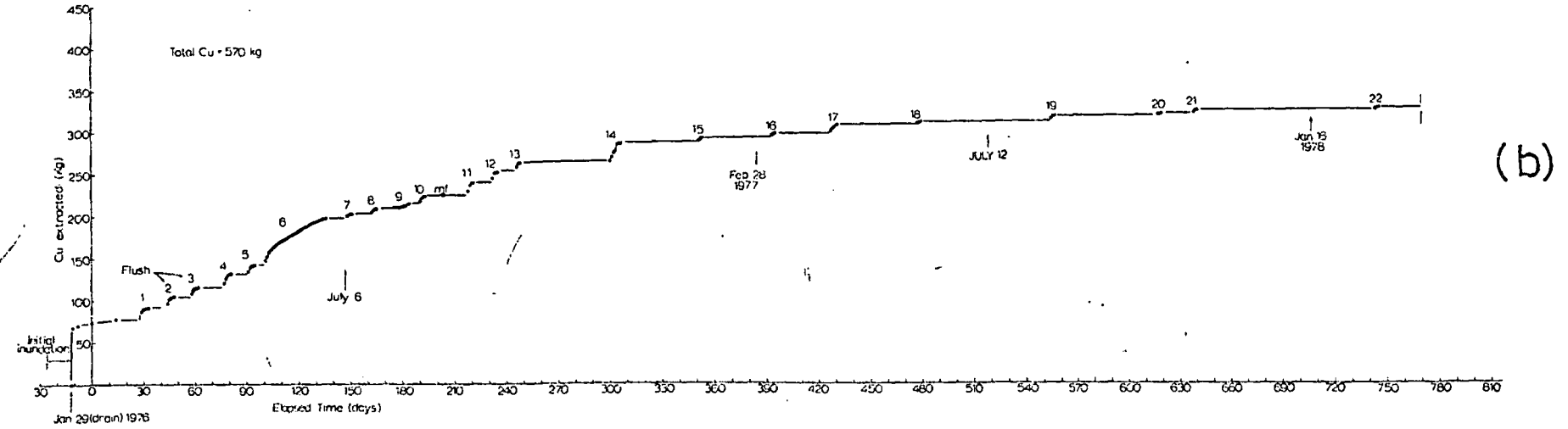

Fig.6. Comparison of Duval-Sierrita copper extraction (and scale tests) (a) and Kennecott-Santa Rita copper extraction data (b). The flush numbers (cycles) noted in (a) correspond to those shown in Fig.5. The (mf) shown in (b) represents a so-called mini-flush mainly for chemical analysis purposes.

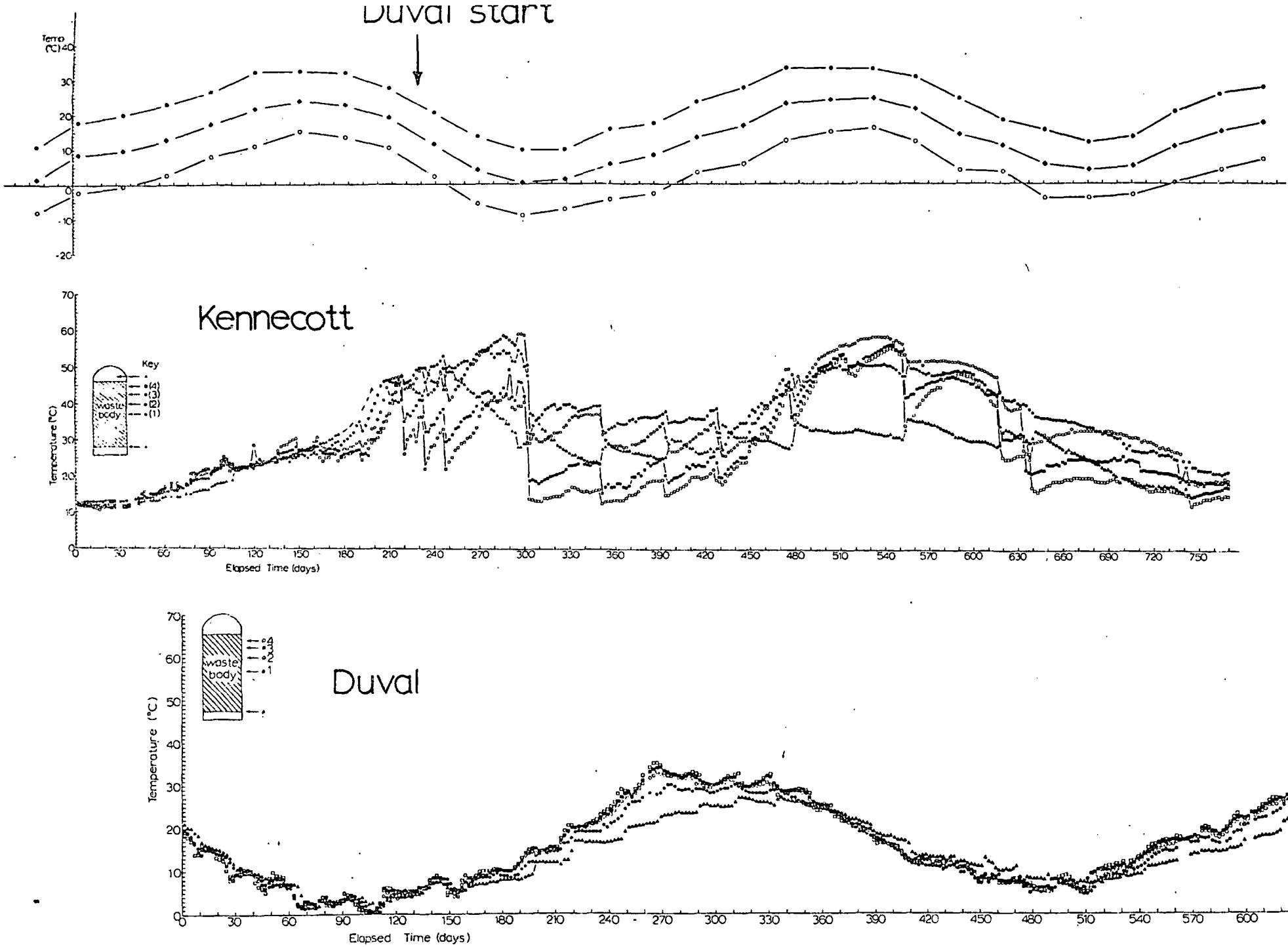

Fig.8. Comparison of large waste-column temperature profiles with each other and with the mean monthly (annual) temperatures at the test site. The monthly temperature curves represent the mean monthly maximum, average and minimum temperatures respectively. The Kennecott column zero time coincides with the monthly temperature zero as shown [illegible] the Duval column zero is shown displaced to the right (Oct. 3, 1976).

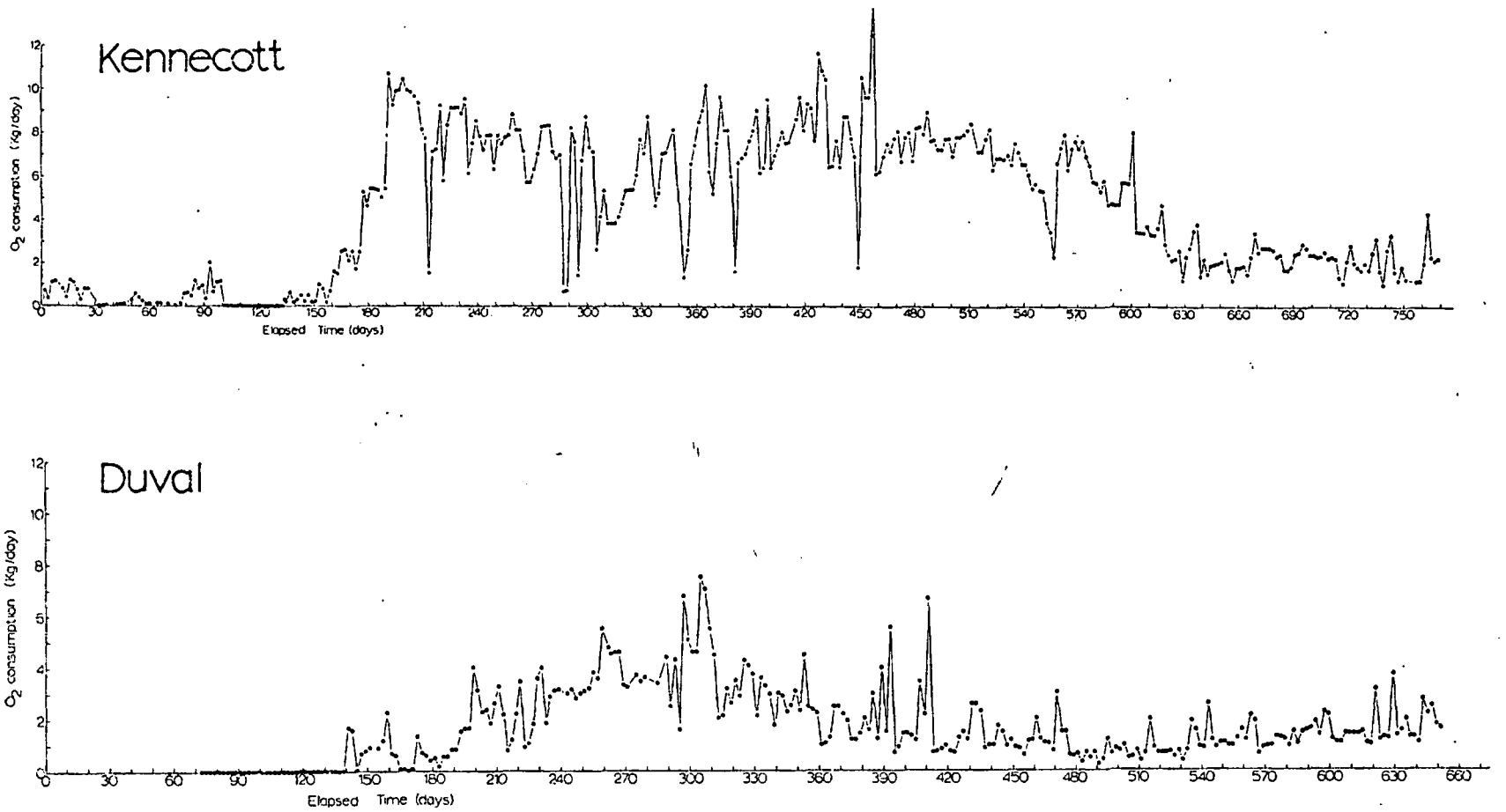

Fig.9. Comparison of daily total oxygen consumption in the two large waste bodies. Zero time refers to those shown in Fig.8. The Kennecott air flow takes varied between roughly 70 l/min and 35 l/min while the Duval column air flows were similar and are shown in Fig.5.

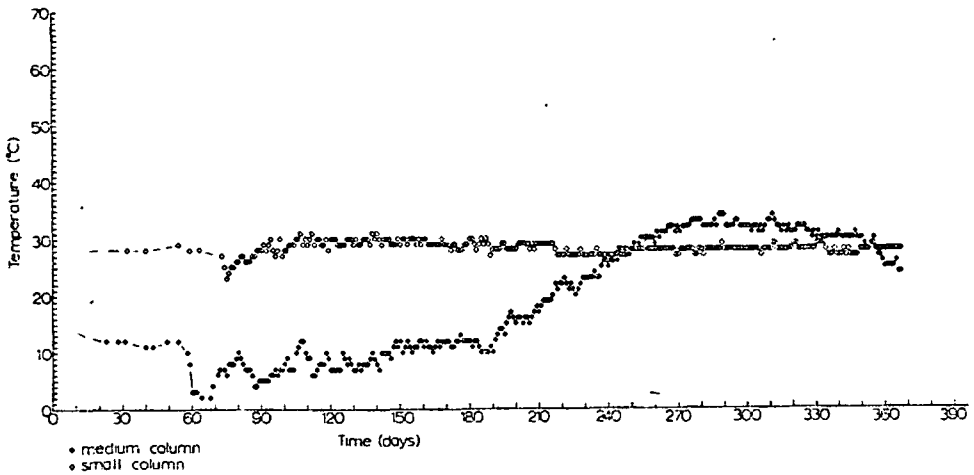

Fig.7. Small-scale Duval-Sierrita waste-column temperature profiles. Zero time corresponds to zero time in Figs. 5 and 6(a).

Figure 12 shows the permeability in the Kennecott waste column following the last flush [22 in Fig.6(b)]. This should be compared with the initial wet body permeability shown in Fig.2. While the initial permeability discontinuity exists in Fig.12, it is shifted somewhat (upward) and altered from Fig.2. Overall, the permeability is higher at the conclusion of leaching the Kennecott waste body, and this is probably another indication of solution channel development during leaching as well as the alteration (degradation) of the rock. Figure 12 shows the general nature of the waste body as it was unloaded. As noted, a hard layer was formed between access port locations 1 and 2 [Fig.1(a)]. This layer formed a slab more than a meter in diameter and roughly 0.25 m thick, and was composed of fine host-rock material (silicates, aluminosilicates, etc.), microcrystals of pyrite in various stages of reaction (and consequently some traces of elemental sulfur were present) large numbers of small gypsum crystals, and jarosites (iron hydroxides) generally coating everything; rendering a yellow-orange coloration throughout. This region was probably somewhat different from the other regions of the waste body and it consumed some acid, forming the gypsum and precipitating the iron from solution. There was no indication of copper precipitation in this regime. The gypsum crystals and other particulates were packed tightly together in this regime, and its porosity was certainly very different from most of the rest of the waste body.

It might be expected, on examining Figs. 2 and 12, that some dead spaces would occur in the Kennecott column as well as perhaps some backmix flow [1]. This is confirmed to some extent by the [Cl^-]-tracer data shown in Fig.

13. The pulse shapes seem to rule out any significant bypass flow, and indeed there was no evidence of such flow in ultraviolet photographs following dye staining and systematic unloading of the waste rock from the top of the column. There was also no evidence of wall channeling around the perimeter of the tank, and flow was concentrated primarily within a region of 2 m radius from the center. In preliminary examinations of several ports following the post mortem of the Kennecott column, U.V. dye photographs tend to indicate that the solution channels allowed roughly 60—70 percent of the waste to be directly contacted. Consequently, the channeling could be completely responsible for the cessation of leaching since 100% of the copper in this contacted volume could have been leached. Figure 6(b) shows in fact that 60% of the total copper was leached. A more detailed analysis of this feature is underway and the results will be published elsewhere.

Unfortunately, as indicated earlier, it was not possible at the time this study was summarized, to compare the Kennecott waste body post mortem with the Duval column. It was also not possible to conduct a more extensive mathematical analysis of the data, particularly the tracer data in Fig.13. However, the results presented, and especially the comparisons made, illustrate that many factors influence the efficient leaching of porphyry copper waste rock, including chemistry, microbiological phenomena, heat generation, fluid and air flow (and convection), and related transport phenomena. All of these factors also change progressively with time, and are altered in the way in which they interact. It is apparent from the results presented in Figs. 2 and 12 as well as Figs. 8 and 10 that the waste body depth (or height), permeability, and solution flow rate are important factors affecting copper leaching from low-grade waste as previously alluded to by Cathles and Apps [8]. It is possible that the Kennecott waste body heating near the mid-point of the column (Fig.8) is due in part to the permeability discontinuity shown in Figs.2(a) and 12 as a result of dead-space production and water retention, thereby promoting enhanced reaction and local heating.

A significant feature differentiating the two large leaching experiments was the fact that the Kennecott experiment utilized tailings water from Chino Mines (New Mexico) which was already high in iron (4 g/l) and the bacterial population was 10^5 cells/cc. The Duval experiment, on the other hand, began with well water and both the iron and bacterial levels had to be developed. Bacterial levels were equivalent to the Kennecott solution at the end of the neutralization period. This certainly could have had a very significant effect on the leaching. However, the fact that the iron and bacterial levels reached similar values makes this a very elusive point indeed.

While this study has attempted to compare two very distinct waste-leaching regimes, the comparison has been qualitative and incomplete. There are many unknown factors and interactions governing the total leaching picture. It is not known, for example, why the temperatures in the Kennecott column began to decline (Fig.8) at the end of the test program, although this must have involved alterations in the waste chemistry and the lixivant chemistry. A prob-

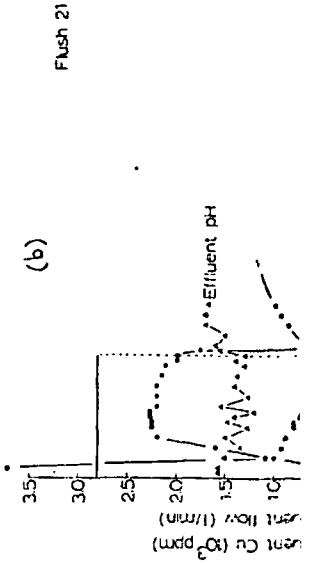

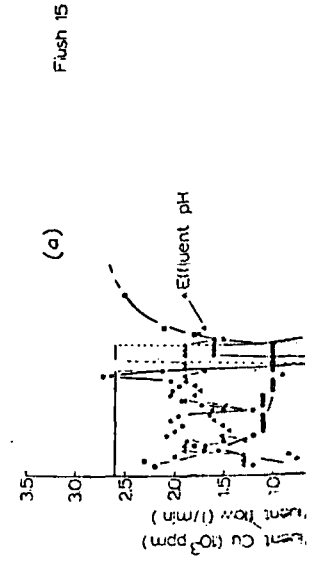

bypass flow, and indeed
tographs following dye
rom the top of the column.
l the perimeter of the
egion of 2 m radius from
rts following the post
aphs tend to indicate
ercent of the waste to be
ıld be completely respon-
copper in this contacted
n fact that 60% of the
f this feature is underway

ible at the time this
aste body post mortem
onduct a more extensive
acer data in Fig.13.
mparisons made, illustrate
porphyry copper waste
na, heat generation, fluid
phenomena. All of these
altered in the way in which
ed in Figs. 2 and 12 as
height), permeability, and
pper leaching from low-
Apps [8]. It is possible
-point of the column
ty shown in Figs.2(a) and
tention, thereby promoting

leaching experiments was
ngs water from Chino
(4 g/l) and the bacterial
on the other hand, began
s had to be developed.
ution at the end of the
a very significant effect
bacterial levels reached

ery distinct waste-leaching
complete. There are many
l leaching picture. It is
ne Kennecott column began
hough this must have in-
ivant chemistry. A prob-

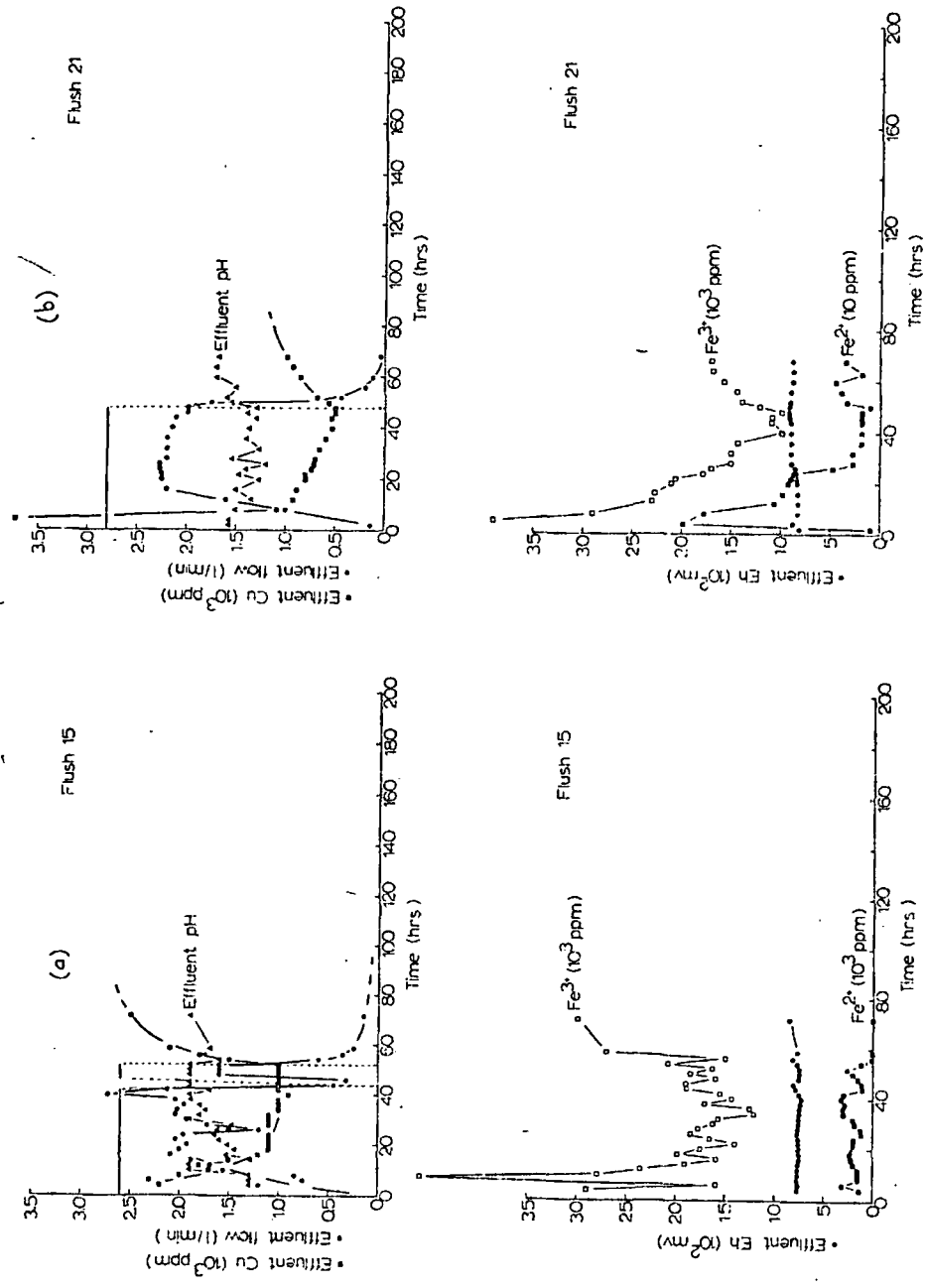

Fig.10. Examples and comparison of the details of the flushes or leaching cycles for the Kennecott-Santa Rita waste column as shown in Fig.6(b). The solid line ending as a dotted step represents the solution onfluent flow rate. (a) shows data for flush No. 15 while (b) shows data for a later flush (No. 21).

bable explanation would involve the fact that essentially all of the solution-contacted rock had been leached of copper. Further analysis of these waste bodies will be necessary to more fully unravel the interacting parameters, and a more rigorous mathematical modeling and testing of the experimental results will certainly provide additional clarification. The present results are also indicative of a failure to scale the leaching data for a very high acid-consuming chalcopyrite waste and this will require some additional attention in future tests or analysis of the present data.

SUMMARY AND CONCLUSIONS

This paper has dealt with a qualitative comparison of experimental leaching and related data for two very different porphyry copper-waste bodies: A Kennecott-Santa Rita, mainly chalcocite waste and a Duval-Sierrita, mainly chalcopyrite waste. Initial permeability, draining flow characteristics, and leach solution application cycles have been described as these might relate to the copper extraction and other leach-related phenomena. It has been shown that in one case, waste-body heating was somewhat independent of annual temperature cycles while the temperature profile in the other system was strictly controlled by ambient temperature variations. Whether a waste-body temperature is controlled intrinsically or extrinsically (from within or without) probably depends upon a number of parameters including the mineralogy, solution chemistry, bacterial activity and perhaps is significantly controlled by solution flow, air convection, permeability, and other phenomena such as oxygen mass transfer, acid consumption of gangue and other host minerals.

On the basis of the results presented and the comparisons made, the following specific conclusions are drawn:

(1) Permeability of a waste body has an important influence on leaching as a result of its relationship to solution flow and air convection, which are the principal transport agents giving rise to leaching reactions.

(2) Permeability changes which occur during the course of leaching as a result of decrepitation, channeling, or the development of zone structures either by precipitation, reactions producing agglomeration, and related phenomena can alter the heat and air convection, solution flow patterns, etc. and have a significant effect on the rate of reactions attendant to the recovery of metal values in solution.

(3) Scaling of copper sulfide leaching, particularly chalcopyrite waste leaching, is a very complex task requiring far more than a consideration of simple geometrical parameterization. To the extent that permeability, solution flow, heat and air convection are altered in different regimes and size distributions, this must be better understood and included in any successful model involving laboratory scale-up. To a large extent, the important features of heap or dump leaching of chalcopyrite waste do not seem to be readily amenable to scale-up from laboratory experiments.

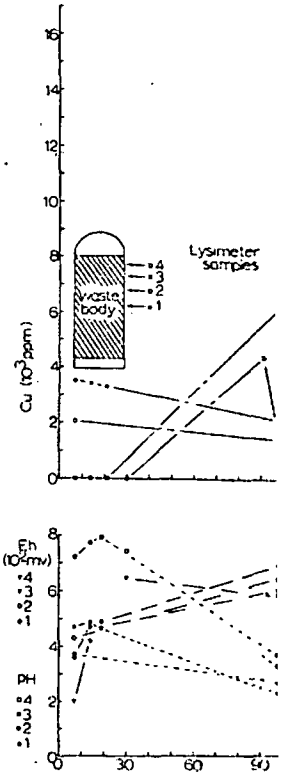

Fig. 11. Cu, Eh, and p
by solution sampling
imbedded within the
tion details].

y all of the solution-
alysis of these waste
acting parameters,
g of the experimental
he present results are
r a very high acid-
ne additional attention

f experimental leaching
r-waste bodies: A
)uval-Sierrita, mainly
characteristics, and
s these might relate
mena. It has been
hat independent of
le in the other system
ons. Whether a waste-
cally (from within or
ers including the mineral-
is significantly con-
and other phenomena
gue and other host

isons made, the follow-

ıfluence on leaching
ınvection, which are the
ns.
ırse of leaching as a re-
f zone structures either
ıd related phenomena
terns, etc. and have a
he recovery of metal

ıalcopyrite waste
ı a consideration of
t permeability, solu-
nt regimes and size
led in any successful
the important features
seem to be readily

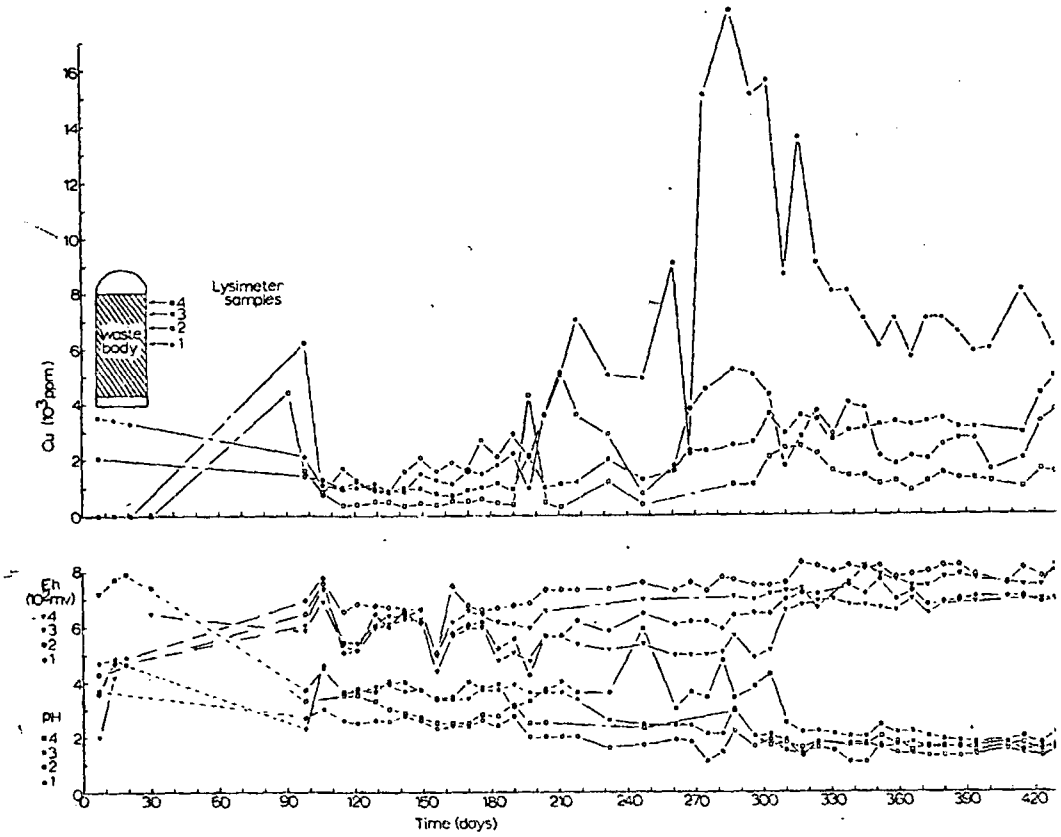

Fig.11. Cu, Eh, and pH profiles within the Kennecott-Santa Rita waste body determined by solution sampling at the access port locations shown from the porous-cup lysimeters imbedded within the waste rock at the respective locations [see Fig.1(a) for specific location details].

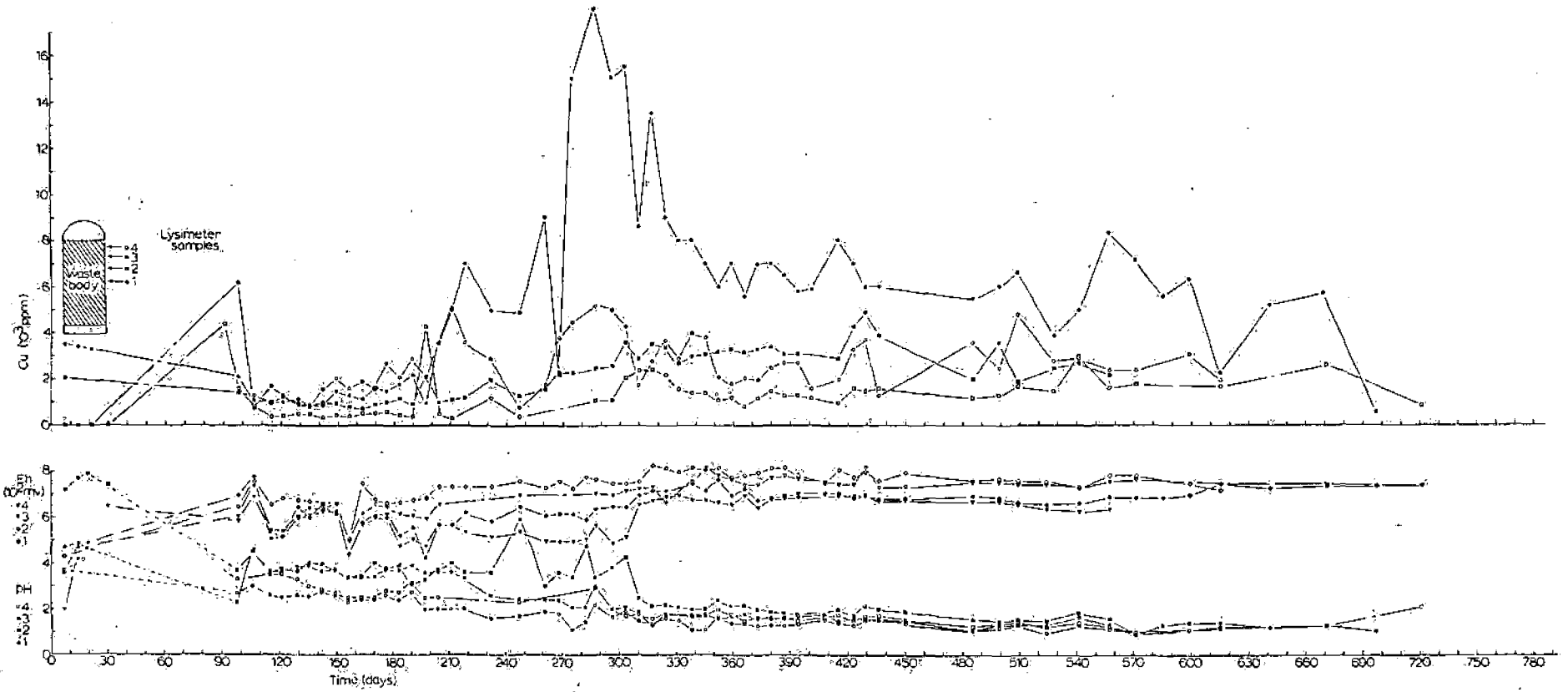

Fig.11. Cu, Eh, and pH profiles within the Kennecott-Santa Rita waste body determined by solution sampling at the access port locations shown from the porous-cup lysimeters imbedded within the waste rock at the respective locations [see Fig.1(a) for specific location details].

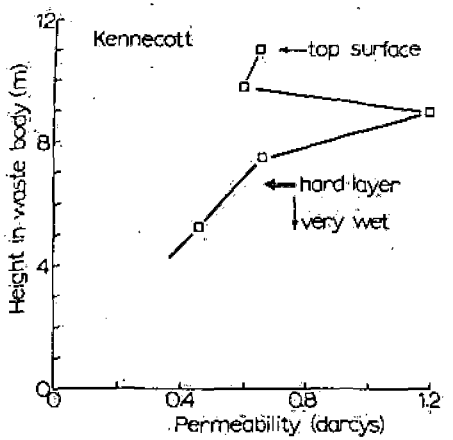

Fig. 12. Kennecott-Santa Rita waste-body permeability profile at the conclusion of leaching experiments (approx. 800 days from start up) for comparison with Fig. 2.

Fig. 13. [Cl^-] tracer and effluent pH data for Kennecott-Santa Rita waste body at the conclusion of leaching (approx. 800 days from start up). It is to be noted that the Cl^- tracer pulses indicated by symbol are an indication of the time of addition and not the initial concentration to scale. The concentration is apparent where the symbol is defined. Note also that the onfluent and effluent flow rates are not equal in steady-state periods. This occurs in large part due to variations in onfluent rate and effluent lag. It is also indicative of hold-up or related flow phenomena. Both onfluent and effluent flow rates were directly measured using a graduated container and a stop watch.

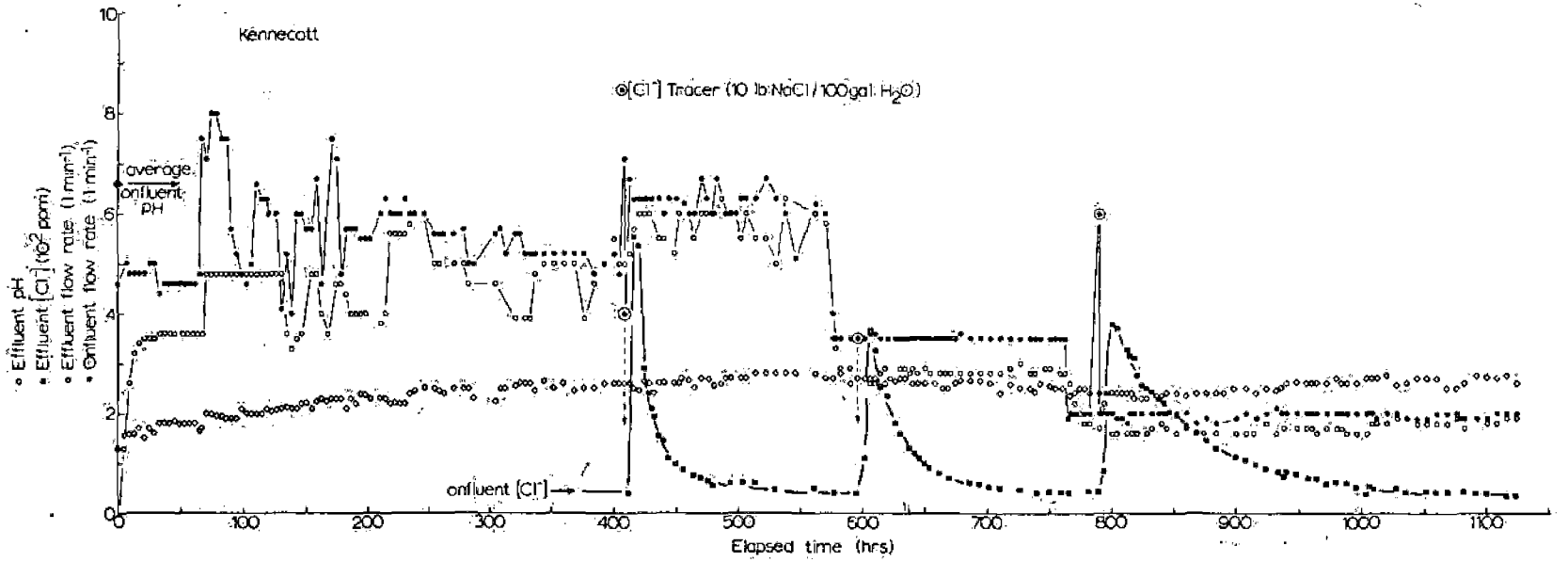

(4) Large-scale experiments such as those outlined herein can provide for a more realistic assessment of a leach dump regime or unit and provide for an opportunity to directly test flow and transport models and compare the results with tests conducted on actual dumps. The [Cl^-] tracer data presented herein is a good example of experimental data which can be tested in this way.

(5) Detailed leaching studies combined with post-mortem (or post-leaching) investigations on a large scale as reported herein can begin to provide some realistic indications of the important parameters which are involved in the leaching process.

ACKNOWLEDGEMENTS

This research was supported in part by the Kennecott Copper Corporation, Metal Mining Division, and by the National Science Foundation (RANN) under grant No. AER-76-03758 and AER-76-03758-A01. The comments and discussions with members of the NSF-Project Oversight Committee — L.M. Cathles, M. Wadsworth, K. Temple, R. Groves, J. Grunig, E.E. Malouf, N. Arbiter, J. Apps, D.A. Reese, and W.J. Schlitt — were especially important in attempting to execute and interpret the experiments described in this paper, and they are gratefully acknowledged. The help of many students in gathering and maintaining these data is also appreciated, and special thanks must be extended to Mack Stallcup, Stewart Ingham, and Sara MacMillan. Finally, a special acknowledgement is made to Drs. W.J. Schlitt and J.D. Stephens of Kennecott's Research Center in Salt Lake for their guidance during the post-mortem procedures.

REFERENCES

1 J. Szekely and N.J. Themelis, Rate Phenomena in Process Metallurgy, Wiley-Interscience, New York, 1971.
2 L.M. Cathles, D.A. Reese and L.E. Murr, Dump leaching theory, experiment and practice, in Proc. American Nuclear Soc. Topical Meeting on Energy and Mineral Recovery Research, DOE CONF-770440, Tech. Info. Center, 1978, p. 584.
3 R.W. Bartlett, A combined pore diffusion and chalcopyrite dissolution kinetics model for in-situ leaching of fragmented copper porphyry, in D.J.I. Evans and R.S. Shoemaker (Eds.), Int. Symp. on Hydromet., AIME, New York, 1973, p. 331.
4 R.L. Braun, A.E. Lewis and M.E. Wadsworth, In place leaching of primary sulfide ores: laboratory leaching data and kinetic model, in F.F. Aplan, W.A. McKinney and A.D. Pernichele (Eds.), Solution Mining Symp., AIME, New York, 1974, p. 295.
5 R.J. Roman, B.R. Benner and W. Becker, Trans. SME/AIME, 256 (1974) 247.
6 R.J. Roman, Trans. SME/AIME, 262 (1977) 73.
7 J.A. Harris, Proc. Australian Inst. Mining and Met., No. 230, 1969, p. 91.
8 L.M. Cathles and J.A. Apps, Met. Trans., 6B (1975) 617.
9 L.E. Murr and J.A. Brierley, The use of large-scale test facilities in studies of the role of microorganisms in commercial leaching operations, in L.E. Murr, A.E. Torma and J.A. Brierley (Eds.), Metallurgical applications of bacterial leaching and related microbiological phenomena, Academic Press, New York, 1978, p. 491.

ON THE EFFECT OF ANISOTROPY IN EXPLOSIVE FRAGMENTATION

John K. Dienes
Theoretical Division, Group T-3
University of California
Los Alamos National Laboratory
Los Alamos, NM 87545

INTRODUCTION AND SUMMARY

An alternative to the use of the plasticity theories to characterize the dynamic behavior of rock is to represent the effect of flaws by statistical methods. We have taken such an approach to study the fragmentation of oil shale because it appears to have a large number of advantages. Foremost among these is that by considering the effect of cracks on rock behavior it becomes possible to address the underlying physics directly and to understand the phenomena that occur during fragmentation. In addition, in such an approach the parameters that characterize material properties have a straightforward physical interpretation and can often be determined by direct measurements. Mean crack size and the number density of cracks are important examples. In a more physical approach it should also be possible to encompass a wider range of scales with a few parameters than in a phenomenological theory. For instance, we note that plasticity theory does not naturally account for rate effects, though they can be artificially introduced through additional functions, which are determined empirically. In our SCM (Statistical Crack Mechanics) theory, however, rate effects are naturally accounted for by introducing the speed of crack growth to characterize the behavior of unstable cracks. It was shown by Dienes and Margolin (1980) that this is sufficient to represent the observed rate effects in oil shale, which are very large. Similarly, size effects are known to be important in rock mechanics, with small samples showing much higher strength than large ones, and such effects are accounted by statistical methods without introducing any new physics. Another serious concern is that the dilatancy observed when rocks are sheared is not modelled in a natural way by plasticity theories. In a micromechanical approach, however, cracks open during loading and may remain open on unloading, and this appears to be the essence of dilatancy. An additional advantage is that it becomes possible to compute permeability from an analysis of intersecting cracks with such a theory.

An attempt to formulate an isotropic statistical theory by Dienes (1978a) was abandoned because it could not incorporate the effects of shear cracks, which we believe are important under compressive loading, and because it appears to be important to permit cracks with certain orientations to grow while others remain fixed in size. This is particularly the case in oil shale, in which bedding cracks play an important role. The current theory, which allows for anisotropic crack distributions, has now been coupled to the SALE hydrodynamic code, making it possible to compute explosion, impact or other dynamic processes. In addition to summarizing the theory, the object of this paper is to show that a spherical explosive calculation with SCRAM using published mechanical properties of oil shale agrees well with experiment.

SCRAM

In the preceeding symposium a theoretical approach to Statistical Crack Mechanics was described and some results based on the SCM computer program were presented. SCM returns the stress as a function of time when supplied with a tensor strain rate history, accounting for growth and coalescence of cracks. In SCRAM the SCM subroutine is coupled to a general purpose code, SALE, written by Amsden, Ruppel and Hirt (1980) which integrates the equations of continuum motion. Although in the current work SALE is used as a Lagrangian code, it has the capability to calculate deformation using an Eulerian mesh, or with a mesh which passes through the continuum in an arbitrary manner. Hence, SALE is an acronym for Simplified Arbitrary Lagrangian Eulerian.

A central idea of SCM is to represent the strain rate as the sum of several parts. The first is a strain rate due to distortion of the matrix material, which is characterized as a Maxwell solid. The second is a strain rate due to distortion of an ensemble of open microcracks. The third results from interfacial sliding of shear (closed) cracks. The fourth is a strain rate due to unstable crack extension, and the fifth is the result of material rotation. Expressions for these quantities have been derived in Los Alamos oil shale quarterly reports, and here we shall only summarize the main results. For the matrix strain rate we put

$$d^e_{ij} = C_{ijk\ell}\dot{\sigma}_{k\ell} \qquad (1)$$

where the dot is used to denote the rate of change of stress. It is not the Zaremba-Jaumann-Noll stress rate, nor its generalization described by Dienes (1979b), for the rotation terms are accounted for separately below.

In addition to the matrix deformation we account for the influence of microcracks, which are considered as an ensemble of flat circular cracks. The theory is exact in the sense that the opening of an isolated circular (penny-shaped) crack under an arbitrary (static) state of stress is known. Though one might consider more general cracks, the influence of shape appears to be quite small. We consider the crack statistics to be defined by a distribution function $N(c,\Omega,t)$ in which Ω designates, symbolically, crack orientation. Then $N(c,\Omega,t)\Delta\Omega$ represents the number of cracks with orientation near Ω whose radii exceed c with normals in the range of solid angles represented by $\Delta\Omega$. It is shown by Dienes and Margolin (1980) that the strain rate due to opening of these cracks is given by

$$d^o_{ij} = \beta^o \dot{\sigma}_{ij} \int_\Omega d\Omega\, n_i n_j n_k n_\ell \int_0^\infty dc \frac{\partial N^o}{\partial c} c^3 \qquad (2)$$

where the n_i are the components of the unit crack normal, N^o denotes the distribution of open cracks, and

$$\beta^o = 8(1-\nu)/3\mu \quad , \tag{3}$$

with ν and μ the Poisson ratio and shear modulus. Since the general solution for a crack in an anisotropic material is not known, we have to use average values for μ and ν if the matrix is considered anisotropic. In the current calculation, however, we will be considering the material to be isotropic, and will assume that the observed anisotropy arises from cracks in the bedding planes, so that the theory is self-consistent in this example. The superscript in N^o is used to denote the distribution of open cracks. The criterion for cracks to be open is that the normal component of traction $\sigma_{ij}n_in_j$, be positive (tensile).

In addition to the strain resulting from crack opening there may be a significant contribution from interfacial sliding of closed cracks. By arguments a little more complicated than for open cracks, we have obtained the expression

$$d^S_{ij} = \beta^S \dot{\sigma}_{k\ell} \int_\Omega d\Omega\, b_{ijk\ell} \int_o^\infty dc\, \frac{\partial N^S}{\partial c}\, c^3 \tag{4}$$

for the rate of strain due to shear cracks in which

$$\beta^S = 8(1-\nu)/3\mu(2-\nu) \tag{5}$$

and

$$b_{ijk\ell} = n_in_k\delta_{j\ell} + n_jn_k\delta_{i\ell} - 2n_in_jn_kn_\ell \quad . \tag{6}$$

Here N^S denotes the distribution of closed (shear) cracks - those for which the normal component of traction is negative (compressive).

If the normal force on a closed crack is significantly greater than the tangential force, friction may prevent interfacial sliding. In this case we say that the crack is locked, and N^S is set to zero. The normal component of traction is given by

$$B = \sigma_{ij}n_in_j \tag{7}$$

and the tangential stress by

$$\tau = \sqrt{A - B^2} \tag{8}$$

where

$$A = \sigma_{ij}n_j\sigma_{ik}n_k \tag{9}$$

is the magnitude squared of the traction acting on a crack. The locking criterion is simply

$$A < (\bar{\mu}^2+1)B^2 \tag{10}$$

where $\bar{\mu}$ is the coefficient of friction.

Cracks become unstable when the far-field stress is large enough. The effect of unstable crack growth on a microscopic level is to produce additional strain rate at the macroscopic level. According to data collected by Stroh (1957), under high stresses cracks propagate at about a third of the longitudinal wave speed. We denote this constant speed by $\dot{c}$. The stability criterion we use is given by Dienes and Margolin (1980) as

$$A > \nu B^2/2 + \zeta \tag{11}$$

where

$$\zeta = \pi E\gamma(2-\nu)/4c(1-\nu^2) \quad , \tag{12}$$

and is an extension of the Griffith criterion. For shear cracks the stability criterion is significantly more complicated because of the effect of interfacial friction. Dienes (1978c) finds

$$c < \pi\gamma\mu(2-\nu)/2(1-\nu)(\tau-\tilde{\tau})(\tau-3\tilde{\tau}) \tag{13}$$

where

$$\tilde{\tau} = \bar{\mu}B \tag{14}$$

and τ is the shear stress defined above.

Crack growth is quite different from crack opening, as it involves a change in crack diameter rather than crack width. If we write

$$\varepsilon^o_{ij} = \beta^o\sigma_{k\ell} \int_\Omega d\Omega\, n_in_jn_kn_\ell F^o(\Omega) \tag{15}$$

as the strain due to open cracks, it may change because of either changes in stress, $\sigma_{k\ell}$, or changes in the distribution, $N^o(c,\Omega,t)$ which influences ε^o_{ij} through

$$F^o(\Omega) = \int_o^\infty dc\, c^3\, \frac{\partial N^o(c,\Omega,t)}{\partial c} \quad . \tag{16}$$

The rate of change of strain due to the crack growth can be written as

$$d^{go}_{ij} = \beta^o\, \sigma_{k\ell} \int_\Omega d\Omega\, n_in_jn_kn_\ell\, \dot{F}^o(\Omega) \tag{17}$$

where

$$F^o = \int_o^\infty dc\, c^3 \frac{\partial N^o}{\partial c} \quad . \tag{18}$$

There is a similar contribution due to unstable extension of shear cracks which we write as

$$d_{ij}^{gS} = \beta^S \sigma_{k\ell} \int_\Omega d\Omega\, b_{ijk\ell} F^S \tag{19}$$

where

$$F^S = \int_o^\infty dc\, c^3 \frac{\partial N^S}{\partial c} \tag{20}$$

and the integral is taken over all unstable, closed cracks that are not locked. The total strain rate due to crack extension, d_{ij}^g, is the sum of the expressions in (17) and (19).

The need to account for material rotation was mentioned above, and arises from the effect of material rotation on the stress tensor. It is shown by Dienes (1979d) that the strain rate due to material rotation is given by

$$d_{ij}^r = Y_{ik}W_{kj} - W_{ik}Y_{kj} \tag{21}$$

where

$$Y_{ij} = \beta^o Z_{ijk\ell}\sigma_{k\ell} + \beta^S\left(z_{ik}\sigma_{kj} + \sigma_{ik}z_{kj} - 2Z^S_{ijk\ell}\sigma_{k\ell}\right) + C_{ijk\ell}\sigma_{k\ell} \tag{22}$$

and for moderately small distortions W_{ij} is the vorticity. If the deformation is large it is shown by Dienes (1979b) that W_{ij} should be replaced by a rate of material rotation, Ω_{ij}, and the current code has this capability. In (22)

$$Z^o_{ijk\ell} = \int_\Omega d\Omega\, n_i n_j n_k n_\ell F^o \quad , \tag{23}$$

$$Z^S_{ijk\ell} = \int_\Omega d\Omega\, b_{ijk\ell} F^S \quad , \tag{24}$$

and

$$z_{ij} = \int_\Omega d\Omega\, n_i n_j F^S \quad . \tag{25}$$

At high pressure the cracks are closed and locked and material behavior is governed by a high-pressure equation of state which we assume to be isotropic and have the Mie-Gruneisen form described by McQueen et al. (1970). However, since material behavior in the linear regime is already accounted for by the preceeding (anisotropic) representation, the linear behavior must be subtracted out of the equation of state. If we take the general form of the equation of state to be

$$p = G_o\rho_o I + f(\rho) \tag{26}$$

where I denotes the internal energy and ρ, the density; and also assume the linear form

$$u_S = c + Su_p \tag{27}$$

between shock velocity, u_S, and particle velocity, u_p, then it is straightforward to show that

$$f(\rho) = k\theta\left(1-G_o\theta/2\right)/(1-S\theta)^2 \tag{28}$$

where θ is used to denote the compression

$$\theta = 1 - \rho_o/\rho \quad . \tag{29}$$

It follows that the high-pressure portion of the stress tensor is given by

$$\dot\sigma_{ij}^h = \left[\left(k\rho_o/\rho^2 - f_\rho\right)\dot\rho - G_o\rho_o\dot I\right]\delta_{ij} \quad . \tag{30}$$

where k is the bulk modulus.

The preceeding results can be summarized by

$$d_{ij} - d_{ij}^r - d_{ij}^g = H_{ijk\ell}\dot\sigma_{k\ell} \tag{31}$$

where

$$H_{ijk\ell} = \beta^o Z_{ijk\ell} + \beta^S\left(z_{j\ell}\delta_{ik} + z_{i\ell}\delta_{jk} - 2Z^S_{ijk\ell}\right) + C_{ijk\ell} \quad . \tag{32}$$

In the current version of SCM it is assumed that initially all the cracks are exponentially distributed and active, that is, free to grow if the stress is great enough to make them unstable. As a result of intersections, however, we envisage that many cracks will become inactive. Without intersections failure of rock samples would be catastroptic with the largest cracks free to propagate through the sample. This is not what is usually observed, and we believe that this is, at least in part, because the material behavior is modified by crack intersec-

tions. We denote by $L(c,\Omega, t)$ the number of active cracks with orientation Ω whose radii exceed c, with a similar definition of $M(c,\Omega,t)$ for the inactive cracks. The total number density of cracks, N, is the sum of L and M. When cracks with the mean size, $\bar{c}$, are unstable we consider all the cracks with that orientation to be unstable. This is a great simplification, and does not cause a major error since the smallest cracks do not contribute significantly to the overall behavior. It is shown by Dienes (1978a) that L satisfies the Liouville equation

$$\dot{L} + \dot{c}L' = -\dot{M} \tag{33}$$

where L' denotes the derivative with respect to c and

$$\dot{M} = kL \tag{34}$$

is the rate at which active cracks become inactive. It can be shown that for $c > \dot{c}t$

$$L = N_o \exp[-(c-\dot{c}t)/\bar{c}-kt] \tag{35}$$

and

$$M = (N_o k/\bar{c}\beta)[\exp(\beta t-c/\bar{c}) - \exp(-c/\bar{c})] \tag{36}$$

whereas for $c < \dot{c}t$, $L = 0$ and

$$M = (N_o k/\bar{c}\beta)[\exp(-kc/\dot{c}) - \exp(-c/\bar{c})] \quad . \tag{37}$$

Here,

$$\beta = \dot{c}/\bar{c}-k \tag{38}$$

and k describes the rate at which cracks become inactive. Dienes (1978a) gives an estimate for k in the case of an isotropic distribution. Since it has become clear that isotropy is too strong an assumption, we have formulated a more general theory with the parameters depending on orientation. We assume that the crack orientations are lumped into a finite number of bins (currently 9) with average orientation, Ω_j.

For oil shale it is natural to divide the distribution of cracks into a bedded set and an isotropic set. Then, it can be shown that

$$k_j = (4\pi^2\dot{c}/\alpha)(\pi^2 L\bar{c}^{-2} + N_b\bar{c}_b^{-2} \sin\theta_j) \tag{39}$$

where L represents the number density of isotropic cracks; N_b, the number density of bedded cracks; θ_i, the angle of the ith bin with the bedding planes; $\bar{c}$, the mean size of isotropic cracks; $\bar{c}_b$, the mean size of bedded cracks, and α, a crack intersection parameter, typically 4.

The fragmentation theory has been incorporated into a family of subroutines called SCM. The simplest use of the subroutine is with a driver that prescribes the strain rate for SCM, which then prints out stress and strain at prescribed intervals. Verification of SCM was described in the preceeding symposium. One method was to run hystersis loops simulating triaxial test conditions and verify that the behavior was credible and that the residual energy had the correct sign. Another test was to run loading histories to a fixed strain at different strain rates. The final stresses were strongly strain rate dependent, and are in qualitative agreement with experimental data obtained by Grady and Kipp (1980). Quantitative comparisons are not feasible because the crack statistics for the samples tested are not available. The most definitive test of SCM was to determine the moduli of the cracked material for several kinds of loading from computer output and compare with analytic solutions, which can be obtained when the crack distribution is isotropic.

COMPARISON OF SCRAM WITH EXPERIMENT

The original purpose of the spherical shots carried out by Fugelso (1978) was to determine an effective yield strength for oil shale by embedding in it spheres of high explosive and comparing radiographs of the cavity produced with numerical calculations. Such a comparison was made by Dienes (1978d) using plasticity theory and an average yield strength of 100 MPa (14500 psi) for 1.85 g/cc oil shale and showed fair agreement. The discrepancy was due primarily to asymmetry of the cavity which is aspirin-shaped, having vertical sides and rounded top and bottom. In order to explain this curious shape, calculations were made with a number of variations on the anisotropic plasticity theory developed by Dienes (1979a), but in no case were there any significant deviations of the cavity from a spherical shape. It was, therefore, most gratifying to find that SCRAM could calculate the shape accurately. In the remainder of this section we discuss the experiment, details of the calculation, and present an explanation of the cavity shape.

The spherical explosive experiment was set up by machining a one-inch hole with a hemispherical bottom in an irregular block roughly a foot across. A one-inch sphere of PBX-9501 was placed in the hole, which was then filled with clay. The detonation mechanism for the spheres has been carefully designed to result in spherical detonation waves. Tests on shales of different densities were made, but in this paper we will be concerned only with the cavity in 1.85 g/cm^3 material. A radiograph was made at 30 μs and is reproduced in Fig. 1. The horizontal lines are evidence of the layered structure, and the aspirin-shape is evident.

In order to obtain a credible explanation of the cavity shape using numerical calculations it is important to establish a priori the properties of the oil shale. Since the current theory is based on crack statistics, one could go for direct measurements of crack size and number density, and this is the approach taken at SRI, as discussed by Seaman, Curran, and Shockey (1976). There is an alternative, however, which may be more conservative and is much easier to implement, and that is to infer crack statistics from simple mechanical properties such as strength and elastic moduli. This allows us to avoid

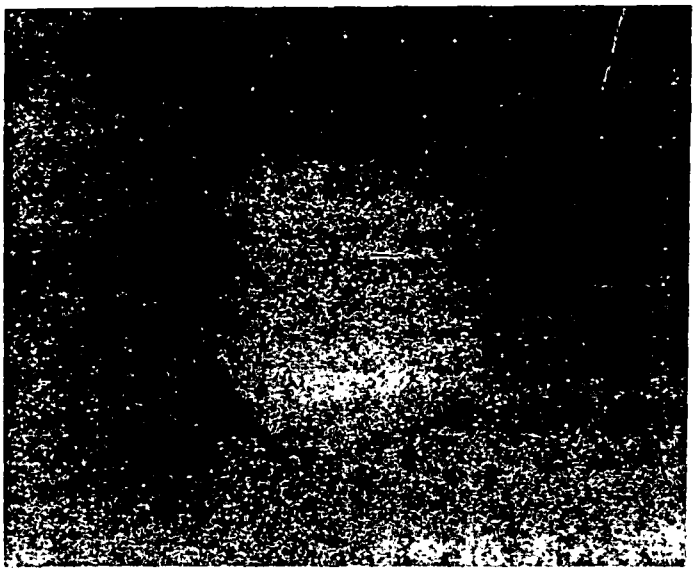

Fig. 1. Radiograph of the cavity produced in oil shale at 30 μs by a one-inch sphere of explosive.

difficult questions such as how to characterize cracks that are not penny-shaped, what to do about characterizing flaws that are not cracks, such as inclusions and crystal boundaries, and how to determine volumetric properties from observations on a surface. Though Dienes (1979c) has addressed the problem of inferring volume statistics from observations on a plane, the circumstances are somewhat idealized and have not been verified by direct observation. Perhaps more to the point, mechanical properties are available for oil shale and crack statistics are not.

According to ultrasonic measurements by Olinger (1976) the elastic properties of oil shale with density 1.85 g/cm^3 considered as a transversely isotropic material are given by c_{11} = 21.7 GPa, c_{33} = 13.2 GPa, c_{44} = 4.2 GPa, c_{12} = 8.0 GPa and c_{13} = 6.0 GPa. In terms of Young's modulus and the generalized Poisson ratios Dienes (1976) finds E = 17.5 GPa, E' = 10.8 GPa, ν = 0.276, ν' = 0.204, and ν'' = 0.332. In order to determine crack size, we make use of the Griffith criterion and tensile strength measurements by Youash (1969), who has tested a number of anisotropic materials at varying orientations. He finds that rich oil shale varies in strength from 300 psi when loaded across the bedding planes to 1600 psi when loaded in the bedding planes. The lean varied from 900 to 1400 psi with orientation. Dynamic measurements have been made by Schuler, Lysne and Stevens (1976) who find that rich oil shale has a dynamic tensile strength averaging 2645 psi and the lean, 3340 psi, with no apparant dependence on orientation. For the SCRAM calculation we assume a tensile strength of 1250 psi when loaded across the bedding planes and 2500 psi when loaded in the bedding planes. Much more work needs to be done to characterize the tensile strength.

To determine the crack statistics we begin with the fracture toughness relation

$$\sigma^2 c = K^2/\pi = 2E\gamma \tag{40}$$

and an estimate by Grady (1980) for K of about 1 MPa $m^{\frac{1}{2}}$. To estimate the surface energy, γ, we need a value of E, which we take as the Young's modulus when loaded in the bedding planes and is given above. Then, γ = 7.57 J/m^2. In the current analysis we make the assumption that the anisotropy is entirely due to the effects of penny-shaped cracks in the bedding planes. Since these cracks do not affect the stiffness measured in their plane, the Young's modulus of the matrix material and the in-plane modulus are the same. Using the theory of the preceeding section and the assumption that the crack radii are exponentially distributed with mean $\bar{c}$ it is straightforward to show that the compliance matrix has the form

$$\mathbf{H} = \begin{pmatrix} 1/\bar{E} & -\bar{\nu}/\bar{E} & -\bar{\nu}/\bar{E} & 0 \\ -\bar{\nu}/\bar{E} & 1/\bar{E} & -\bar{\nu}/\bar{E} & 0 \\ -\bar{\nu}/\bar{E} & -\bar{\nu}/\bar{E} & 1/\bar{E}+\beta^o N_b h & 0 \\ 0 & 0 & 0 & \beta^s N_b h+1/2\bar{\mu} \end{pmatrix} \tag{41}$$

where N_b is the number of bedding cracks per cm^3 and

$$h = 6\bar{c}^3 \tag{42}$$

The fourth-order material tensor in (32) can be replaced by a 9x9 matrix and the stress and strain tensors redefined as 9-vectors. Because of the symmetry of the stress and strain tensors, there are only 6 independent components, and it is sufficient to consider a 6x6 matrix to characterize the material. For axisymmetric deformations there are only 4 independent stresses and strains, and it is possible to redefine H as a 4x4 matrix. In (41) $\bar{\nu}$, $\bar{E}$, and $\bar{\mu}$ denote properties of the isotropic matrix material. $\bar{\mathbf{H}}$ is somewhat different from the general compliance matrix for a transversely isotropic material

$$\mathbf{H} = \begin{pmatrix} 1/E & -\nu/E & -\nu'/E & 0 \\ -\nu/E & 1/E & -\nu''/E & 0 \\ -\nu'/E & -\nu''/E & 1/E' & 0 \\ 0 & 0 & 0 & 1/2\mu \end{pmatrix} \tag{43}$$

To bring $\bar{\mathbf{H}}$ and H into approximate agreement we take $\bar{E}$ = E, and $\bar{\nu}$ to be the average of ν, ν', and ν'', which is 0.27. Then $\bar{H}_{12} = \bar{H}_{13} = \bar{H}_{23} = -1.55$, whereas H_{12} = -1.58, H_{13} = - 1.16 and H_{23} = -1.90, all in inverse

megabars. Thus the error is on the order of 20%. However, $H_{11} = \bar{H}_{11} = H_{22} = \bar{H}_{22}$. To complete the representation of oil shale with bedded cracks, we require that

$$1/E + \beta^{o} N_b h = 1/E' \quad . \tag{44}$$

The number density of bedding cracks can be obtained from this result if $\bar{c}$ (hence h) is known. To estimate $\bar{c}$ we consider the strength of the samples tested by Youash which is determined by the largest cracks they contain. The crack size $\tilde{c}$ such that on average there is just one crack greater than $\tilde{c}$ in radius in the volume V is given by

$$V N_b e^{-\tilde{c}/\bar{c}} = 1 \tag{45}$$

If we consider an ensemble of samples of size V, the mean size of the bedding cracks exceeding $\tilde{c}$ in radius is given by

$$\bar{\bar{c}} = \int_{\tilde{c}}^{V^{1/3}} Vc \frac{\partial N}{\partial c} dc \cong c \, \ell n(VN_b/e) \quad , \tag{46}$$

provided that $V >> \bar{c}^{-3}$.

To complete the estimate of $\bar{c}$ we use the preceeding result and write the fracture toughness relation for penny-shaped cracks (given, for example, by Tetelman (1967)) as

$$\sigma_p^2 \bar{\bar{c}} = (\pi/4) K_p^2 = (\pi/2)\gamma E/(1-\nu^2) \quad . \tag{47}$$

Combining these results we have

$$\bar{c} = \frac{\pi \gamma \bar{E}}{2(1-\nu^2)} \frac{1}{\sigma_p^2 \, \ell n(VN_o/e)} \tag{48}$$

Though the result depends on assumptions about sample size and crack shape, it is somewhat insensitive to them, and the reader should not infer that different assumptions would lead to very different results. Strictly speaking, we do not have N_b at this point, and the solution should proceed iteratively. We anticipate, however, and note that on the basis of exploratory calculations with SCRAM the cavity shape seems about right for $N_b = 100$. We estimate V, the sample volume for the Youash tests, to be 5 cm^3. With the isotropic matrix parameters $\bar{E}$ and $\bar{\nu}$ given above and $\sigma_p = 8.62$ MPa (1250 psi) we find $\bar{c} = 0.058$ cm. With this result (44) can be solid for the number density, and we find $N_b = 107$ cm^{-3}. In addition to the bedded cracks there are isotropically distributed cracks. Their mean size is taken as 0.0145 cm on the basis that the strength across the bedding planes is half the strength in the bedding planes, and critical crack size goes as the inverse square of strength.

The high pressure behavior is specified by the Gruneisen parameter $G = 1.5$ and the slope of the $u_s - u_p$ line, $S = 1.5$. In addition, it is necessary to specifiy the coefficient of friction, which we take to be $\bar{\mu} = 0.2$. The high explosive is represented as an ideal gas expanding adiabatically with a ratio of specific heats $\gamma = 3$ and and initial energy of 1000 cal/g. Though this is not the best representation of the explosive, it gives good results so long as the pressure remains above a few kilobars, as it does in the current problem. The volume of the explosive products, which is necessary and sufficient to compute the pressure in the adiabatic approximation, is obtained by numerical integration.

The SCRAM calculation was run with a time step of 2×10^{-7} sec using a polar coordinate system, with the (spherical) cavity edge a coordinate surface. Cells near the cavity have a radial dimension of 1 mm and are very nearly square. Away from the cavity the cell dimensions increase geometrically with a growth rate of 10%. The initial pressure in the cavity is 167 kilobars, and it results in an essentially radial motion of the oil shale at early times since the material behavior at high pressure is dominated by its (isotropic) equation of state. At later times cracks begin to open and to grow as a result of tensile hoop stresses. The effect of anisotropy at later times may be seen in Fig. 2 which illustrates the

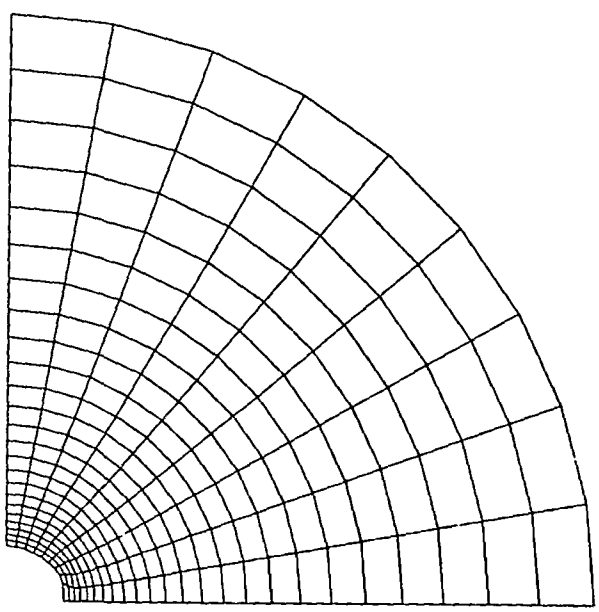

Fig. 2. The grid distortion in oil shale at 30 μs due to detonation of a one inch explosive sphere.

grid distortion. The strain in cell 19, which is adjacent to the intersection of the equator and the cavity, is strongly influenced by the dilatant effect of the bedding cracks. The average density of the cell gets very low, on the order of 1 g/cm^3, at late times. The calculated cavity shape is compared with

the radiographic shape at 30 μs in Fig. 3. The difference in the two shapes appears to be within the resolution of the radiograph. The reason for the pill shape of the cavity is the extreme dilatancy of the material in cell 19, which causes the displacement at the edge of the cavity to be dominated by strain normal to the bedding.

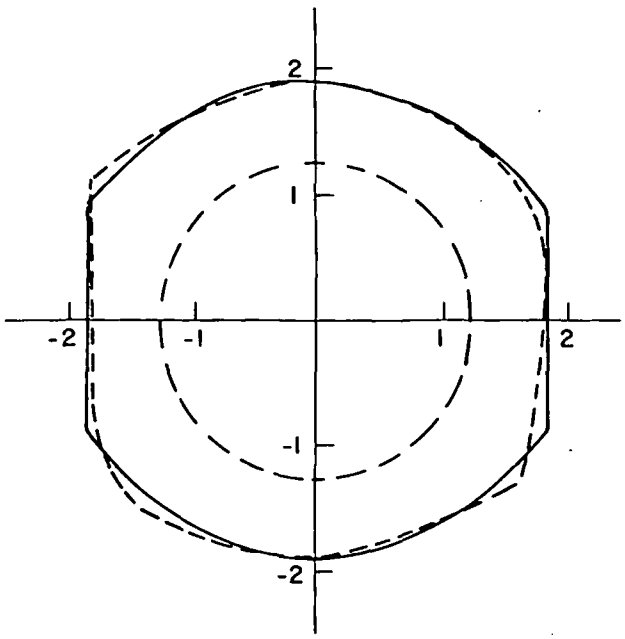

Fig. 3. Comparison of the radiographic cavity shape at 30 μs with a SCRAM calculation.

REFERENCES

Amsden, A. A., H. M. Ruppel, and C. W. Hirt, 1980, "SALE: A Simplified ALE Computer Program for Fluid Flow at All Speeds," Los Alamos National Laboratory report LA-8095.

Dienes, J. K., 1976, "Generalized Ratios of Elastic Moduli for Oil Shale," in Explosively Produced Fracture of Oil Shale, Los Alamos National Laboratory report LA-6521-PR.

Dienes, J. K., 1978a, "A Statistical Theory of Fragmentation," in Proceedings of 19th U.S. Symposium on Rock Mechanics, Stateline, Nevada.

Dienes, J. K. 1978b, "Rate Formulation of the Constitutive Law for a Flawed Material," in Explosively Produced Fracture of Oil Shale," Los Alamos National Laboratory report LA-7871-PR.

Dienes, J. K., 1978c, "The Effect of Friction on the Behavior of Shear Cracks," in Explosively Produced Fracture of Oil Shale, April 1978-March 1979, Los Alamos National Laboratory report LA-8104-PR.

Dienes, J. K., 1978d, "Cavity Formation in Oil Shale," in Explosively Produced Fracture of Oil Shale, January-March 1978, Los Alamos National Laboratory report LA-7338-PR.

Dienes, J. K., 1979a, "Theory of Explosions in Anisotropic Media," Proceedings of the Euromech Colloquium 115, Mechanical Behavior of Anisotropic Solids, Villard-de-Lans, France.

Dienes, J. K., 1979b, "On the Analysis of Rotation and Stress Rate in Deforming Bodies," Acta Mechanica 32, 217-232.

Dienes, J. K., 1979c, "On the Inference of Crack Statistics from Observations on an Outcropping," 20th U.S. Symposium on Rock Mechanics, Austin, Texas.

Dienes, J. K., 1979d, "Rate Formulation of the Constitutive Law for a Flawed Material, Revised," to appear as a Los Alamos National Laboratory report.

Dienes, J. K. and L. G. Margolin, 1980, "A Computational Approach to Rock Fragmentation," in Proceedings of the 21st U.S. National Symposium on Rock Mechanics, Rolla, Mo.

Fugelso, E. 1978, "Flash X-ray Studies of the Dynamic Expansion of a Spherical Cavity in Oil Shale," in Explosively Produced Fracture of Oil Shale, January-March, 1978, Los Alamos National Laboratory report LA-7338-PR.

Grady, D. E. and M. E. Kipp, 1980, "Oil Shale Fracture and Fragmentation at Higher Rates of Loading," Proceedings of the 20th U.S. Symposium on Rock Mechanics, Austin, Texas.

Grady, D. E., 1980, Verbal Communication, Oil Shale Conversion Symposium, Denver, Colorado.

McQueen, R. G., S. P. Marsh, J. W. Taylor, J. N. Fritz, and J. W. Carter, 1970, "The Equation of State of Solids from Shock Wave Studies," in High-Velocity Impact Studies, Academic Press, New York.

Olinger, B., 1976, "Elastic Constants of Oil Shales," in Explosively Produced Fracture of Oil Shale, Progress Report No. 1, Los Alamos National Laboratory report.

Schuler, K. W., P. C. Lysne, and A. L. Stevens, 1976, "Dynamic Mechanical Properties of Two Grades of Oil Shale," Int. J. Rock Mech. Min. Sci. and Geomech., 13, pp. 91-95.

Seaman, L., D. R. Curran, and D. A. Shockey, 1976, "Computational Models for Ductile and Brittle Fracture," J. Appl. Phys. 47, No. 11.

Stroh, A. N., 1957, "A Theory of the Fracture of Metals," in Advances in Physics, Vol. VI.

Tetelman, A. S. and A. J. McEvely, Jr., 1967, Fracture of Structural Materials, John Wiley and Sons, New York.

Youash, Y., 1969, "Tension Tests on Layered Rocks," Geological Society of America Bulletin, 80, p. 303-306.

2-2 ... US ... on Rock mech

"Rock mech from R&D to Application

June 28 - July 2 1981 at MIT

login SM1-DOC

LISP

(OK, POWER)

(ENTRY)

(SELECT SDBASE)

(FIND_LIBRARIES 'OTTA')

OR

(FIND_FILES_IN_DIR '/DIBNES')

Int. J. Rock Mech. Min. Sci. Vol. 8, pp. 181–202. Pergamon Press 1971. Printed in Great Britain

ON THE FRACTURE PROCESS IN BLASTING*

H. K. KUTTER†
Imperial College of Science and Technology, London
and
C. FAIRHURST
University of Minnesota, Minneapolis, Minnesota

(*Received* 15 *September* 1970)

Abstract—In order to clarify the respective roles of stress wave and gas pressure in the fragmentation of an underground blast the fracture process in the zone immediately around the borehole was studied by separating the two principal blast forces analytically and experimentally. In model tests the explosion wave was simulated by the pulse generated by an underwater spark discharge, and the expanding combustion products by pressurized oil.

The wave-generated radial fractures around the cavity were investigated in detail and the diameter of the fractured zone was found to approach six hole diameters for a spherical charge and nine hole diameters for a cylindrical charge. The stress field generated by the pressurized gas in this star-cracked cavity was shown to be identical to that of a pressurized and uncracked 'equivalent cavity' whose diameter is equal to that of the fractured zone. A very large region is therefore stressed by the gas, and consequently considerable crack extension can be expected.

The influence of boundary conditions, i.e. preexisting fractures, static stress field, and close free surface, on the wave and gas-generated fracture pattern, was investigated in detail. Preexisting fractures grow to larger lengths than new ones and cause a fracture-free zone in their immediate vicinity. Cracks grow preferably in the direction of maximum principal stress of superimposed stress fields. Cracks pointing towards the free surface are longer than the ones pointing away from it.

The gas pressure was shown to play an important role in blasting, but it was also shown to be only effective if the cavity and free surface have been preconditioned by the stress wave.

1. INTRODUCTION

THE violence and extreme rapidity of explosions pose formidable obstacles to research in rock blasting. It is generally impossible to directly observe more than the final size and shape of the crater or pile of fragments. Advances have been made through use of small-scale model testing and ultra high-speed photography but present understanding is still far from complete.

Much blasting research tends to be concentrated on one aspect of the blasting process to the exclusion of other significant effects. Some investigators consider the major portion of fragmentation to be caused by the initial explosive strain pulse generated in the rock. Others similarly attribute all but a small part of the blasts effects of the gas pressure developed in the borehole after passage of the detonation wave and the associated strain wave

* This study formed part of a thesis submitted to the School of Mineral and Metallurgical Engineering, University of Minnesota, and it was financially supported by the U.S. Bureau of Mines and conducted at the Twin Cities Mining Research Center, U.S. Bureau of Mines, Minneapolis, Minn.
† Former address: University of Minnesota, Minneapolis, Minnesota.

in the rock. A comprehensive theory concerned with the combined effects of both strain wave and gas pressure has not yet been devised. This paper presents an attempt to consider, in simplified fashion, both effects and their interaction.

Theoretical considerations and actual measurements indicate that although 'the strain pulse' [1–4] and 'gas-pressure' [5–8] effects are each part of a continuous pressure–time variation in the rock, the two may be validly considered separately. It must be recognized, however, that the rock subjected to the 'gas-pressure effect' has been preconditioned by strain wave impulsive loading. A major difficulty of estimating each effect in conventional blasting is the rapidity with which one follows the other. It is virtually impossible to separate them. For the experiments described below, special procedures were devised in order to permit separation. The wave action was generated by the 'electrohydraulic effect', i.e. a high-voltage underwater-spark discharge. The quasi-static pressure of the expanding gases was simulated by static oil pressure. With the forces thus separated, it was possible to study the breakage process as a successive sequence of crack initiation and fracture propagation. The force interaction is of particular importance in the zone around the charge and consequently most attention was given to fracture development in this region. Since the stress wave is emitted before the gas pressure becomes fully active the dynamically generated fractures are essentially completed by the time the combustion products start to expand. It is logical, therefore, to discuss the dynamic fracture process before that of the quasi-static gas-pressure process.

For completeness, a short review of the physical phenomena involved in an underground explosion and relevant to this investigation is presented first.

2. SUCCESSIVE PHYSICAL PHENOMENA OF A CONTAINED EXPLOSION

All forces, dynamic and quasi-static, generated in an explosion result from the detonation of a contained chemical charge, i.e. the very rapid chemical reaction of a thermodynamically unstable substance, resulting in the creation of great heat and high-density gases. The violence of the detonation process is governed by the velocity of the detonation wave within the explosive. Chemical properties, density, homogeneity and size of the charge together determine the velocity of detonation. The pressure generated is in turn a function of the detonation velocity. After the initial almost instantaneous rise, the pressure–time curve falls smoothly at a decreasing rate.

As the rapidly expanding high-pressure gas impacts the surrounding rock material, an intense pressure wave is emitted into the rock. The more the combustion products and the 'precursor' shock wave are able to expand before they encounter the rock boundary, the lower the peak pressure will be at the moment of impact. (This is in principle the effect of 'decoupling' where the borehole pressure exerted on the borehole wall is reduced by making the diameter of the latter larger than that of the charge.) Thus, the pressure acting on the borehole wall rises almost instantaneously to its peak, which for all practical purposes can be assumed to be of the order of one-half to one-quarter of the detonation pressure, and then decays more or less exponentially due to the cooling of the gases and the outward expansion of the cavity. The duration of this pressure pulse is of the order of a few hundreds of microseconds. Although the gas pressure initially drops quite rapidly, it remains high enough to continue the expansion of the cavity and to exert a quasi-static pressure on the rock boundary for a relatively long time. In some cases, venting of the gases through the borehole or through large cracks may drastically reduce the duration of gas-pressure action.

The amount of energy contained in the wave is generally acknowledged to be only a small

fraction of the calculated total energy released by the explosive. Test blasts in granite gneiss [9] revealed wave energies of the order of 10–18 per cent of the total energy released; in salt the wave energy was found to be 2–4 per cent only [10]. The remaining part of the explosive energy is contained to a large extent in the expanding high-temperature, high-pressure gas. This may lead one to ignore the wave energy completely and to treat the blasting problem as one of adiabatic gas expansion only. In the immediate vicinity of the hole, however, the wave energy is highly concentrated and produces extensive breakage in that region. This significantly modifies the hole boundary on which the gas pressure subsequently acts.

When the strain wave reaches the free surface of the rock, it is reflected and may cause spalling of surficial slabs. This spalling has been widely explored [1] and sufficiently demonstrated [3]. It will not be discussed further here. The fracture zone immediately around the charge has received little study; it will be discussed in detail later in this paper.

Basically, three zones of varying destruction and deformation can be distinguished around a contained explosion [11]; a strong-shock (hydrodynamic) zone (most significant in nuclear explosions); a transitional, non-linear zone; and the elastic region. In the first zone, which lies in the region immediately around the cavity, the explosive stresses exceed several-fold the compressive strength of the rock so that the rock is intensely crushed and shattered. This excessive disintegration is associated with a correspondingly high energy consumption. In the hydrodynamic zone the elastic rigidity of the rock is completely insignificant. The adjoining nonlinear zone is characterized by increasing importance of the shear resistance, although the wave stresses are still substantially above the yield strength. The fracture phenomena in this zone range from severe crushing through plastic deformation to partial fracturing, the particle size rapidly increasing with radial distance. The outer region exhibits predominantly radial fracturing produced by the tangential component (hoop stresses) of the elastic precursor wave. The elastic region is the largest one being theoretically without an outer limit. Attention in this paper will, however, be restricted to that part of the elastic region which has fractures generated in it. Even this fractured part is large compared to the inner two zones. It is consequently the most interesting one as regards breakage around a contained explosion in brittle rock. The hydrodynamic and nonlinear zones are only of any practical importance as far as they act as a stress filter and determine what percentage of the explosive generated stress pulse is emitted from the inner boundary of the elastic region.

Wave propagation in the elastic zone is marked by a peak amplitude lower than the elastic limit of the rock, and by a constant velocity. Analytical expressions for an explosion-generated elastic wave are available for spherical [12–14] and cylindrical [15–17] charges. The most relevant result with respect to breakage is the attenuation of the wave; for a step-rise pulse the peak amplitude of the radial stress component is theoretically proportional to r^{-1} for the spherical case, and to $r^{-\frac{1}{2}}$ for the cylindrical case, where r is the radial distance from the center of the shot hole. Furthermore, the frequency spectrum of the wave is a function of the charge size, the low-frequency portion increasing with charge size. The theoretical solutions are based on the principle of energy conservation. In rock, however, energy will be absorbed in the form of friction, heat and fracturing. Consequently, more rapid attenuation of the stress amplitudes than indicated above are to be expected. Empirically the relationship $\sigma_{peak} = \sigma_0 r^{-n}$ with $n = 1{\cdot}5$–$3{\cdot}0$ depending on the type of rock, has been found to hold for the radial stress component. Very little attention has been paid so far to the tangential stress component of the wave. Although it attenuates faster than the radial component and becomes negligible at larger distances, it is nevertheless, the major cause of

fracture in the region around the charge. It is therefore surprising that practically no field measurements of this tangential component are available.

Fracturing within the elastic zone is due solely to the tangential stress. The radial stress component is basically compressive with a peak amplitude smaller than the compressive strength of the rock, and therefore it cannot be the cause of any fracture initiation. Under the influence of the wave, the rock particles are moved radially outwards resulting in a strain and tensile stress in the tangential direction. As the tensile strength of rocks is considerably smaller than their compressive strength, the tangential stress of the wave is large enough to cause radial fractures, even though the associated radial compression has fallen below the compressive strength. These fractures can result either from the continuation of cracks generated in the non-linear zone, or from new cracks initiated from microfractures inherent in the rock. Once the tangential stress has attenuated below a critical value, the wave passes through the rock medium without further breakage.

As the dynamic stresses of the wave propagate outwards, the expanding combustion products start to penetrate into the primarily radial cracks and exert a high quasi-static pressure on the so-extended cavity boundary. This results in an increase of the crushed zone radius, since the static strength and the yield limit are lower than the dynamic ones. Extension of existing cracks and possible creation of new radial cracks due to the elastic hoop

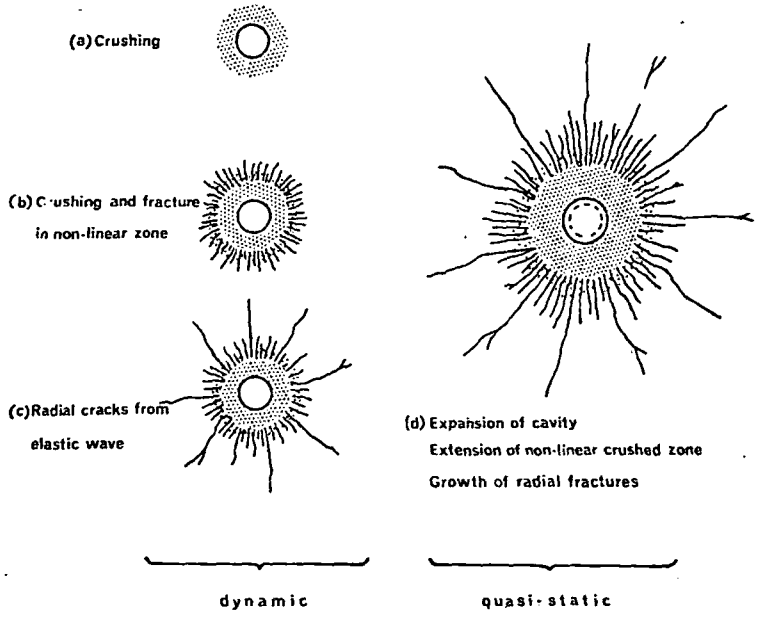

FIG. 1. Consecutive stages in the fracture process of a fully contained explosion.

stresses, may also occur. A detailed study of the stress distribution and associated fracture phenomena around such a pressurized radially cracked cavity forms the basis for the section below on the role of the gas pressure. Figure 1 summarizes schematically the consecutive stages in the fracture process of a fully contained explosion.

3. STRESS-WAVE GENERATED FRACTURES AROUND THE CAVITY

Although the presence of heavy rock breakage in the zone immediately around the charge of an underground explosion is easily visible, very little attention has been paid to

its analytical investigation. However, in some cases such as in presplitting, the fractures around the borehole are of extreme importance. Even for cratering blasts the events in the immediate vicinity of the shot hole play a decisive role in the determination of the final crater dimensions. With the exception of very large charges the breakage due to crushing and plastic behavior is confined to a very small region close to the hole and can be safely neglected. The elastic zone is consequently of prime interest. The outgoing wave causes brittle fracture of the rock. In contrast to reflection breakage, it is the tangential tensile stress component of the outgoing wave rather than the radial compressive component, which determines the extent of rock failure. It is noteworthy that no blasting experiment or field test has been reported where the tangential stress was measured in addition to the radial stress or strain.

Theoretical model

Specification of the temporal and spatial distribution of the tangential stress wave form is necessary to allow prediction of the approximate length of the radial wave-generated cracks. Using SHARPE's solution [12] for an exponential pulse emitted from a spherical cavity, KUTTER [18] determined numerically the attenuation of the peak tangential tensile stress for various pulse parameters and material properties. The input radial pulse, i.e.

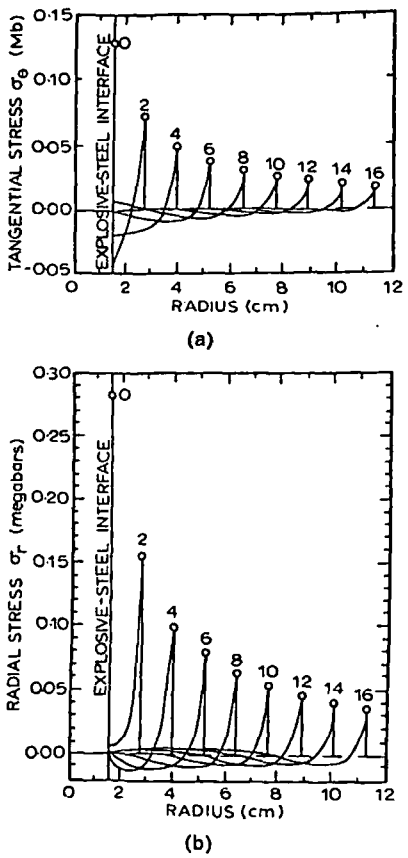

FIG. 2. Tangential (a) and radial (b) stress of a spherical exponential pulse after various time intervals after emission. The numbers on the curves denote time in microseconds (after ALLEN and GOLDSMITH[28]).

the forcing function simulating the interaction of the explosive and rock was assumed to be of the form:

$$p(t) = p_0 e^{-\alpha t}$$

where p_0 is the peak pressure at the borehole wall, α is the time constant, and t the time. The analysis reveals that the originally exponential pulse rapidly develops a tensile tail as it moves away from the source. This stress reversal is particularly pronounced for the tangential stress component. This can be clearly seen in Fig. 2 which shows the tangential and radial components of the stress pulse at increasing times after emission. Kutter plotted the computed results from the attenuation of the tensile tangential peak of a spherical pulse in normalized form (Fig. 3) and found that in the region immediately around the cavity the

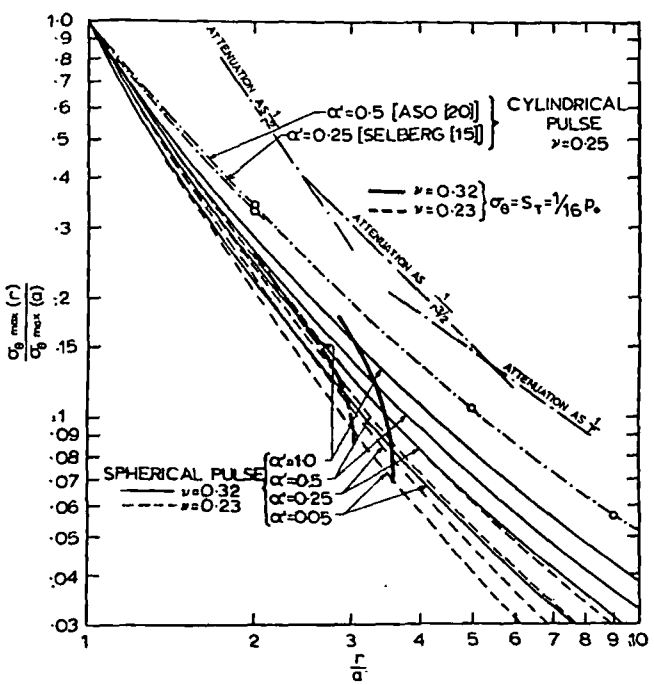

FIG. 3. Peak stress of the tangential tensile tail for an exponential pressure pulse, $p = p_0 e^{-\alpha t}$; (α' is a dimensionless parameter equal to $[\alpha \cdot a/c]$).

tensile peak of a spherical pulse is approximately inversely proportional to the 2nd power, and that of a cylindrical pulse to the 3:2 power of the distance from the source. The values for a pulse emanating from a cylindrical source are taken from SELBERG [15].

For the E and ν values of rock and a α-value for a typical production blast, the peak tangential tension $\sigma_{\theta\,max}$ at the wall of the spherical cavity was calculated to be about $0{\cdot}5$–$0{\cdot}7\,p_0$, and for the cylindrical cavity this value appears to be between $0{\cdot}6$ and $1{\cdot}0\,p_0$. Furthermore, the tensile peak was found to travel with approximately the same velocity as the wave front. For the spherical wave, the length of the tensile tail following the tensile peak is about $1{\cdot}7$ times the pulse length preceding it; for the cylindrical wave the corresponding ratio is about 3.

This stress information allows a rough prediction of the extent of the wave-generated fractures, provided several simplifying assumptions are made as follows:

(1) The rock is considered to be homogeneous, isotropic and perfectly elastic.
(2) The rock breaks in a brittle manner and the operative failure criterion is that of maximum tensile stress. (This is in agreement with Griffith's failure criterion, as long as the magnitude of the maximum principal stress is less than three times the magnitude of the minimum principal stress, where a tensile stress is negative.) The dynamically determined, rather than the lower static tensile strength is taken as the failure limit.
(3) The rock is completely stress-free prior to the explosion.
(4) Energy dissipated in fracture is considered negligible in comparison to the total wave energy. In this way elastic wave propagation is not altered by the formation of fractures.
(5) The cavity is of sufficient size with respect to the charge such that no crushing occurs around the hole. The peak wall pressure p_0 is consequently assumed to be equal to the dynamic compressive strength of the rock. In other words, all crushing and inelastic behavior is confined to the region inside the assumed cavity.

Since tangential stresses are the most tensile the majority of cracks will propagate in the radial direction. The radial cracks are assumed to terminate at that radial distance where the tensile stress $\sigma_{\theta\,\max}$, has attenuated to a value below the dynamic tensile strength of the rock. More precisely, this is the critical radial distance from the source beyond which no *new* cracks will be generated. With the above assumption (5) and a further assumption of a fixed ratio of 16:1 between dynamic compressive and dynamic tensile strength, the radial distance beyond which no further crack generation occurs can be found and marked in Fig. 3. Two heavy curves are plotted for Poisson's ratio, ν of 0·23 and 0·32. The critical radial distance is thus found to be approximately four times the cavity radius.

A similar conclusion can be reached for the cylindrical charge. The tension (tangential to the wall) for the cylindrical case is higher and the rate of attenuation is smaller. Consequently longer radial cracks are to be expected. Going through the same procedure as in the spherical case, the radius of the crack tip for the cylindrical cavity is determined to be approximately six times the hole radius. Thus, the crack length in the cylindrical case is almost twice as great as that for a spherical charge of the same cavity radius.

The above radii can only be considered to define the limit for the generation of new cracks, since extension of existing cracks can still take place even when the tensile stress has dropped below the critical value for initiating new cracks. Crack extension can taken place approximately as long as tension is applied normal to the crack tip, that is to say, as long as the full length of the tensile tail of the tangential stress has not yet passed by the slower propagating crack tip. Assuming a maximum crack propagation velocity and applying the earlier referred to length of the tensile tail, the additional crack extension Δl can then be expressed in the form [19]

$$\Delta l = \frac{1{\cdot}7\, t'_{\max}}{2{\cdot}35\sqrt{\left(\frac{1-\nu}{1-2\nu}\right)-1}} \cdot a$$

where a is the cavity radius, ν is the Poisson's ratio of the rock, and $t'_{\max}$ the dimensionless rise time for the tangential tensile peak [19]. For the cylindrical case the factor 1·7 in the

above expression changes to 3·0. As a practical example, for a rock with $\nu = 0{\cdot}26$, and a stress pulse similar to those from production blasts, Δl is predicted to be 1·6 hole radii for the spherical charge and 2·5 hole radii for the cylindrical charge. Thus the total radius of the fractured zone becomes now 5–6 hole radii and 8–9 hole radii for the spherical and cylindrical cases respectively.

There is another theoretical observation which is worth noting. At a certain distance from the cavity the radial stress component (complementary to the tangential tensile peak stress) also becomes tensile and eventually exceeds the tangential component. The preferred fracture direction beyond this radial distance is therefore no longer radial, but suddenly becomes tangential. A radial crack thus terminates with one or two small branches running normal to it. This feature is often observed and appeared frequently in the model tests described later. For the spherical pulse, the numerical analysis gives this critical radius as between 3 and 4 hole radii, depending mainly on Poisson's ratio of the rock.

The question may arise: "to what extent are the theoretical results for a simple exponential pulse valid for an actual explosion-generated wave?" A comparison between the results for the mathematically more complicated, but also more realistic, pulse shape used by Aso [20] and those for the simple exponential pulse which roughly fitted over the more complicated shape reveals practically the same tensile peak for both wave shapes. Further refinement is therefore not justified.

Experimental results

For a process as complicated as the generation of fractures by dynamic waves, theoretical solutions can cover only a few very simplified situations. Supporting experimental investigations are essential for a deeper understanding. Extensive tests on two-dimensional models were therefore performed. In order to be able to achieve a sufficiently accurate repeatability, and easy variation of the peak input pressure, a nonchemical explosive source was used: the 'electrohydraulic effect' caused by an underwater spark discharge offered itself as an excellent explosive wave generator.

When a high-voltage spark is discharged across an electrode gap, a plasma and vapor channel is built up between the electrodes. This channel expands very rapidly because of the concentrated electric field and the extremely high temperatures developed within the spark channel. The surrounding medium is impacted by the channel walls, and a pressure peak of the resulting 'explosion' wave is produced. The peak pressure increases with the density of the surrounding medium. Thus, in order to produce high explosion pressures, the spark gap is submerged in water. The peak pressure changes not only with the density of the surrounding medium, but also with gap width, discharge voltage and other electric parameters of the discharge circuit. Details of the electric circuit and the parameters of the generated pressure pulse are described elsewhere [21].

Two-dimensional samples, i.e. plates and discs with circular holes mostly situated in the center, were positioned between the spark electrodes for dynamic loading tests. The charge hole was filled with water and a spark was initiated through its center in a direction normal to the sample. The water was contained in the cavity of the sample by means of small Plexiglass caps which were sealed with a thin film of grease (Fig. 4).

In order to reduce reflection of the emitted wave from the boundary of the sample, a wave trap was put around the circular sample discs. Aluminum segments were attached to the rock disc with a thin film of grease and kept in this position by a tightened chain (Fig. 4). The reflected tensile pulse is then trapped in the ring since no tension could be transmitted

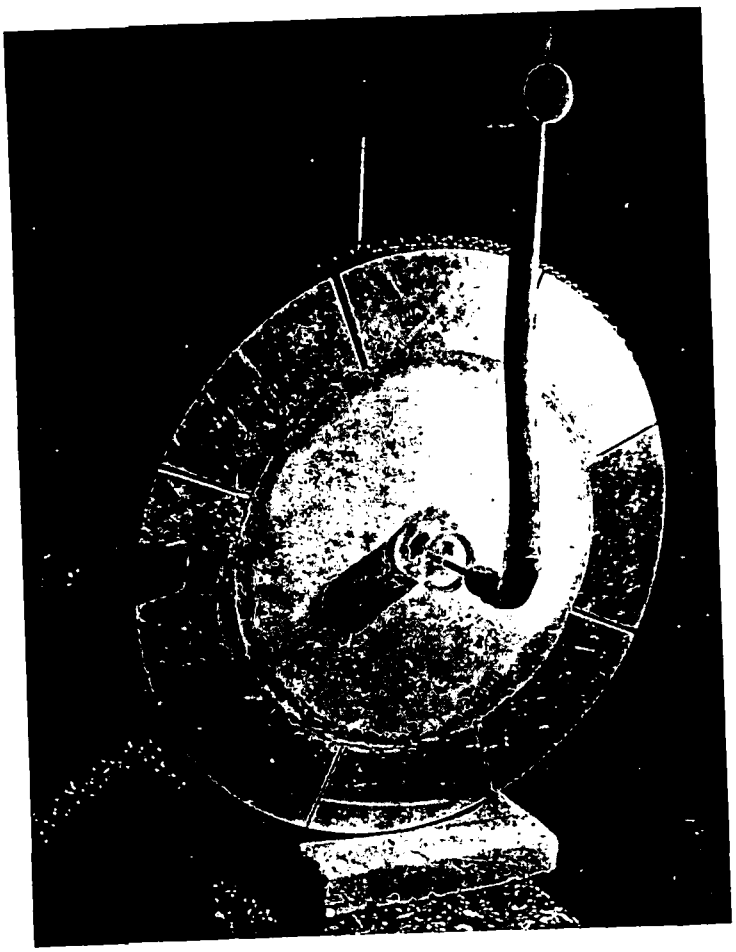

FIG. 4. Rock disc with aluminum wave trap in spark gap.

RM f.p. 188]

FIG. 5. Wave-generated fracture pattern in 12-in. diameter glass disc of $\frac{3}{16}$ in. thickness after spark discharge through the centerhole.

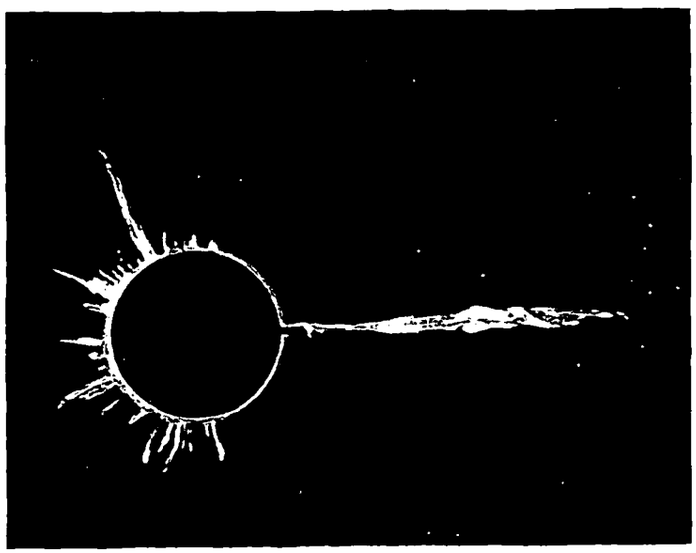

(a)

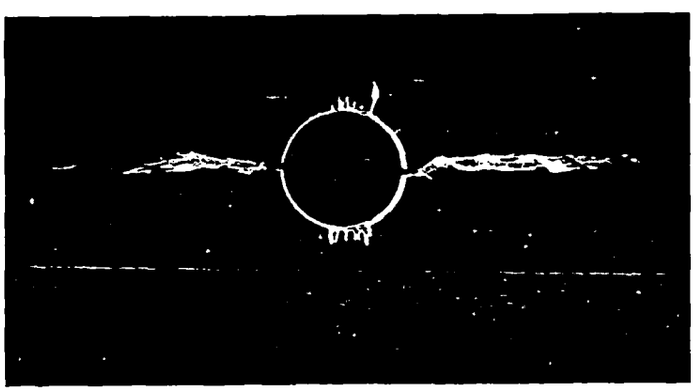

(b)

FIG. 7. Dynamic fracture patterns around cavities with one and two preexisting cracks. Stress relief in the vicinity of the preexisting crack(s) is demonstrated by crack-free regions on either side of the preexisting crack(s).

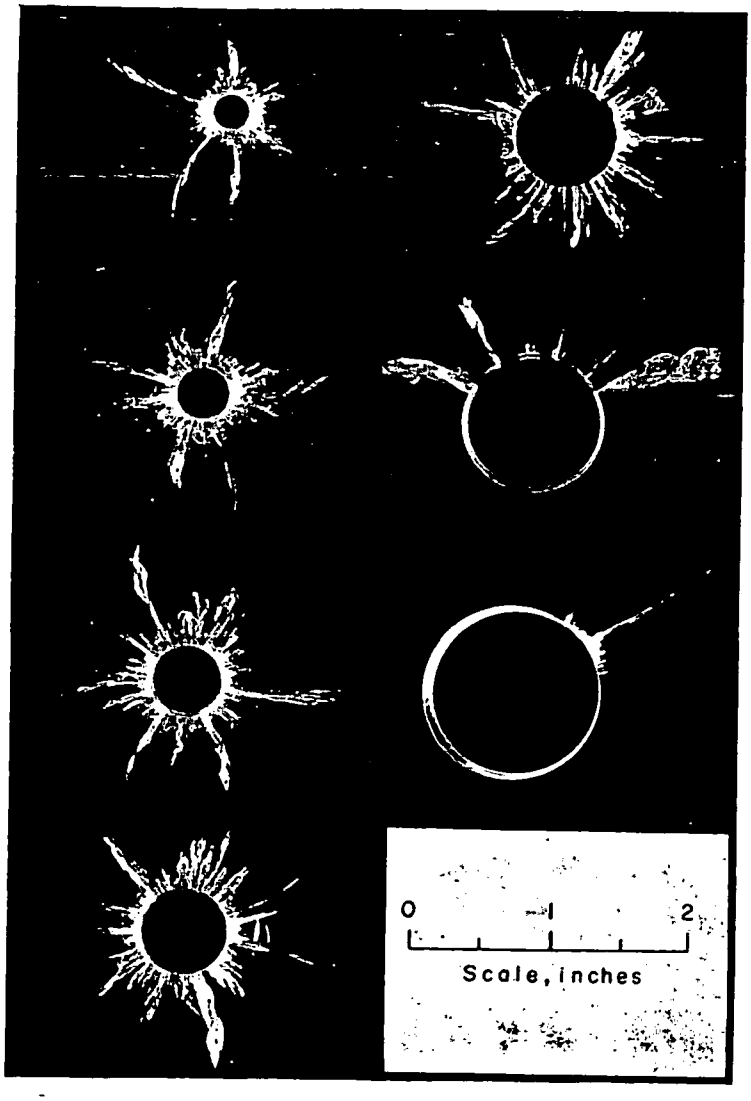

FIG. 8. Fracture patterns in Plexiglass generated by identical pulses from holes of increasing diameter.

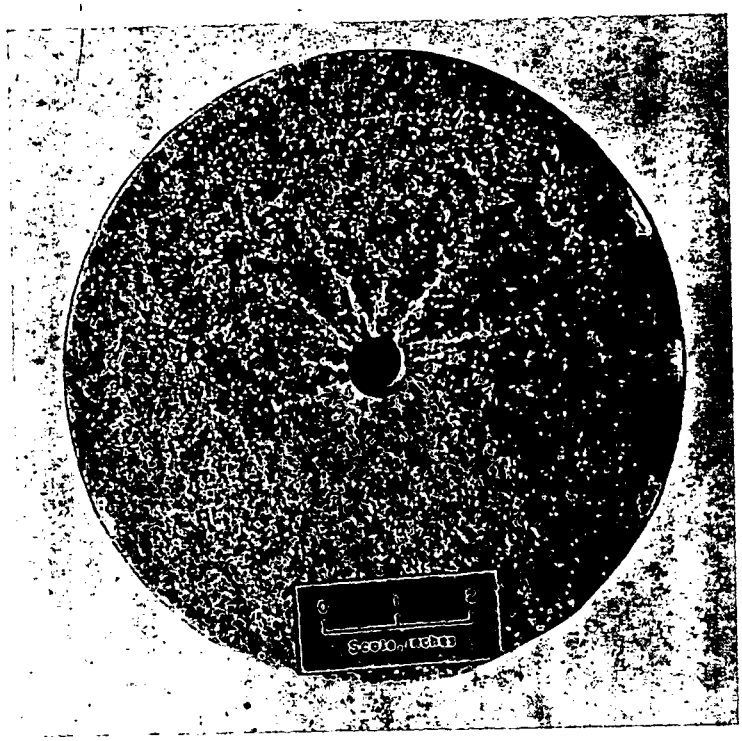

FIG. 9(a)

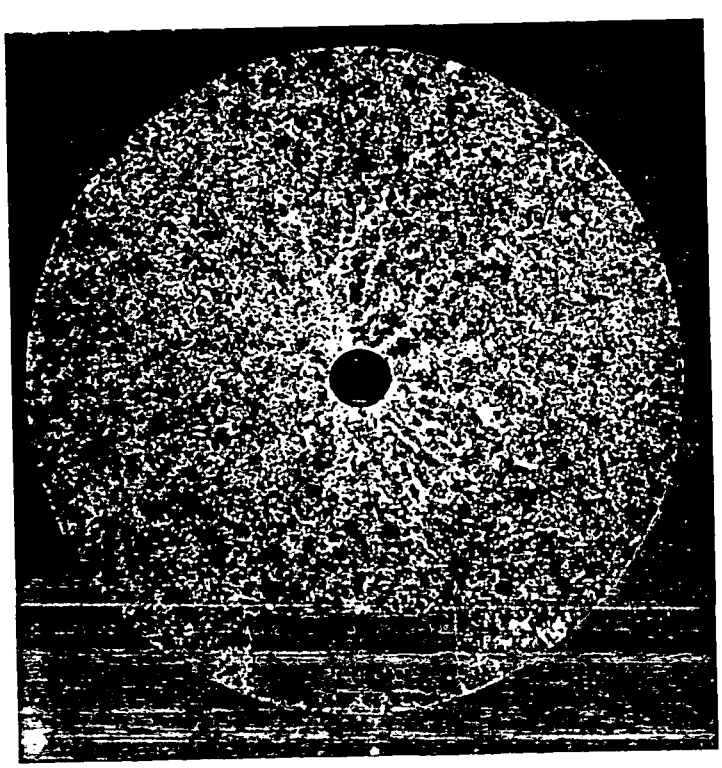

FIG. 9(b)

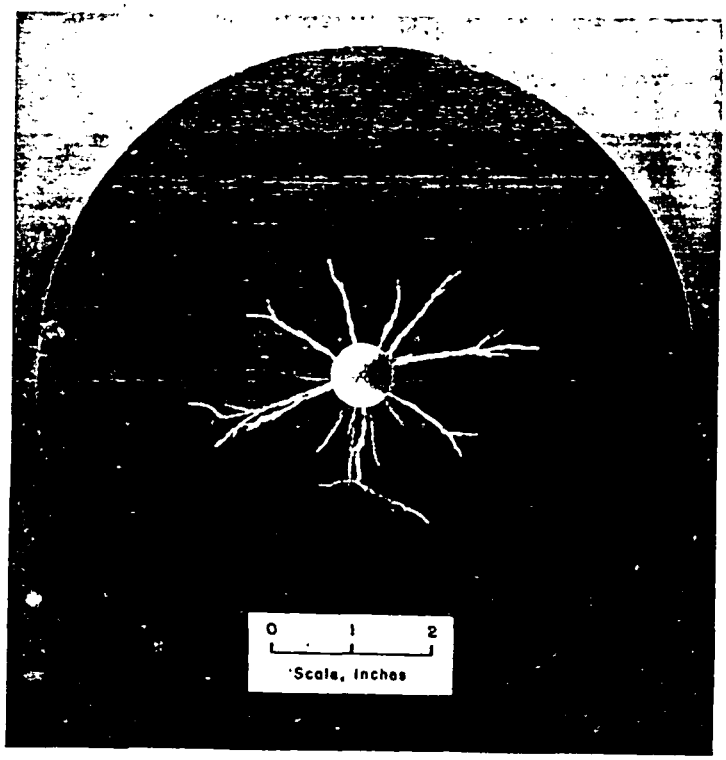

FIG. 9(c)

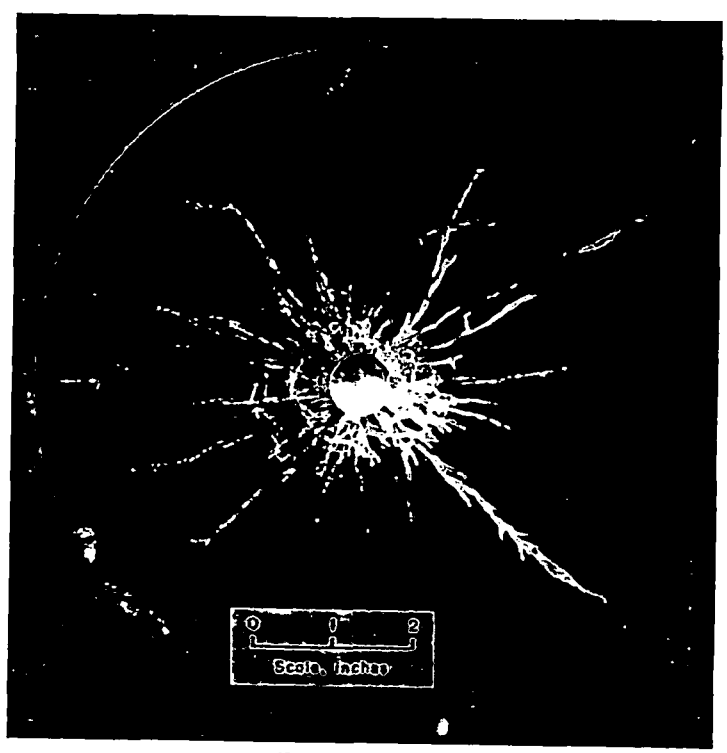

FIG. 9(d)

FIG. 9. Wave-generated fracture patterns around cavities in rock discs. (a) Tennessee marble, (b) Charcoal granite, (c) Basalt, (d) 'Belgian Black' slate.

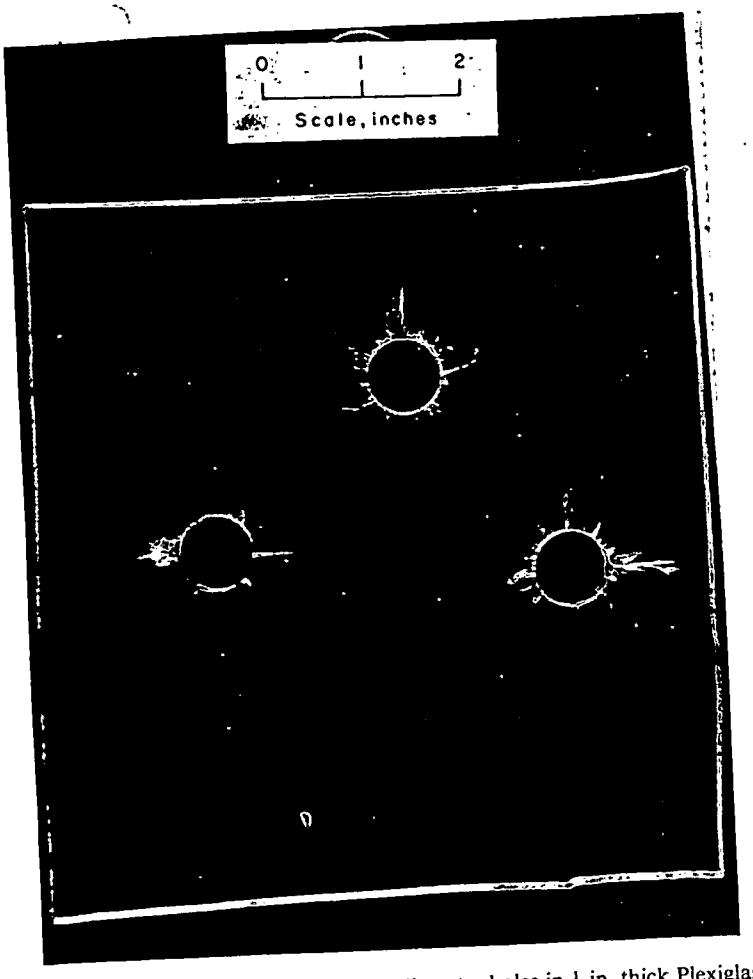

FIG. 10. Wave-generated fracture pattern around $\frac{3}{4}$-in. diameter holes in $\frac{1}{2}$-in. thick Plexiglass plate, demonstrating the influence of the free surface.

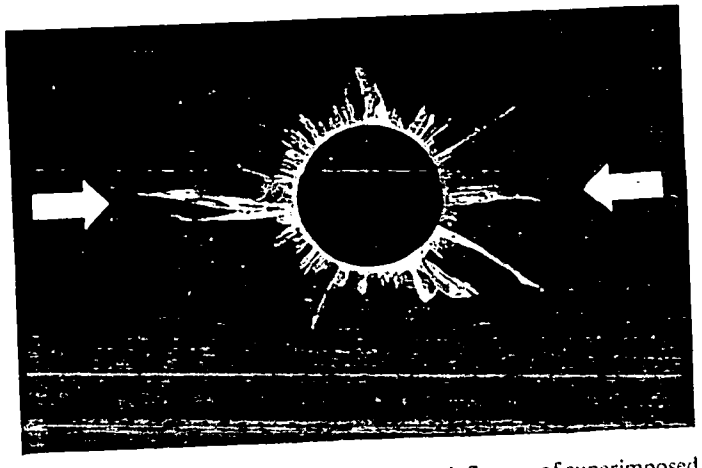

FIG. 11. Wave-generated fracture pattern in Plexiglass showing influence of superimposed uniaxial compressive static stress field in direction of the arrows.

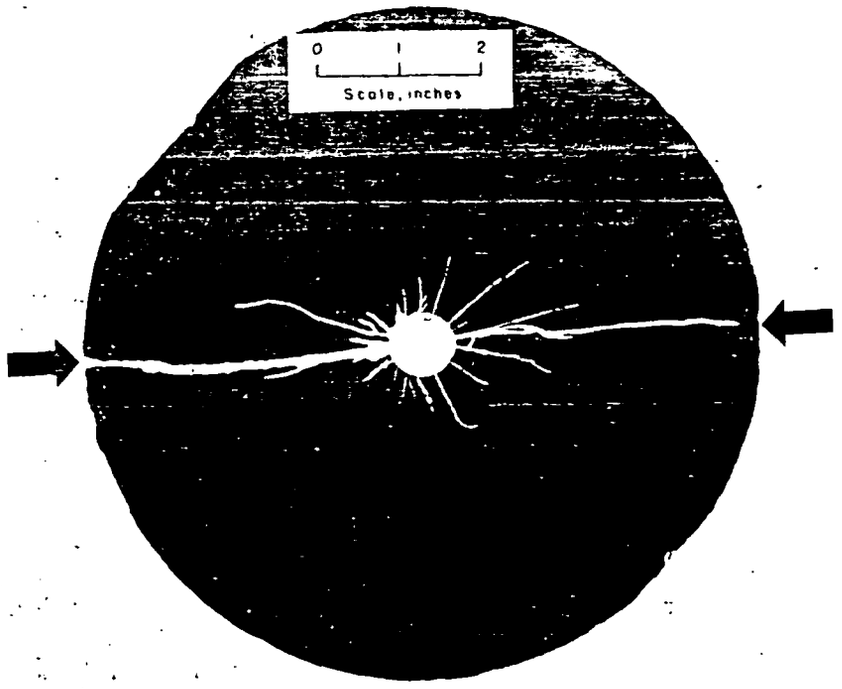

(a)

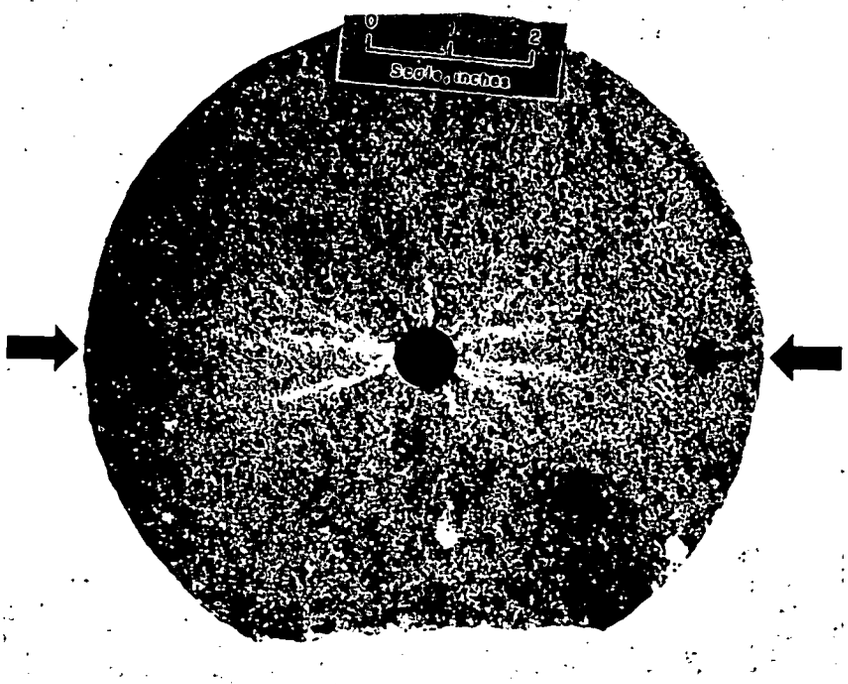

(b)

FIG. 12. Wave-generated fracture pattern in rock discs under uniaxial compressive static stress field in direction of arrows. (a) 'Belgian Black' slate, (b) Tennessee marble.

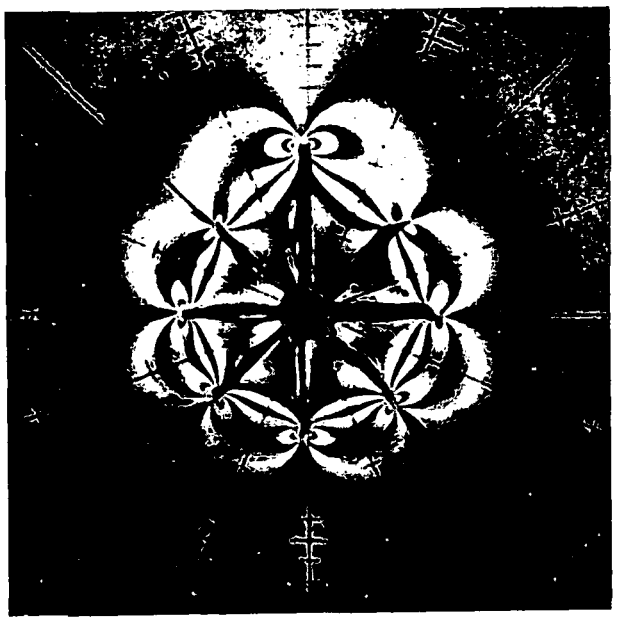

(a)

(b)

FIG. 13. Isochromatic fringe pattern for (a) a star-cracked cavity with one longer crack and (b) for 'equivalent cavity'.

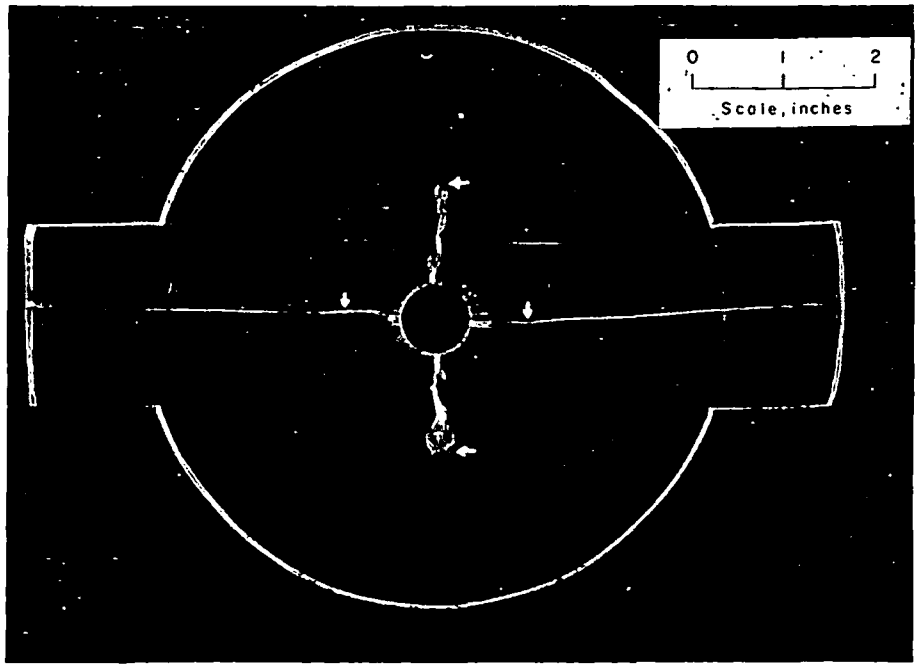

FIG. 15. Fracture pattern in Plexiglass disc after pressurizing of precracked cavity under uniaxial compressive stress field. The large arrows indicate the direction of the static stress field and the small arrows the tips of the preexisting cracks.

cross the metal–rock boundary back into the sample. Because of the good match in acoustic mpedances between rock and aluminum, almost the total wave energy was transmitted nto the ring. This very simple method of trapping the wave once it has passed through the ample facilitated reliable fracture studies.

Explosive fracture patterns in rock were found to be quite difficult to see and became isible only after special treatment of the samples with fluorescent penetrant.* A large part of the fracture tests was therefore performed on glass and Plexiglass samples, where the racks were easily visible. Glass is more brittle than most rocks, whereas Plexiglass is more luctile and has a wave velocity lower than that of most rocks. At high rates of loading, nowever, the fracture pattern in both translucent materials appears to be practically identical vith that in rock. Only the scale, i.e. the length of the cracks is different.

A typical two-dimensional fracture pattern in glass caused by explosive loading of the entral cavity is shown in Fig. 5. A zone of dense radial fractures can be observed immediately nround the hole. The fracture surfaces are rough and strongly riffled and consist mainly of numerous small cracks whose width is smaller than the thickness of the plate. The zone erminates rather abruptly at a certain radius. Bordering it is a second zone with much wider paced radial cracks. These fractures have a mirror-like surface and penetrate through the ull thickness of the disc. They are evenly and symmetrically distributed around the center-nole. The appearance of these longer cracks seems to indicate a much slower fracture growth. t was further observed that the cracks of the first zone frequently make a distinct and sharp urn as they reach the boundary between the two zones. CHRISTIE and KOLSKY [22] observed similar fracture phenomena in specimens of glass and plastics under impact loading.

The very dense, radial fractures of the first zone are caused by the tensile hoop stresses of the outgoing wave described earlier. In this region the hoop stresses exceed the dynamic ensile strength of the material and consequently form a number of tiny, radial cracks. These racks start separately but do not have much time to grow before the short-duration-pulse nas passed on, since the velocity of crack propagation is much lower than that of the pro-pagating wave. These very densely distributed, independent, small cracks eventually join because of residual stresses at the individual crack tips, thus forming longer fractures with very rough and uneven surfaces. This type of fracture terminates very rapidly at the radius where the tangential tensile stress of the wave drops below the tensile strength of the material.

The wider spaced, radial fractures of the second zone are the extension of some of the racks of the first zone. Their mirror-like and smooth surfaces indicate very clearly that they were each formed by the extension of one individual crack, rather than by the joining of many independent 'cracklets'. It also appears that these fractures propagated at a slower rate. Two major reasons for the formation of these fractures can be proposed; viz.

(1) Due to the discontinuity of displacement along the ring formed by the crack tips, residual hoop stresses are active. They will extend those cracks whose growth ensures the maximum decrease in strain energy.
(2) Although the tensile stress of the wave has dropped below the critical value for initiating new cracks, it will still be sufficient to extend already existing cracks. Less stress is required to cause a crack to grow than to form it.

The mirror surface definitely identifies these cracks as running cracks. A crack extension can take place as long as the full length of the tensile tail has not yet passed by the more

* The penetrant used was ZYGLO Type ZL-22 manufactured by Magnaflux Corp., Chicago, Illinois.

slowly propagating crack tip. The analytical expression for approximate length of this additional crack extension was presented in the previous section.

The earlier observation that a lower stress is required to extend a crack than to initiate one, was demonstrated in a few simple fracture tests in Plexiglass. A disc with four prefabricated cracks of different lengths radiating from a central hole was dynamically loaded at the hole boundary. A few new cracks appeared in the zone immediately around the hole, but no fracture initiation took place at intermediate distances where the extension of the prefabricated cracks was still considerable. An approximately linear relationship was found between crack extension Δl, and length l, of the preexisting crack (Fig. 6). In a full-scale blast in the field the prefabricated cracks of the model are represented by preexisting joints, weaknesses or bedding planes in the rock. In the presence of such preexisting discontinuities, the major crack generation will be in their direction and certainly no uniform fracture can be expected.

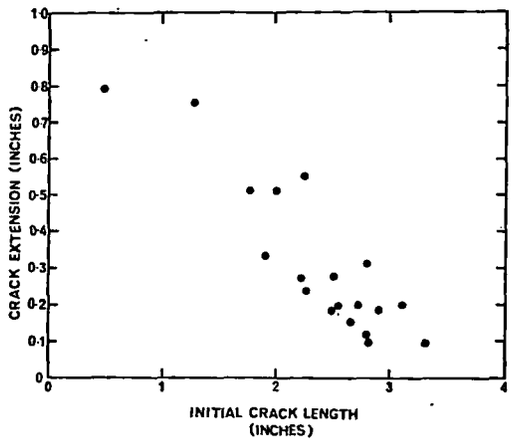

FIG. 6. Dynamic crack extension vs original crack length in spark-loaded Plexiglass disc with $\frac{3}{4}$-in. diameter centerhole.

A few comments on the rather regular and wider spacing of the radial cracks in the second zone seem warranted: as soon as a crack begins to extend, the hoop stresses are released in its immediate vicinity. This release acts in the form of a wave radiating from the crack tip. Thus, within a certain angle of the crack, the chance for new radial cracks is minimized and practically no other radial fractures can start. At points sufficiently far away from the crack, the peak tensile stress is reached before the relief wave arrives and hence an extending crack forms there. This crack in turn again relieves an area around it from hoop stresses. The second zone is thus made up of radially running cracks alternating with fracture-free, stress-relieved segments. The resulting total fracture pattern constitutes, therefore, a very symmetrical arrangement of cracks. In a series of experiments performed on Plexiglass plates of $\frac{1}{2}$-in. thickness, this hoop stress-relieving effect of cracks was demonstrated. Three-quarter-inch diameter center holes of discs with one, two, and four prefabricated cracks were spark-loaded. Figure 7 shows the resulting fracture patterns with a clearly visible stress-relief zone around the prefabricated cracks in which no new radial cracks were generated. In the samples with four symmetrically arranged cracks no new cracks appeared, only the existing ones were extended.

In a last series of tests on Plexiglass the question of the influence of the hole diameter on the degree of fracturing was investigated. A number of discs with centerholes varying in

diameter from $\frac{1}{4}$ to $1\frac{1}{4}$ in. were loaded by a constant input pulse from the spark discharge. The holes were again filled with water to ensure perfect coupling. The resulting fracture patterns are shown in the photographs of Fig. 8. One might expect the longest radial cracks around the smallest cavity, since the peak pressure at the borehole wall is the largest for this case. The experiment showed, however, that the crack lengths for small and medium-sized holes are approximately the same. The crushed and densely fractured zone is largest for the small hole. The generation of these dense fractures is accompanied by a high rate of stress attenuation and thus, despite the higher input pressure, the wave from the smaller hole attenuates to the same stress as the originally weaker wave from the only slightly crushed medium-sized hole at approximately the same radial distance. Furthermore, waves originating from small holes attenuate faster because a small cavity radius a causes a faster stress drop due to the previously given $\sigma_\theta \propto (R/a)^{-3/2}$ relationship. A very practical conclusion can be drawn from these tests: An increase in charge size and in brisance of the explosive or a decrease in decoupling do not necessarily lead to a larger fractured zone or improvement in fragmentation.

Thus, the basic fracture phenomena and the general fracture pattern around a hole, as generated by the outgoing wave, have been established and analysed in theoretical terms and demonstrated in glass and Plexiglass samples. Although the basic principles which determine the dynamic fracture process around an explosive charge were believed to be the same for brittle rock as those for glass and Plexiglass, a separate test series was necessary to verify these concepts and conclusions for rock, the actual material of interest.

For this purpose, four representative rock types were chosen. The properties measured in the laboratory are listed in Table 1. Also listed in this table are laboratory values for the so-called 'dissipation function' [23] or internal friction $1/Q$, which is defined as the ratio of the 'band-width' (frequency interval between half-power points) to the mid-band frequency of a resonance curve (displacement amplitude plotted vs. frequency). For small damping the logarithmic decrement Δ of free vibrations is related to this function in the form $\Delta = \pi/Q$. Thus, the internal friction is small when $1/Q$ is small.

The rock samples were discs of $8\frac{3}{8}$ in. in diameter and 1 in. thickness, with a $\frac{3}{4}$-in. diameter hole in the center. The rock discs were dynamically loaded by spark discharge with a wide range of effective input pressures. The resulting radial fracture patterns, of which typical examples are shown in Fig. 9, turned out to be very similar to those observed in glass. Although not quite as distinct, the two zones of dense and widely spaced fractures are again visible. Branching of the cracks in their later stages seemed to be quite common, particularly in basalt. No crushing could be observed on any of the more than forty samples. Each rock type was exposed to the full range of pressures available from the discharge set-up. All fracture patterns were carefully recorded and a linear relation between crack lengths and peak input pressure was found. This linear increase in crack length with input pressure applied to both fracture zones.

For a given input pressure the crack lengths for granite, marble and basalt were approximately the same, whereas the fractures in slate are up to twice the length of those in the other three rock types. According to the previously developed theory, the crack length should be inversely proportional to the dynamic tensile strength of the material. This would lead to the conclusion that the tensile strength of the slate is considerably smaller than that of the other three rocks. The results from static tensile pull tests, however, invalidate this conclusion. The values for the average tensile strength (Table 1) would rather suggest very long cracks for the granite and marble and the shortest ones for basalt.

TABLE 1. PHYSICAL PROPERTIES OF THE FOUR REPRESENTATIVE ROCK TYPES

Rock type	Basalt	Belgian Black slate	Charcoal granite	Tennessee marble
Density (g/cm³)	2·97	2·70	2·72	2·69
Young's modulus (10^6 lb/in²)	14·50	11·30	7·40	10·22
Poisson's ratio	0·30	0·32	0·26	0·32
P-Wave velocity (ft/sec)	22,200	21,200	15,700	20,000
Shear wave velocity (ft/sec)	11,800	10,900	9850	10,450
Tensile strength (Pull test) (lb/in²)	3700	1850	1200	1240
Compressive strength (lb/in²)	48,800	—	33,000	31,000
Internal friction $1/Q$	252	158	480	189

This difference between the experimental and theoretical results can be partly explained by the absence of any damping or 'internal friction' component in the theoretical model. However, even by taking the $1/Q$ values into account, the differences would not disappear. For instance, slate and marble have about the same 'internal friction', approximately equal dilatational wave velocity, the same Poisson's ratio, and similar tensile strengths, but produce cracks of widely different length; or on the other hand, granite and marble have approximately the same tensile strength and their respective crack lengths were almost the same, despite a vast difference in energy absorption. There is no doubt that energy absorption is a critical factor in the analysis of the dynamic fracture process, and the tests have clearly shown that neither tensile strength nor wave velocity alone determine the length of the radial fractures. But it also became clear that the 'dissipation function' does not yet represent a satisfactory answer. A thorough theoretical and experimental investigation of the dynamic behavior of rock is therefore necessary before a more reliable prediction of wave-generated fractures becomes possible.

An encouraging start in this direction was undertaken by HAKALEHTO [24] who found, with the use of the Hopkinson split-bar method, that the limit to maximum energy transmission is determined by the maximum stress amplitude which can be transmitted unattenuated through the rock specimen.

The previously discussed fracture phenomena were in principle those for a dynamically loaded cavity in an infinite and stress-free medium. All blasting shots, however, take place near a free surface and frequently, for instance, in tunneling, within a static stress field. Both conditions should, therefore, be considered in a study of the fracture process in actual blasting. The presence of a free surface in the near vicinity of a contained explosion is essential for effective fragmentation of the rock, and is a prerequisite for the formation of a crater. As remarked earlier, the phenomenon of scabbing or spalling produced by reflection

of the outgoing pulse is well known and has been extensively investigated. Since the fracture process in the region around the cavity is of main concern here, only those aspects of the reflected wave which affect the immediate fracture pattern around the borehole will be discussed.

When the reflected wave with its tensile radial and tangential component travels back from the free surface, it passes over the region around the hole where it previously had generated radial fractures. Thus, renewed tension is applied particularly to those crack tips which point towards the free surface. The steeper a crack is inclined towards the free surface, the larger will be the tensile stress acting normal to the crack and, consequently, the longer its secondary extension.

This influence of the free surface on the final length of the wave-generated radial fractures was demonstrated with Plexiglass plates. Holes at variable distances from the free boundary were spark-loaded. The resulting fracture patterns (see Fig. 10) indicate quite distinctly preferred fracture in the direction of the shortest line between hole boundary and free surface. In the absence of any gas pressure, only the reflected wave can account for these longer cracks pointing towards the free surface. Thus, the role of the reflected stress wave in cratering is not only to cause scabbing, but also to extend the radial fractures from the cavity towards the free surface.

The influence of a static stress field on the fracture pattern is of importance for underground explosions where either a gravitational or tectonic stress field acts in the region of the borehole. Such a stress field, unless it is hydrostatic, causes a nonuniform stress concentration around the wall of the cavity. That part of the boundary which is under tangential tension will favor the formation of radial cracks, whereas that under tangential compression will suppress it. The zone with the highest tension will always produce longer and denser fractures under dynamic loading by the wave. Although an *in situ* stress field is biaxial in most cases, it is only the difference between the two principal stresses in the plane normal to the borehole axis which will cause a nonuniformity in the fracture pattern. Hence, only a uniaxial static stress field will be considered here.

From the stress concentration around a hole in a plate under uniaxial compression we know that maximum tangential tension at the internal boundary is at those points which, seen from the center of the cavity, are in the direction of the applied stress, and maximum tangential compression is at the points on a line in a direction normal to the applied stress. When the compressive wave is then emitted into the plate from the boundary of the hole, the preferred radial fracture direction will be in the direction with the highest tangential tension, i.e. the direction of the maximum principal stress.

To experimentally verify the fracture process of a dynamically loaded cavity in a uniaxial static stress field, diametrically compressed Plexiglass discs were spark-loaded in the manner described earlier. The uniaxial stress was applied in the form of a bolt-tightened clamp applied at diametrically opposed edges of the disc. The exact force exerted by the clamp was not measured but was in the range of 1000 lb. A typical fracture pattern around a hole in a Plexiglass disc is shown in Fig. 11. The arrows mark the direction of the superposed static stress field. The preferred fracturing in the direction of the maximum principal stress is clearly visible.

In one particular test the influence of a prefabricated crack on the fracture pattern under uniaxial static load was studied. A Plexiglass disc with two prefabricated, diametrically opposed, radial cracks was clamped and spark-loaded. The static stress field acted in a direction normal to the two prefabricated cracks. The resulting fracture pattern indicated

no extension of the prefabricated cracks, but long new cracks were generated in the direction of the applied static stress field. This example demonstrates the important role that *in situ* stresses play in the formation of wave-generated fractures. It is evidently so great, that the relatively easy process of crack extension and progression is suppressed at some locations in favour of crack initiation at others.

Dynamic fracture tests with additional uniaxial static stress were also performed on rock discs. The resulting fractures demonstrate very clearly the influence of the static stress field upon preferred crack direction. Figure 12 shows the results obtained in slate and Tennessee marble. Some of the cracks in the slate, which originally started in a radial direction other than that of the maximum principal stress, eventually curve off into the direction of the applied static stress field.

4. FRACTURE EXTENSION UNDER QUASI-STATIC GAS PRESSURE

Introduction

As mentioned previously, the energy stored in an explosive charge in the form of potential chemical energy is released upon detonation, partly as energy contained in the transient stress wave and partly as energy contained in the expanding combustion products. The kinetic and strain energy of the transmitted stress wave can be determined from stress pulse measurements in the rock at various distances from the explosion. The remaining part of the total energy can be approximately identified as energy stored in the highly compressed combustion gases, although a certain percentage of it will be lost in the form of heat transferred into the surrounding rock. The relatively small amount of energy in the propagating stress wave indicates that the major portion of the explosive energy must be associated with the expanding gas. It would thus seem logical to expect a large number of fractures or extended cracks around an underground explosion, due to the gas pressure.

Nevertheless, almost all previous investigators have neglected and disregarded the gas action and solely concentrated on the wave action, particularly reflection breakage. As a result, very little is known about gas-pressure effects. This is due in part to the negligible attention it has received but also to the adverse conditions which exist in the region around the charge. The stress wave can be measured at a relatively large distance from the source and a rough estimate of the wave parameters in the borehole vicinity can be obtained by extrapolation. The quasi-static stress field of the gas pressure attenuates much faster with distance and thus is hardly picked up by a pressure sensor outside the fracture zone. Furthermore, any sensitive pressure or strain gage is likely to be damaged by the high preceding stress wave before the quasi-static stress ever becomes active.

Because of this lack of information on the gas pressure any study of the fracture process caused by the expanding gases has to rely either on theoretical derivations, which give gas pressures in the range of 10–20 per cent of the peak wall pressure, or to be limited to a qualitative investigation of the general principles and fracture phenomena involved. The latter approach has been chosen here. No numerical results for specific cases are derived, but generally valid principles are established.

The 'equivalent cavity'

The gas pressure in the cavity is active for a considerably longer time than the transient stresses of the emitted wave. The stress field caused by the gas pressure can therefore be considered to be quasi-static and secondary in time to the stress wave. This means that the

wave-generated radial fractures around the cavity already exist when the gas starts to expand. The gas can therefore penetrate into the cracks. In investigating the degree and type of fragmentation caused by the gas pressure one then has to consider the pressure as acting over a much larger opening than the original borehole. What kind of stress field is generated by a pressurized radially-fractured cavity? KUTTER [25] investigated this problem analytically and defined as 'equivalent cavity' that size of hole which, when under the same pressure, produces in the region beyond the radial fractures the same stress field as the pressurized, radially-fractured borehole. He made a number of simplifying assumptions, such as considering the rock elastic and isotropic, limiting the extent of the dynamically induced fragmentation to symmetrically distributed radial cracks of equal length and (in order to allow a static stress analysis) assuming the gas pressure to remain constant during crack extension. With these assumptions the problem could be reduced to that of an infinite plate under biaxial tension and plane strain, containing a central circular hole with radial cracks. The analytical solution of the stress field around a star-cracked cavity was then obtained by conformal mapping. Although the solution is only for the two-dimensional case or cylindrical borehole it is valid to apply the results concerning the 'equivalent cavity' also to the three-dimensional opening of a spherical charge.

The results showed very clearly that with increasing crack number the stress field approaches that of an uncracked cavity with a diameter approximately equal to that of the radially fractured region. The more radial cracks there are, the closer the similarity. Six, equally spaced cracks bring the two solutions already very close together. Thus for the practical purpose of predicting fracture propagation produced by the gas, the full gas pressure can be assumed to act over an equivalent cavity which has a diameter equal to that of the cracked zone close to the borehole.

It may, however, be unrealistic to assume that in practice the gas penetrates into all the cracks since these may initially be very tight, hairline cracks. It is more than likely that a considerable pressure drop occurs by gas flow into the cracks. An idea of the influence of partially pressurized cracks can be obtained by examining three limiting cases: (1) the pressurized uncracked hole, (2) the radially fractured hole with gas pressure acting in the hole only and (3) the radially fractured hole with full gas pressure acting in the hole and in the cracks.

With the cavity as the unit circle, R the radius of the cracked region, r the radial distance from the center of the cavity to any arbitrary point, and p the gas pressure, the principal stresses outside the fractured zone of a cylindrical hole are for

Case (1) $$\sigma_r^{(1)} = -\sigma_\theta^{(1)} = p\frac{1}{r^2}$$

Case (2) $$\sigma_r^{(2)} = \frac{p}{r};\ \sigma_\theta^{(2)} = 0 \qquad \text{For } 1 < r < R$$

$$\sigma_r^{(2)} = -\sigma_\theta^{(2)} \simeq p\frac{R}{r^2} \qquad \text{For } r > R$$

Case (3) $$\sigma_r^{(3)} = -\sigma_\theta^{(3)} \simeq p\frac{R^2}{r^2}.$$

Thus, for the cylindrical hole, the radial and tangential stresses in the three cases are related in the ratio:

$$\sigma^{(1)} : \sigma^{(2)} : \sigma^{(3)} = 1 : R : R^2.$$

For the spherical case the same basic equilibrium conditions yield a slightly different relation:

$$\sigma^{(1)} : \sigma^{(2)} : \sigma^{(3)} = 1 : R : R^3.$$

This comparison demonstrates very clearly the important role the radial fractures play in determining the stresses around the cavity. For example, the stresses around a pressurized cylindrical cavity with pressurized radial cracks of a length equal to two hole radii are nine times higher than those around a plain, pressurized borehole. The actual field situation will be somewhere between case (2) and case (3), but will approach case (3) as the time progresses. It appears therefore that the gas-induced stresses around a cavity with wave-generated fractures may be more than sufficient for extensive crack propagation and fragmentation.

Another idealization which was necessary for the theoretical analysis but which hardly holds true for the practical case is that of equal crack length. But is the concept of the 'equivalent cavity' still valid or are considerable modifications necessary if for instance one crack is longer than the remaining ones? KUTTER [25] investigated this problem by comparing the photoelastic fringe pattern of: (i) a pressurized cavity with radial cracks all of equal length except one which was longer, with (ii) the fringe pattern of the 'equivalent cavity' having only one small crack equal in length to the amount by which the long crack exceeded the others in the first case. Both fringe patterns proved to be very similar outside the cracked region (Fig. 13). It is therefore valid to consider the stress field outside the fractured zone of a star-cracked cavity, with one crack longer than the rest, as equivalent to an 'equivalent cavity' with one small crack. The fringe pattern also demonstrates very clearly the higher stress concentration at the tip of the longest crack. It therefore follows that the longest crack will require the lowest critical pressure for propagation, i.e. it is the least stable of all the cracks.

Critical pressure for crack extension

The knowledge of the stress field around a pressurized, fractured cavity is not sufficient for determining the critical pressure for crack propagation. For this purpose a failure criterion has to be established. The critical pressure can be predicted theoretically from an extension of the previously described stress analysis of a star crack together with a failure criterion based on energy considerations, i.e. Griffith's failure criterion. This derivation is described elsewhere [25] and only the relevant results are summarized here.

For a given crack length the smallest critical pressure for extension of the fractures is that for two diametrically opposed cracks. The critical pressure increases with the number of cracks which radiate from the cavity. The only exception is that for the single crack which will propagate at a pressure approximately equal to that required for four symmetrically arranged cracks. The crack length significantly influences the critical pressure only for cracks smaller than the cavity diameter; within this range the critical pressure increases appreciably with decreasing crack length. For cracks longer than the hole diameter there is no significant decrease in the critical pressure.

In practice, therefore, crack extension is likely to continue, once initiated, since the critical pressure decreases with increasing crack length. The decrease in gas pressure due to cavity expansion and gas penetration into the cracks is therefore not necessarily a reason for termination of crack growth. Also, for effective extension of the fracture by gas, the dynamically generated fractures should be as widely spaced as possible, and the dense radial fracture zone should be kept at a minimum, so that the secondary dynamic fractures are of sufficient

ı for optimum crack growth. The crushed and highly fractured zone appears to have an se effect on crack extension under gas pressure, as well as being undesirable because ;h energy absorption.

rimental results

:est series modelling the gas pressure action was conducted on two-dimensional samples :rify and demonstrate the theoretical principles derived above. The pressure exerted ıe expanding combustion products was simulated by oil pressure. The pressurized oil contained in the center-cavity by sandwiching the sample disc between two hardened less-steel plates (Fig. 14). For photoelastic tests the bottom plate could be exchanged plate with a window, similar to the top plate. With this experimental set-up the oil

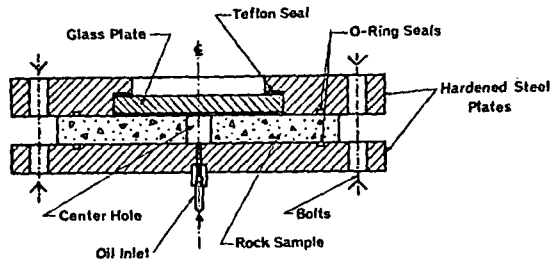

FIG. 14. Cross section of pressure cell for static loading of cavities.

:ssure was acting not only on the hole boundary and in the cracks, but also over the flat :a of the sample which lay within the O-ring seals. The stress in the direction of the hole s, however, can be considered to be of negligible influence on the crack extension process. The major objective of this static test series was to demonstrate the overriding influence preexisting radial fractures on the critical pressure. Because of the ease of fracture servation the first test series was performed on Plexiglas discs with a centerhole and with rious arrangements of radial cracks i.e. different lengths from sample to sample but of ual lengths within each sample. The cracks were induced with a thin saw blade, and an ra-thin dental saw was used for the tip section of the crack. The samples were inserted o the pressure cell and pressurized to failure. The striking decrease in critical pressure th the presence of radial fractures was successfully shown. The critical pressure for a vity with radial cracks was found to be 50 per cent or less of that for an uncracked hole. the limited number of tests on Plexiglass little systematic influence of the crack length the critical pressure was found. The uncertain variations in the sharpness of the fabricated ıck tips together with the fact that, according to the theoretical curves, there is no sub-ntial variation in the critical pressure for crack lengths in the range of one to three vity radii, may account for this deviation from the theoretical results.

In another series, spark-fractured discs were subjected to internal static load. The remark-le result of these tests was the observation that, without exception, the longest crack vays propagated first and in the process it also caused the extension of the crack diametric-y opposed to it. The sample thus failed without any appreciable growth of the remaining lial cracks. The discs always broke into two halves.

To study the influence of a superposed, external static stress field, a Plexiglass sample ich had been previously loaded dynamically by a uniaxial external stress, was subse-ently loaded statically in the cell. Under the static loading, however, the external stress

field was rotated 90° compared to that for the dynamic loading. Thus, before pressurizing the cavity, the longest cracks were normal to the direction of the external stress field. After loading the sample to its critical pressure, the failure did not occur in the direction of the longest crack, but in the direction of the superimposed stress field. The resulting fracture pattern is shown in Fig. 15 where the small arrows indicate the crack tips before static loading, and the large arrows indicate the direction of the external stress field. This test rather strikingly demonstrates the enormous influence that an *in situ* stress field can have on the final fracture process.

In a final test series a large number of the previously described dynamically fractured rock discs were subjected to static 'gas loading' inside the centerhole and cracks. Only those dynamically fractured rock discs, whose radial fractures were small enough not to stretch beyond the O-ring seal of the pressure cell were used. For comparison a series of uncracked rock discs with a plain centerhole was also loaded to failure. Here again, the enormous decrease of the critical pressure due to the presence of radial fractures became

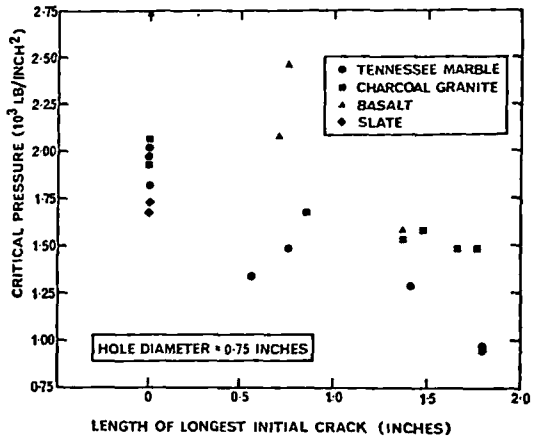

FIG. 16. Critical pressure for rock discs vs length of largest crack before static loading.

apparent. As in the Plexiglass discs, the longest crack was the first to grow and cause failure. The relationship between longest crack length (before static loading) and the critical pressure is illustrated in Fig. 16. It is seen that the critical pressure appears to decrease approximately linearly with increasing crack length. These test results thus prove again that for effective crack extension under gas pressure the presence of dynamically induced fractures is essential. Of some side interest are the pressures for the failure of the discs with a plain centerhole. The critical pressure for this type of expansion test gives an indirect measurement of the tensile strength. Comparing these values with those from the pull test yields practically no agreement. Although again basalt is the rock with the highest tensile strength, some of the strength values are higher, others are lower than in the pull test. It probably is significant that in this test the slate appears to be the rock with the lowest tensile strength.

Finally, the influence of a free surface on the development of gas expansion fractures will be examined. The presence of a free surface close to the contained explosion is an essential requirement for crater formation. Although the free surface is of particular importance for wave-generated fractures, it also influences the fracture process due to gas expan-

sion. The closer the free surface is situated to the 'equivalent cavity', the more will it influence the hoop stresses around it.

Relevant conclusions can be drawn from the analytical solution for the plane case of a semi-infinite plate containing a pressurized circular hole. The solution to this problem can be derived from the general case of the stress field in regions delimited by two circles, as given by SAVIN [26]. The tangential tensile stress at the boundary of the cavity is no longer uniform as in the earlier case of a cavity in an infinite medium, but varies with the angle ϕ [see Fig. 17(a)]. It maximizes at those points of the hole contour for which ϕ is a maximum:

$$\sigma_{\theta\,\max} = p\,\frac{d^2 + R^2}{d^2 - R^2}.$$

The maximum tension thus increases as the cavity approaches the free surface. Tensile stresses are also generated at the free surface, with a maximum at point A. However, for most blast geometries, where d is generally larger than the cavity diameter, the surface tension is smaller than the tensile hoop stresses. Applying the analytical results to the actual blasting situation and in particular to the fracture process due to gas expansion, one now has an additional criterium for preferred fracture direction. Those radial fractures within the 'equivalent cavity' which terminate in the zones of maximum tangential tension, propagate at the lowest critical pressure and represent therefore a preferred fracture direction. These

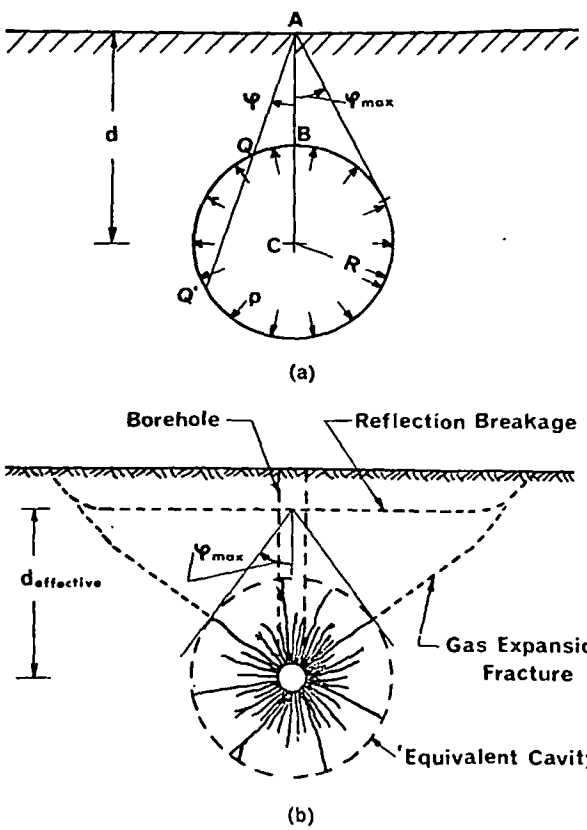

FIG. 17. Influence of free surface on stress distribution around cavity. (a) Semi-infinite plane containing a circular hole. (b) Schematic of crater geometry.

cracks grow towards the free surface and probably determine largely the final crater boundary in the vicinity of the charge. One has to keep in mind that the free surface at the time of the gas action has already been altered by reflection breakage and the effective parameter ϵ greatly reduced from its original value [Fig. 17(b)] thus further increasing the tensile hoop stresses compared to those computed from the original blast geometry. This is thus yet another way in which preconditioning by the precursory wave can aid fragmentation by the gases, i.e. generation of the radially fractured 'equivalent cavity' and surface slabbing are beneficiary if not absolutely necessary.

There are situations where a free surface is completely absent. Such is the case for presplitting, where a smooth fracture plane is created in solid rock. There, of course, the above described surface effects are missing, but all the other earlier described fracture phenomena are valid. KUTTER and FAIRHURST [27] have given a detailed explanation of the fracture mechanism in presplitting based on these experiments and fracture investigations.

5. SUMMARY AND CONCLUSIONS

The fracture phenomena which occur in the immediate vicinity of a charge in an underground explosion have been examined in detail, by studying the effects of the emitted stress wave and of the expanding pressurized gas separately. The problem was explored theoretically by wave and stress analysis and experimentally by fragmentation tests on Plexiglass and rock models. In the model tests the explosion wave was simulated by a pulse generated by underwater spark discharge, and the expanding combustion products by pressurized oil. In this way, i.e. by separating the two principal forces which act in an underground explosion, it was possible to assess the respective roles each plays in the blasting process.

The fracture pattern generated by the wave is that of a dense, radially fractured zone immediately around the cavity, followed by a ring of wider spaced radial cracks. It was found that the width of the radially fractured zone depends not only on the tensile strength and wave velocity of the rock, the input pressure and the detonation velocity of the explosive, but to a large degree also on the extent of energy absorption in the rock mass. It was furthermore demonstrated that, for a given borehole size, increase of explosive charge beyond an optimum amount does not increase the fractured zone but results only in additional crushing around the cavity. The diameter of the fractured zone was theoretically computed to be around six hole diameters for a spherical charge, and nine hole diameters for a cylindrical charge. It is in this expanded or 'equivalent cavity' that the gas pressure becomes active rather than, as generally assumed, the original borehole. The concept of the 'equivalent cavity' leads then to a more extensive stressed region and consequently to more extensive crack propagation by gas expansion.

This, in summary, constitutes the basic fracture process. It is altered and influenced, however, by:

1. Preexisting fractures, such as joints, bedding planes and discontinuities, which dominate the nature of the fracture pattern. No new fractures are generated in their immediate vicinity but preexisting ones are extended to greater lengths at lower stresses than newly generated fractures would be. The enormous influence of the geologic structure, i.e. joint spacing and separation, schistosity and lamination of beds, on the result of a blast can be demonstrated and explained in this way.
2. The underground stress field. Both wave and gas-generated fractures propagate preferably in the direction of the maximum principal stress. This effect has been

shown to be so strong that it can even eliminate the influence of preexisting fractures. This effect explains the difficulty in presplitting the roof section of deep tunnels.

3. The nearby free surface. Besides the well-known phenomenon of reflection breakage, the presence of a free boundary also favors the generation and extension of those cracks which point towards the surface.

Finally, this investigation has demonstrated that high-pressure gases play a considerably more important role in blasting than generally anticipated and admitted. It has been equally clearly demonstrated that the gas pressure alone would not be very effective. Only the preconditioning, i.e. the precracking and effective widening of the cavity by the emitted wave and the reduction of the burden by surface spalling make it possible that the expanding gases are fully utilized in rock fragmentation. Neither the strain wave nor the gas pressure can therefore be considered exclusively responsible for rock fragmentation in blasting. Each has an important role.

REFERENCES

1. Rinehart J. S. On fractures caused by explosions and impacts. *Colo. Sch. Mines Q.* **55**, (4) 155 (1960).
2. Duvall W. I. and Atchison T. C. *Rock Breakage by Explosives*, p. 52, U.S. Bureau of Mines R.I. 5356 (1957).
3. Starfield A. M. Strain Wave Theory in Rock Blasting, *Proceedings of the Eighth Symposium on Rock Mechanics*, University of Minnesota, Minneapolis (1966).
4. Hino K. Theory of blasting with concentrated charge. *J. ind. Explos. Soc. Japan* **15**, (4) 233–249 (1954).
5. Porter D. D. *Crater Formation in Plaster of Paris Models by Enclosed Charges*, p. 96, M.S. Thesis T-940, Colorado School of Mines (1961).
6. Langefors U. and Kihlström B. *The Modern Technique of Rock Blasting*, p. 405, Wiley, New York (1963).
7. Clark L. D. and Saluja S. S. Blasting mechanics. *Trans. Am. Inst. Min. Engrs* **229**, 78–90 (1964).
8. Saluja S. S. Mechanism of Rock Failure under the Action of Explosives, *Proceedings of the Ninth Rock Mechanics Symposium*, Colorado School of Mines, Golden, AIME, New York (1968).
9. Fogelson D. E., Duvall W. I. and Atchison T. C. *Strain Energy in Explosion-Generated Strain Pulses*, p. 17, U.S. Bureau of Mines R.I. 5514 (1959).
10. Nicholls H. R. and Hooker V. E. *Comparative Studies of Explosives in Salt*, p. 46, U.S. Bureau of Mines R.I. 6041 (1962).
11. Kisslinger C. *The Generation of the Primary Seismic Signal by a Contained Explosion*, p. 85, Acoustics and Seismic Laboratory, Institute of Science and Technology, University of Michigan, VESIAC State-of-the-Art Report 4410-48-X (1963).
12. Sharpe J. A. The production of elastic waves by explosion pressures—I. *Geophysics* **7**, (2) 144–154 (1942).
13. Blake F. G. Jr. Spherical wave propagation in solid media. *J. acoust. Soc. Am.* **24**, (2) 211–215 (1952).
14. Duvall W. I. Strain-wave shapes in rock near explosions. *Geophysics* **18**, (2) 310–323 (1953).
15. Selberg H. L. Transient compression waves from spherical and cylindrical cavities. *Ark. Fys.* **5**, (7) 97–108 (1952).
16. Heelan P. A. Radiation from a cylindrical source of finite length. *Geophysics* **18**, 685–696 (1953).
17. Jordan D. W. The stress-wave from a finite cylindrical explosive source. *J. Math. Mech.* **11**, 503–552 (1962).
18. Kutter H. K. Tangential tensile peak of spherical waves. To be published.
19. Kutter H. K. *The Interaction between Stress Wave and Gas Pressure in the Fracture Process of an Underground Explosion in Rock, with Particular Application to Presplitting*, p. 234, Ph.D. Thesis, University of Minnesota, Minneapolis (1967).
20. Aso K. *Phenomena Involved in Presplitting by Blasting*, p. 177, Ph.D. Thesis 66-1, Department of Mineral Engineering, Stanford University (1966).
21. Kutter H. K. *The Electrohydraulic Effect: Potential Application in Rock Fragmentation*, p. 35, U.S. Bureau of Mines R.I. 7317 (1969).
22. Christie D. G. and Kolsky H. The fractures produced in glass and plastics by the passage of stress waves—III. *J. Soc. Glass Technol.* **36**, 65–73 (1952).
23. Huntington H. B. The elastic constants of crystals. *Solid St. Phys.* **7**, 213–351 (1960).

24. HAKALEHTO K. O. *A Study of the Dynamic Behavior of Rock Using the Hopkinson Split Bar Method*, p. 82, M.S. Thesis, University of Minnesota (1967).
25. KUTTER H. K. Stress analysis of a pressurized circular hole with radial cracks in an infinite elastic plate. *Int. J. Fracture Mech.* 6, (3) 233–247 (1970).
26. SAVIN G. N. *Stress Concentration around Holes*, p. 430, Pergamon Press, Oxford (1961).
27. KUTTER H. K. and FAIRHURST C. The Roles of Stress Wave and Gas Pressure in Presplitting, in *Proceedings of the Ninth Rock Mechanics Symposium*, Chap. 14, Colorado School of Mines, Golden, AIME, New York (1968).
28. ALLEN W. A. and GOLDSMITH W. Elastic description of a high-amplitude spherical pulse in steel. *J. appl. Phys.* 26, (1) 69–74 (1955).

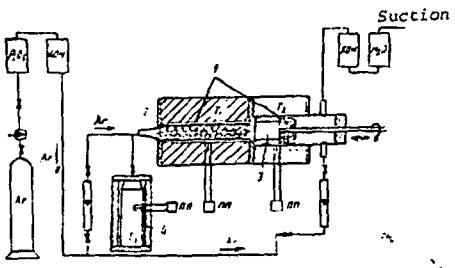

Fig.1 Diagram of the experimental apparatus. 1) Quartz reactor, 2) titanium sponge, 3) drum with microspheres, 4) chloride evaporator.

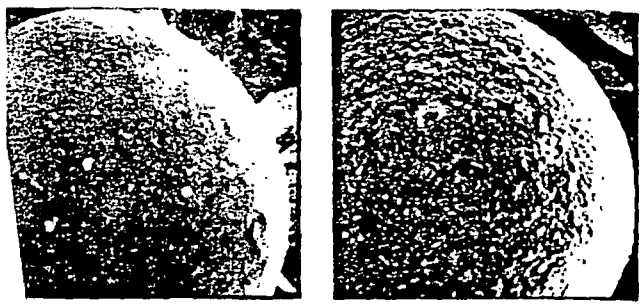

a b

Fig.2 Photomicrographs of the surface of zirconium dioxide spheres; initial particles (a) and particles coated with titanium (b).

UDC 669.295.054+669.292

Oxidation of vanadium in solutions during recovery from titanium production wastes

L V Denisova, V I Cherkashin, A V Skiyar, T M Petrenko and V M Pechennikova (Institute of Titanium - Zaporozh's Industrial Institute)

Summary

Ammonium persulphate has undoubted advantages over sodium hypochlorite as a solid oxidising agent. The oxidation process occurs without dilution of the solutions, without reduction of the acidity, and without negative side effects. The length of the process is measured in minutes.

The mechanism and kinetics of the oxidation of vanadium by ammonium persulphate were investigated. It was shown that the process is described by second-order reactions. The activation energy of the process at temperatures above 60°C amounts to 26.9kcal/g-atom.

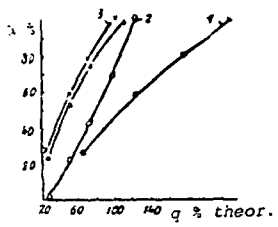

Fig.1

The dependence of the degree of oxidation of vanadium on the consumption of the oxidising agent at temperatures °C: 1 - 50, 2 - 70, 3 - 80, 4 - 90.

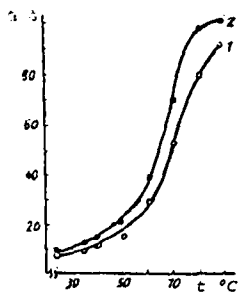

Fig.2

The effect of temperature on the degree of oxidation of vanadium. Samples taken 5 (1) and 10 (2) min.after addition of oxidising agent.

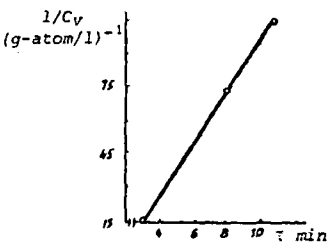

Fig.3 Variation of the reciprocal of the concentration of unoxidised vanadium (g-atom) during oxidation.

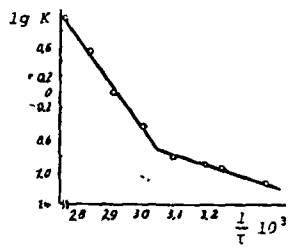

Fig.4 The dependence of the logarithm of the rate constant on the reciprocal of the temperature during the oxidation of vanadium by ammonium persulphate. Length of process 5 min.

Table: Variation of the rate constant and temperature coefficient of the rate constant with variation of temperature

t °C	K l/min·g-atom	Temperature coefficient
23	0.076	-
35	0.112	1.49
40	0.132	1.24
50	0.166	1.25
60	0.38	2.28
70	1.05	2.76
80	3.55	3.39
90	9.56	2.71